DOE/DP/10560-6
Distribution Category: UC-400

DOE/DP/10560--6

DE90 001996

INERTIAL FUSION RESEARCH

1988 ANNUAL TECHNICAL REPORT

KMS Fusion, Inc.
3621 South State Road
Ann Arbor, Michigan 48108

Prepared for the U.S. Department of Energy
San Francisco Operations Office
under Contract No. DE-AC03-87DP10560

Executive Editor: Dr. J. T. Larsen

Period Covered: October 1987–September 1988

MASTER

DISTRIBUTION OF THIS DOCUMENT IS UNLIMITED

DO NOT MICROFILM
THIS PAGE

TABLE OF CONTENTS

DOE/DP/10560--6

DE90 001996

FOREWORD

As we near the end of the 1980s, we are becoming more aware of the environmental problems we are creating for ourselves. Hardly a day goes by without some mention in our newspapers of the increased pollution about us. From massive oil spills to the greenhouse effect, to acid raid, to the destruction of the ozone layer, to the pollution of the atmosphere over our cities, to nuclear reactor accidents, all of these portend a monumental disaster in the coming decades. Our continued population growth, coupled with our demand for more conveniences and labor-saving devices, requires an ever-increasing expenditure of energy. Because our energy economy is based upon fossil fuels, most of the environmental problems will only continue to get worse. Yet none of us wishes to return to the lifestyle of a century ago, in which the motor car was only a dream and air travel thought to be impossible. We must find a solution that will allow continued energy production while minimizing the impact on our surroundings. As we prepare to enter the last decade of the century, we must take an active role in making the earth a better place for future generations to live. KMS Fusion (KMSF) has been striving for more than 17 years to accomplish one purpose: the development of a clean, safe, and abundant source of energy—fusion energy.

More than one year ago, we set in motion a plan to strengthen KMSF's participation in the federally funded inertial confinement fusion (ICF) program sponsored by the Department of Energy. We have increased our research into target fabrication technology while maintaining a high level of effort in our fusion experiments. With this strategy, we have become closely integrated into the mainline fusion efforts at the national laboratories. KMSF is enlarging its responsibility for a broader development of advanced targets for future experiments and for producing the precision targets needed for today's experiments. This has resulted in a wider range of technical tasks and programmatic responsibilities being assigned to KMSF. With this increased participation in the national program have come increased resources, some of which we expect to devote to on-site support at the national laboratories during the next year.

The national ICF program has achieved some remarkable successes during the past two years. Technical accomplishments have given us the confidence to develop plans for the next step toward demonstrating the production of fusion energy. The ICF program began to address the issues and requirements for the next fusion facility, dubbed the Laboratory Microfusion Facility, in 1985. A comprehensive planning period was initiated. The first phase of that effort was completed in the summer of 1988, and defined the issues and parameters associated with the target chamber area. The second phase, to be completed in 1990, will address the driver issues. After completion of both phases, a plan will be put forth for the construction of the facility, which would be the forerunner of a demonstration power plant.

This Annual Technical Report summarizes the unclassified components of our ICF research activities for the period beginning October 1987 through September 1988. The report is organized into three main technical sections: the first is devoted to our progress in materials development and target fabrication technology, the second describes our research in laser technology development, and the third covers laser/plasma interaction experiments.

In the coming years, we look forward to continued technical achievements. These successes will lead to the eventual demonstration of unlimited clean energy production. The realization of our goal will be accomplished only by many hours of experiments, trials and errors, accompanied by the heartbreak of failure and rewarded by the joy of success. The researchers at KMSF are brought together by this challenge; these researchers have made the commitment to provide a better environment for future generations.

Jon T. Larsen
Vice President, Fusion Programs

TARGET FABRICATION TECHNOLOGY

SECTION ONE

Scientific Editor, Dr. R. L. Downs

Introduction

One of KMS Fusion's materials and target research functions is to provide program-wide support for inertial confinement fusion (ICF) target experiments. We provide this support in a variety of areas. In addition to supplying targets for the program, we conduct research and development work in target fabrication techniques, coating processes, and characterization methods to ensure that these targets meet today's and tomorrow's needs. We also maintain a significant research effort in cryogenic technology, since targets with liquid or solid fuel are essential to future progress in ICF. Finally, we have increased our level of effort in developing the technology for fabricating and characterizing multimillimeter-diameter shells, which have near-term application in cryogenics research and long-term application for use with large ICF drivers.

Cryogenic Technology

Beta-Heating Modeling Studies. The use of thermal energy from β-particles (produced in tritium decay) to sublime DT ice in a large fuel capsule and generate a uniform ice layer continues to be an important area of research. During the course of this year, our mathematical (computational) model describing this process was refined and expanded to improve its predictive capabilities for the behavior of frozen fuel in a realistic (nonideal) experimental cryogenic environment.

Beta-Heating Equipment Modification and Capabilities. Last year we built a cryogenic apparatus and tested the β-heating model's prediction that ice redistribution could occur in a reasonable time. The isothermal nature of the system was demonstrated by showing that frozen HD in a 1 mm glass shell does not move over a three-day period, even when exposed to optical documentation illumination. Using the same shell with DT, we have now shown that the structure of a thin frozen fuel layer undergoes spontaneous change over a period of hours that can be attributed only to sublimation induced by β-heating.

After modifying the apparatus to accommodate larger shells with low aspect ratios (<20) and incorporating a "tent" (polymer film) mounting scheme for the shells, we conducted experiments with a 3 mm shell that contained sufficient fuel to produce an approximately 30 μm uniform ice layer. For recording the movement of the condensed fuel, we incorporated "sandwich" holographic interferometry, a technique first developed "on the bench," into the β-heating apparatus.

Cryogenic DT Pressure Intensifier for Los Alamos National Laboratory. The DT pressure intensification module we designed for Los Alamos National Laboratory (LANL) was fabricated at LANL and we assisted in its installation and initial testing. The results of our work on this and the other cryogenic topics is described in Section 1.1.

Polymer Shell Technology

Stripping Gas Droplet Generator. Using a double-nozzle stripping gas droplet generator and a vertical drying column, we have produced thin-walled polystyrene (PS) shells in size ranges suitable for all current target needs. This simple method has proven so successful that it has replaced our previous fabrication method.

Effect of Molecular Weight on Polystyrene Shell Formation. With our acoustically destabilized single-orifice droplet generator, we explored the effect of polymer molecular weight on PS shell properties and discovered that the production of thin-walled PS shells was restricted to a fairly narrow "average" molecular weight of the polymer, achieved by blending high and low molecular weight components.

Statistical Experiments. In addition to examining the effect of polymer material properties on shell characteristics, we began a series of statistically designed experiments to identify and then optimize the effect of shell blowing conditions on shell characteristics. All of our progress in polymer shell technology is described in Section 1.2.

Glass Shell Technology

Development activities, reported in Section 1.3, continued in three areas: Macroshell™ targets with diameters greater than 2 mm and low aspect ratios (for use in β-heating experiments), shells with diameters from 1 to 2 mm and very thin walls (for Nova experiments), and shells with submillimeter diameters and thick walls (also for Nova). Several approaches are being investigated to fabricate this wide variety of shells.

Macroshell™ Target Development. We continued development work on the two-step process for producing Macroshell™ targets. This process involves formation of a spherical void in a glass cylinder and subsequent machining into a shell on a three-point lapping apparatus. We built and installed a lapping device, patterned after one in use at LANL, and used it to make shells from borosilicate glass cylinders. A sample of these shells was tested for compressive and tensile strength. Since two of the three shells subjected to high pressure failed the tensile strength test, a development effort was initiated to enhance the strength of the shells.

Permeant Gases in the Furnace Ambience. Most of our glass shells are still fabricated in drop tower furnaces. We have found that replacing air in the furnace with a gas that can rapidly diffuse through the shell wall results in much larger shells. Use of such a gas allows the blowing gases present in the starting materials to expand the shell to much larger sizes than would otherwise be produced. The phenomenon is well established for water vapor as the diffusing gas and it has also been shown qualitatively for helium. This year, more quantitative measurements of this phenomenon with helium and neon were taken. We hoped that helium and neon would be alternatives to water for producing large, thin shells from metal-organic gel starting materials. These gases might make larger shells and would not corrode the inner shell surfaces as does water vapor. A few such shells were produced, but the quality was poor. When used in the absence of water vapor, the dry gases promoted severe fragmentation of the starting material. Yields of large shells were extremely low, and serious doubts were cast on the utility of this approach to produce thin-walled shells with diameters from 1.5 to 2.0 mm.

Gel Composition Study. A current high priority for ICF experiments is shells that are less than 1 mm in diameter, have moderately thick walls, and are of higher quality than has previously been available. To increase the quality of these shells, we investigated the effect on shell size and wall thickness uniformity of total alkali concentration in a sodium-, potassium-, and rubidium-containing borosilicate glass. Using a fixed alkali ratio, optimized in previous experiments, we varied the total alkali oxide ratio from 5 to 35 mol% and identified a maximum in shell wall thickness uniformity at 20 mol% total alkali oxide. Subsequent statistically designed experiments identified the best processing conditions for highest quality shells with a given size and wall thickness.

Coating Technology

Development of CH(GDP) Polymer Coatings. We attained a significant improvement in the surface smoothness of CH coatings deposited by glow discharge polymerization (GDP) onto glass. The reduction (and, in some cases, elimination) of surface mounds and a dramatic reduction in background texture were accomplished through a series of modifications of the coating apparatus. Complete elimination of the background texture was finally achieved with the use of a helical resonator coater of Lawrence Livermore National Laboratory design. Density and refractive index measurements were made on the CH(GDP) films.

Using an RF-excited oxygen-argon plasma, we successfully etched (thinned) both CH(GDP) coatings on glass shells and free-standing parylene films.

Development of Target Diagnostic Layers. A combination of several techniques was required to meet requirements for targets with special features useful for diagnosing the implosion process. A thin 4π coating of KCl was produced by evaporation onto glass and plastic shells. Since water vapor attacks the KCl coating rapidly once the coating system is opened to the atmosphere, we modified the coater to incorporate an RF coil and introduced a hydrocarbon gas to produce a thin, protective coating (in situ) of a CH(GDP) material on top of the KCl. To provide shells with perturbations or bumps of specified dimensions, we developed a technique to deposit aluminum through a carefully designed mask. Bumps of low-atomic-number material were produced by heating and attaching PS beads to a CH-coated shell.

Measurement of CH(GDP) Properties. We have begun work to determine the density and the index of refraction of CH(GDP) films. This is important in shell characterization, which is critical to the correct interpretation of ICF experiments. Details of this work, as well as the other areas of coating technology mentioned above, may be found in Section 1.4.

Characterization Technology

Measurement of the Thickness and Uniformity of KCl Coatings. Radiography is being developed to determine the uniformity of KCl-coated PS shells and, in combination with weighing a batch of shells before and after coating, it has also been used to establish shell-to-shell coating variation from a batch average coating thickness.

Corrections for Radiographic Image Analysis. Distortions arising from the fast Fourier transform (FFT) of radiographic images of ICF targets have been identified through a detailed examination of the whole analysis procedure. Systematic errors have been corrected and the magnitude of random errors established.

Characterization of Macroshell™ Targets. The geometrical properties of transparent multimillimeter glass shells, or the spherically shaped cavities in glass matrices that are precursors to the shells, are being determined by FFT of their optical images. These images are obtained with a newly purchased optical profile projection instrument, from which shape contour data can be automatically acquired and subsequently analyzed by computer. This results in a greatly accelerated analysis process. Using this system, we believe that the uncorrectable procedural errors for noncircularity measurements are less than 0.1%.

Characterization work is reported in Section 1.5.

SECTION 1.1

Cryogenic Technology

Heat generated by the radioactive decay of tritium (β-heating), for a sufficient amount of tritium, will cause DT ice inside a spherical shell to sublime. The thicker regions of a nonuniform layer are slightly warmer than the thinner regions, so the net effect of sublimation from the warmer regions to the colder regions is to produce a uniform ice layer. Since 1985, we have been working to develop a model of this process. We have made considerable progress in modeling both the rate of DT ice redistribution and the final ice configuration, and have accounted for realistic enclosure designs and temperature distributions.

On the experimental front, significant progress has been made at both Los Alamos National Laboratory[1] (LANL) and KMS Fusion[2] (KMSF) in the demonstration of this process in the laboratory. Selected experimental results have been incorporated in the model to increase the accuracy of its predictive capability for DT ice redistribution rates.

1.1.1 Production of Uniform Solid DT Layers by β-Heating: Modeling Studies

Analytical and computational modeling permits us to address three questions: (1) How rapidly will the DT ice in a fuel capsule redistribute itself? (2) What will be the final configuration of this ice? (3) What experimental constraints or system design criteria must be emphasized to ensure an acceptable rate of redistribution and final ice uniformity?

We know from previous work that, for a spherically symmetric enclosure, there exist realistic methods of positioning and holding a cryogenic DT target that would cause less than a 1% ice layer nonuniformity.[3] We have just completed a new mathematical/numerical formulation to model those features of the experimental hardware that can affect this achievable ice distribution.

The new formulation incorporates a two-dimensional representation of the mass/energy transfer in calculating the rate of DT ice redistribution. It is based upon a combination of selected experimental results, a diffusivity representation for the DT mass transfer, and a pseudo-thermal conductivity to describe the transfer of energy across the gas/vapor phase (where "gas" refers to ^{3}He and "vapor" to gaseous DT) of the cryogenic target. Consistent with the results of our one-dimensional modeling,[4] the important physical parameters are target temperature and dimensions, the ^{3}He background pressure in the target (related directly to the target age), and total DT content in the target.

The redistribution of DT ice is a transfer of mass that is driven by the local deposition and transfer of energy produced in the radioactive decay of tritium. For targets relevant to near-term experiments, this β-energy is deposited primarily in the ice layer. Eventually, this thermal energy must be removed from the target. It is transported by the following mechanisms:

1. Sublimation and condensation associated with DT ice redistribution.
2. Gaseous conduction across the gas/vapor volume.
3. Radial and tangential conduction through the ice and the target wall.
4. Conduction along the target support.
5. Conduction/convection through the exchange gas that couples the target to the enclosure.

The heat transfer, in reality, is quite complex and multidimensional. However, because of geometric symmetry, two dimensions, in either spherical or cylindrical coordinates, are sufficient to evaluate this redistribution. Our formulation is in cylindrical coordinates.

Conclusions and Approximations. The solution of the general problem is complex, and the computational resources necessary to solve these mathematical descriptions numerically are significant. Based on our previous work, certain conclusions and/or approximations appear realistic, which simplify the mathematical description of the temporal behavior of the DT ice/vapor interface.

First, except for the nominal cool-down period for the cryogenic DT target, heat effects that result in spatial and temporal temperature changes in the target can be neglected. Although the position of the ice/vapor interface will vary with time, the temperature distribution in the ice and shell wall is essentially constant. In the vapor phase, the thermal capacity is very small and can be ignored. Thus, a steady-state approximation to the heat-transfer computations in the ice and vapor phases is appropriate. This gives "snapshots" of the target and permits an estimate of the heat-transfer and associated ice-redistribution rates.

Second, consistent with our original one-dimensional description of DT ice redistribution, we have chosen to describe the two-dimensional mass transfer as diffusive also. However, we use a multiplication factor on the diffusivity (calibration factor), which is determined by comparing predicted time constants with experimental time constants. In this manner, the model's performance allows us to interpolate between different experimental conditions with confidence. The driving force for this mass transfer is the DT concentration gradient within the gas/vapor volume. At the DT ice/vapor interface, the concentration of DT in the vapor is set by the ice/vapor equilibrium behavior (phase rule).

Third, for the targets of interest, the temperature differences that are predicted to occur across the gas/vapor phase between the opposing ice/vapor interfaces, even for appreciable ice layer nonuniformity, are small, especially for shell materials that have high thermal conductivity.

Because the concentration of DT in the vapor at the ice/vapor interface is set only by the temperature, and because the temperature difference across the DT vapor volume is small, we assume the concentration is in ice/vapor equilibrium, just as it is at the ice/vapor interfaces. The advantage of this approach is that a complex heat- and mass-transfer problem is reduced to one of only apparent heat transfer (as long as an appropriately defined heat-transfer coefficient is used). This modified heat-transfer problem in the gas/vapor phase couples naturally to the heat transfer within the ice layer.

Heat-Transfer Problem. The question is how to represent the effective thermal conductivity. This conductivity must account for the heat transfer associated with the DT mass flow, and the heat transfer by normal thermal conductivity.

For normal thermal conductivity k_H we use the mole fraction average of the gas/vapor phase constituents DT and ^{3}He,

$$k_H = k_{DT}\, y_{DT} + k_{^3He}\, y_{^3He},$$

where k_i is the thermal conductivity of the i^{th} component, and i is either DT or ^{3}He; y_{DT} is the fractional DT partial pressure and the total pressure is $P_T = P_{DT} + P_{^3He}$, giving $y_{^3He} = 1 - y_{DT}$; and P_{DT} is the vapor pressure of DT.

The equivalent thermal conductivity due to the energy carried by the diffusing DT is expressed as

$$k_{\text{mass}}\left(\frac{dT}{dx}\right) = q_{DT} = \Delta HMD\,\frac{\delta C}{\delta x} = \Delta HMD\,\frac{dC}{dT}\left(\frac{dT}{dx}\right) ,$$

where k_{mass} is the effective thermal conductivity due to mass flow, ΔH is the heat of sublimation, D is diffusivity, C is concentration, x is generalized distance, T is temperature, M is the calibration multiplier, and dC/dT is given by

$$\frac{d}{dT}\left[\frac{P_{DT}}{\mathrm{RT}}\right] = \frac{d}{dT}\left[\frac{Ae^{-B/T}}{RT}\right] = \frac{A}{R}\,\frac{e^{-B/T}}{T^2}\left[\frac{B}{T} - 1\right] ,$$

where $P_{DT} = Ae^{-B/T}$ is the standard vapor pressure expression.

Based upon k_{mass} and k_H, we chose to express the effective thermal conductivity as the sum of the two. This gas/vapor phase heat transfer is coupled at the ice/vapor/gas interface by two relationships, equal temperatures and equal heat flux, respectively, as

$$T_{\text{ice}} = T_{\text{vapor}}$$

and

$$k_{\text{ice}}\left[\frac{dT}{dn_{\text{ice}_{V/I}}}\right] = k_{\text{effective}}\left[\frac{dT}{dn_{\text{vapor}_{V/I}}}\right] ,$$

where n is the normal direction.

The mass transfer due to sublimation and condensation is determined by evaluating, at the ice/vapor/gas interface, the quantity,

$$\rho_{\text{ice}} \Delta H \frac{d\delta(\phi)}{dt} = k_{\text{ice}} \left(\frac{dT}{dn} \right)_{\text{ice}} \left(\frac{k_{\text{mass}}}{k_{\text{mass}} + k_{\text{H}}} \right) ,$$

over the range of ϕ, where ϕ is the angular coordinate of the two-dimensional system of this effective heat-transfer problem.

Modeling Computations. We have conducted computations of the β-heating phenomenon for selected target designs and conditions, and compared them to experimental results* reported by Hoffer and Foreman.[5] For our computations, the nominal temperature within the target was held at 19K (just under the triple point for DT). Our preliminary results of predicted time constants, compared with Hoffer and Foreman's measured time constant, yielded a calibration factor of 2.6.

Figure 1-1 shows the predicted time constants as a function of the calibration factor. The thermal conductivity used for copper is equal to 318 times that of glass. The log-log plot is surprisingly linear, which allows for a reasonably accurate estimate of the calibration factor. Additional modeling runs were conducted with this calibration factor.

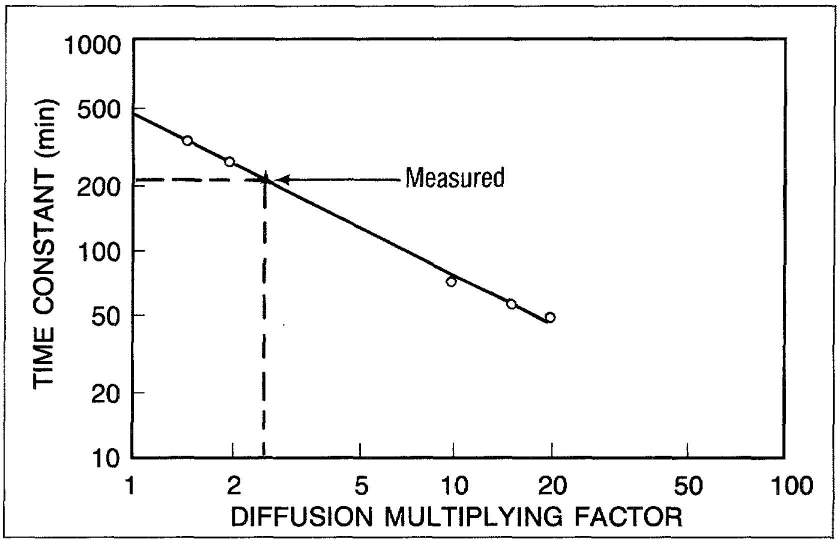

Fig. 1-1. The diffusion multiplying factor used in our two-dimensional model is determined by comparing predicted time constants with measured time constants. Input parameters for the model were based on the LANL experiment to which it is compared: A copper target 5 cm × 2.02 cm (o.d. × wall) that contained a DT ice layer formed from 16-day-old DT gas. The measured time constant for the experiment, 219 min, corresponds to a diffusion multiplying factor of 2.6.

---

*Hoffer and Foreman's experiments were conducted with a cylindrical chamber with a length-to-diameter (L/D) ratio of 1 and a diameter of 5.74 mm. This chamber was within a copper block that had a maximum diameter of 28.7 mm. The L/D ratio of 1 gives a reasonable approximation to a sphere.

Figure 1-2 shows how the time constant is predicted to change with the product of the thermal conductivity and thickness of the shell material. A thin-walled glass shell, with its low thermal conductivity, is projected to have a smaller time constant than a thick-walled shell of a material with a much higher thermal conductivity. This type of behavior is expected, since the target wall is an alternative path for the β-energy to escape the target. This path does not lead to DT ice redistribution.

Figure 1-3 shows the variation of time constant with tritium age of the target. As the tritium undergoes β-decay, the ^{3}He by-product builds up in concentration, which impedes the transport of DT vapor from one area to another. The calibration factor used in the calculation is 2.6 and the target has the thermal conductivity of copper. Since the model has been normalized to one experimental point, the validity of the predictions is expected to be excellent for future experiments using aged tritium.

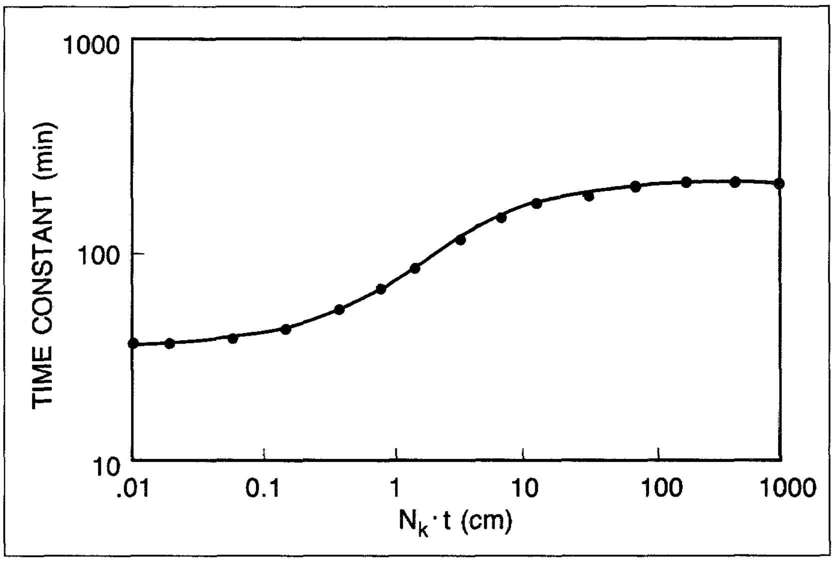

Fig. 1-2. The excess heat generated in thicker portions of the DT ice can reach the external surface of the shell in several ways; the thermal conductivity of the shell material is an important factor in determining the rate of heat transfer. In our model, the thermal conductivity of the shell material has been normalized to that of glass. The thermal conductivity of a shell material other than glass is obtained by the use of a multiplying factor N_k. Here the shell conductance is defined as the product of the thermal conductivity and thickness $N_k \cdot k_{gl} \cdot t$, where k_{gl} is the thermal conductivity of glass and t is the thickness of the shell. For ease of analysis and evaluation, however, the time constant is plotted as a function of the product $N_k \cdot t$.

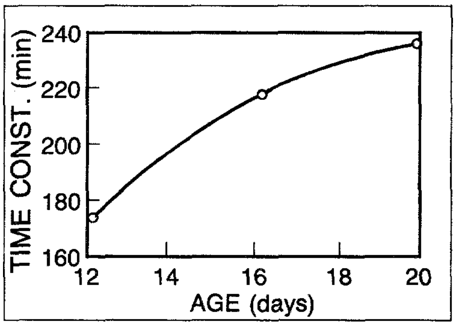

Fig. 1-3. Because the build-up of ^{3}He impedes the transport of DT vapor from one area of the target to another, the time constant increases with increasing tritium age of the target. The input parameters for the analysis depicted here are the same as those given in Fig. 1-1, except that the diffusion multiplying factor is set to 2.6 and the tritium age is varied.

For additional information, please contact Mr. A. J. Martin

1.1.2 Production of Uniform Solid DT Layers by β-Heating: Equipment Modification and Capabilities

The design of the apparatus built for β-heating experiments reflects a compromise between our needs to (1) produce an isothermal environment for the fuel capsule and (2) be able to document the fuel layer.[6] The original design proved successful for shells approximately 1 mm in diameter with a high aspect ratio (ratio of diameter to wall thickness) but was inadequate for larger shells (2 to 7 mm in diameter) with low aspect ratios.

The limitation in the original system is due to the diameter of the sapphire windows in the experimental chamber (see Fig. 1-4).

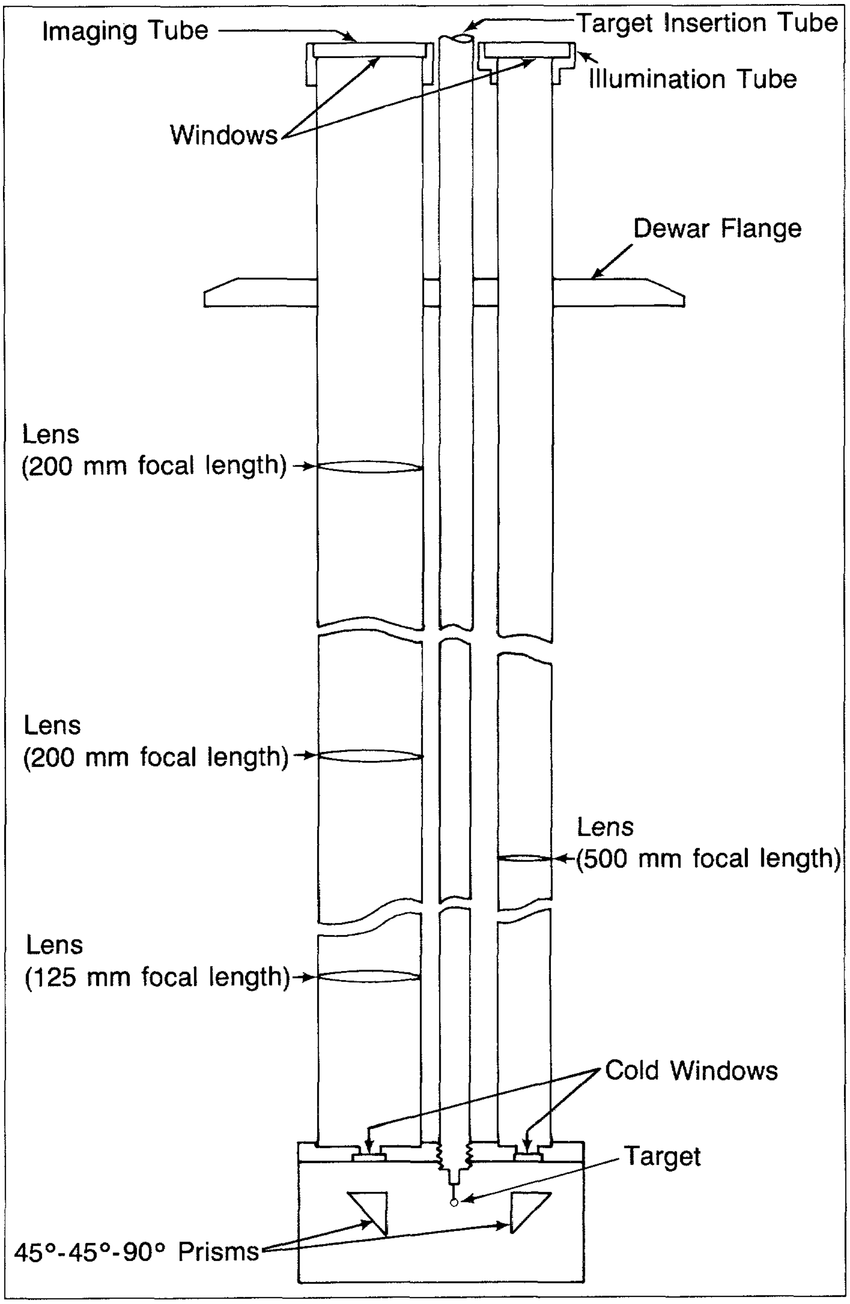

Fig. 1-4. In the initial β-heating experimental apparatus, the cold sapphire windows acted as apertures in the optical documentation system.

Since glass shells act as slightly divergent lenses, the information collected by any optical system is limited by the effective aperture of the first lens or by an aperture in the system prior to the first lens. As the aspect ratio of the shells decreases, the divergence increases, causing the Macroshell™ fuel capsules to exceed the divergence limits required for an adequate evaluation of the fuel layer.

We replaced the sapphire window on the imaging side of the optical system with a larger, thicker window that had a 15.8 mm clear aperture, which ensures that the refractive information limits are set by the aperture of the first imaging lens.

Figure 1-5 shows the limits of the modified and unmodified systems. For any target whose diameter and aspect ratio place it to the right of one of the curves, the refractive limitations are set by the first optical lens. For targets that fall to the left of one of the curves, the limitations are set by the window aperture. The largest and thickest target that the modified system can handle is 7.8 mm in diameter with an aspect ratio of 23.6. The 7.8 mm value is set by the size of the target mount; the limiting aspect ratio is found from the figure.

HD Experiments. Our initial experiments using a 1 mm diameter glass shell filled with HD established that the experimental apparatus did indeed produce an isothermal environment for the target.[6] In these experiments, a shell was suspended from a long, thin, insulating fiber inside the experimental chamber (see Fig. 1-6). The steady-state temperature of this target is determined by a balance between four thermal mechanisms: (1) the generation of energy by β-decay, (2) conduction of energy out of the target by the fiber, (3) convection of energy through the exchange gas, and (4) radiation exchange between the target and the environment. (Radiation exchange can either cool or heat the target. Cooling occurs when the target is at 20K, but this mechanism is only approximately 10% of the cooling by conduction through the fiber. Heating occurs if there is residual radiation leakage through the sapphire windows.) Using HD as the condensed fuel layer eliminates any source of energy within the capsule since no tritium is present. A high vacuum within the chamber eliminates convection through the exchange gas. As a result, absorption of any radiant energy leaking into the chamber is balanced by conduction through the fiber.

Figure 1-7 illustrates the results for these experiments. A 1000 μm diameter glass shell that contains 50 atm of HD is suspended from a 1 cm long, 28 μm diameter glass fiber. Figure 1-7a shows the shell immediately after the solid layer was formed; there is a considerable amount of detail in the crystal structure of the fuel layer. Figure 1-7b shows the same shell three days later. A one-for-one comparison of the details shows that the fuel layer did not change in this time. Lack of any sublimation over three days leads us to conclude that any residual radiation leaking into the experimental chamber was negligible.

DT Experiments. With the assurance that thermal radiation is negligible, the behavior of DT fuel can be evaluated under the same environmental conditions. Figure 1-8a shows a 980 μm

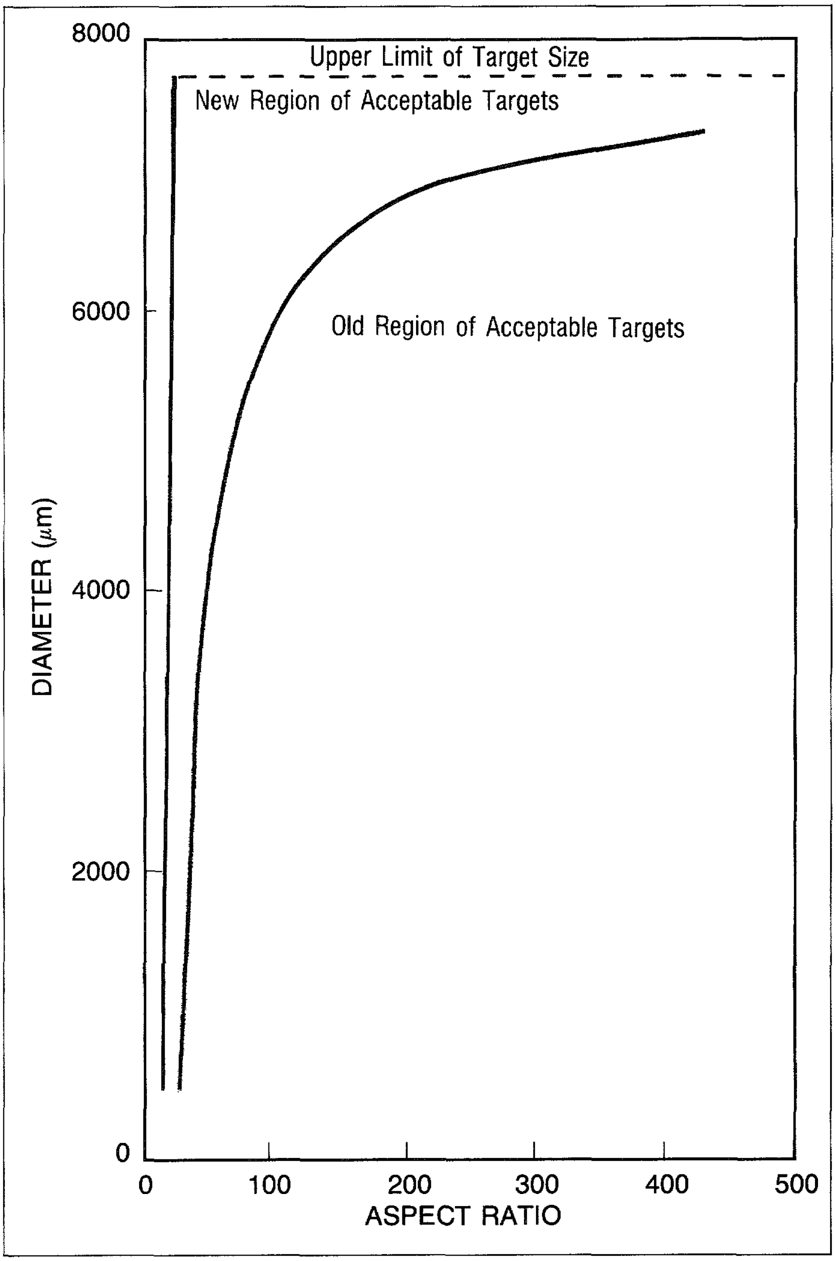

Fig. 1-5. Increasing the aperture of the sapphire window on the imaging side of the documentation system greatly increases the range of usable shells in the experimental apparatus.

diameter glass shell that contains 50 atm of gaseous DT and is suspended from a 1 cm long, 36 μm diameter glass fiber. Figure 1-8b shows the shell at low temperature (>20K) in the experimental chamber when the exchange gas pressure is a high (<0.1 mTorr) vacuum. At this temperature, the fuel is liquid and the dark band shows that gravity has caused the liquid to pool at the bottom of the shell. To freeze the fuel, helium exchange gas is added to the experimental chamber. Figure 1-8c shows the shell with the fuel frozen into a solid layer.

The need for some exchange gas to freeze the DT fuel demonstrates that the β-decay energy within the shell is sufficient to overcome the cooling through the fiber and the small amount of radiative cooling, and still keep the fuel in the liquid state. Comparing these results to those for the HD shell shows that the apparatus is sensitive enough to control the effects of β-decay energy within shells with diameters as small as 1 mm.

Figure 1-9 illustrates the β-heating effect in such small shells. Although the addition of a small amount of exchange gas to the experimental chamber keeps the fiber-mounted, DT-filled shell below the triple point of the fuel, the fiber is a significant perturbation on the symmetry of the thermal environment. The fiber acts as a conduit to improve the extraction of heat at the site where the fiber is attached. Over a period of time, a fuel

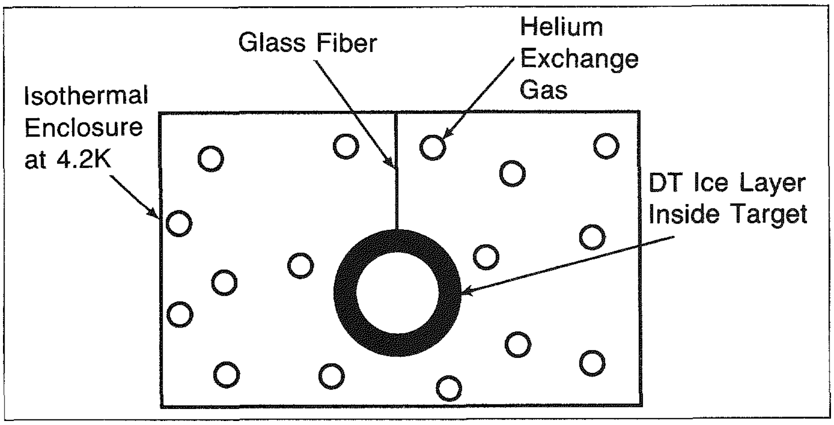

Fig. 1-6. Mounting the shell on the end of a long, thin glass fiber allows us to control the thermal mechanisms occurring within the experimental chamber.

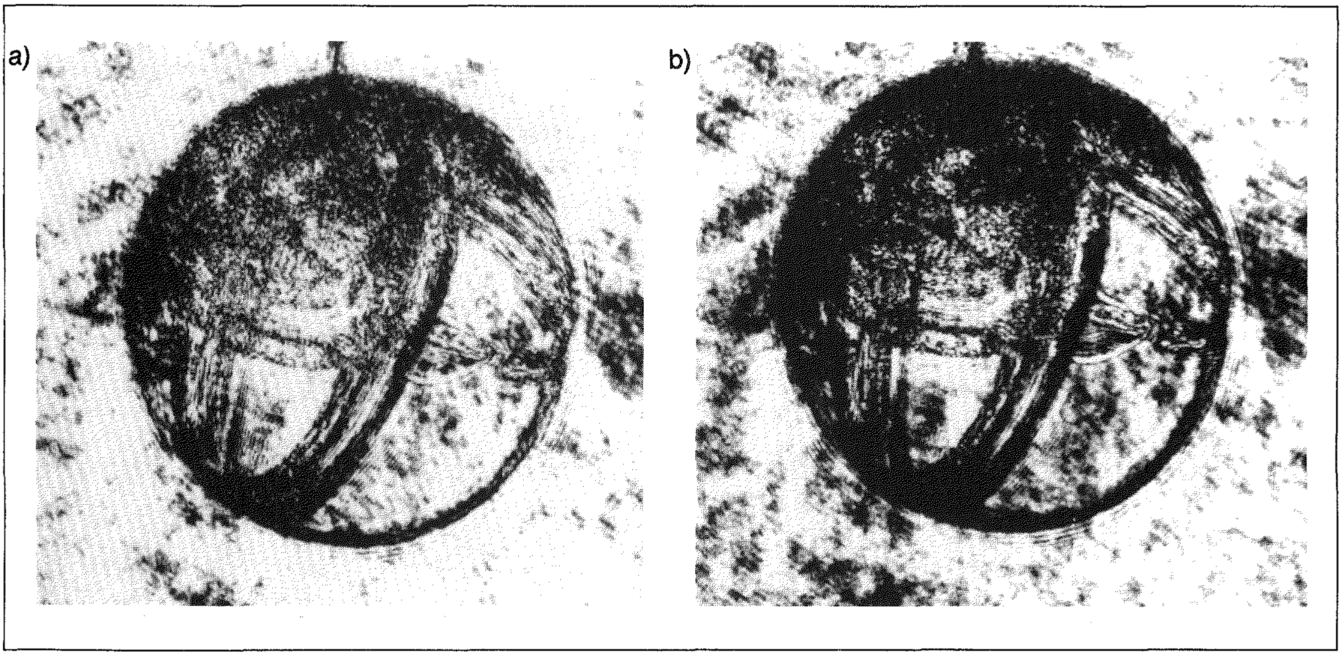

Fig. 1-7. Experiments with HD-filled shells show that any radiation leakage into the experimental chamber is negligible. The solid HD layer formed on day 1 (a) is identical to the solid HD layer on day 3 (b).

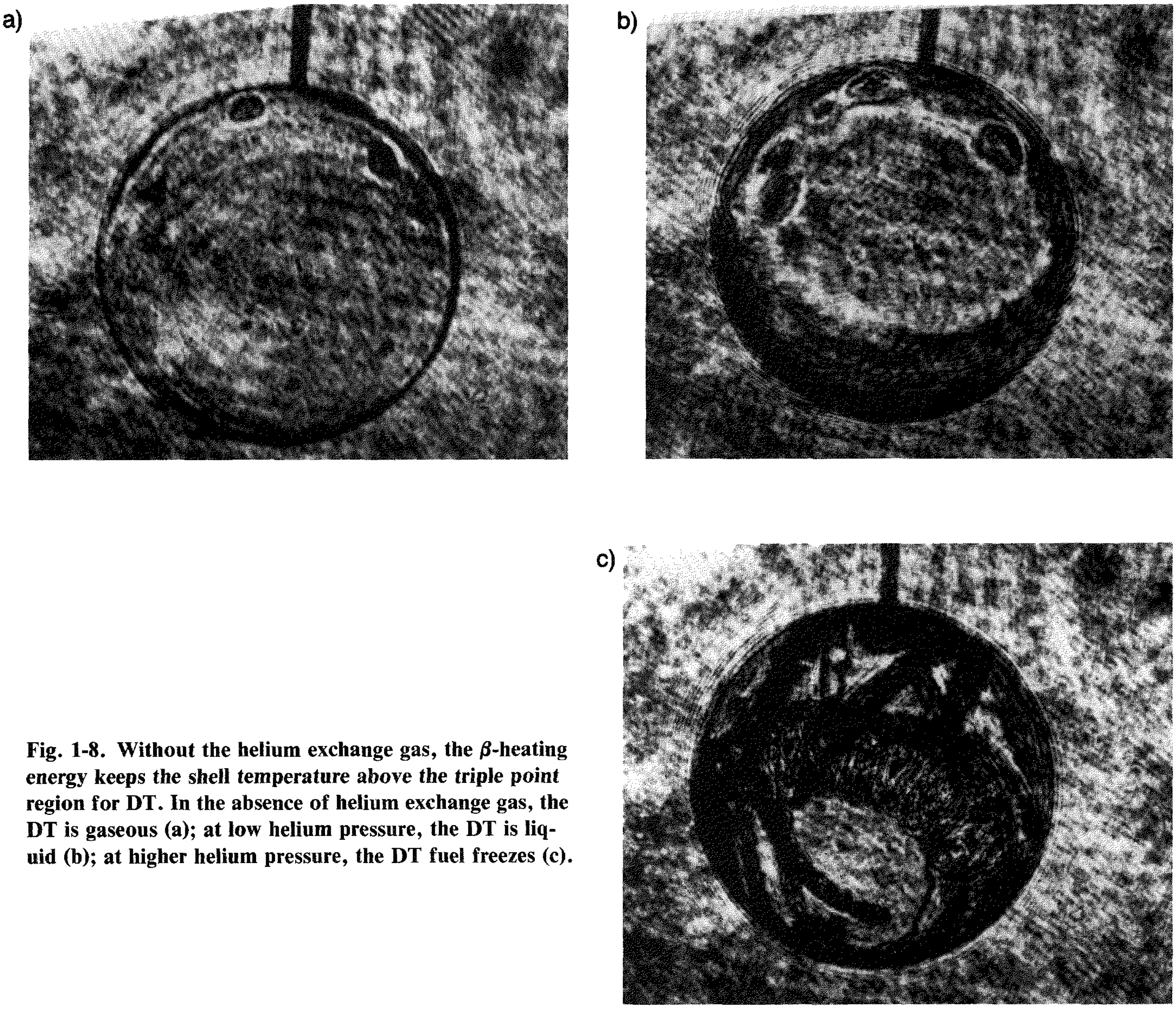

Fig. 1-8. Without the helium exchange gas, the β-heating energy keeps the shell temperature above the triple point region for DT. In the absence of helium exchange gas, the DT is gaseous (a); at low helium pressure, the DT is liquid (b); at higher helium pressure, the DT fuel freezes (c).

layer that is initially somewhat uniformly distributed on the shell wall will eventually sublime toward the area of fiber attachment.

Figure 1-9a shows the DT fuel layer at the start of the experiment and Fig. 1-9b is the same shell three days later. A comparison shows that the fuel layer has changed considerably. Clearly, the fuel layer has sublimed between various points within the shell volume.

The fuel mobility illustrated within the DT target above, and the lack of fuel mobility within the HD shell, shows that the β-heating effect will occur even for very thin fuel layers. The fuel layer within this DT shell would only be 7 μm thick if the fuel were distributed uniformly.

The mean free path of the β-particles within DT ice is more than this thickness, which means the low-energy end of the β-particle spectrum is being deposited and providing the heat source. Even for thicker fuel layers where more β-energy is

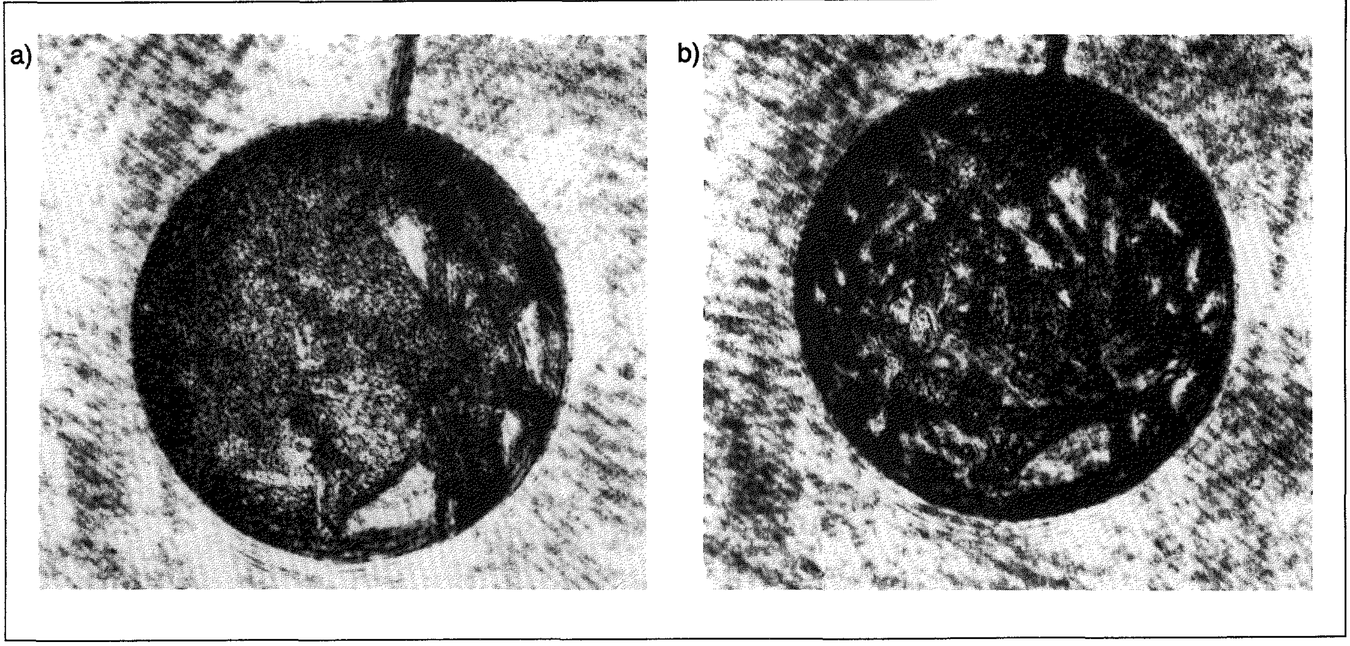

Fig. 1-9. The β-energy deposited within a fuel layer approximately 7 μm thick causes the fuel to migrate within the shell. This is evident in the change in the solid DT layer between day 1 (a) and day 3 (b).

deposited, the few inside micrometers will be heated sufficiently to affect the sublimation process.

As mentioned earlier, the glass mounting fiber acts as a point contact cooling fin. The shell will have a temperature gradient across its volume. Although this was advantageous for the experiments described above, it is intolerable for experiments designed to measure the uniformity limits of the β-heating effect. We desire a mounting system that minimizes the perturbation. An acceptable mounting configuration is illustrated in Fig. 1-10. The shell is captured between two thin (~0.1 μm) films of Formvar® mounted on a metal washer. The shell will be uniformly cooled over its entire 4π surface area.

Figure 1-11 illustrates an important point that we observed using this mounting configuration. Figure 1-11a is an interferometric image of the liquid pool within a 890 μm diameter shell filled at room temperature with 66 atm of DT. Figure 1-11b is an interferometric image of the same shell just below the triple point of the DT fuel. The solid layer is considerably more uniform than the liquid pool from which it grew. As energy is slowly and uniformly extracted over the entire 4π surface area of these DT-filled shells, a redistribution of fuel takes place as the shell passes through the triple point region of the fuel. This is observed consistently for DT fuel layers, but is not seen in HD fuel layers. Although these results leave many questions unanswered, they indicate that slow cooling through the triple point region may be the preferred operational sequence for all β-heated targets. It may be possible to start out routinely with a relatively uniform solid DT layer by cooling slowly through the triple point region and then using the β-heating effect to improve or complete the formation of the uniform layer.

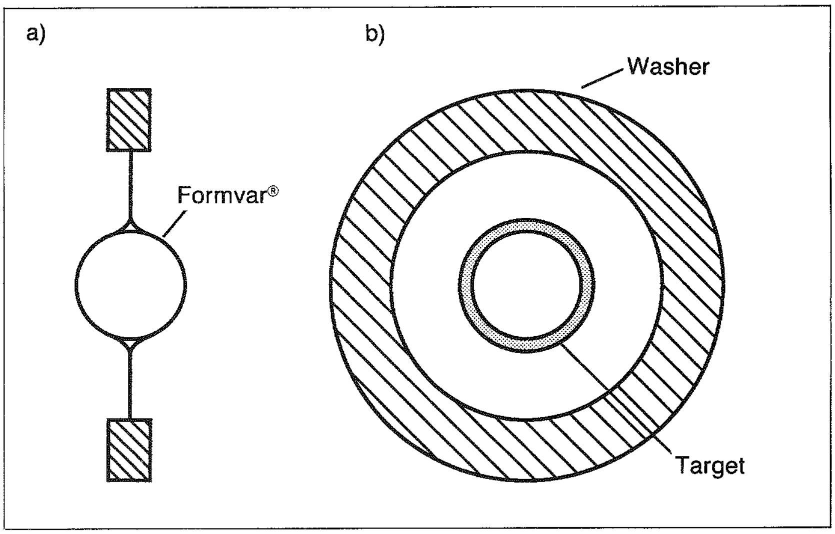

Fig. 1-10. Mounting the shell between two thin Formvar® films ensures that the shell will be uniformly cooled over its 4π surface area. The target and mount are shown here in a side view (a) and a front view (b).

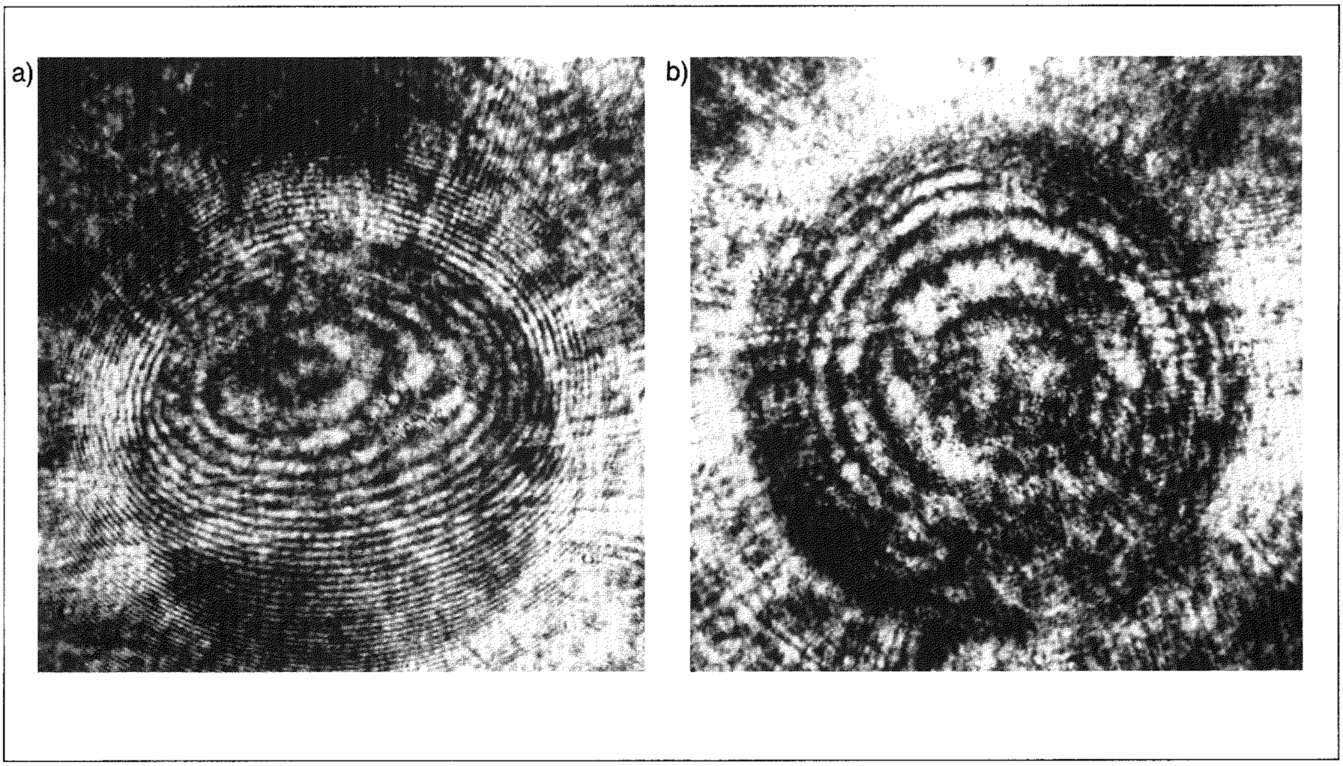

Fig. 1-11. Slowly cooling the shell through the triple point region allows a fairly uniform solid layer to grow out of the liquid pool.

For additional information, please contact Dr. D. L. Musinski

Sandwich Holography. For shells larger than 1 mm in diameter, the shell wall can easily dominate most documentation techniques. The optical phase shift due to the glass thickness becomes so large that standard interferometric techniques for evaluating the fuel layer become insensitive to fuel layer uniformity.

We are developing a holographic interferometry technique for evaluating targets containing liquid or solid cryogenic fuel layers.[7] This technique, which requires superimposing two separate holograms, is the most sensitive optical method, and the resultant interferometric image is due only to the condensed fuel. The technique effectively cancels the phase shift due to the transparent container and images only the fuel layer uniformity.[8]

The basic problem with the traditional technique is alignment of the two holograms on the same film, requiring that the total optical and experimental system remain stable between exposures. Laser systems such as Nova or Omega have inherent natural vibration spectra that limit the stability of any optical target-documentation system. For such systems, the probability is high that the two images will be offset, with each exposure catching the system at a different point of the vibration cycle. The β-heating process requires long times (hours and possibly days) between holographic exposures, and it is unlikely that the system can be kept stable enough.

An alternative technique is to expose the two holograms on separate film plates at different times and then mechanically align the two plates during reconstruction. Called "sandwich holography,"[9] the technique circumvents the stability problems described above. Our experiments showed that sandwich holography is practical. By proper selection of a fiducial within the images, accurate alignment of the two holograms can be achieved and the fuel layer uniformity evaluated. Since exposure times required for each plate can be kept short enough to eliminate vibrational effects, this technique can be applied directly to systems such as the Nova and Omega laser systems.

Sandwich holography is also an excellent documentation technique for β-heating experiments. Single holograms of the target can be exposed at regular time intervals. These holograms can then be reconstructed in various pairs to obtain a complete record of the fuel layer evolution. A hologram of the target with gaseous fuel can be reconstructed with holograms of the same target with either liquid or solid fuel. Two liquid-layer holograms can be reconstructed to follow the condensation process, or two solid-layer holograms can be reconstructed to follow the solid layer migration.

When the two exposures are taken on separate plates, they must be aligned mechanically. If the two holograms are not precisely aligned, then extraneous phase shifts complicate interpretation of the image. The use of background phase information is a way to measure the degree of misalignment between the two holograms. The background field of view contains phase information generated by all of the path length variations in the optical system. This means that, during reconstruction, if precise alignment is not achieved, the background field of view will contain a phase pattern due to alignment errors. Adjustment is made to the relative position of the two holograms until the background field of view exhibits a zero phase gradient. Then the interferogram is due solely to the change in state of the fuel between the two exposures. Interpretation of that image is identical to that for classical interferometric images of cryogenic targets.

Figure 1-12 illustrates the results. Figure 1-12a is the holographic image of the target with the fuel in the vapor state, and Figure 1-12b is the holographic image of a target with the fuel condensed as a liquid layer. Note that the liquid layer in this image is thicker at the 7:00 position. Figure 1-12c is the first image of the holographic interferometry reconstruction. The phase gradient (fringes) within the background field of view clearly shows that the alignment of the two holograms is slightly off. Figure 1-12d is the holographic interferometry image with nearly zero phase gradient in the background field of view. By comparing Figs. 1-12c and 1-12d one can see that, as the phase gradient in the background field of view is removed, the center of the interferometric pattern within the shell is translated laterally along the direction of the phase gradient. This observation, which is identical to that observed for classical interferometry, confirms that the use of zero phase gradient within the background is the correct fiducial to use for determining alignment between the two holograms.

Figure 1-13 is a sketch of the exposure fixture we used in our experiments.[10] The two 1 in. × 3 in. film plates are supported on three points at a compound angle. The three point supports and basic design of the fixture allow gravity to align the plates accurately. During the first exposure, only one plate is used, with the emulsion facing away from the imaging beam. The second exposure is taken with a spacer plate between the beam and the holographic plate. The emulsion on this second plate faces the beam. During reconstruction, the two emulsions are placed face to face in the fixture. Alignment is achieved by allowing the two plates to settle into their equilibrium positions due to gravity.

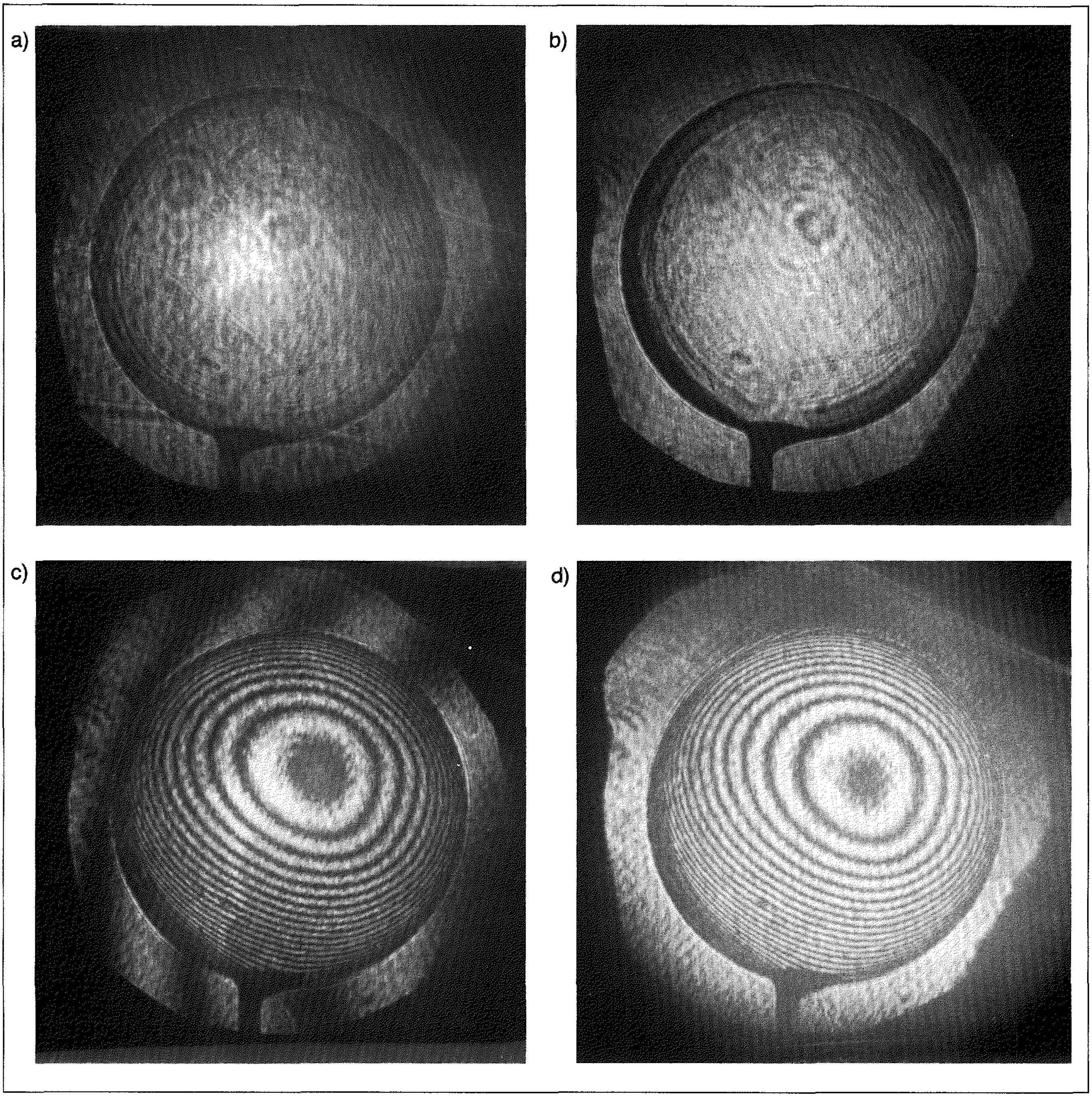

Fig. 1-12. Combining a vapor (a) and a liquid-layer (b) hologram results in a holographic interferometric image of the change in fuel state (c). If the two holograms are not precisely aligned a phase gradient appears in the background field of view (c). When the two holograms are precisely aligned, the background has a zero phase gradient (d). With a zero background phase gradient, the image can be interpreted.

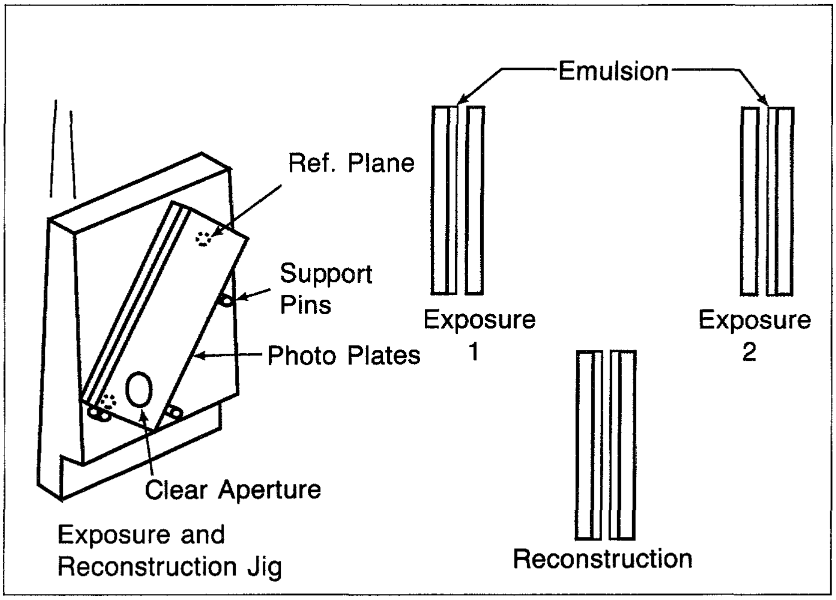

Fig. 1-13. The fixture used for sandwich holography is very simple; it relies on gravity to register the film plates properly. The technique ensures that the two emulsions are in intimate contact during reconstruction.

For additional information, please contact Mr. T. R. Pattinson

1.1.3 Cryogenic DT Pressure Intensifier for Los Alamos National Laboratory

This year the staff at LANL fabricated and assembled the cryogenic pressure intensifier that KMSF designed for their facility. We conducted numerous cryogenic experiments using the system, determined the operating characteristics, and worked out operational modifications and procedures.

Figure 1-14 is a schematic of the cryogenic pressure intensifier system. Figure 1-15 is a photograph of the system as constructed at LANL. Half of the insulating G-10 clamshell assembly is removed for clarity in the photograph. The finned, copper heat-transfer plate is at the top of the photograph. This plate keeps the top of the condensation tube at room temperature. The slender neck of the stainless steel condensation tube is the portion along which the natural temperature profile is established during low-temperature operation. The lower portion of the tube, the larger cylindrical region, is the condensation volume. This region is cooled by liquid helium flowing through a spiral channel cut into the surface of the condensation tube and sealed with a cylindrical sleeve. Liquid helium is introduced through the short tube on the bottom of the system and the vapor is exhausted through the longer tube that loops out of the top portion of the condensation volume. The two bellows on the helium transfer lines allow the condensation tube to contract freely during cooldown. They prevent stresses from building up between the condensation tube and the containment vessel (not shown in the photograph).

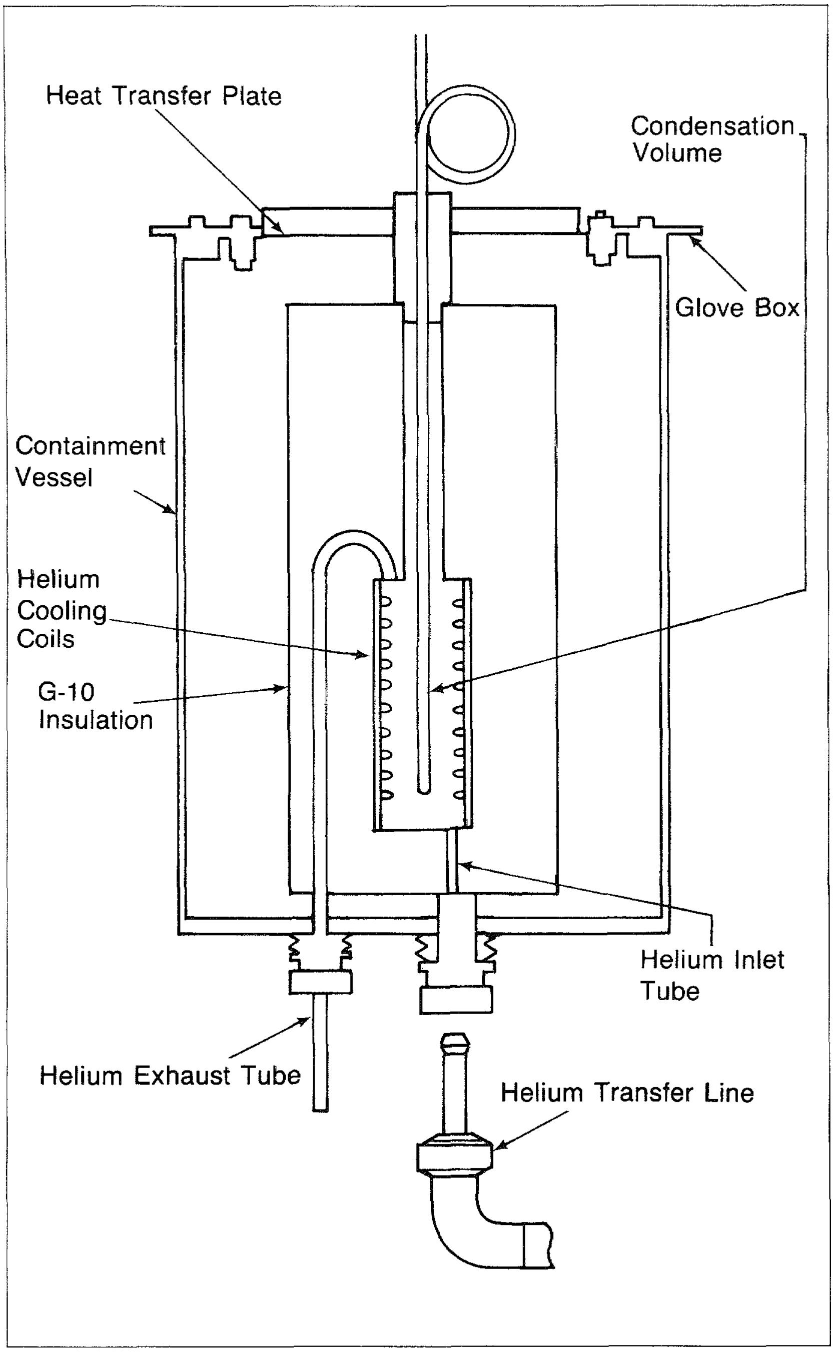

Fig. 1-14. All of the major components of the cryogenic-based DT pressure intensifier system are shown in this schematic diagram.

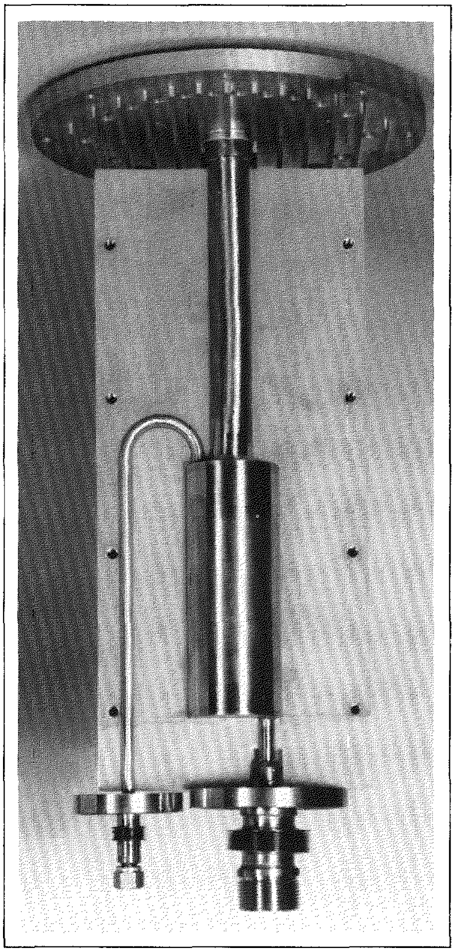

Fig. 1-15. The pressure intensifier system is shown with half of the G-10 insulation removed for clarity. The components of the system are identified in Fig. 1-14.

Our testing procedure for the system was designed to measure the dynamic thermal characteristics and the operating response of the hardware under normal operating conditions. We needed to ensure that the system would cool down in a reasonable time, consume a limited amount of liquid helium, and return to room temperature relatively quickly. The cool-down times averaged approximately 15 min, and liquid helium consumption averaged 16 l per run. The system's temperature rise back to room temperature exhibited the exponential tail typical of all thermal systems approaching equilibrium. The time constant of this profile was approximately 11 min. This implies that after three time constants (33 min) the pressure of the gas in the condensation vessel is 95% of its final value. We also found that we could accelerate the warming process by circulating warm gaseous nitrogen through the apparatus.

An important safety feature we designed into the system is an inherent limitation on the amount of isotopic hydrogen that the system can condense. Limiting the amount of condensation limits the ultimate pressure that the system can attain. This precludes the possibility of overpressurizing the vessel.

We found that, as fabricated, the system was limited to a working volume of 6 cm^3 at a pressure of 100 MPa. The operational characteristics are illustrated in Fig. 1-16. The pressure/volume experimental range that the intensifier system can service covers nearly of of LANL's requirements. The starting point of 6 cm^3 at 100 MPa is shown as the single point. Expanding that mass of fuel into various load volumes (volumes in addition to the starting point volume) results in the curve labeled "single condensation." Thus, the system can service any point below this curve in a single condensation. The curve labeled "double condensation" results from isolating the system from the load volume, performing a second condensation, and expanding that additional mass into the load volume. The system can service any point below this curve with two condensations. The third curve results from adding additional mass to the load volume from a third condensation. The initial performance was less than the design specifications, and two condensations would

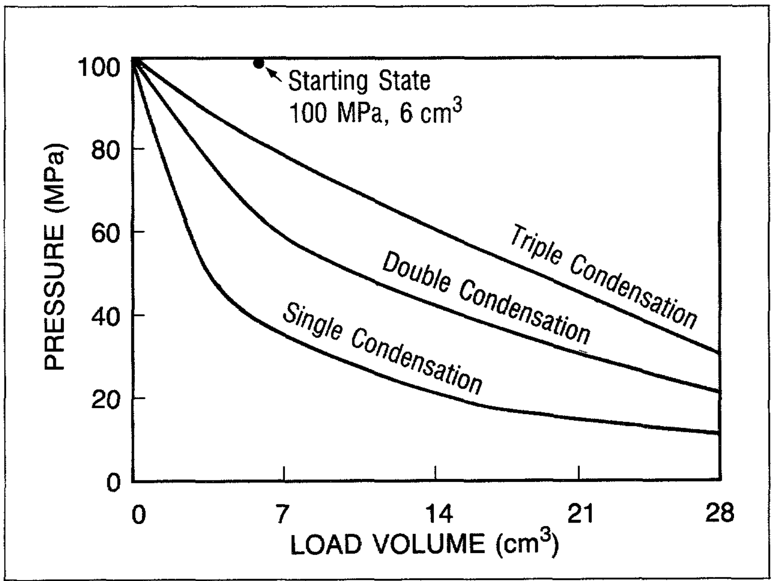

Fig. 1-16. The starting state volume (6 cm^3 at 100 MPa) can be expanded into various load volumes by undergoing one or more serial condensations. These three curves illustrate the final volume/pressure combinations that can be achieved by one, two, or three sequential condensations.

be required to meet the maximum design point specified by LANL. A simple modification to increase the capacity of the system was devised. This was to slightly ream and deepen the gun-drilled hole in the condensation tube to increase the capacity for condensation. However, it was decided that the system, as fabricated, met LANL's revised requirements, so the modifications were not made. The system is now available for testing and tritium qualification.

For additional information, please contact Mr. M. T. Mruzek

SECTION 1.2

Polymer Shell Technology

The size and aspect ratio of polystyrene (PS) shells that can be routinely produced were significantly increased this year. Shells with diameters in excess of 500 μm and wall thicknesses in the 2 to 4 μm range can now be fabricated in large quantities. Technical developments in several areas expanded our production capabilities.

The stripping gas droplet generator technology, transferred here from Lawrence Livermore National Laboratory (LLNL) last year as a shell coating technology, has been successfully adapted to shell fabrication. Because of its simplicity, the stripping gas droplet generator has replaced the concentric-orifice hollow droplet generator for fabricating PS shells. While the stripping gas droplet generator, as currently configured, does not produce a monodispersed droplet stream, the product obtained using this device can be sieved into size ranges that supply all of our current needs for PS shells.

Polystyrene with a molecular weight around 100,000 (100 K) was found to be the best material for forming high-aspect-ratio shells. A number of commercially available resins were tested, with intermediate molecular weights (such as 100 K) obtained by blending commercial resins with higher and lower molecular weights.

We are beginning to use statistical methods to study all of our shell forming processes. Statistical design is a powerful tool for characterizing complex processes with many interrelated variables, and has been highly successful at predicting the behavior of our glass shell forming processes. Successful application to polymer shell fabrication should allow us to respond more quickly to changes in shell specifications.

1.2.1 Stripping Gas Droplet Generator

The stripping gas droplet generator, which was built and tested last year for coating shells with poly(vinyl alcohol) (PVA), was adapted for the production of PS shells. The PVA coating technology was transferred from LLNL, where this technique is also used for the production of PS shells.[11]

Several different solvents were tested to determine their effects on the shell forming process with this droplet generator. A commercially available PS with a molecular weight of 200 K was used for these initial experiments. Methylene chloride seemed to form shells most easily, so we used it for subsequent experiments. Tetrahydrofuran (THF) was tested as a blowing agent, but was only marginally effective.

These experiments were conducted on our 6 m drying column, with the top half of the column at 200°C, and the bottom half at room temperature. Larger shells (>400 μm) that had a dent in the wall were formed with this profile. The dents were apparently formed by adiabatic contraction of the gas inside the shell (which was still in a fluid state) as the shell passed through the steep temperature gradient between the last 200°C section and the first room-temperature section. This problem was eliminated by setting one 0.76 m heating section just below the last 200°C zone at 50°C. When the temperature gradient is reduced, gas diffusion into the shell becomes effective in reducing the pressure gradient across the shell wall.

We also tested this system with a PS that had an average molecular weight of 88 K. It was formed by blending 22 K PS and 300 K PS in solution. This material had excellent shell forming properties. Shells in excess of 550 μm in diameter, with wall thicknesses in the 4 to 6 μm range, can be produced with good yields. Shell wall uniformity is adequate for the present application.

A number of experiments have been conducted to characterize the performance of the stripping gas droplet generator. The two most important variables for operation of the stripping gas droplet generator are the stripping gas flow rate and the solution injection rate.

First, an automatic injection device was constructed to quantify the solution injection rate. This device used a stepper motor to drive a syringe plunger, which injects droplets into the drying column at a controlled rate. The stripping gas droplet generator with the automatic injector in place is shown schematically in Fig. 1-17.

Quantitative control of the stripping gas flow rate allowed us to fully characterize the droplet generator's performance in terms of the two most important process variables, solution and stripping gas flow rates. Figure 1-18 is a representative plot of some of the data obtained from these experiments. It shows the median values of shell outside diameter (o.d.) obtained for various droplet generator operating parameters. It is evident that maximum shell size is obtained at a stripping gas flow rate of 1.2 l/min and a solution flow rate of 8.5 μl/s. Also, it can be seen that shell size is affected by both the stripping gas flow rate and the solution flow rate. Statistical experiments are currently underway to study the shell forming process in more detail; they are described in Section 1.2.3.

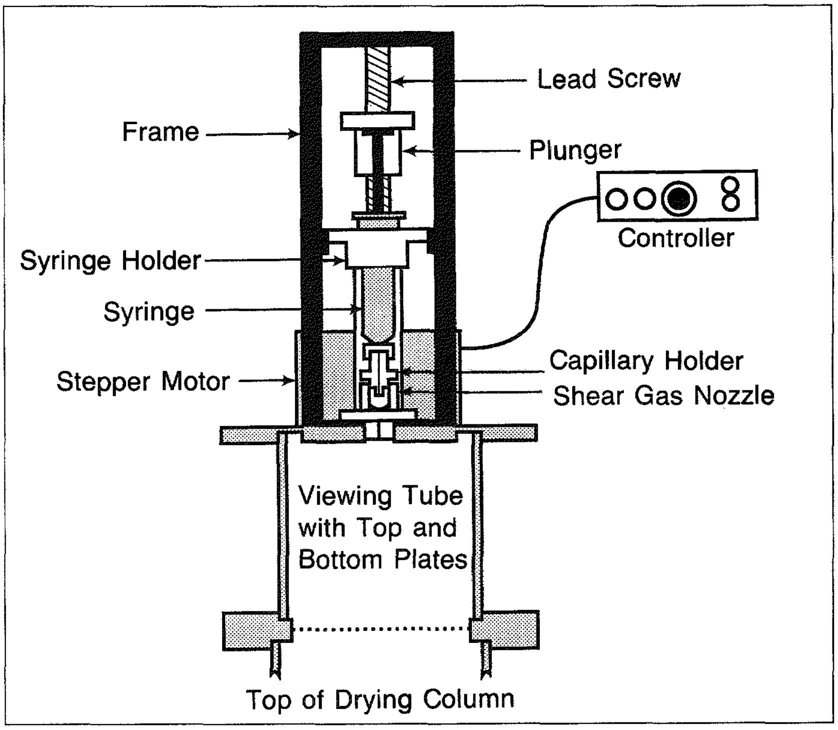

Fig. 1-17. Addition of the automatic solution injector to the stripping gas droplet generator allowed us to characterize the droplet generator's performance in terms of solution injection rate and stripping gas flow rate. Precise control of these rates is required to produce shells with the desired qualities.

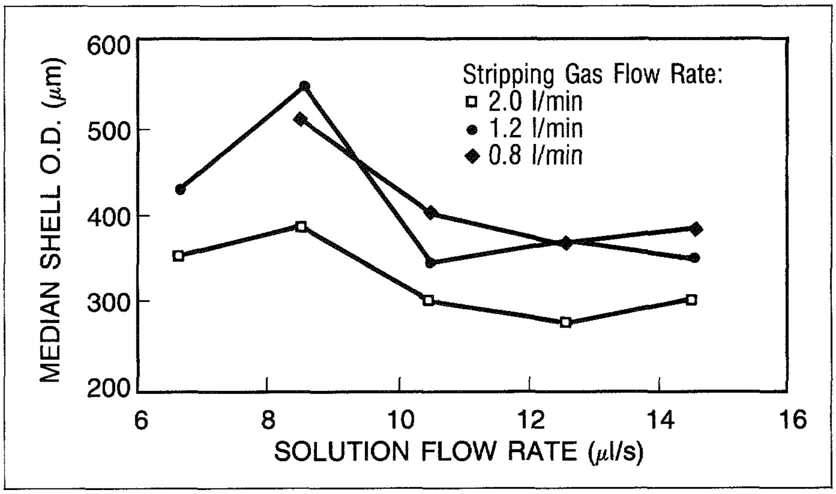

Fig. 1-18. The PS solution injection rate and the stripping gas flow rate influence the diameters of PS shells formed by drops from the stripping gas droplet generator.

For additional information, please contact Dr. T. P. O'Holleran

1.2.2 Effect of Molecular Weight on Polystyrene Shell Formation

Early experiments with the stripping gas droplet generator suggested that the molecular weight of the PS used to prepare the feedstock might have a significant influence on the characteristics of the final product. Polystyrene of two different average molecular weights was tested to determine the effect of molecular weight on the shell formation process. Our "standard" PS (XP6065 from DuPont) has an average molecular weight of 200 K. The new materials had molecular weights of 300 K and 22 K. Unfortunately, both the 300 K and 22 K molecular weight materials exhibited inferior shell forming properties. We wanted to test a PS with molecular weight around 100 K, but such a material was not commercially available. We also wanted to restrict our choices to commercially available material to avoid the expense associated with custom synthesis. A PS with an average molecular weight of 88 K was formed by blending the 300 K and 22 K molecular weight materials in solution. The resulting PS was actually 24% (by weight) 300 K molecular weight PS, and 76% 22 K molecular weight PS.

This material had excellent shell forming properties. Shells in excess of 550 μm in diameter, with wall thicknesses in the 4 to 6 μm range, were produced with good yields. Shell wall uniformity was adequate for present requirements.

The acoustically destabilized droplet generator was used to investigate the effects of polymer molecular weight on the shell forming process. This droplet generator was chosen largely because of its excellent control over droplet size. Five commercially available polystyrenes were used in this study. Their molecular weights (according to the manufacturers) were 45 K, 200 K, 192 K, 250 K, and 300 K. In addition, the highest and lowest molecular weights (300 K and 45 K) were blended in solution with methyl ethyl ketone (MEK) to give molecular weights of 105 K, 200 K, 192 K, and 250 K. Shell forming experiments were performed in the 3 m drying column, using several different temperature profiles and drop sizes.

Polymer molecular weight had the most striking effect on shell wall thickness. Figure 1-19 illustrates this effect for shells formed from two different drop sizes. The dramatic reduction in wall thickness at 105 K molecular weight is obvious. Neither shell diameter, wall uniformity, nor process yield showed such a remarkable effect. While no explanation of this phenomenon can be offered at this time, it does agree with the observations of Grens and others at LLNL.[12]

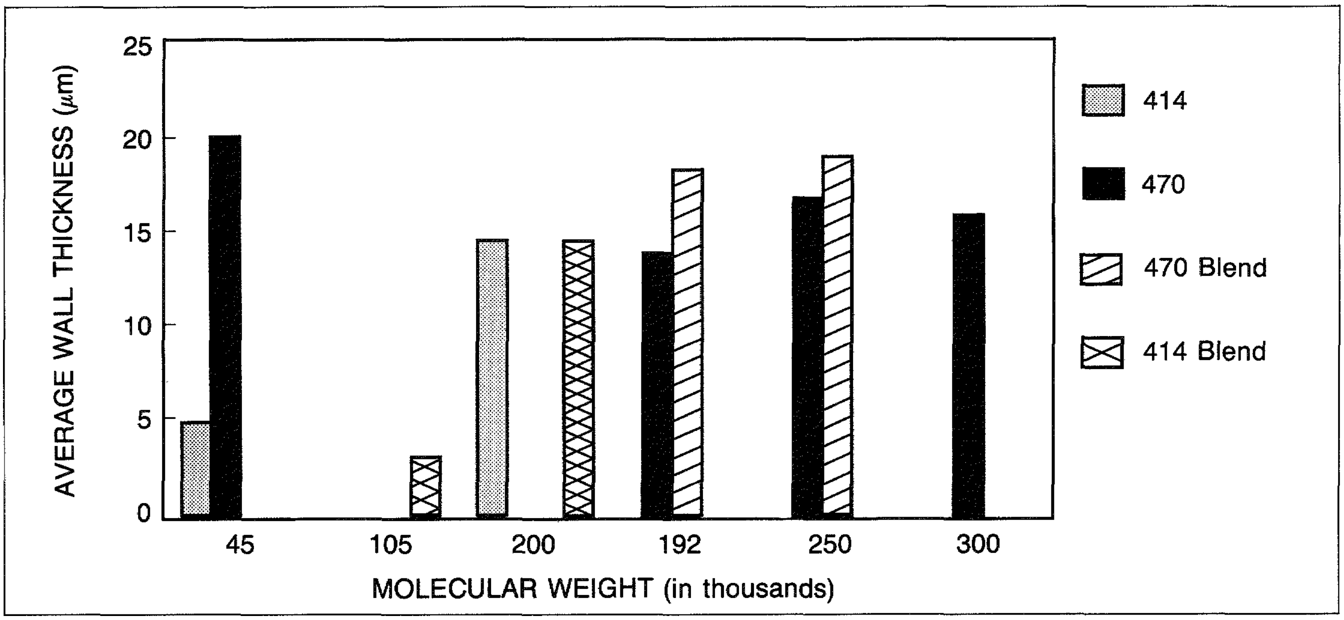

Fig. 1-19. Polymer molecular weight has a noticeable effect on the wall thickness of PS shells produced by the acoustically destabilized (single-orifice) droplet generator. The numbers in the legend to the right of the chart indicate the diameters (in μm) of the droplets from which the shells were formed. "Blend" indicates that the molecular weight was obtained by mixing the 45 K and 300 K molecular weight resins.

For additional information, please contact Dr. T. P. O'Holleran

1.2.3 Statistical Experiments

The previous sections make clear that our modifications of equipment and our exploratory research have resulted in two systems for making PS shells. Both systems are complicated; many experimental parameters are present. However, the systems are not fully explored and need to be optimized for shell production.

We have begun optimizing the systems using statistically based experimental designs. The optimizing experiments are of two types, screening experiments and response-surface experiments. Screening experiments are used to identify the experimental parameters with significant effects on resulting shell characteristics. Response-surface experiments relate the significant experimental parameters to the resulting shell characteristics. Screening experiments were completed this year using the Plackett-Burman[13] design. Response-surface experiments are underway.

Eight parameters were examined by the screening experiments for the stripping gas droplet generator system. Each parameter was tested at two values. If confidence levels were below 90% but still fairly high, we have noted that a given effect "may" be present.

Parameters examined for stripping gas droplet generator system:

Tower Temperature Profile

Two profiles were examined, one with 180°C at each end and 250°C in the middle and another with a constant 217°C.

Past experience had led to the varying profile. The experiments showed that the varying profile leads to significantly higher shell wall uniformity and shell yield.

Polymer Concentration

Examined at 2% and 10% by weight using a blend of 76% 22 K and 24% 300 K PS. The experiments showed that the higher concentration increased shell diameter and shell yield.

Blowing Agent Concentration

Examined at 0% and 10% THF. The experiments showed that the presence of this higher concentration of THF results in smaller shells!

Solvent Type

Two solvents were examined, methylene chloride and MEK. Methyl ethyl ketone may increase shell yield.

Solution Injection Rate

Examined at 2 μl/s and 18 μl/s. The shell diameter decreases at the higher injection rate.

Stripping Gas Rate

Examined at 1.2 l/min and 2.0 l/min. In contrast to earlier results, the experiments detected no statistically significant effects.

Stripping Gas Type

Argon and nitrogen were compared. The diameter may increase with argon.

Downdraft

Examined at 0 and 12 l/min downdraft flow rate. The experiments detected no significant effects.

The acoustically destabilized droplet generator system had 11 parameters examined by screening experiments. Actually many more experimental parameters exist, but they are not independent of each other. For instance, in order to obtain a particular working drop size, adjustments are made to flow rate, acoustic intensity, frequency, pulsed voltage, and deflection voltage. Our choices were limited to the 11 independent experimental parameters, as required by the statistical technique. Each parameter was tested at two values.

Parameters examined for acoustically destabilized droplet generator system:

Polymer Molecular Weight

Examined at 45 K and 250 K. The experiments show only a possible increase in shell diameter as molecular weight increases.

Polymer Concentration

Examined at 2% and 10% PS by weight. Increasing concentration definitely increases shell diameter. The yield and wall uniformity may also be affected.

Solvent

Examined 100% MEK and 50:50 MEK:methylene chloride. The wall thickness may increase slightly with 100% MEK.

Blowing Agent Concentration

Examined 0% and 10% styrene. The shell diameter and yield may increase slightly with the presence of a blowing agent.

Solution Cooling

Examined cooling or not cooling the solution before injecting into the tower furnace. The experiments detected no significant effects.

Drop Size

Examined 400 μm and 500 μm drop sizes. Increasing drop size increases the diameter and possibly wall uniformity.

Tower Temperature

Examined 370/270/370°C and 300/300/300°C. Shell diameter increases with the straight profile, but wall uniformity may increase with the varying profile.

Downdraft

Examined at no flow and 10 l/min. A downdraft may increase yield.

Vessel Pressure

Examined at 8 psi and 25 psi. Shell diameter increased as vessel pressure decreased.

Vessel Pressurizing Time

Examined at 15 min and 12 h. Yield may increase slightly with short vessel pressurizing time.

Run Time

Examined at 3 min and 12 min. At longer run times, shell diameter decreases and yield may decrease.

The screening experiments give a statistical probability that a particular parameter has a truly significant effect on shell properties. Table 1-1 shows the parameters that have at least a 90% probability of a significant effect on a shell property. No parameters had a strongly significant effect on wall thickness.

Table 1-1. Experimental Parameters with ≥90% Probability of a Significant Effect on a Shell Property

Outside Diameter		Wall Uniformity		Yield	
DG	Tower Temperature	SG	Tower Temperature	SG*↑	Tower Temperature
SG*,DG*↑	Polymer Concentration			SG*↑	Polymer Concentration
SG*	Blowing Agent			SG	Solvent
SG	Solution Injection Rate			DG	Downdraft
DG*	Drop Size			DG	Run Time
DG*	Vessel Pressure				
DG*	Run Time				

*: ≥ 95% probability of significance
↑: ≥ 99% probability of significance
SG: Stripping Gas Droplet Generator
DG: Hollow Droplet Generator

For additional information, please contact Mr. W. J. Miller

SECTION 1.3

Glass Shell Technology

The size, wall thickness, and uniformity requirements for glass targets for the inertial confinement fusion (ICF) program have been increasing steadily in recent years. The present and future specifications for glass shells for ICF work can be grouped in distinct categories by diameter and wall thickness: (1) multimillimeter, thick-walled glass shells (Macroshell™ targets) for the study of uniform DT ice layer formation (β-heating); (2) 1 to 2 mm, thin-walled shells for Nova or PBFA II targets; and (3) submillimeter, thick-walled shells for Nova targets.

The sizes of these targets are dissimilar enough to require three separate development efforts with significant departures from or advancements of current shell fabrication technology (which is based on a sol-gel/drop tower furnace system). Because of their mass and size, the Macroshell™ targets could not be produced in our vertical drop tower furnaces. Instead, during the last few years, we have been developing the technology and methodology for forming multimillimeter spherical voids in glass preforms for subsequent machining to produce uniform hollow spheres.

The fabrication of 1 to 2 mm glass shells requires an advancement of our vertical drop tower furnace technology. Glass shells 1 to 1.5 mm in diameter can be made from sol-gel feedstock with our present furnace systems, using >0.95 atm water vapor in the furnace ambience to help expand the forming shells. The yield of acceptable shell quality in this size range is very low. Furthermore, these shells often contain detectable quantities of water, resulting in large corrosion features on the internal surfaces. Thus, we have not been able to make shells with acceptable qualities in the 1.5 to 2 mm diameter range by this method. We have investigated the efficacy of the permeant gases helium and neon as substitutes for water vapor for making large shells.

Finally, we have been investigating the effect of the composition of the gel feedstock on shell formation. The motivation for this investigation is to develop better control and reliability of the process, and specifically to increase the shell size range and wall uniformity for the thick-walled shells of current interest.

1.3.1 Macroshell™ Target Development

We are investigating methods of fabricating and characterizing Macroshell™ targets for ICF experiments. Large diameter (2 to 10 mm) glass Macroshell™ targets are essential for the study of DT ice layer formation by β-heating (see Section 1.1) and are potentially useful for neutron production experiments for ICF drivers like Nova or PBFA II. The technology developed to fabricate these fuel containers may also be useful in the fabrication of polymer shells that could be targets for the proposed Laboratory Microfusion Facility.

Shells for β-heating require high sphericity, medium aspect ratios (diameter-to-wall ratio ranging from 25 to 100) to meet strength requirements, and high permeability for fuel diffusion through the relatively thick walls. Because of the large shell mass and the high viscosity of the glass during shell formation, conventional fabrication methods, such as the vertical drop tower or torch spray methods, have not been successful in producing shells that meet the stringent requirements necessary for cryogenic experiments. Therefore, we have developed an alternative target fabrication method to provide research quantities of highly spherical shells with uniform wall thicknesses.

The fabrication process is a two-step procedure. First, a glass preform containing a nonspherical cavity is heated to high temperatures to make the cavity spherical. The cavity is rotated in a horizontal tube furnace[14] to counterbalance the buoyant forces acting on it. Second, excess glass surrounding the spherical cavity is removed by a mechanical lapping and polishing process. A three-point lapping device (shown in Fig. 1-20) allows the cavity to be centered within a wall of desired thickness and surface fin-

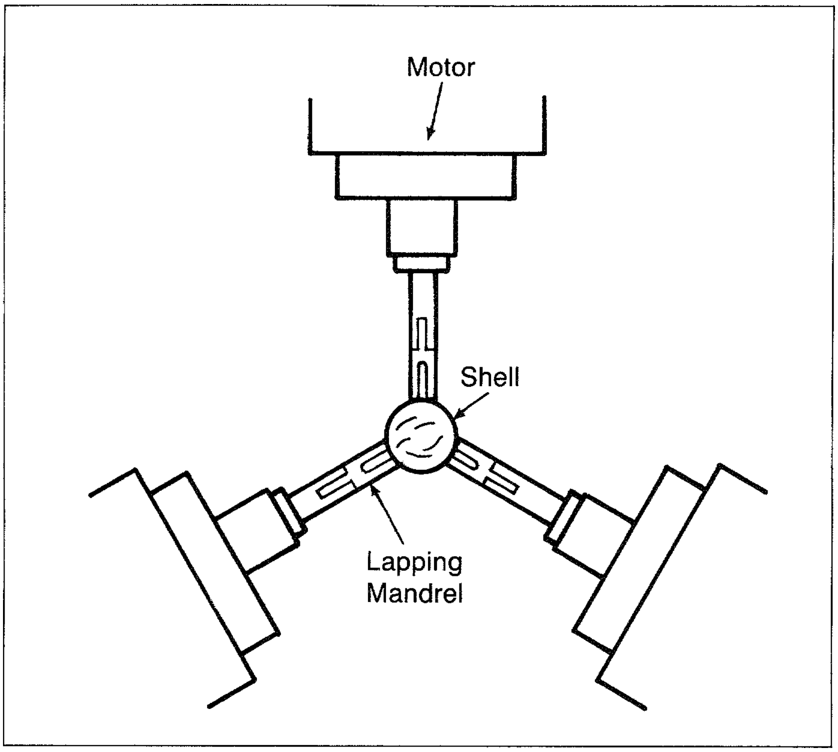

Fig. 1-20. This three-point lapping system is used to fabricate a uniform shell wall around a spherical cavity suspended in a glass matrix. The shell wall is formed with a succession of diamond slurries of decreasing grit size, followed by a final polish with cerium oxide powder.

ish. This lapping technique was transferred to KMS Fusion from Los Alamos National Laboratory in the fall of 1987.

High-Silica Glass. High-silica glass is the preferred material for Macroshell™ targets because of its high hydrogen permeation rate, which minimizes fueling times, as well as its high wall strength and high degree of chemical durability. For initial experiments, Vycor® glass (96% $SiO_2 + B_2O_3$) was preferred for its low working temperature, but it proved to be inferior to fused silica (99+ % SiO_2). Fused silica glass was substituted for Vycor® because the heat treatment produced microscopic air bubbles throughout the Vycor® glass. Bubbles at the cavity/glass interface are potentially troublesome since they prevent the formation of a uniform wall, reduce optical clarity, and weaken the shell wall.

The high working temperature of fused silica glass has made production of spherical cavities in fused silica preforms difficult. Our current furnace is capable of generating temperatures near 1800°C. The viscosity of fused silica glass at this temperature necessitates long processing times to produce spherical cavities. Consequently, glasses with lower silica content (lower viscosity) were used while this cavity treatment method was being developed.[15] The first cavities formed in a fused silica glass were produced this year. The cavities have a nominal 3 mm diameter and vary in levels of sphericity.

Wang and Day[16] have shown that a succession of heat treatments results in measurable improvements in cavity sphericity for some glass compositions. We have applied a serial heat treatment procedure to cavities suspended in a fused silica matrix; our results substantiate Wang and Day's findings. The initial processing temperature is set as close as possible to the working temperature of the glass for several hours. Each of the subsequent processing temperatures are incrementally decreased by 25° to gradually reduce the surface tension forces at the cavity/glass interface. This procedure allows the sample to cool at a slower, more uniform rate, which minimizes the temperature gradient across the sample mass. Optimal processing temperatures and times are still under investigation. However, in recent experiments, cavity noncircularity values have improved from levels greater than 10% to 1.5%.

Borosilicate Glass. Until highly spherical fused silica shells can be provided on a regular basis, borosilicate glass shells will be used in the β-heating studies. Five cavities formed in a borosilicate glass matrix were processed into shells. Each shell was fabricated using the three-point lapping system (Fig. 1-20). The shell wall was formed with a succession of diamond slurries of decreasing grit size, followed by a final polish with cerium oxide powder. Following the polish, all shells, excluding shell 1 of Table 1-2, were annealed at 565°C for 30 min. Some properties of these shells are listed in Table 1-2. Sample characterizations were performed using the optical profile projector (OPP) system, which is described in Section 1.5.3.

Three of these samples were subjected to compressive and tensile strength proof tests. The shells were individually pressurized

Table 1-2. Characterization Data for Borosilicate Shells Lapped on the KMSF Three-Point Lapping System

Shell No.	I.D. (μm)	Avg. Wall (μm)	Anneal Time (min)	Tensile Test Temp. (°C)	Tensile Test Pressure (atm)	Buckling Test Temp. (°C)	Buckling Test Pressure (atm)	Cavity Noncircularity (%) View 1	View 2	View 3
1	3850	108	–	348	186	25	184	1.0	1.6	–
2	2900	57	–	–	–	–	–	0.6	0.7	0.4
3	4000	131	30	354	183	25	200	0.4	0.6	0.7
4	3340	130	30	350	100	350	25	0.3	1.3	0.5
5	2650	124	30	–	–	–	–	2.8	2.6	–

with helium to twice the anticipated DT fuel pressure. The compressive strength test consisted of pressurizing the shell exterior to the indicated pressure level (Table 1-2) at room temperature. The tensile strength test involved the permeation-filling of each shell to a designated pressure (Table 1-2) at a nominal temperature of 360°C. Once the gas fill was complete, the gas external to the shell was vented from the sample chamber at temperature.

Shells 1 and 3, pressurized near 180 atm, survived the compressive strength test; however, both failed the tensile strength test. The tensile test failure reduced both shells to powder, which suggests a high failure stress for the shells. The failures are attributed to imperfections on the outer shell surface, formed during the lapping operation. Shell 4 survived both tests; however, the fill pressure was reduced to a 25 atm differential for the compressive test and 100 atm for the tensile test.

Shell 4 received an acid etch not performed on the other shells. The acid etch was designed to limit stress intensification at the tips of surface flaws, which originate during lapping. However, the etch caused the shell to become opalescent. A microscopic examination revealed submicrometer surface pits, which are indicative of selective leaching of the borosilicate phase in this phase-separated glass. The use of an acid etch to relieve stress and the need to maintain shell transparency will require the use of a single-phase glass such as fused silica.

For additional information, please contact Mr. L. A. Scott

1.3.2 Permeant Gases in the Furnace Ambience

The partial displacement of air with permeant gases (gases that diffuse through the shell material) in the furnace ambience during shell blowing can produce a significant increase in the diameter of shells. This effect is the basis of our long-standing practice of using a high partial pressure of water vapor in the furnace ambience to produce shells of large diameter. A simple model describing this effect has been formulated from basic principles by Anderson and Miller.[17] However, the utility of this effect for making large-diameter shells and the general validity of this model have not been tested quantitatively.

There is an advantage to using other permeant gases, such as helium or neon, for making shells of large diameter. These unreactive gases, unlike water vapor, will not corrode the glass surfaces or weaken the shells. We seek to quantitatively verify the model with these gases.

Preliminary results from experiments with helium in an unsealed two-piece process tube, which required a continuous make-up flow of helium to maintain a steady-state helium concentration, agreed only qualitatively with the model;[17] we were unable to measure the helium concentration in the furnace ambience directly. In addition, the aerodynamic drag on the sedimenting glass shells due to the helium flow significantly increased the residence time of the shells in the furnace.

During the past year, we conducted further shell-blowing experiments in a sealed furnace with a one-piece process tube that contained static, uniform permeant gas mixtures with known concentrations of water vapor, helium, or neon. From this work, we concluded that the permeant gases cause an increase in shell size that is consistent with the predictions of the Anderson-Miller model. The model fails at high concentrations (>0.9 atm) of permeant gas, probably because the high levels of permeant gas produce a significant fraction of large shells that are too thin to survive, so that the product consists primarily of the remaining smaller, thick-walled portion of the shell population. Furthermore, we found that gel fragmentation was severe in dry permeant gas mixtures. Even though permeant gases cause an increase in shell size, the extensive fragmentation of the gel, by producing low-mass particles, limited the effectiveness of the dry permeant gases for making shells of large diameter. Even low levels of water vapor in the furnace ambience dramatically decreased gel fragmentation.

Experimental. Shell-blowing experiments were conducted on a vertical 1 m, 1500°C furnace that was equipped with a one-piece sealed process tube, a sealed gel injector, and a gas inlet system for the controlled addition of permeant gases to the static furnace ambience. The permeant gases were helium, neon, or water vapor; the nonpermeant gas in the furnace ambience was air or oxygen. The air or oxygen concentration in the gas mixture in the furnace was determined with an oxygen monitor; since the system was leak-tight, the remainder was equivalent to the partial pressure of the permeant gas. The equipment and procedures were described previously.[18]

Results. The effect of an increase of the partial pressure of a permeant gas in the furnace ambience is an increase in the shell radius. As shown in Figs. 1-21, 1-22, and 1-23, the three permeant gases produced similar trends of increasing shell size with increasing partial pressure of permeant gas, for permeant gas concentrations up to 0.9 atm. Between 0.9 and 1 atm permeant gas pressure, where the model calculations display a significant curvature, the data invariably were significantly lower than the

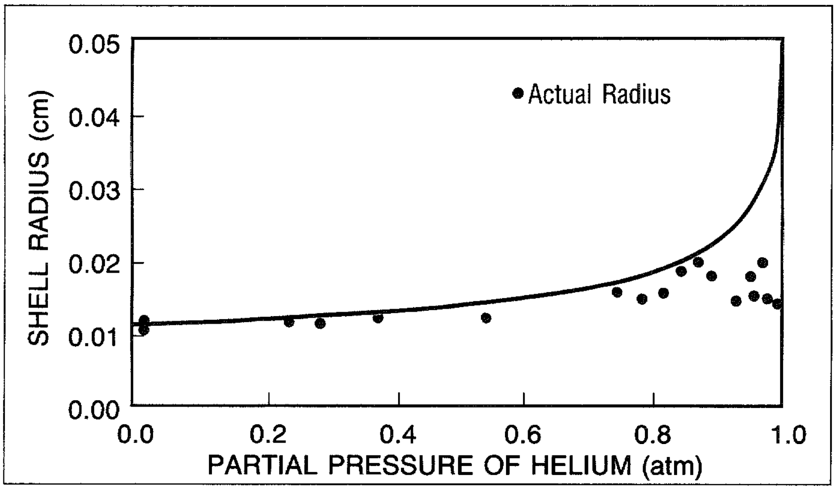

Fig. 1-21. At concentrations greater than 0.85 atm, the effect of helium in the furnace ambience deviated significantly from the predictions of the model.

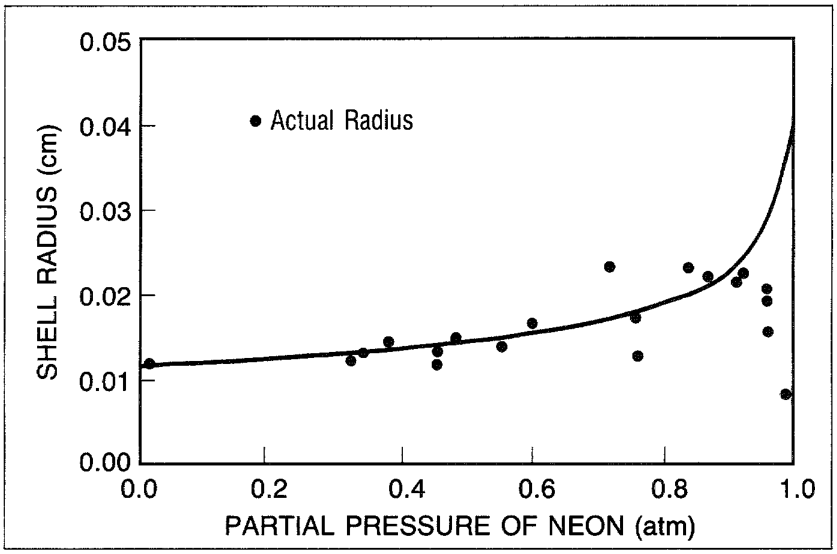

Fig. 1-22. The neon data fit the model predictions only for partial pressures less than 0.9 atm, where the model has a relatively flat response slope. As was the case with the helium data, the shell sizes were significantly less than the model predictions for neon concentrations greater than 0.9 atm.

model predictions. The greatest deviation was in the data for neon, the least permeant of the three gases, for which the shell radius decreased with increasing neon pressure beyond 0.9 atm. The reason for this deviation is not clear. However, the large number of thin-walled shards that are produced in high partial pressures suggest that these levels of permeant gas rapidly expand and rupture the large, thin-walled shells, while the smaller, thick-walled shells survive.

The shell size distributions in these experiments broadened markedly with increasing permeant gas pressure. This effect was least for water vapor, and worst for dry helium and dry neon.

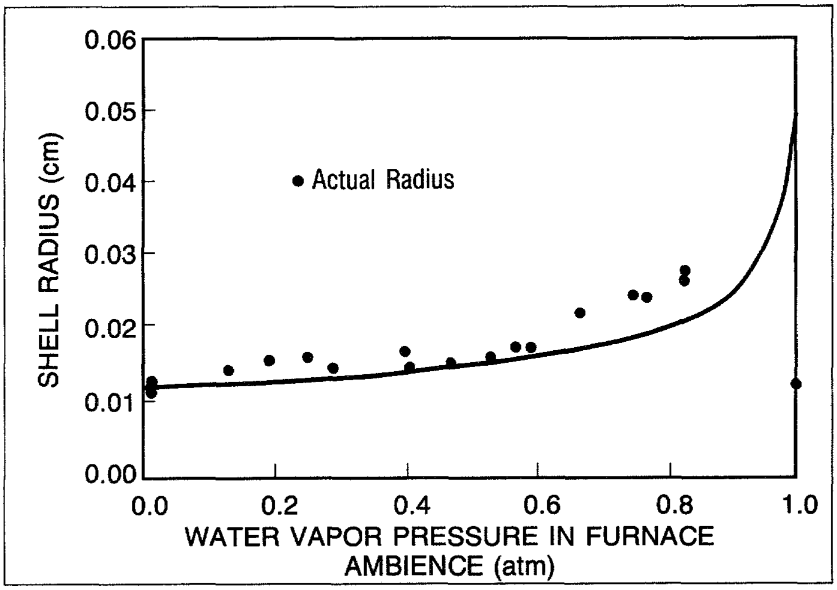

Fig. 1-23. The data for water vapor are consistent with the predictions of the model. These data corroborate results obtained from earlier experiments that used an open furnace process tube.

In addition, the quality of the shells (sphericity, wall uniformity, intrawall bubbles) decreased precipitously with increasing pressure of dry helium and dry neon. At high levels of dry permeant gas, many of the large, thin shells were partly collapsed or puckered, while the smaller, thicker shells had poor wall uniformity and intrawall bubbles. Few, if any, acceptable shells were found in shell batches produced in dry helium or dry neon. Water vapor (which reduces glass viscosity) markedly improved shell quality.

A comparison of the median shell mass for the various batches in these experiments, normalized to the mass of glass formers contained in the gel, indicated that extensive gel fragmentation dominated these experiments and may have obscured the true effect of permeant gases on the blowing of shells. In addition, despite the efficacy of dry permeant gases in increasing the size of shells, the fragmentation of the gel effectively limits the ultimate attainable size of the shells.

As shown in Fig. 1-24, the effects of helium and neon on fragmentation of the gel or the forming shell in the furnace were similar. Both gases produced shells with similar radii and similar mass. However, the median shell mass was less than 5% of the glass mass contained in the gel feedstock, and was identical for helium and neon, indicating that the greater thermal conductivity of the helium gas was not a significant factor in gel fragmentation. Moreover, even though there is a relationship between shell radius and partial pressure of the gas, the normalized mass was essentially constant for all values of partial pressure of helium or neon.

The normalized mass of shells produced in water vapor was significantly higher than for dry helium and neon. While every

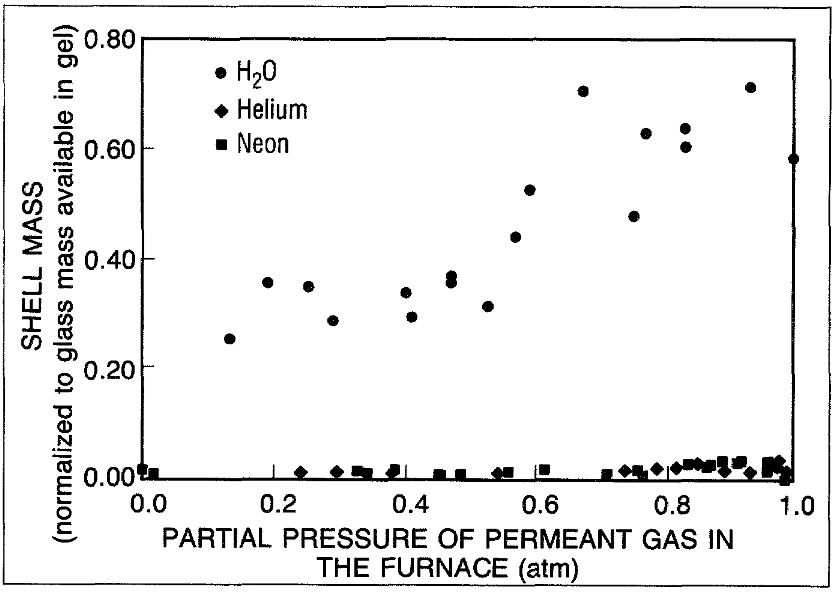

Fig. 1-24. The permeant-gas shell-blowing experiments were dominated by fragmentation of gel feedstock in the furnace. Dry air, helium, and neon produced shells whose median mass was less than 5% of the glass mass of the gel feedstock. Water vapor produced thick-walled shells whose median mass ranged from 30% to 70% of the glass mass of the gel, depending on the water vapor pressure.

batch from the water vapor experiments contained some small shells with diameter, wall thickness, and shell mass that were comparable to those in the helium and neon experiments, these shells represented the lower tail of the mass distribution of the shell batches. The major portion of the mass of each batch consisted of very thick-walled, massive shells, whose radii were comparable to the shells produced with helium and neon. Furthermore, as shown in Fig. 1-24, the normalized shell mass of the batches made with water vapor was not constant, but was related to water vapor pressure. The normalized shell mass in the control batches made in dry air was less than 0.05, equivalent to that of the dry helium and neon experiments. By comparison, 0.1 to 0.5 atm water vapor yielded a constant normalized shell mass of 0.3; increasing the water vapor pressure beyond 0.5 atm monotonically increased the normalized shell mass.

Thus these data indicated that the moisture content of the furnace ambience is a critical variable in gel fragmentation. It may be that the water vapor rapidly reacts with the surface of the gel, and may thus reduce the gel viscosity at the gel surface sufficiently to minimize spalling.

Conclusions. The displacement of air in the furnace ambience with permeant gases causes an increase in shell size that is consistent with the predictions of the Anderson-Miller model. The model fails at high concentrations (>0.9 atm) of permeant gas, probably because the high levels of permeant gas produce a significant fraction of large shells that are too thin to survive and consequently rupture. The product thus consists primarily of the remaining smaller, thick-walled portion of the shell population.

Furthermore, we found that gel fragmentation was severe in dry permeant gas mixtures. Even though permeant gases cause an increase in shell size, the extensive fragmentation of the gel into low-mass particles limited the effectiveness of the dry permeant gases for making shells of large diameter. Even low levels of water vapor in the furnace ambience dramatically decreased gel fragmentation. In addition, high levels of dry helium or dry neon yielded shells with a very broad size distribution and extremely poor quality that were unsuitable for ICF targets.

For additional information, please contact Mr. M. A. Ebner

1.3.3 Gel Composition Study

The ICF program uses glass shell targets of ever larger diameters and wall thicknesses. Our glass shell fabrication technology must be able to produce shells with increased diameters and wall thicknesses, as well as to improve the average wall uniformity over the entire size range.

Using our drop tower technology we are pursuing two approaches: (1) optimization of the key experimental processing parameters, and (2) optimization of the feed-stock gel composition. In the early 1980s we emphasized the processing parameters, achieving greater control and reliability over the process as well as extending the shell size range. More recently we have concentrated on the gel feedstock.

Determining an Optimal Alkali Concentration. Previously we reported the results of experiments designed to find the optimal alkali ratio in an alkali-borosilicate gel.[19,20] Keeping the total alkali oxide content (i.e., total oxide equivalent molar percentage) at 15%, we systematically determined the optimal Na:K:Rb ratio to be 1:1:4.

Our next step was to find the optimal alkali content in the gel for the optimal alkali ratio. We examined gels ranging from 5% to 35% alkali oxide. Each gel was tested, by varying known processing parameters, under conditions to make smaller, thin-walled shells ($\simeq 100$ to 600 μm diameter × $\simeq 0.5$ to 8 μm walls) and also under conditions to make larger, thick-walled shells ($\simeq 200$ to 800 μm diameter × $\simeq 2$ to 14 μm walls). Five different shell runs were performed under each set of conditions with each gel. Since cesium was not included in the earlier experiments to determine optimal alkali ratios, we also examined a 15% cesium oxide gel.

Shell diameters slowly decreased and shell wall thicknesses increased as the alkali oxide content increased. The most important trend is shell wall uniformity, measured by the percentage of class A shells in a batch. (A class A shell has less than 10% nonconcentricity in a single-view interference photograph.) As shown by Fig. 1-25, class A increases with gel alkali oxide content for the thinner, smaller shells, but attains its maximum at about 20% for the thicker-walled shells. Cesium did not improve wall uniformity in the 15% gels.

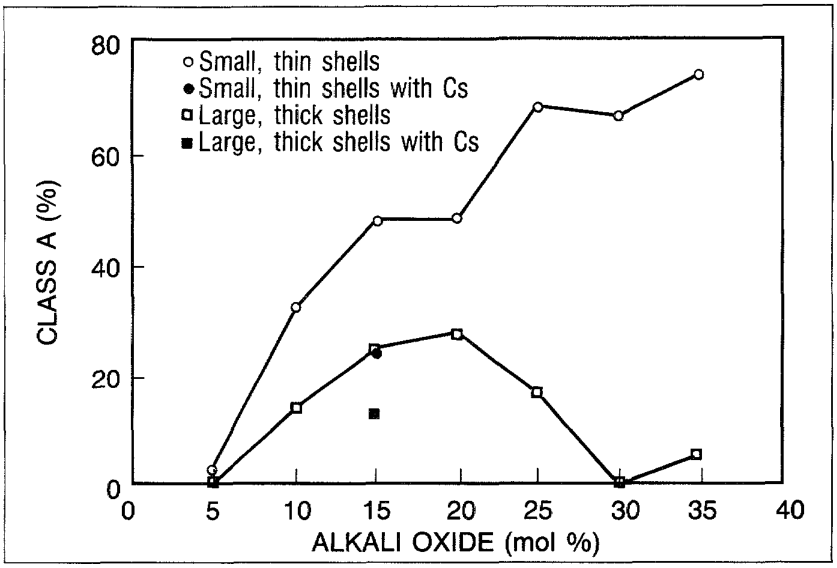

Fig. 1-25. The percentage of class A shells in a batch is affected by the alkali concentration in the feedstock gel. Each symbol represents the median of five batches run under different processing conditions.

Since larger, thicker shells are of greater interest, the 20% gel was selected for further study.

Modeling the 20% Gel. Further study of the 20% gel required the development of an empirical model quantitatively relating the key processing parameters to the resulting glass shell characteristics. Two sets of experiments were performed, screening experiments to identify the key processing parameters and response-surface experiments to quantitatively relate the key parameters to the resulting glass shell characteristics. This type of experimentation was previously discussed.[20,21,22]

The screening experiments examined 11 parameters, which consisted of five gel parameters and six environmental parameters. The gel parameters were gel size and four gel pretreatments (exposure to humid air, autoclaving, vacuum oven drying, and pyrolysis). The environmental parameters were furnace temperature, shot size, shot interval, number of shots, water vapor pressure, and the use of a portal to partially close the top of the vertical furnace tube. Of these, four were found to be key parameters worthy of further study: gel size, autoclaving, pyrolysis, and water vapor pressure in the vertical furnace tube.

Response-surface experiments were completed for the four key parameters using a Box–Behnken[23] experimental design. However, the resulting polynomial equation did not reliably predict the results of shell batches run at the extreme values of the parameters. We added some extreme points to the design. The new polynomial equation is reliable.

The calculated response surfaces show that this gel produces good quality shells over a large range of shell sizes. Figure 1-26 shows the response surface for diameter. The calculated overall size range extends to 1100 μm diameter and 14 μm thick walls, shown by Fig. 1-27.

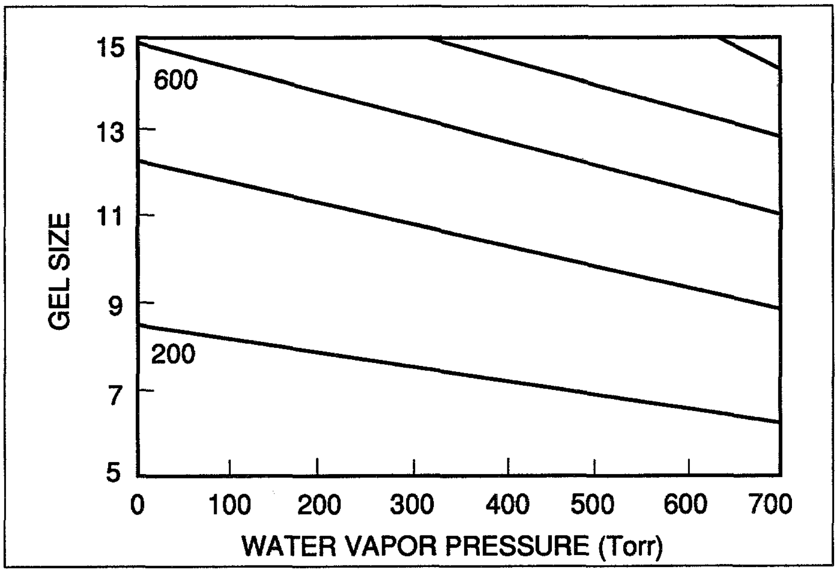

Fig. 1-26. Experiments were conducted to establish a relationship between gel size, water vapor pressure, and the diameters of the final shells. These curves were calculated from an empirically derived polynomial equation. Any combination of gel size and water vapor pressure that lies on the line labeled 200 will result in a batch of glass shells that have a predicted median diameter of 200 μm. The curves show that increasing the water vapor pressure and/or gel size increases the diameter of shells produced from a given gel size.

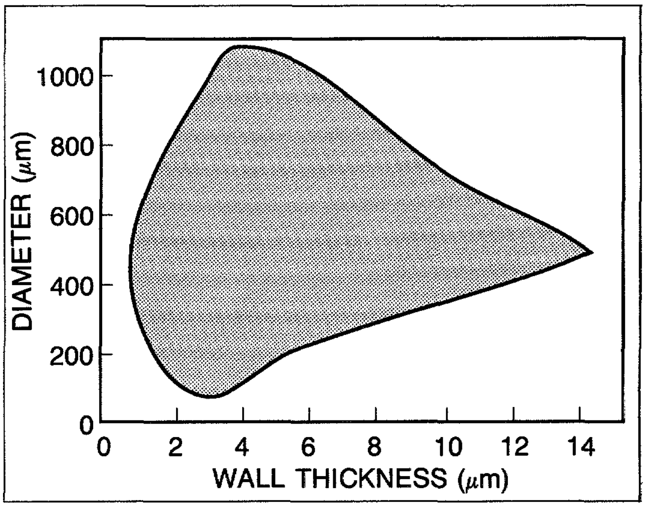

Fig. 1-27. The range of shell sizes from the optimal gel is very large. The darkened area shows the calculated median batch diameters and wall thicknesses that can be obtained over the entire range of the four key parameters.

Large Shells with the 20% Gel. The response-surface experiments were performed using gel sizes up to 425 μm. In order to extend the shell size range further, we examined shell fabrication using our largest gel sizes, 425 to 500 μm and 500 to 600 μm. We performed a pseudo-response surface design using gel size, furnace temperature, and water vapor pressure as variables. The results were fit to a simple four-parameter polynomial. The calculated shell size range is shown in Fig. 1-28. The tower furnace temperature has a strong effect on diameter, as shown in Fig. 1-29. We have not observed this trend with smaller gel sizes.

The percentage of class A shells is low in this size range, but the class B shell percentage is reasonably high. Class B shells have greater than 10% nonconcentricity in a single-view interference photograph, but do not have other defects [i.e., Class B

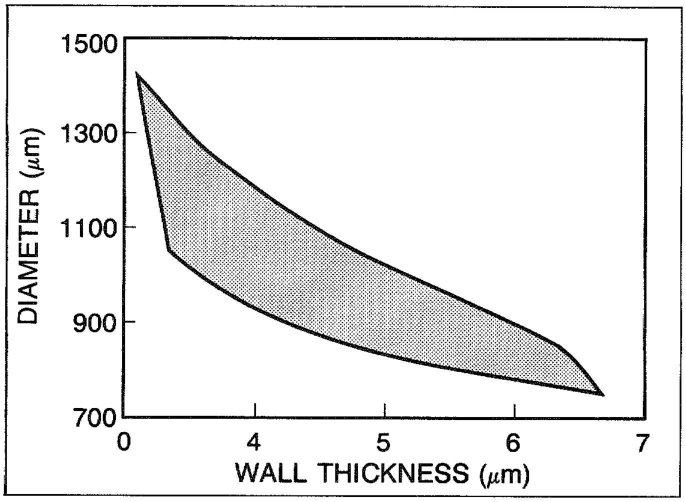

Fig. 1-28. Shells of very large diameter can be prepared using the largest gel sizes of the optimal gel.

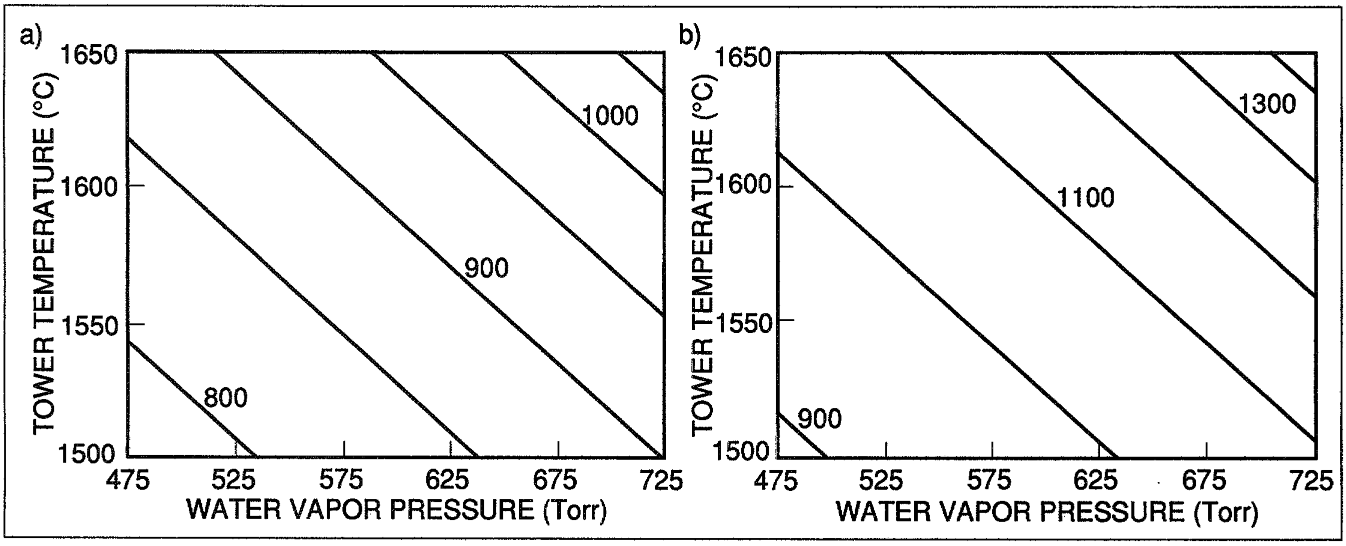

Fig. 1-29. For gel sizes from 425 to 500 μm (a) and 500 to 600 μm (b), the tower furnace temperature, along with gel size and water vapor pressure, has a strong effect on diameter. This effect has not been observed with gels of smaller size. Any combination of tower temperature and water vapor pressure that lies on a line labeled 900 will result in a batch of shells that have a predicted median diameter of 900 μm.

shells have P_1 defects (nonconcentricity) but not P_2 (ellipticity) and greater]. However for some implosion experiments, this level of nonconcentricity is acceptable.

Conclusions. We are increasing the size range and wall uniformity of our glass shells. We have found and quantitatively explored a superior gel containing 20% alkali oxide in the ratio of Na:K:4 Rb. The new gel produces shells over a large size range with very good wall uniformity.

For additional information, please contact Mr. W. J. Miller

SECTION 1.4

Coating Technology

During 1988 the main coating activity was in the improvement of the glow discharge polymerization (GDP) coatings in terms of surface finish and deposition rate, and the development of new coating procedures necessary for the fabrication of complex diagnostic targets. The improvement of the GDP coatings was accomplished by a redesign of the existing coating system and ultimately by copying the Lawrence Livermore National Laboratory (LLNL) design that has been tested over a number of years. The development of "Gaussian"-bump targets involved a considerable amount of exploratory work since there was no precedent for these tasks. Also, the deposition of KCl and NaCl over 4π of the surface of 350 μm diameter spheres was a "first" and required solving challenging problems. The following section addresses each one of these topics in detail.

1.4.1 Development of CH(GDP) Polymer Coatings

Study of Deposition Parameters. Many of the requests for composite glass/polymer fuel shells are satisfied by depositing a coating of CH onto a glass shell by GDP. Before this year, such coatings were typically marred by cauliflower-like surface textures with superimposed mound-like structures (see Fig. 1-30). The severity of the features on the coated shells is a function of processing parameters (including deposition chamber geometry,

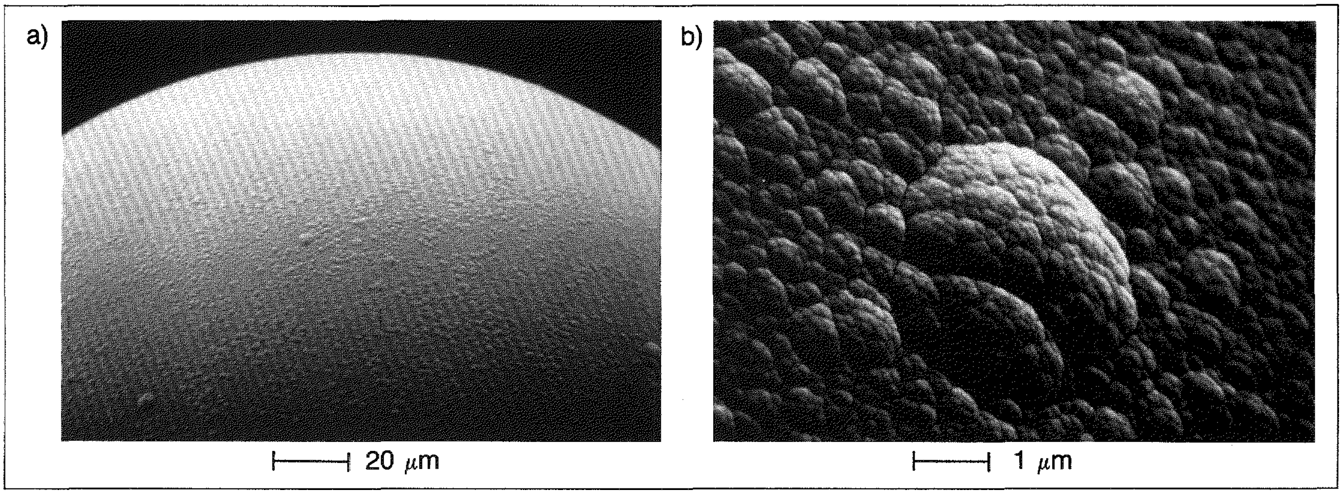

Fig. 1-30. Before improvements were made to the coating system, shells exhibited surface features that were dominated by a cauliflower-like structure and occasional mounds. This is apparent in SEM photographs of a 350 μm diameter glass shell coated with 20 μm of CH(GDP) at magnifications of 500× (a) and 10,000× (b).

gas composition and flow rates, reaction pressure, and RF power and input configuration). In an effort to improve the surface finish of our CH(GDP) coatings, we performed experiments that varied some of the deposition parameters. While more work is still needed, we are now able to produce much smoother coatings.

At the outset, we determined that it was indeed the deposition parameters, and not the shell substrates, that were responsible for the roughness of the coated surfaces. Some of our glass shells were coated in the helical resonator plasma generator GDP deposition system developed at LLNL. This generator can produce coatings with ultrasmooth surface finishes[24] (although it, too, has idiosyncrasies that are not fully understood and therefore warrant investigation). We found that, for a narrow range of operating conditions, the helical resonator system did indeed produce GDP coatings with no discernible surface features. The glass shell surface cleanliness in our process was adequate and, under certain operating conditions, surface mounds and cauliflower-type background structures do disappear.

To investigate the influence of the operating parameters on the surface finish, we built a developmental system (GDP system 3) that was able to simulate the running conditions of the helical resonator. The operating conditions that yielded a better surface finish were then transferred to our production coaters (GDP systems 1 and 2). The use of a separate development system minimized production down-time.

The initial configuration of GDP system 3 is shown schematically in Fig. 1-31. The shells were rolled and bounced on a metal pan (driven by a piezoelectric transducer) under the glow near the end of the tapered plasma tube. The gas, typically a mixture of hydrogen and butadiene, entered at the top. The plasma was excited with 7.5 W of 13.56 MHz RF energy.

Figure 1-32 is a scanning electron microscope (SEM) photomicrograph of a typical GDP coating on a 350 μm glass shell. The cauliflower-type background and mound-like structures are still there, but reduced in size. The "debris" visible in this picture represents gas-phase nucleated polymer that has dropped onto the surface of the shell. We believe that the deposition of these particles leads to the mound-like structures seen on the earlier GDP coatings. The growth of such surface imperfections has been described by Letts.[25]

The first modification of this system was the addition of a "skirt" below the plasma tube. This was done to divert the gas flow directly onto the bouncing, rolling shells (Fig. 1-33). Typical GDP coatings on glass shells produced using this new deposition configuration are shown in Fig. 1-34. The new configuration resulted in the complete disappearance of mound-like structures on the surface. Use of the skirt below the plasma tube appears to have changed the flow characteristics of the gas such that gas-phase nucleated particles could not stay long enough to grow to significant size. The cauliflower-like background surface texture was also improved, but was still not as smooth as was seen with the helical resonator.

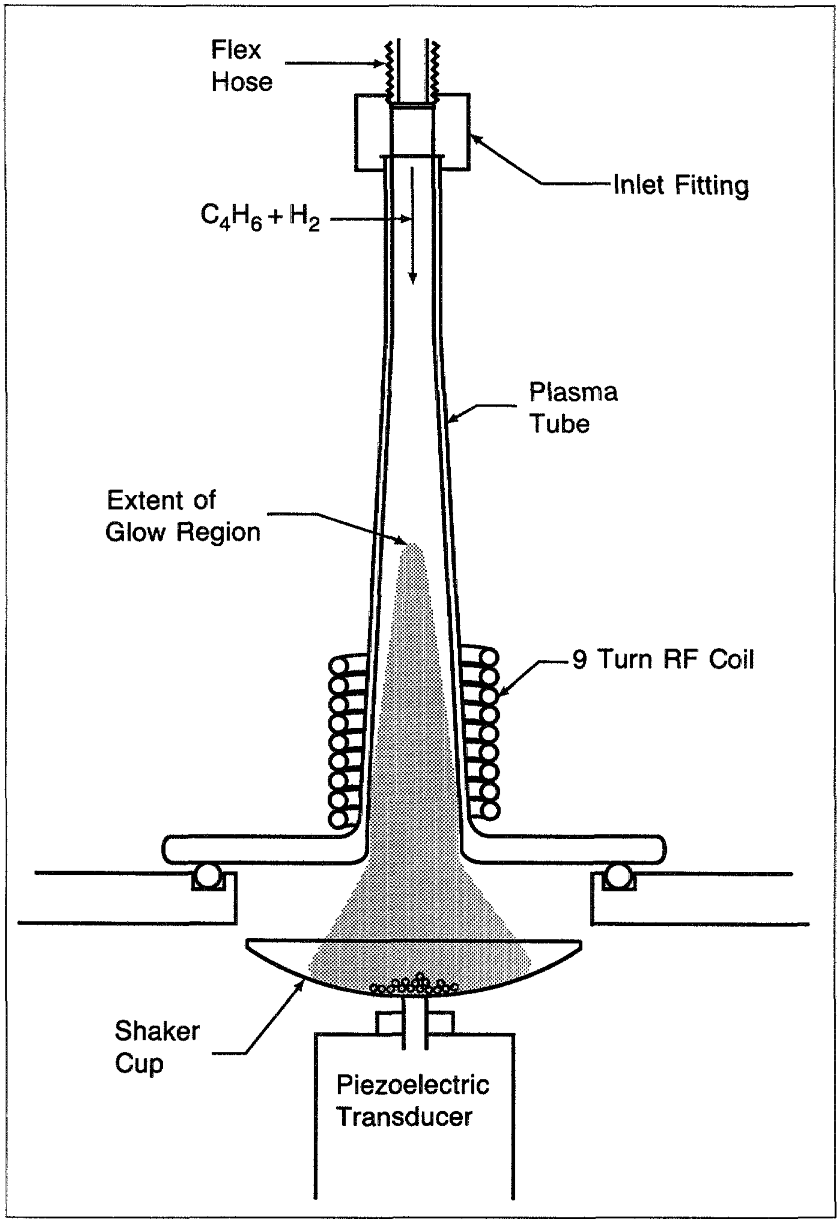

Fig. 1-31. To investigate the influence of the operating parameters on the surface finish of coated shells, we built a developmental system that was able to simulate the running conditions of the helical resonator. The initial configuration of our system is shown here. The plasma is created by a 13.56 MHz RF source.

Our next modification, also inspired by the LLNL helical resonator, was to add a fan to cool the plasma tube. This was done to keep coating material from flaking off of the wall of the tube and the bouncer pan, since such flaking limited the RF power intensity to a maximum of 7.5 W. The addition of the cooling fan did reduce flaking and resulted in much improved coatings, although the cauliflower-like texture was not completely eliminated. However, we were still not able to operate successfully above 7.5 W since flaking occurred at higher RF power.

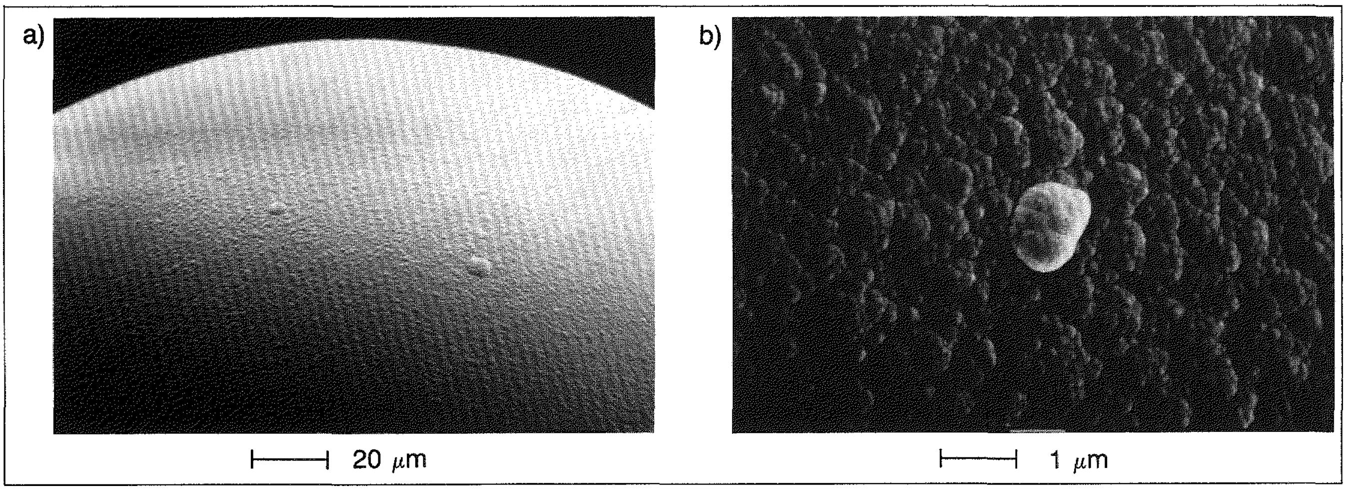

Fig. 1-32. The system depicted in Fig. 1-31 was used to deposit a 39 μm CH(GDP) coating onto a glass shell. The coated shell is shown here at magnifications of 500× (a) and 10,000× (b). Operating conditions were 76 mTorr pressure, 0.3 sccm butadiene, 7.0 sccm hydrogen, and 7.5 W of 13.56 MHz RF power. The apparent deposition rate was 0.41 μm/h.

The LLNL helical resonator is equipped with forced-air cooling and can operate at 20 W. When we used a helical resonator on our production GDP coater system 1, CH coatings were produced with featureless surfaces (Fig. 1-35). Operation at reduced power levels with the helical resonator composite system led to a recurrence of a cauliflower-like background surface finish. This suggests that higher RF power (~20 W) is required to eliminate cauliflower-like background features.

We therefore conclude that mound-like growth structures in CH(GDP) coatings can be reduced by adjusting gas flow conditions to deter the growth of gas-phase nucleated particles. We also conclude that the background cauliflower-like surface finish appears to be affected by plasma parameters, including RF power. More work is needed in this area to identify the mechanism responsible for the reduction of the cauliflower-like surface texture.

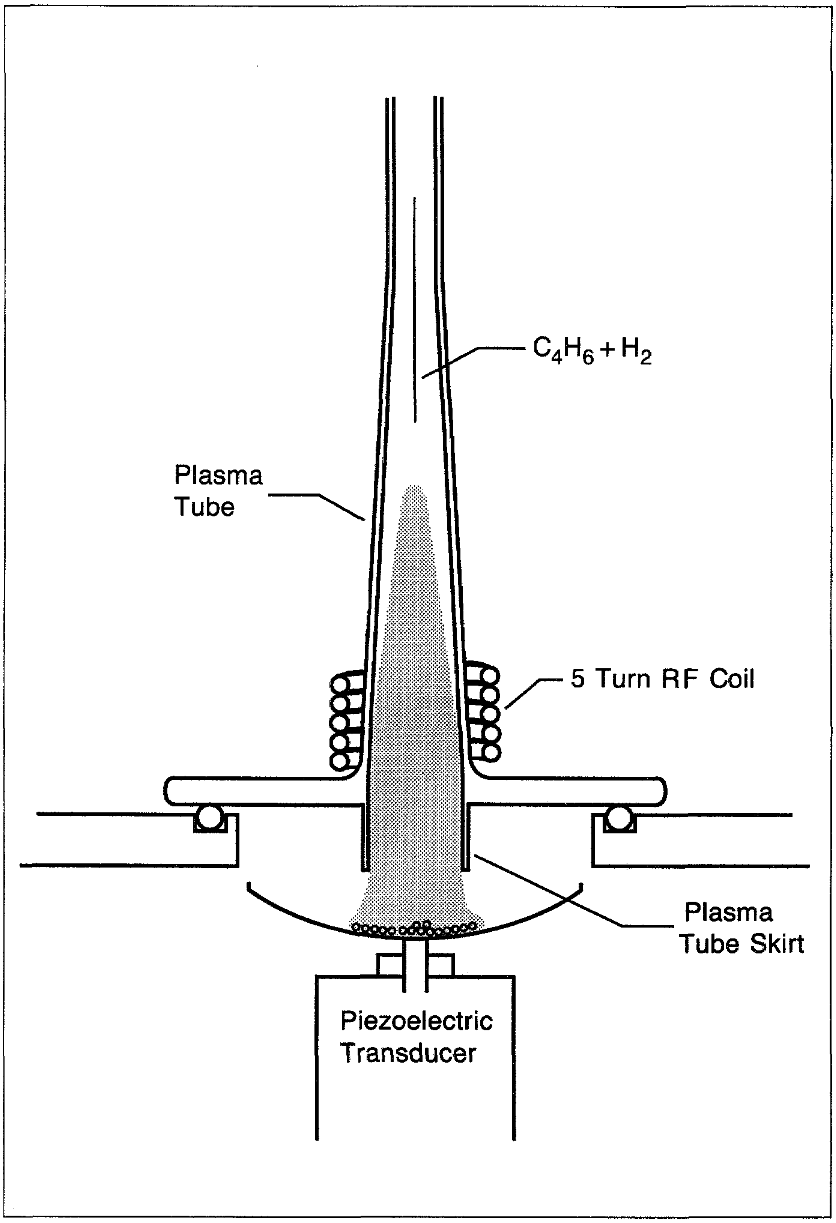

Fig. 1-33. A "skirt" was added to the GDP coating system depicted in Fig. 1-31 to divert the gas flow more directly onto the bouncing shells. This appears to have changed the flow characteristics of the gas such that gas-phase nucleated particles cannot stay long enough to grow to significant size.

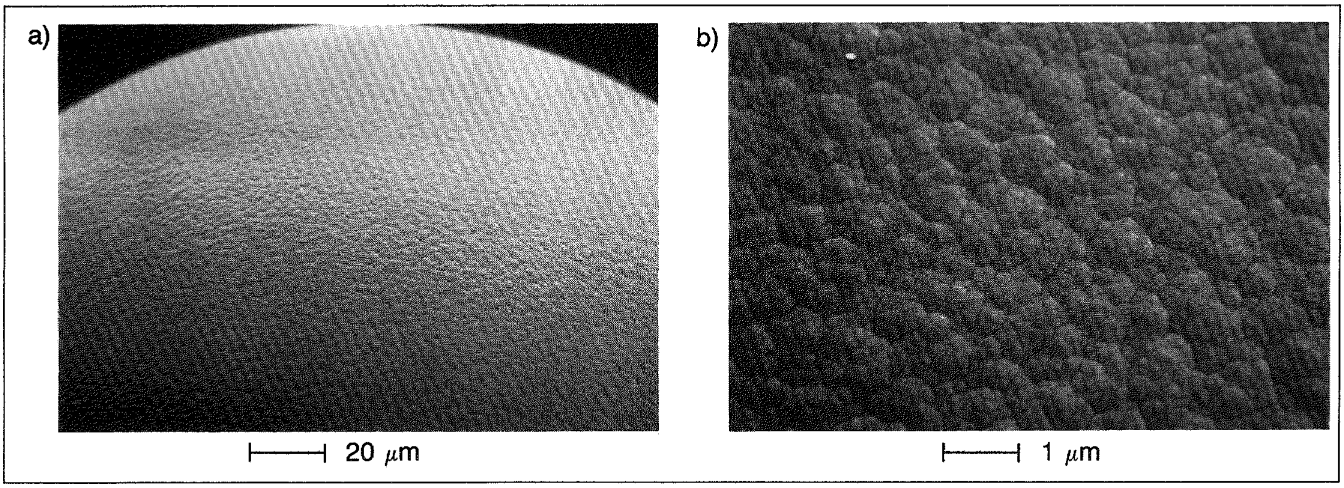

Fig. 1-34. The system depicted in Fig. 1-33 was used to deposit a 39 μm CH(GDP) coating onto a glass shell. The coated shell is shown here at magnifications of 500× (a) and 10,000× (b). Operating conditions were 75 mTorr pressure, 0.3 sccm butadiene, 7.0 sccm hydrogen, and 7.5 W of 13.56 MHz RF. The deposition took place at an apparent rate of 0.6 μm/h.

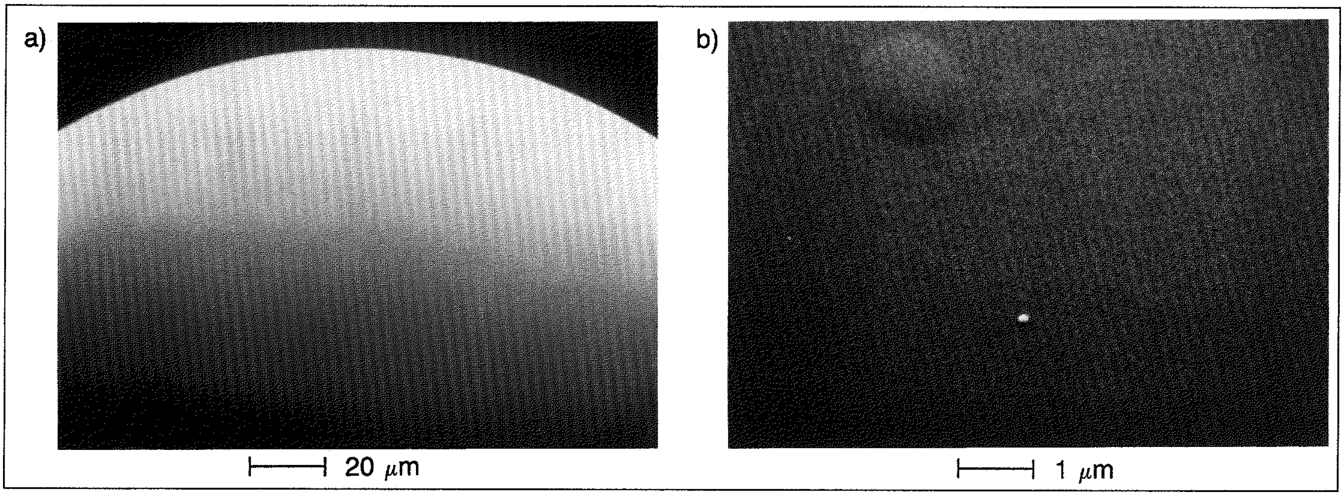

Fig. 1-35. Very smooth coatings can now be produced, as shown in this SEM photograph. This shell was coated with 30 μm (CH)GDP using a composite helical resonator (KMSF GDP coating system 1) operating at 72 mTorr pressure, 0.4 sccm trans-2-butene, 10.0 sccm hydrogen, and 20 W of 42 MHz RF. The apparent deposition rate was 0.57 μm/h.

For additional information, please contact Dr. R. L. Crawley

Surface Improvement and Thickness Adjustment by Plasma Etching. The need to improve the surface finish of polymer shells and to reduce the wall thickness of some shells led us to investigate the use of a plasma etching technique. In this process, we use an RF-excited oxygen-argon plasma to etch polymer shells. Etching occurs when the radicals or ions (namely, oxygen) from the plasma react chemically with the polymer material to form a gas (which is then pumped out of the system). We successfully applied this etching process to polystyrene (PS) shells, CH(GDP) coatings, and parylene coatings.

The surface finish resulting from these experiments varied with the type of polymer being etched. Etching of PS, whose structure contains long chains of high molecular weight, yielded a post-etch surface with some sub-micrometer size particle clusters. CH(GDP) coatings produced in the helical resonator, on the other hand, showed no visible change from the originally smooth surface. Experiments with much rougher CH(GDP) coatings on glass shells showed a marked improvement in the surface quality after etching. A "smoothing" effect reduced the larger domes and cauliflower-like background so effectively that the final surface finishes began to approach those made by the helical resonator. In fact, the results achieved on CH coatings from GDP were so good that we used the process to thin CH(GDP) coatings that had inadvertently been made too thick.

The surfaces of etched parylene films were featureless and comparable to the best etched GDP shells. More than 30 parylene thin films were etched for a KMS Fusion (KMSF) laser/ plasma interaction experimental campaign. During this campaign specifications were changed, and etching was done "on the fly" to adjust the already fabricated targets to the new thickness requirements.

Differences in the surface finish between these three etched polymers are caused by differences in their molecular structures. It has been reported that the noncrystalline portion of a polymer is more easily etched than the crystalline phase.[26] Studies also show that long-chain polymers with adjacent functional groups bonded to the backbone etch at different rates in localized areas.[27] Aromatic structures especially are known to fragment, forming free radicals which are open for reaction. Polystyrene, which has a long chain and a benzine-ring functional group, may present areas that are crystalline in structure and, more importantly, show fragmentation processes. The CH coating produced by GDP, however, is highly crosslinked due to the glow discharge process and therefore has virtually no crystallinity. Parylene is also a long-chain polymer but, unlike PS, its benzene ring is a constituent of the carbon backbone and not a dangling side group. This structure could explain its relatively homogeneous etching, producing a surface much like that of etched GDP.

In an attempt to improve the finish of an etched polymer surface further, we performed a few experiments with a pure hydrogen plasma. Post-etch surfaces of PS were devoid of any cluster formation, an improvement over the oxygen process. There was evidence, however, of sub-micrometer craters that were very faint and shallow. The etch rate was also appreciably reduced. A two-part run using the oxygen etch to reduce the shell wall thickness quickly, followed by a short hydrogen etch to remove the cluster formation, produced a finer surface finish and provided information for further improvements.

For additional information, please contact Mr. J. C. Daukas

1.4.2 Development of Target Diagnostic Layers

KCl Layers. Targets designed to measure the hydrodynamic stability of an imploding shell require an embedded layer of KCl as an x-ray emitting source. Evaporation is the simplest method for producing films of KCl since it has a fairly high vapor pressure (10^{-4} Torr) at a temperature easily accessible using simple tantalum evaporation boats. The cohesive energy of KCl is high (7.0 eV) and therefore the molecule is stable at evaporation temperatures.

For materials like KCl the films produced are generally polycrystalline. The film structure depends on the flux of evaporated material, the directionality in the flux (with respect to the growing film surface), substrate and background gas cleanliness, and the mobility of the molecules on the film surface.

The objective was to uniformly coat spherical glass and polymer microspheres (shells) with KCl. This is accomplished by shaking or bouncing the shells in a cup with the evaporant flux streaming from above in a fashion similar to that used for CH(GDP) coatings. A schematic of the deposition chamber appears in Fig. 1-36. The background pressure in the evaporator before deposition is near 6×10^{-7} Torr. The source is a baffled tantalum boat for downward evaporation and the shaker pan is a stainless steel cup attached to a lead zirconium titanate (PZT) crystal as a transducer. The source-to-substrate distance is 15 cm. A shutter is placed over the cup to keep chunks of evaporant from falling into the pan during the initial temperature rise of

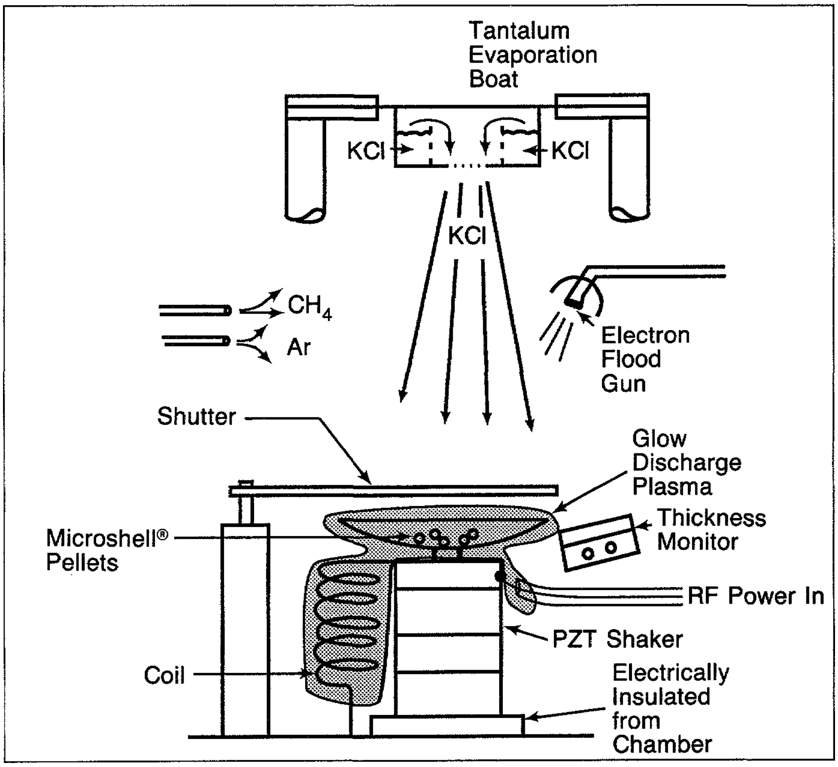

Fig. 1-36. Diagnostic layers of KCl are deposited in the apparatus depicted here schematically. A plasma discharge maintained around the shaker pan by an external RF source is used to place a thin polymer coating over the KCl layer.

the source. To maintain a constant deposition rate, a thickness and rate monitor is used.

Causing shells to bounce under high vacuum proved difficult. The shells picked up static charges and clumped together, making it impossible to coat them uniformly. This problem was solved with the addition of another tungsten filament with a small bias (10 to 50 V) to flood the shells with electrons. With proper adjustment of the electron current into the cup, the shells actually repelled each other slightly and shell clusters did not form.

In this way, we were able to bounce-coat both glass and PS shells. The large (300 μm diameter) and thick (10 μm walls) shells bounce best. By preparing the shells properly, we can also coat smaller and thinner shells.

During the course of this study it became apparent that the deposited film texture is affected to a great degree by the absorption of water vapor. Initial KCl deposits were made on flat glass substrates as a thickness calibration. One of these is shown in Fig. 1-37. The large "salt-like" grains appear more pillow-shaped and not as sharply angular as one would expect. We next coated 380 μm glass shells in the bouncer described above. A typical shell is displayed in Fig. 1-38. One can see that the grains are not as large in this case. We found that the differences between the two films were a result of different exposure times to water vapor.

Assuming that moisture gives rise to such differences, a method was needed to protect these films while they were re-

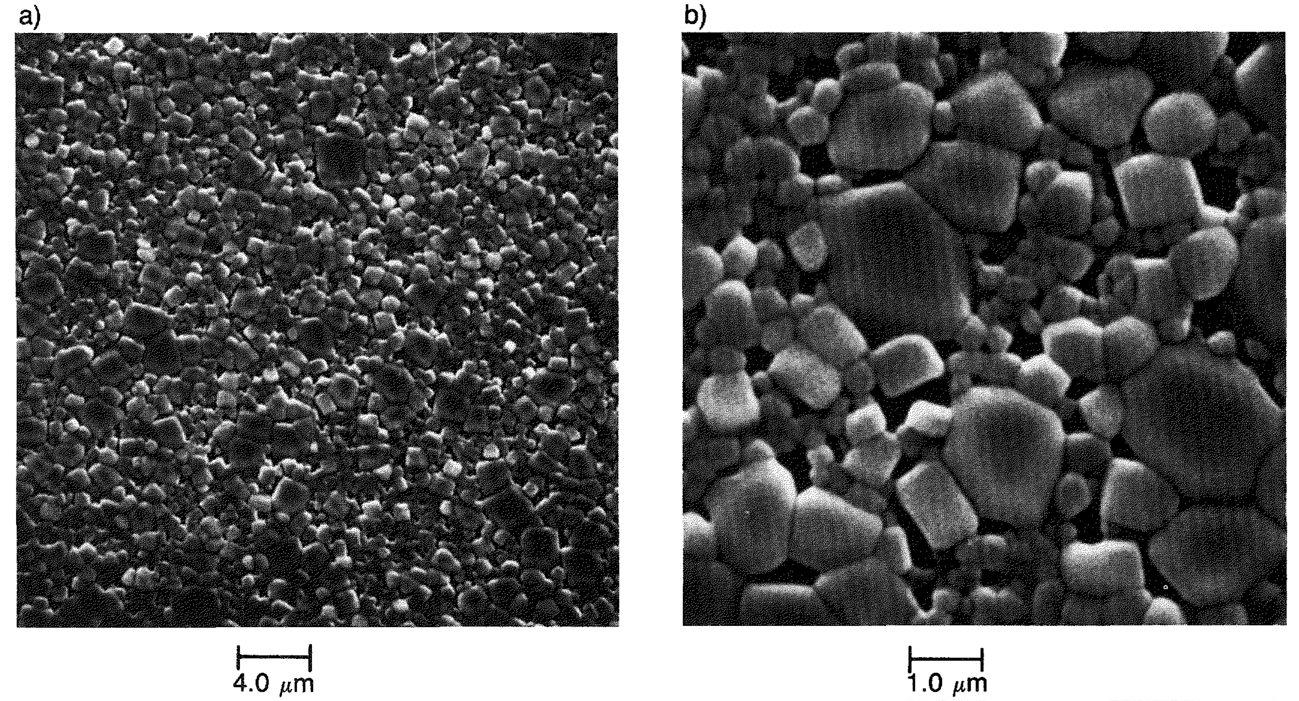

Fig. 1-37. Initial KCl deposits were made on flat glass substrates as a thickness calibration. A 0.25 μm thick KCl film on a glass slide is shown in these SEM photographs at magnifications of 2500× (a) and 10,000× (b). Large grains are apparent.

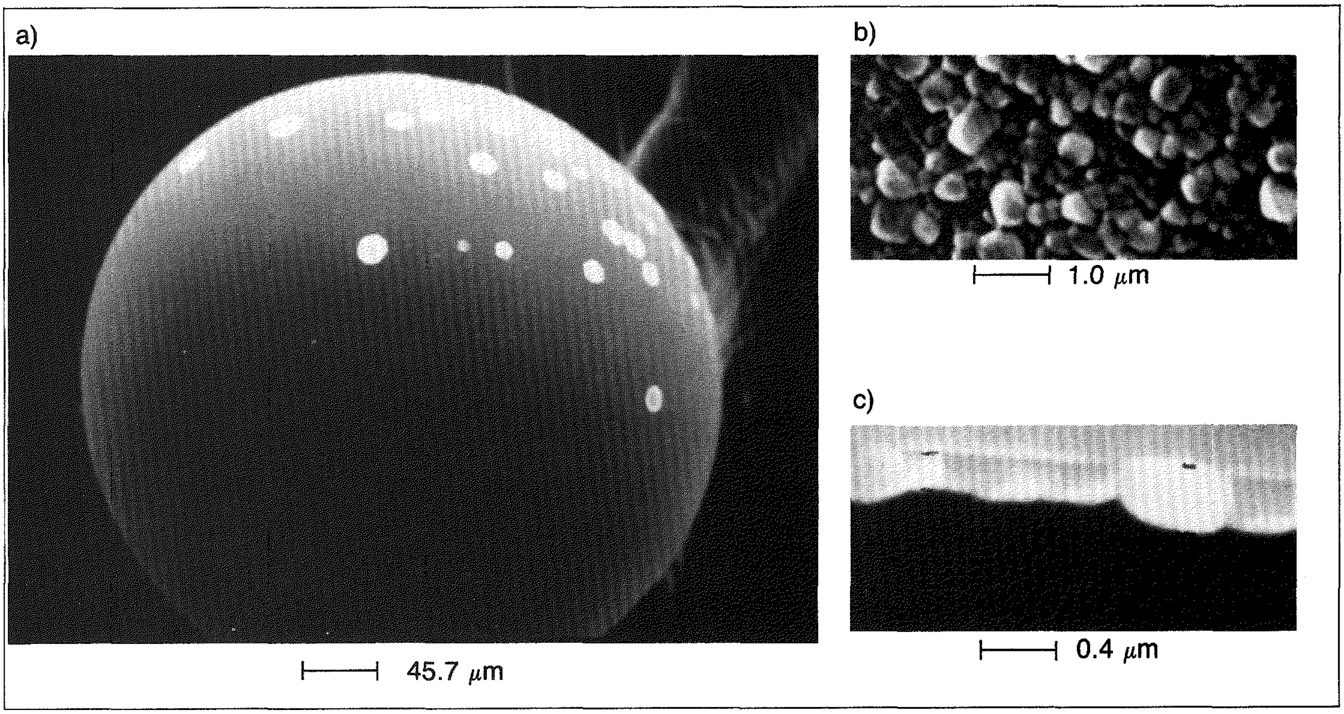

Fig. 1-38. A 0.25 μm KCl film on a 380 μm diameter glass shell is shown in SEM photographs at magnifications of 200× (a), 10,000× (b), and in cross-section at 25,000× (c). These grains are not as large as those shown in Fig. 1-37; we determined that the crystallite size is influenced by the presence of water vapor.

moved from the coating system, examined, and prepared for subsequent film deposition. To test the idea of encapsulating the KCl before exposing it to air, we added a layer of gold. Since the gold layer is only 300 Å, the texture visible is due to KCl alone. The smaller grain sizes are less than 1 μm and are acceptable for the required targets.

Unfortunately, the targets required for experiments cannot contain these gold layers since they interfere with the diagnostics of the experiments. It is difficult to etch away the gold since KCl is a grain structure. In addition, deposition of gold on bouncing shells presents a problem in itself. The gold layers "cold weld" during bouncing and tear away from the KCl. The deposit ends up being nonuniform and the shells pick up debris from the cup as well.

Ideally, it would be best to deposit the thick polymer layer after the KCl in the same system to avoid exposure of the salt to air. An alternative, which we were able to accomplish, is to encapsulate the KCl with a thin (0.1 μm thick) layer of hydrocarbon polymer in the KCl deposition chamber before transporting the shells into the standard GDP deposition chamber. A schematic of the modification made to the evaporation chamber and shaker cup is also shown in Fig. 1-36. The entire PZT is floated off electrical ground (chamber walls) and a shielded lead brings RF power to the cup. The coil shown allows the cup to be at DC ground so that the electron flood gun mentioned above works properly.

We have shown that KCl can be coated onto bouncing shells of both glass and polymer by evaporation and that the resulting graininess of the surface is acceptable for the preparation of diagnostic targets. The structure of this layer is very sensitive to water vapor and needs to be protected against water absorption. A technique was developed whereby the KCl can be hermetically sealed against moisture to maintain the film uniformity until the shells can be overcoated with the main GDP layer.

A deposition rate study has shown that growth rates much higher than 0.8 Å/s yield films having coarse grain structure, although still much less than 1 μm in size on average. At 0.8 Å/s the grain sizes are 0.1 to 0.2 μm in diameter.

Work on the deposition of other salts (other chlorides, fluorides, and iodides especially) is in progress.

For additional information, please contact Mr. G. B. DiMaggio

"Gaussian" Bumps. In addition to the embedded KCl diagnostic layers, we have produced localized perturbations in the thickness uniformity of Microshell® target walls. These perturbations serve as diagnostic aids to study implosion dynamics for the ICF program.

The first type of perturbation is a CH "Gaussian" bump applied to the outer surface of a CH-coated PS Microshell® target. The second type of perturbation is an aluminum Gaussian bump. The bump is applied directly to the surface of a glass Microshell® target prior to the application of a thick CH overcoat. The fabrication processes for the two types of bumps are quite different and are discussed separately below.

The CH Gaussian bumps on the surface of the CH coating are fabricated in the following manner. A PS bead approximately 20 to 25 μm in diameter is attached to the CH coating surface by static "cling." A hot soldering gun with a tapered tip is then brought to the vicinity of the bead. The radiant heat from the gun softens the bead sufficiently for it to flow into the shape of a Gaussian bump. The intensity and the duration of the heating process control the ultimate shape of the bump. Bumps fabricated in this manner are reproducible and have a full width at half-maximum (FWHM) of 30 to 40 μm and a height of 7 to 10 μm. The CH bump shown in Fig. 1-39 has a FWHM of 38 μm and a height of 8 μm. The substrate is a PS shell that has been coated with a 0.5 μm KCl layer followed by 27 μm of CH by GDP.

The coating process of electron beam evaporation is utilized for the production of aluminum Gaussian bumps. A glass Microshell® substrate is placed in a pinhole mask assembly, which is shown schematically in Fig. 1-40. The assembly contains a pinhole, approximately 35 to 40 μm in diameter, through which aluminum vapor passes during the evaporation process. The vapor condenses on the shell/substrate surface in the form of a bump rather than a continuous, uniform layer. The dimensions of the bump are determined by the geometry of the pin-

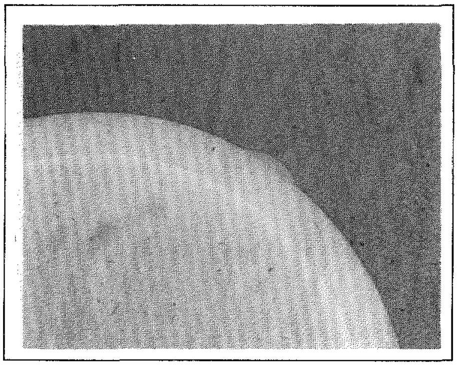

Fig. 1-39. Localized perturbations in the thickness uniformity of shell walls are called for in some cases. One type of perturbation is a CH "Gaussian" bump made from a PS bead melted onto the shell. Such a bump is shown in this x-ray photograph of a PS shell with a multilayered coating of KCl and CH. The bump has a FWHM of 38 μm and a height of 8 μm.

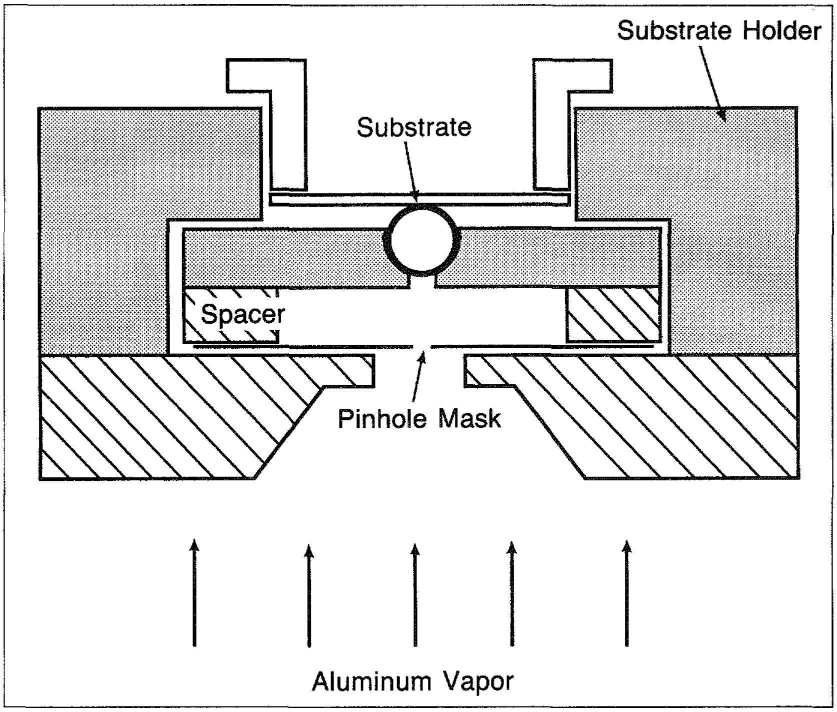

Fig. 1-40. The aperture assembly used to produce aluminum "Gaussian" bumps on shells requires accurate placement of the pinhole with respect to the centerline of the shell. The aluminum vapor passes through the pinhole, traverses the distance of the spacer, and is deposited on the surface of the spherical substrate.

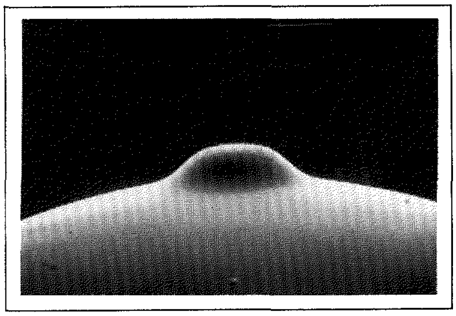

Fig. 1-41. An aluminum "Gaussian" bump deposited onto a glass shell substrate is shown in this SEM photograph. The bump has a FWHM of 35 μm and a height of 9 μm. After the bump was deposited, this shell was overcoated with a thick CH layer.

hole mask assembly as well as the distance between the assembly and the evaporant source.

A model of the bump formation process has been developed to help predict the bump shape as a function of substrate diameter, pinhole size, spacer distance, and evaporant source location. The model thus serves to minimize trial-and-error time to fabricate aluminum Gaussian bumps with the requested specifications. These bumps have been repeatedly produced having a FWHM of 35 to 40 μm and a height of 5 to 10 μm. An aluminum bump that was deposited onto a glass Microshell® target is shown in Fig. 1-41; it has a FWHM of 35 μm and a height of 9 μm.

For additional information, please contact Mr. S. R. Murrell

1.4.3 Measurement of CH(GDP) Properties

Determination of the Density of GDP Films. For the analysis of ICF target experiments it is important to know the density of the materials from which the target is made. One such material is CH(GDP), which is applied as a coating over other materials. Because its density is not well known, we undertook to determine the density of GDP films as a function of the operating conditions of the GDP deposition system.

The chief obstacle to such a density determination is the difficulty in obtaining samples of CH(GDP) film that are large enough to permit measurement of both volume and weight. Our approach was to coat microscope slides on one side with a GDP film. Each of these 1 in. × 3 in. × 1 mm substrates was set on top of another slide to ensure that only one side of the substrate was coated. The volume of the film was then determined from the area of the substrate covered by the film and the average thickness of the film. (We did not correct for deposition on the edges of the slide since the area of the edges is only 1% of the total area, and the deposit is thinnest there.)

It was found that the thickness of the GDP film depends on the position of the substrate relative to the RF coil and the gas flow (a description of the GDP coating apparatus may be found in Section 1.4.1 of this report). The thickness varied considerably over the length and width of the microscope slide. The thickness can vary up to 50% along the slide, and up to 20% across it. Therefore, many thickness measurements are needed to obtain a useful number for the average thickness.

The average density measured from the data collected is 0.97 g/cm^3 ±5%. So far, in several experiments with constant deposition parameters, we have not found a dependence of density on location in the deposition system. Efforts to obtain a deposition profile of the substrates will lead to more accurate density measurements. By depositing GDP on a reflective surface, such as chromium-coated glass, interference fringes can be observed that provide a visual profile of coating nonuniformity and may then be compared with profilometer-measured thicknesses.

For additional information, please contact Ms. A. R. Soltis

Measurement of Index of Refraction of GDP Films. Knowledge of the index of refraction of GDP films is important for the determination of coating thicknesses by interferometry. Observations in the past led to the suspicion that the index of refraction might change from coating run to coating run. It is our objective to determine a possible dependence of index of refraction on the operating parameters of the GDP system. Samples of GDP film were fabricated with trans-2-butene or 1,3-butadiene as the precursor organic gas. The index of refraction of the GDP films was measured by ellipsometry. These measurements indicate that the index of refraction for GDP films fabricated from 1,3-butadiene ranges from 1.58 to 1.54, and for trans-2-butene it ranges from 1.53 to 1.49. In addition to the dependence on the precursor we also noticed a dependence on the position of the sample substrate in the GDP reaction chamber. The lower values of the index of refraction numbers occur downstream from the RF excitation coil. The sample substrates were silicon chips (10 × 5 mm) that were ultrasonically cleaned and rinsed with filtered isopropanol alcohol. The sample substrates were placed in three different locations along the axis of the reaction chamber. Before deposition, they were plasma-etched in argon gas for 40 min. The GDP deposition runs were 2 min when using 1,3-butadiene and 5 min when using trans-2-butene. These deposition runs were timed so that about 1000 to 2000 Å of GDP were deposited on the substrates. This thickness range was chosen because it permits precise measurements of thickness and index of refraction with ellipsometry.

The index of refraction and the thickness of the GDP films are measured under dry nitrogen within a few minutes after removal from the deposition chamber to avoid uptake of water vapor from the ambient laboratory air. Although our measurements of the index of refraction show a distinct trend with respect to the location in the reaction chamber we feel that the method can be improved by providing samples with more uniform films than the ones used in these experiments. Efforts to produce such films are in progress. Measurements to investigate the dependence of the index of refraction on the other operating parameters (e.g., power and gas flow) will be conducted in the future.

For additional information, please contact Mr. T. E. Alberts

SECTION 1.5

Characterization Technology

We have expanded and refined radiography and Fast Fourier Transform (FFT) techniques both for a broader range of measurements and improved accuracy. A new procedure combining densitometry and FFT of radiographs can characterize inorganic salt coatings on shells. A careful analysis of FFT procedures has yielded techniques for greatly improving the accuracy of radius, thickness, and nonuniformity measurements in routine radiographic shell analysis. We have adapted FFT to projected optical images of Macroshell(TM) spheres, and expanded it to three dimensions. We can now determine the best-fitting ellipsoid for a void, and locate it precisely in three dimensions in a Macroshell(TM) sphere.

1.5.1 Measurement of the Thickness and Uniformity of KCl Coatings

Targets for specific experiments often have structural requirements designed to elucidate a particular physics issue. Such a target is one that has a coating of KCl on a polystyrene (PS) shell, as discussed in Section 1.4.2. We are developing a method to characterize such a coating, for both average mass per unit area (areal density) of KCl on each shell and coating uniformity. This method involves both gravimetric and radiographic techniques. While this work is still in progress, one batch of coated shells has been characterized by gravimetric/radiographic methods. As more operational experience is gained, we anticipate improvements in the methods.

A batch of 25 selected PS shells, nominally 310 μm in diameter with 10 μm thick walls, was weighed, then coated with KCl and a few hundred angstroms of CH(GDP) polymer (this was done to protect the KCl from atmospheric attack; see Section 1.4.2). After coating, the 25 shells were weighed. The mass change was 6.3 μg. Twenty of these coated shells and a similar set of uncoated PS shells were then characterized radiographically. For the radiographic characterization, these sets of shells were placed upon a high-resolution optical plate (image detector) and exposed to an x-ray source (accelerating voltage in the range of 5 to 6 kV). After plate development, the images were digitized by an Eikonix-digitizer/Leitz-Laborlux-microscope system and analyzed.

Three types of image analysis were performed. For the first type, the Eikonix was used as a ruler. In this mode, edge-detection schemes were employed to determine shell inside and outside diameters and wall thickness. The outside diameter was used in the determination of average coating areal density.

Based upon the outside diameters of the coated shells and the total KCl mass deposited, the average areal density for all the shells was calculated as

$$Ct_{\mathrm{KCl}} = \Delta M_{\mathrm{KCl}}/(\pi \Sigma D_i^2) = 7.4 \times 10^{-5}\ \mathrm{g/cm}^2,$$

where ΔM_{KCl} is the total mass of KCl deposited, pro-rated for 20 shells; D_{i} is the individual shell outside diameter; and Σ is the summation over all shells.

To determine the individual shell average coating, we used the radiographic image pixel intensity in both the center region and the background of each shell, for both the coated and uncoated shells. Figure 1-42 shows the behavior of this intensity ratio (as intensity ratio minus 1) for these two types of shells as a function of the polymer shell thickness, as already determined with the edge detection logic (the thickness of the coated shells had a small contribution, about 0.4 μm, due to the coating). The data for the uncoated shells was least-square-fitted to a line through the origin, the best data point. This slope was also used for the coated-shell data. This is an excellent approximation. Calculations using x-ray attenuation data for the polymer (and the KCl coating) for the areal densities involved predict linearity between intensity ratio and polymer areal density. Thus, the same slope is used to show this variation of intensity with polymer thickness.

Because of the greater x-ray attenuation of the KCl compared to the polymer, the intensity ratio data for the coated shells is significantly displaced from that of the uncoated shells. For these combined sets of data, the average difference in intensity ratios corresponds to the average areal density of the KCl coating of 7.4 × 10^{-5} g/cm^2 (a small correction was made for the

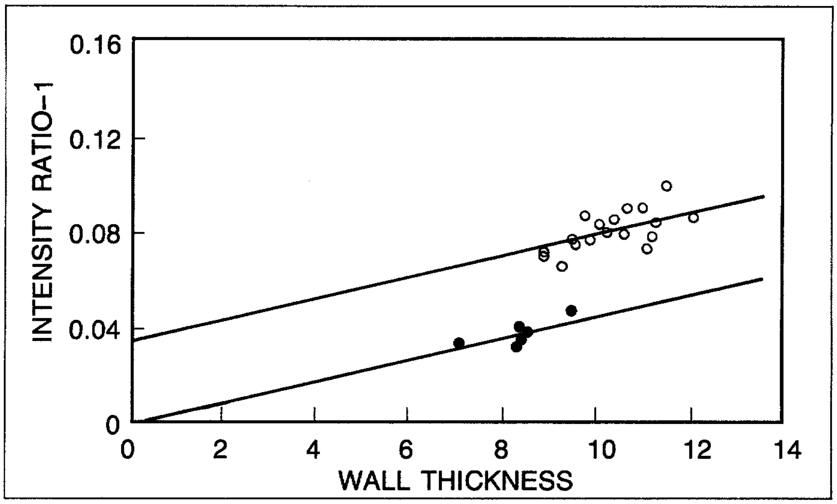

Fig. 1-42. Transmitted x-ray intensity ratios are shown for uncoated (filled circles) and KCl-coated (open circles) PS shells. Because the x-ray attenuation of the KCl is greater than that of the PS, the intensity ratio data for the coated shells is significantly displaced from that of the uncoated shells. The lines are linear least-squares fits.

difference in average shell wall thickness). The scatter in this intensity ratio data for these coated shells is due to both the shell-to-shell variation in average coating thickness and the noise in the data. These combined data sets are equivalent to one piece of data for the calibration of intensity ratio as a function of KCl areal density. Thus our analysis of the variation of intensity ratio to determine coating areal density is restricted to a linear behavior.

In summary, for the 20 shells that were radiographed, seven shells had an average coating within 5%, an additional three shells were within 10%, and an additional five shells were within 20% of the batch average coating. Five shells had a larger deviation from the batch average coating.

To determine the uniformity of the KCl coating, a comparison is made between the intensity variation along the maximum intensity contours for the coated and the uncoated shells. (One of the edge-detection schemes that is very useful in our image analysis is the maximum intensity contour. In an actual shell radiographic image, this contour is normally quite circular, readily determined, and very close to, but just inside, the inside diameter of the shell.) Figures 1-43 and 1-44 show, respectively, the intensity variation along this maximum intensity contour and the wall thickness variation for a particular uncoated shell. Although the wall thickness varies approximately ±20%, the intensity varies slightly, but does show the expected behavior

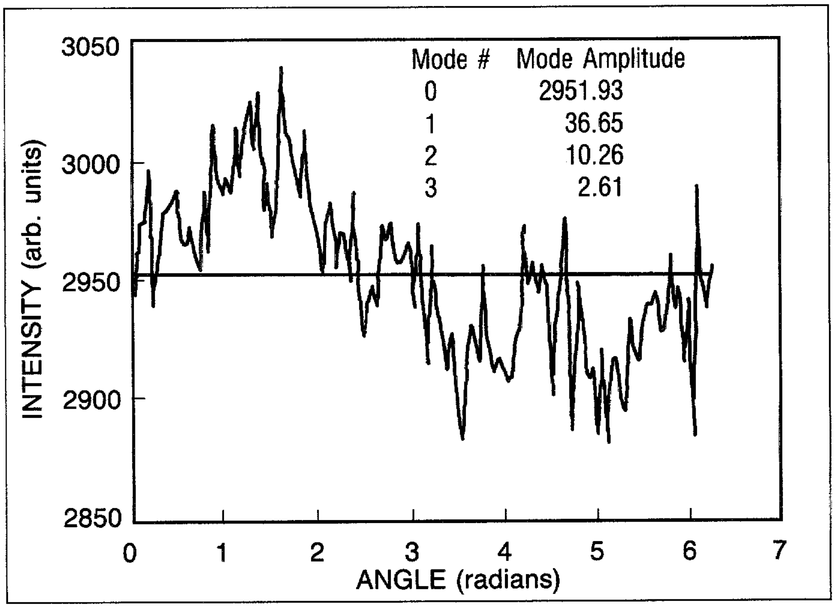

Fig. 1-43. To determine the uniformity of the KCl coating, the intensity variation along the maximum intensity contours of the coated and uncoated shells is compared. The intensity variation along these contours for the image of an uncoated PS shell is shown here. The intensity values of the light transmitted through the radiographic plate range from zero (no light reaching photodiodes during digitization) to 4095 (photodiodes saturated). The first four FFT mode values of the intensity around the shell are shown. The intensity nonuniformity represented by modes 1 through 3 is small compared to the average intensity (mode 0).

(thicker PS gives a higher intensity ratio). Figure 1-45 shows the intensity variation along the maximum intensity contour for a KCl-coated shell. Here the intensity variation is much more significant than for the uncoated shell. In order to conserve space,

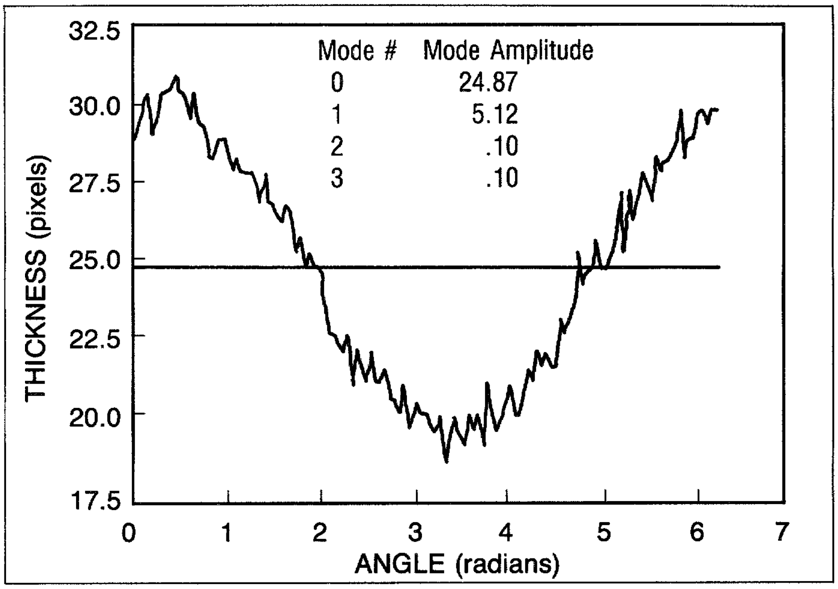

Fig. 1-44. The variation in wall thickness was determined from an image of the same uncoated PS shell depicted in Fig. 1-43. The first four FFT mode values of the thickness are shown. The thickness nonuniformity, dominated by mode 1, is a relatively large fraction of the average thickness, mode 0, indicating a highly nonuniform shell.

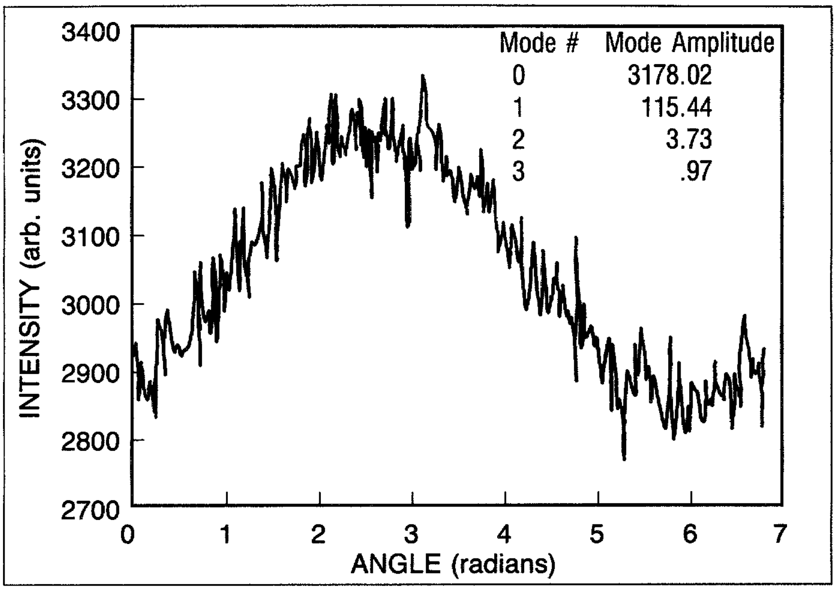

Fig. 1-45. The intensity variation at maximum intensity contour was determined for a KCl-coated PS shell. The first four FFT mode values of the intensity variation around the shell image are shown. The intensity nonuniformity, dominated by mode 1, is a much larger fraction of the average intensity, mode 0, than for a similar uncoated shell image, indicating a nonuniform KCl coating.

the corresponding wall thickness variation for the coated shell has not been reproduced. However, the high-intensity portions of the maximum intensity contour match very well with the thinner portions of the PS shell. Based upon the comparison of intensity variations for the coated shell and for the matching PS shell, the KCl coating thickness variation for the measured shell is just under ±30%.

Radiography is clearly a useful procedure for this type of coating characterization. As our efforts continue, we expect to develop procedure improvements for this or other similar demands. The use of the combination of gravimetry and radiography was necessitated by the absence of appropriate KCl-on-PS standards. The measurements made thus far on this characterization correspond to a single KCl standard, thus requiring that the variation of intensity ratio with coating mass/area be treated as linear. (Computations based upon reported attenuation coefficients lead us to expect at most a slight nonlinearity of intensity ratio with mass/area, although measurements have not been made to show the degree of nonlinearity.)

For additional information, please contact Mr. S. C. Welch

1.5.2 Corrections for Radiographic Image Analysis

Various instrumental distortions interfere with the correct analysis of radiographic images used to characterize the geometric properties of ICF targets. To improve the accuracy of our measurements, we have developed a method to correct for the distortions in the resulting FFT[28] output, without the need of pixel-by-pixel operations on the original image that consume computer time and memory. As a demonstration of these corrections, we use the analyses of the images of one particular type of target of current interest. These targets are glass shells overcoated with CH(GDP). A typical shell has a diameter of about 380 μm with a glass wall thickness of 10 μm and a coating thickness of 30 μm.

Characterization Method. For the first step in the characterization, shells are radiographed with x-ray energies tailored to show the edges of interest clearly. Typically these are the inner edge of the glass wall, the outer edge of the plastic coating, and the interface between the glass and plastic. The shells are in close proximity to the photographic plates, resulting in 1:1 scale profiles of the shells.

The radiographs are digitized by an Eikonix linear array digitizer in conjunction with an optical microscope. The resulting digital images have up to 2048 × 2048 pixels.

Once the image is digitized, the first computer routine of an FFT procedure detects the maximum intensity contour, line by line, and then determines the image center accurately. The outermost edge of the shell image is found using a threshold technique and an accurate center is found for this contour. Using one of these two image centers, the FFT software converts a portion of the overall image information to polar coordinates. The FFT software then performs edge detection on the polar coordinate data.

We use several detection methods, tailored for the various edges encountered. The innermost shell surface is characterized by a ring of high intensity on the images, as it represents the contour of the greatest projected material thickness and hence the least exposure on the plate. To locate this edge, the software scans radial traces of the image for the point of the highest intensity value. Such information is called the maximum intensity contour.

Both the outer surface of the glass and the outer surface of the plastic coating create sharp contrasts in the radiographic image (see Fig. 1-46). The FFT software can detect these edges along radial traces by looking for maximum slopes in the intensity-versus-radius function. The contours so found are called the maximum slope contours.

A preferable method for measuring the outer plastic radius takes advantage of the ideal intensity profile for the outer edge. This profile can be approximated by a square-root function, with a proportionality constant calibrated using an approximately determined edge on the image. The result is a template

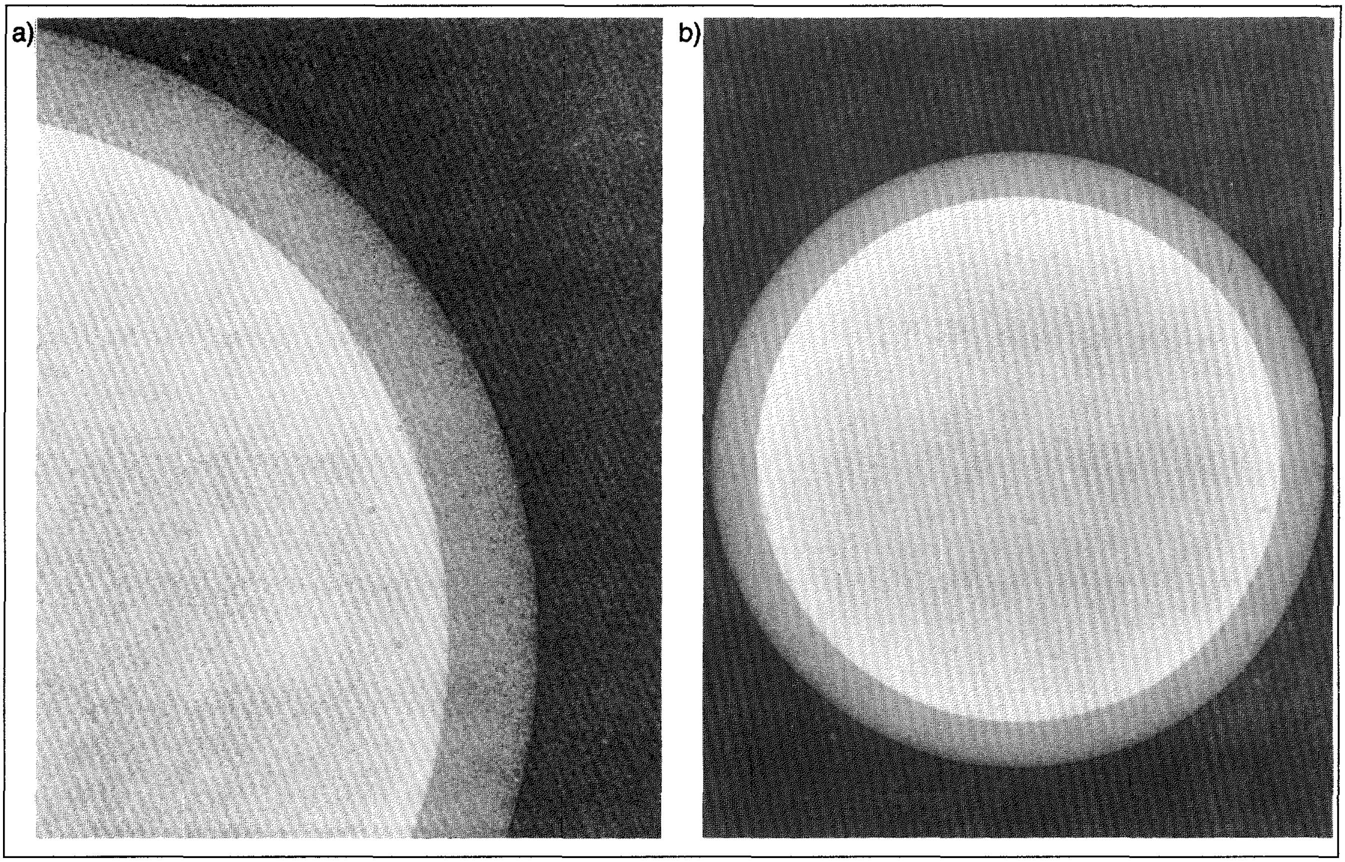

Fig. 1-46. The radiographic image of a GDP-coated glass shell is shown at magnifications of 400× (a) and 200× (b). The gray margin of the shell image corresponds to the coating. (The glass wall in this image is overexposed because the appropriate exposure for the coating was chosen.) Computer analysis of these images yields coating thickness and uniformity.

that the program matches to radial traces to locate the outermost edge.

The edge-detection portion of the FFT package calculates a number of points (typically 128) along an image contour. The points are then subjected to an FFT. In a plot of radius versus angle, this analysis is a curve-fitting to a series of sinusoidal curves of varying frequencies, or modes. An example of such a curve fit is shown in Fig. 1-47. These curves are described by complex mode values calculated by the FFT program. The real and imaginary components of these values contain both phase and amplitude information.

Of particular interest are modes 0, 1, and 2, as these relate to the best-fit ellipse for the shell. Mode 0 corresponds to the radius of a shell image. Mode 1 is especially important for the wall thickness of a shell, as it describes the nonconcentricity of two shell surfaces. Mode 2 describes the ellipticity of a shell image. Both nonconcentricity and ellipticity have directions that can be found using the components of the complex mode values. Higher modes are also calculated, but due to the high quality of these shells, they are primarily due to measurement noise and do not significantly affect shell evaluation.

The first three modes are critical for assessing shell quality, yet all are subject to random and systematic errors. The large number of points examined, together with consistent exposure and development conditions, keep random errors to a minimum. But there are also systematic errors in all three mode measurements introduced by the radiographic process, the optical transfer of the images to the digitizer head, and the digitization process. All three steps degrade (blur) the edges of interest, and

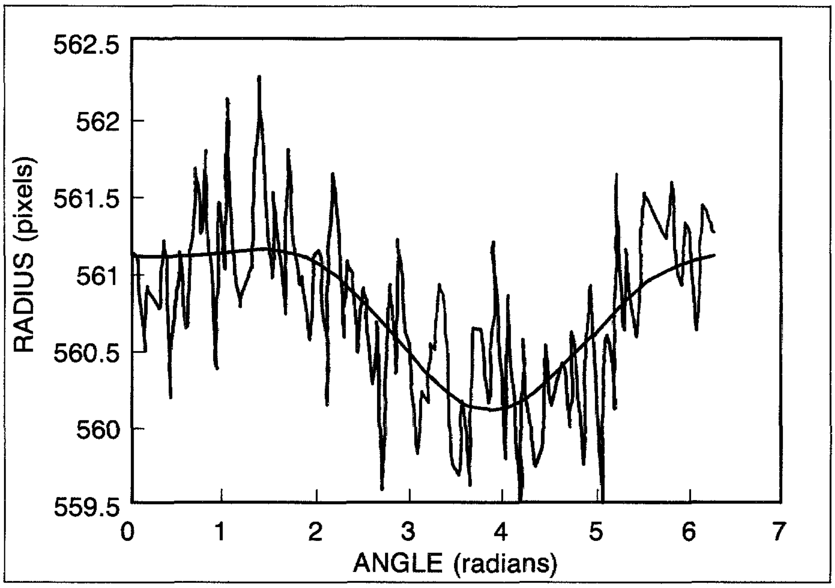

Fig. 1-47. Radiographed glass shells show radius variations (in pixels) as a function of angle, based upon the template edge detection method. FFT of this data gives an equation, $r\ (\theta) = 560.76 = 0.3763 \cos\theta = 0.3322 \sin\theta - 0.0411 \cos(2\theta) - 0.1485 \sin(2\theta)$, derived from the first three terms of the Fourier series.

all but radiography introduce some amount of geometric distortion. The image analysis system requires some corrections to deal with these physical problems, and to produce the most accurate results possible.

Mode 0: Radius Correction. There are two processes that introduce error in measurements of radius values. The first is geometric "pincushion" distortion introduced by the optical microscope. This is manifested qualitatively by a variation of image scale with distance from the image center. This is corrected for by determining a variable scale function and using this to convert radius values from pixels to micrometers.

The second problem is the blurring of edges in various stages of image acquisition. This affects edge-detection schemes in various ways. Analytical study, for example, shows that edges detected by the maximum slope method are displaced inward by an amount dependent only on the final image resolution. In order to study the effects of blurring on radius value, we created a synthetic image with known radii and intensity profiles resembling those of actual shells. We then blurred the images in controlled increments. Finally, actual digitized plate noise was added to ensure a realistic simulation. Figure 1-48 illustrates the radius errors introduced by varying degrees of blurring.

Because the template and maximum slope detectors are affected very differently by blurring, the difference in values they give for the outer radius is a clue for selecting the blurred image most like that of a real shell. A typical difference is on the order of 0.6 to 0.7 μm. A 4 × 4 pixel blurring simulates this well.

At this level of blur, the template-matching detector per-

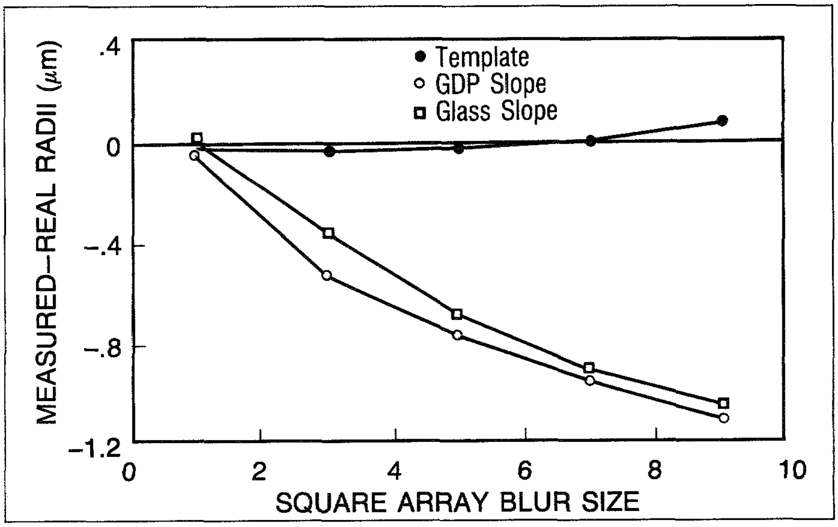

Fig. 1-48. Blurring affects edge detector accuracy. We analyzed a synthetic shell image with exactly known dimensions. Blurring, simulated by averaging filters, introduces errors in radius measurement. Template measurements are affected only slightly. Maximum slope measurements display measurable errors with realistically blurred images. Figures based on the maximum slope for the outer surface of the glass and the outer surface of the coating show similar deviations. Their difference is a good indicator of true thickness.

formed very well in measuring the outer radius, while the maximum slope detector consistently underestimated both the outer edge radius and the glass/plastic interface radius, as expected. Because of the consistency, the maximum slope method gave an accurate coating thickness. Subtracting this accurate coating thickness from the accurate template outer radius yields an accurate glass/plastic radius. Due to the nonlinearity of the x-ray plate response in the high-intensity innermost edge region, questions of inside diameter must be dealt with using interferometric measurements of glass wall thickness.

The corrected radius values are still subject to a random error of about 0.25 μm, as shown by repeated measurements of individual shells.

Mode 1: Nonconcentricity. The Eikonix digitizer suffers from slight asymmetries in its contributions to blurring, and imperfect alignment of the optical axis of the microscope with the image center can introduce slight asymmetrical distortions. These effects are too small to be measured directly, but their effects on nonconcentricity measurements can be seen and corrected.

Because shells are radiographed without regard to the orientations of their flaws, one would expect randomly oriented nonconcentricities. When the mode 1 values are expressed as vectors, or, equivalently, complex numbers with real and imaginary components, one would expect a large number of randomly oriented vectors with an average value of zero. Yet the average value is nonzero, and is similar for a number of batches. Figure 1-49 is a combined plot of mode 1 values from shells of three shell batches of comparable characteristics. The average complex mode 1 value is marked with an **X**.

This average, with a magnitude of about 0.2 μm, can be subtracted from the individual nonconcentricity values to give a more symmetrical range of mode 1 values, reflecting the random orientation of shells. We conclude that this represents the successful correction of systematic error in mode 1. This procedure is being used for coating analysis using maximum slope edge detectors.

Mode 2: Ellipticity. The Eikonix digitizer does not contain a 2048 × 2048 square detector array, but rather a linear 2048-detector array that scans 2048 steps. If these steps are not of the same spacing as the horizontal array of photodetectors, the image will be distorted vertically. If the motion of the array is not exactly perpendicular to the length of the array, the image will be distorted diagonally. Both will distort a circle into an ellipse, and thus affect the mode 2 value for a shell. In addition, a directional component to blurring can affect the edge detectors and introduce a false mode 2 component.

Geometric distortion can be measured directly, but the effects of directional variations in resolution are subtle, varying between edge detectors, and only visible in the actual FFT results. Because of this, we chose to evaluate corrections in a manner similar to that described in the case of mode 1.

We expect the elliptical shells to be randomly oriented on the photographic plate. Thus, when the orientations are represented

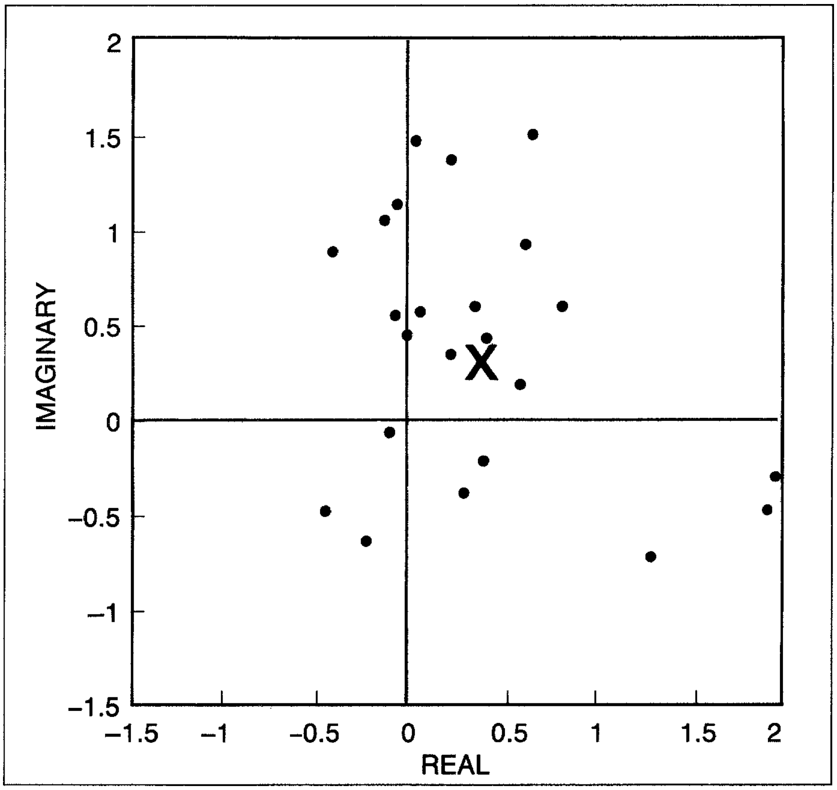

Fig. 1-49. Measured mode 1 values, in pixels (1 μm = 2.6 pixels), are shown for several shells. Without systematic error, these values would be randomly distributed about the origin. Mean mode 1 shows a systematic error, indicated by X, of about 0.5 pixels, or 0.2 μm.

as vectors, we would expect them to be distributed randomly about the origin. There is one caveat here. Because a vector describing ellipse orientation can be drawn in either of two directions, we must use vectors redefined to work as if there were 180° in a circle, thus allowing only one unique vector. Fortunately, the complex mode 2 value acts in just this way. Again, we would expect the average of complex values for a large number of shells to be zero. Figure 1-50 is a plot of mode 2 values measured from a single high-quality shell batch, indicating orientation angles. The actual average is not zero, and this value, derived separately for each edge detector, is considered to be the systematic error in mode 2. The measured geometric distortion of the digitizer accounts for most of this error. Because the effects of this distortion are proportional to image size, a percentage correction is used. The magnitude of the error is about 0.15% to 0.2% of the shell radius. The mode 2 systematic error is routinely subtracted from mode 2 values reported. By comparing corrected mode 2 values of duplicate measurements of the same edge, we estimate a residual random error of about 0.05% of radius.

By careful application of mode 2 corrections, it is possible to reduce uncertainty in mode values to 0.05% of mode 0, or about 0.2 μm. This corresponds to an ellipticity (defined by

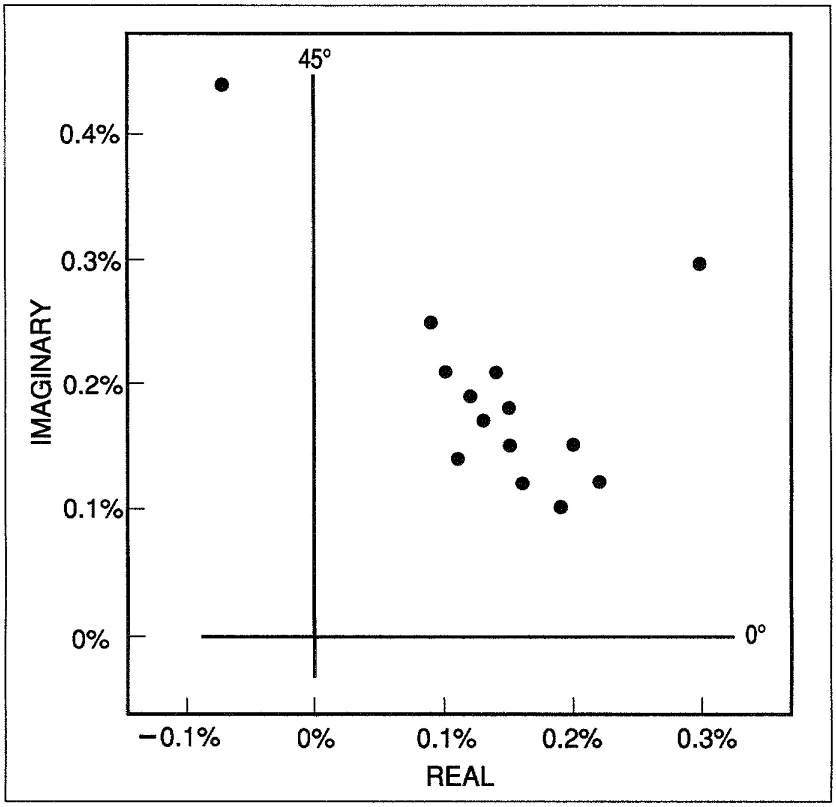

Fig. 1-50. FFT of a batch of randomly oriented glass shells shows systematic tendency toward 0.2% ellipticity in the 20° direction. The general displacement from the origin signals a systematic error, mainly due to image distortion.

1 − A/B) of 0.1%. Similar corrections for mode 1 (nonconcentricity) errors have reduced uncertainty to 0.4 μm. By carefully choosing edge detectors, radius errors can be reduced to about 0.25 μm.

For additional information, please contact Mr. P. C. Alway

1.5.3 Characterization of Macroshell™ Targets

We continue to investigate methods for characterizing large diameter, low and high aspect ratio (diameter/wall thickness) Macroshell™ targets for ICF experiments. Wall uniformity and the sphericity of the inner and outer shell surfaces are the quality characteristics of primary interest. For the process currently being used for manufacturing the Macroshell™ targets (see Section 1.3.1), cavity sphericity is the first property to be determined. We do not have a method to measure sphericity directly. Instead, sphericity is inferred by comparing the circularity of the cavity in several different projections. We developed a method to evaluate cavity image circularity based upon an FFT algorithm to analyze a set of contour data.[29]

For the transparent (glass and polymer) Macroshell™ targets we are producing, we use an optical profile projection (OPP) system to collect the contour data for the cavities and for the final shell. This optical system replaces the electronic data tablet (EDT) system[30] previously used. The OPP measures the cavity or shell diameters directly from an image projected onto a screen. The sample image is scanned and its contour located by an optical sensor that distinguishes a differential in screen light intensity between the silhouette image of the sample and the bright screen background. The contour coordinates outlining the sample image are recorded in a data file for use in an FFT using the capability previously developed for the EDT data.

The OPP-based method offers two main advantages over the EDT method. First, the OPP reduces operator-related errors, since the sample contour is optically evaluated by an optical sensor, and not visually determined by the operator.[31] Second, the OPP offers significantly faster data acquisition and circularity determinations (30 min per contour) compared to the EDT (two or more days elapsed time per contour). This second advantage is crucial for the machining operation, which requires several sets of contour determinations during this procedure.

In normal use, a best guess of an image contour on the OPP is made by the operator. From this best guess, the OPP determines a nominal contour center, and automatically continues the detailed contour determination, starting with the digitization of a pre-selected number of uniformly spaced contour coordinate pairs. Currently this number of coordinate pairs is 50. These points are converted to polar coordinates using the estimated circle center as the origin. Next, 128 equally spaced perimeter radius values are interpolated from the input points. These values are analyzed using the FFT to yield magnitudes and orientations of various mode contributions to nonuniformity. The results of the FFT are a set of mode amplitudes corresponding to sinusoidal deviations from a circle centered on the origin. Mode 0 is the radius of a best-fit circle. Mode 1 is the offset of the best-fit circle from the origin. This value must be zero for a single-contour evaluation. However, if both inner and outer shell contours are measured in one view with the same origin, the mode 1 value is a measure of the nonconcentricities of the centers of the two contours.

Mode 2 describes the elliptical component of the sample's shape. Higher mode values describe components of nonuniformity with frequencies corresponding to the mode numbers. Modes 5 and higher are currently regarded as noise, useful only in establishing contributions from random scatter and isolated spikes in the radius. The results of the FFT give a single figure of merit for percent noncircularity *NC*, which is defined by the expression,

$$\%NC = \frac{2\left[0.5 \sum_{i=2}^{4} (\text{mode amplitude}_i - \text{average noise amplitude})^2\right]^{1/2}}{\text{average radius}} \times 100\% .$$

The percent noncircularity factor was chosen to represent the deviation in shell and cavity contour circularity. The FFT minimizes the consequences of the uncertainty of individual data points and gives the most significant contour nonuniformity, i.e., lower order and deviations from circularity. We estimate that the contribution of uncorrectable procedural errors to noncircularity values is less than 0.1%.

Individual views of a void or shell do not allow characterization in three dimensions. Depending on the level of detail required, a number of views are needed. Two views are adequate to characterize center offset, while three views are needed to fit a sample shape to a three-axis ellipsoid. Offset of inner and outer shell surfaces can be computed as an ordinary vector in three dimensions, whose components are measured in two or three orthogonal planar views.

We are developing a software package to construct a three-dimensional characterization of a Macroshell™ target based on the FFT of three orthogonal views of a shell or cavity. In this program, we have abandoned the conventional parameters used to describe an ellipsoidal form, the lengths of the principal axes and a set of orientation angles. In their place, a set of three-dimensional modes, each representing a type of deviation from spherical shape, was selected. Combinations of these six modes can describe an ellipsoid of any orientation, whether prolate, oblate, or three-axis. The modes were chosen so that two can be evaluated from FFT results of each of three orthogonal views. We have characterized inside surfaces in this manner and are now extending the technique to map the wall thickness of shells.

This method of approximating shell geometry through use of ellipsoidal modes has applications for a wide range of shells that can be approximated by ellipsoidal geometry, and that are measured by radiography, interferometry, or other image-based techniques in which a limited number of views are possible.

For additional information, please contact Mr. L. A. Scott

REFERENCES

1. J. K. Hoffer and L. R. Foreman, *Phys. Rev. Lett.* **60** (1988), p. 1310.
2. M. T. Mruzek, D. L. Musinski, and J. S. Ankney, *J. Appl. Phys.* **63**(7) (April 1, 1988), pp. 2217-2220.
3. *KMS Fusion 1987 Annual Technical Report on Inertial Fusion Research* (KMS Fusion, Inc., Ann Arbor, MI), pp. 77–78. KMSF-U1962.
4. A. J. Martin, R. J. Simms, and R. B. Jacobs, *J. Vac. Sci. Technol. A* **6**(3) (May-June 1988), pp. 1885–1888.
5. James Hoffer and Larry Foreman, private communication, 1988.
6. *KMS Fusion 1987 Annual Technical Report on Inertial Fusion Research* (KMS Fusion, Inc., Ann Arbor, MI), pp. 81-85. KMSF-U1962.
7. *KMS Fusion 1987 Annual Technical Report on Inertial Fusion Research* (KMS Fusion, Inc., Ann Arbor, MI). pp. 86–90. KMSF-U1962.
8. T. P. Bernat, D. H. Darling, and J. J. Sanchez, *J. Vac. Sci. Technol.* **20** (1982), p. 1362.
9. Mils Abramson, *The Making and Evaluation of Holograms* (Academic Press, 1981), p. 97.
10. Ibid, p. 77.
11. A. K. Burnham, J. Z. Grens, and E. M. Lilley, "Fabrication of PVA-Coated Polystyrene Shells," *J. Vac. Sci. Technol. A.* **5**(6) (November-December 1987), pp. 3417-3421.
12. J. Z. Grens, private communication.
13. R. L. Plackett and J. P. Burman, *Biometrika* **33** (1946), p. 305.
14. *KMS Fusion 1984 Annual Technical Report on Inertial Fusion Research* (KMS Fusion, Inc., Ann Arbor, MI), pp. 59-60. KMSF-U1574.
15. *KMS Fusion 1985 Annual Technical Report on Inertial Fusion Research* (KMS Fusion, Inc., Ann Arbor, MI), pp. 92–94. KMSF-U1728.
16. D. E. Day and S. C. Wang, "A Technique for Production of Glass Macroshells for ICF Targets," Report to Los Alamos National Laboratory, November 25, 1987.
17. *KMS Fusion 1987 Annual Technical Report on Inertial Fusion Research* (KMS Fusion, Inc., Ann Arbor, MI), pp. 111-117. KMSF-U1962.
18. *KMS Fusion October-December 1987 Quarterly Progress Report* (KMS Fusion, Inc., Ann Arbor, MI). KMSF-U2021.
19. W. J. Miller and R. P. Belanger, "Optimum Alkali Ratios in Glass Shells," *Fifth Annual Target Fabrication Specialists Meeting*, Las Vegas, NV, March 24–27, 1986.
20. R. L. Downs, M. A. Ebner, and W. J. Miller, "Hollow Glass Microspheres by Sol-gel Technology," *Sol-gel Technology for Thin Films, Fibers, Preforms, Electronics, and Specialty Shapes*, edited by L. C. Klein (Noyes Publishers, Park Ridge, NJ, 1988), Chapter 16.
21. R. P. Belanger and W. J. Miller, "Glass Shell Preparation," *J. Vac. Sci. Technol. A* **3** (1985), p. 1270.
22. W. J. Miller and R. P. Belanger, "Process Control of Hollow Glass Sphere Production," *Second Annual Target Fabrication Specialists Meeting*, Las Vegas, NV, March 29-31, 1983.
23. G. E. P. Box and D. W. Behnken, *Technometrics* **2** (1960), p. 455.
24. *KMS Fusion October-December 1987 Quarterly Progress Report* (KMS Fusion, Inc., Ann Arbor, MI), pp. 81–86. KMSF-U2021.
25. S. A. Letts, "Hydrocarbon Coatings," *Lawrence Livermore National Laboratory 1979 Laser Program Annual Report*, UCRL 50021-79, pp. 4-8 through 4-13.

26. *Applications of Plasma Processes to VLSI Technology*, edited by Takuo Sugano (John Wiley & Sons, NY, 1985).

27. H. Yasuda, "Modification of Polymers by Plasma Treatment and by Plasma Polymerization," *Phys. Chem.* **9** (1977), pp. 805–817.

28. *KMS Fusion 1984 Annual Technical Report on Inertial Fusion Research*, KMS Fusion, Inc., Ann Arbor, MI, pp. 73–75. KMSF-U1574.

29. S. M. Alexander-True, and M. A. True, "Thickness Uniformity Measurements of Plastic Coated Glass Shells by Image Analysis of X-Ray Radiographs," *J. Vac. Sci. Technol. A* **3** (1985), p. 1258.

30. *KMS Fusion 1986 Annual Technical Report on Inertial Fusion Research* (KMS Fusion, Inc., Ann Arbor, MI), pp. 143–144. KMSF-U1871.

31. L. A. Scott, "Characterization of Geometrical Properties of Glass Macroshells and Spherical Cavities in Glass," Report to Los Alamos National Laboratory, February 11, 1988.

DO NOT MICROFILM
THIS PAGE

LASERS

SECTION TWO

Scientific Editor, Dr. N. K. Moncur

Introduction

Focused laser light that illuminates a target surface uniformly is desirable in most laser/matter interaction experiments. Uniform illumination has been difficult to achieve, primarily because of the imperfections in high power laser systems. Small amplitude and phase aberrations introduced by the many optical elements in a multistage laser can produce large intensity nonuniformities at the output, which tend to be mapped onto the target when it is placed in the quasi-near field. At the focal position, the coherence of the laser light is responsible for a large part of the nonuniformity of illumination.

We are exploring two methods to achieve optical smoothing. One, pioneered by the Naval Research Laboratory, is called induced spatial incoherence. The other, now being developed at KMS Fusion, is called the second harmonic aberration correction system. This latter technique corrects for phase aberrations by phase conjugation and Type II frequency doubling.

SECTION 2.1

Induced Spatial Incoherence Capabilities

Induced spatial incoherence (ISI) is a technique for overcoming the nonuniformity of illumination that is attributable to the coherence properties of laser light. The ISI technique employs a wide bandwidth laser beam that is divided into a large number of beamlets, each focused onto the target at a slightly different time. The interference among the overlapped beamlets disappears when averaged over a period that is long in comparison to the laser coherence time, and a very uniform intensity focal pattern is generated.

The Chroma laser oscillator has been modified to generate a wideband pulse, which is then amplified and frequency-doubled to produce a high-power, wideband 2ω (0.53 μm) beam for ISI experiments. A pair of transmission echelons at the laser output divides the beam into one hundred 2 cm × 2 cm beamlets that are focused on target with a single lens.

Optics. Each of the transmission echelons consists of 10 plates of BK7 glass of varied thickness. Because the echelon plates are of different thicknesses, the beamlets experience different delays. The time delay increments Δt are chosen to be larger than the optical coherence time $t_c = 1/\Delta\nu$, where $\Delta\nu$ is the bandwidth of the laser beam. The first echelon consists of ten BK7 plates, each 200 mm long × 20 mm wide, with thickness changing from plate to plate in 0.5 mm increments. The second echelon also has ten BK7 plates each 200 mm long × 20 mm wide, but the plate-to-plate thickness change is 5.0 mm, the total sum of the thickness change of the first echelon. The end result of a beam passing through the two echelons is 100 beamlets with a time delay of $\Delta t = 0.83$ ps from beamlet to beamlet. These beamlets are all then focused on target with a single lens (Fig. 2-1).

The echelon plates were fabricated with very strict tolerances so that the wavefront is not distorted by more than $\lambda/6$ in transmission and so that deviation of the beamlets due to wedge will be less than diffraction effects or the natural divergence of the laser. To prevent reflective losses, the entrance and exit faces of the plates were coated with a dual-wavelength (ω, 2ω) antireflective (AR) coating, so they can be used for either infrared (IR) or frequency-doubled green-light experiments.

Transmission echelons were chosen over reflection echelons for these initial experiments because they are more easily operated and fabricated than the reflective type used by the Naval Research Laboratory.[1] The holders for the transmission echelon plates are very simple and do not require individual alignment controls, as do holders for reflection echelon plates. The transmission echelon can be inserted or removed from the beam without disrupting beam alignment. This makes it easy to conduct experiments that compare the effect of ISI techniques with standard narrowband operation.

Wideband Oscillator. To implement ISI,[1–6] the bandwidth of the laser must be sufficient to ensure incoherent superposition of many beamlets on target. Our approach was to use a Q-switched and modelocked Nd:glass oscillator, as shown in Fig. 2-2. Modelocking was chosen in lieu of a fast Pockels cell switch because we could obtain a shorter pulse with a higher contrast ratio between the main pulse and the background. The problem with prepulse energy [typical in inertial confinement fusion (ICF) experiments] was thus eliminated and a 500 ps pulse was obtained that could be used with a pulse-stacker to generate shaped pulses.

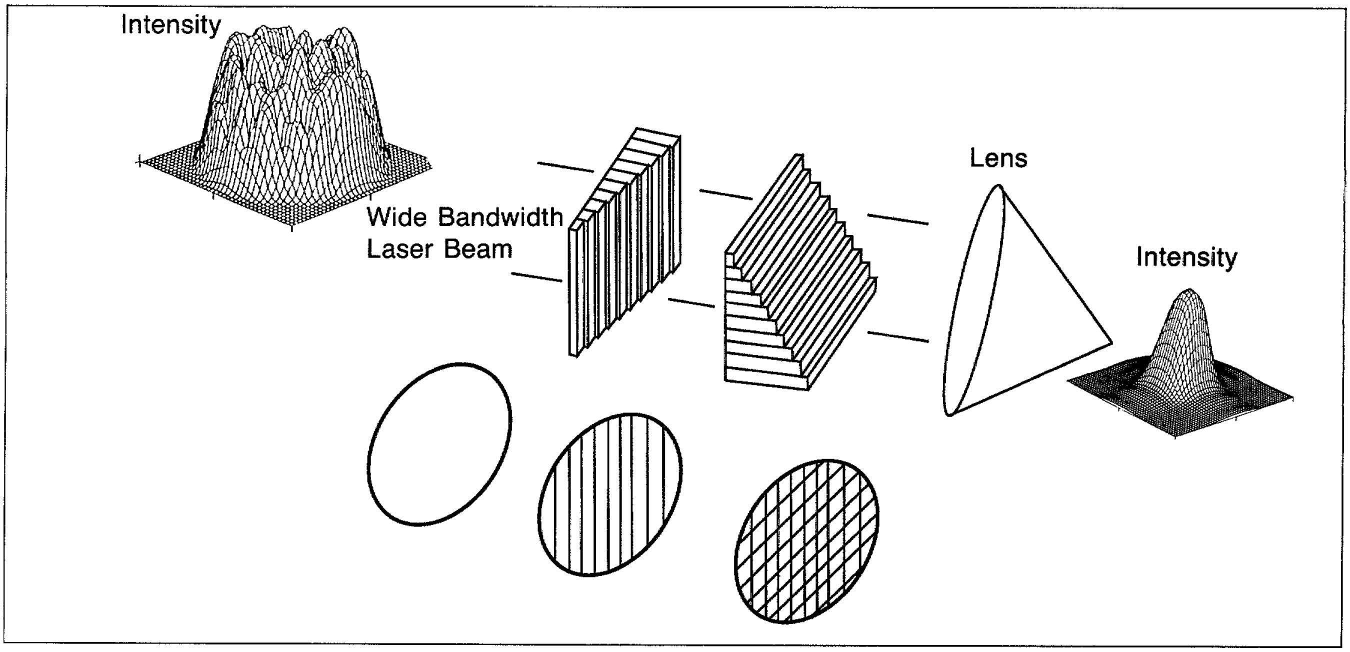

Fig. 2-1. A pair of transmission echelons divides the wide bandwidth nonuniform laser beam into 100 beamlets, which are then focused onto the target by a single lens. The time-averaged intensity is greatly smoothed.

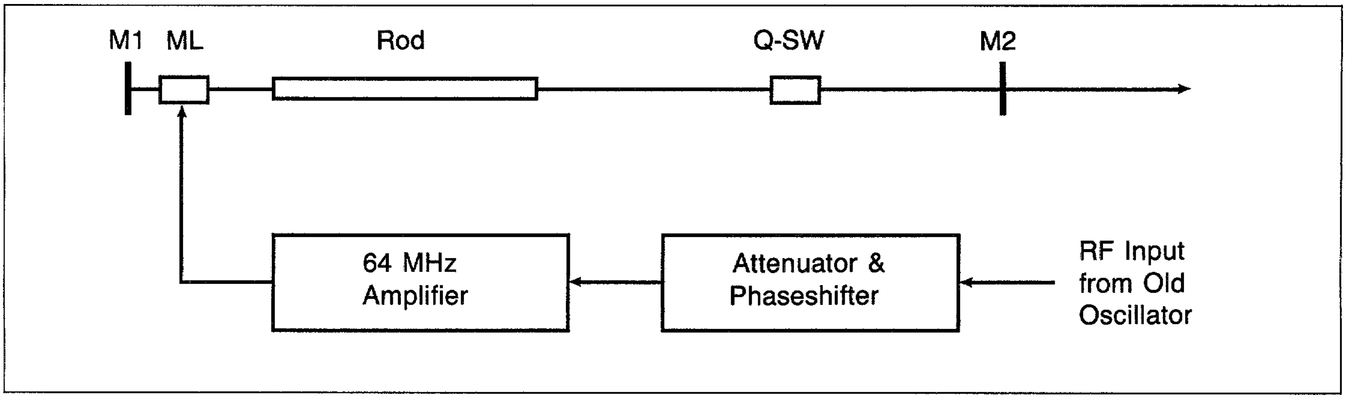

Fig. 2-2. A new optical resonator was built for use in a wideband oscillator. The output is synchonized to the old narrowband oscillator, which is required for the diagnostic instruments used in experiments. In the figure, M1 is a 5 m, 100% reflective rear mirror, ML is an acousto-optic modelocker, Rod is an Nd:glass laser rod, Q-SW is an acousto-optic Q-switch, and M2 is a 75% reflective output mirror.

As opposed to the previous quasi-continuous-wave modelocked and Q-switched Nd:YLF oscillator, which gave a 100 ps pulse that was transform-limited in bandwidth, the new oscillator could not be operated with a prelase period to stabilize it. Any significant prelase period would narrow the bandwidth too much. A Nd:glass laser rod (Kiger Q-98) was used to increase the gain bandwidth to about 140 Å (effective full width at half-maximum) from 11 Å for the Nd:YLF previously used. The spectral bandwidth is later narrowed by the large gain required to build up the laser pulse from spontaneous emission. The spectral narrowing factor (the ratio of the output bandwidth to the initial spontaneous emission bandwidth) is given by

$$\frac{\Delta f}{\Delta f_{\mathrm{sp}}} = \sqrt{\frac{1}{\ln G}} \ ,$$

where Δf is the bandwidth and G is the total gain undergone by the laser pulse in the laser rod during the buildup time. Any losses or extra passes that require additional gain cause more narrowing of the spectral bandwidth.

During this buildup time, the modelocker is narrowing the temporal width of the modelocked pulse by

$$\frac{\tau}{\tau_0} = 1 \Big/ \sqrt{\tanh \frac{t}{t_0}} \ ,$$

where τ_0 is the steady-state pulse width that would be reached in an infinite amount of time and t_0 is the time required to get within 15% of the steady-state value. The steady-state pulse width τ_0 and buildup time t_0 for an amplitude-modulated (AM) modelocked homogeneous laser is given by[7]

$$\tau_0 = \frac{1}{\pi} \sqrt{2\sqrt{\ln 2}} \frac{\sqrt[4]{g_0}}{\sqrt{\delta}} \frac{1}{\sqrt{f_{\mathrm{m}} \Delta f_{\mathrm{sp}}}}$$

and

$$t_0 = \frac{1}{8\sqrt{g_o}\,\delta} \cdot \frac{\Delta f_{\mathrm{sp}}}{f_{\mathrm{m}}} \ ,$$

where g_0 is the round-trip amplitude gain, δ is the modelocker modulation index, f_{m} is the modulation frequency, and Δf_{sp} is the laser medium bandwidth. For the wideband oscillator,

$g = \exp(52)$,
$g_0 = 0.34$,
$\delta = 1.0$,
$\Delta f_{\mathrm{sp}} = 3.78 \times 10^{12}$ Hz,
$f_{\mathrm{m}} = 64 \times 10^6$ Hz,
$\tau_0 = 18$ ps,
$t_0 = 194$ μs.

For a buildup time of 0.6 µs for the Q-switched pulse, the width of the modelocked pulse from the above theory is 334 ps and the spectral bandwidth is 19.4 Å. The measured pulse width is about 350 ps and the measured bandwidth is about 20 Å. Figure 2-3 shows the spectral distribution of the ISI oscillator at buildup time of 0.62 µs.

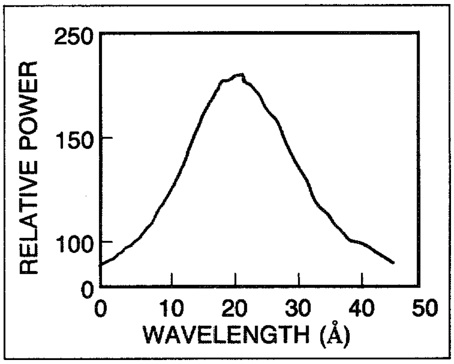

Fig. 2-3. At a buildup time of 0.620 µs, the spectral bandwidth of the modelocked, Q-switched, Nd:glass ISI oscillator with no etalon is a nearly Gaussian-shaped curve with a FWHM of 20 Å.

The bandwidth can be decreased or increased with a 50 µm thick uncoated quartz etalon in the resonant cavity. The etalon can change the effective bandwidth of the resonant cavity,

$$\Delta\lambda_{\mathrm{eff}} = \left[\frac{1}{\Delta\lambda_{\mathrm{sp}}^2} + \frac{1}{\Delta\lambda_{\mathrm{EC}}^2}\right]^{-1/2}$$

and

$$\Delta\lambda_{\mathrm{EC}} = \frac{2\ \ln 2}{F}\ \frac{\lambda^2}{2\pi nd}\ ,$$

where $\Delta\lambda_{\mathrm{EC}}$ is the effective bandwidth of the etalon at the crest of its transmission curve, F is the finesse of the etalon, and nd is the optical thickness. Alignment of the 50 µm etalon with the crest of the laser emission line center gives a narrower effective bandwidth of 85 Å.

If the etalon is aligned so the trough is on the emission line center, the effective bandwidth is given by

$$\Delta\lambda_{\mathrm{eff}} = \left[\frac{1}{\Delta\lambda_{\mathrm{sp}}^2} - \frac{1}{\Delta\lambda_{\mathrm{EC}}^2}\right]^{-1/2}$$

and

$$\Delta\lambda_{\mathrm{ET}} = 2\ \ln 2\ \frac{1+F^2}{F}\ \frac{\lambda^2}{2\pi\, nd}\ .$$

Here the effective bandwidth of the etalon $\Delta\lambda_{\mathrm{ET}}$ at the trough is wider than at the crest by a factor of $(1 + F^2)$. Use of the etalon at the trough tends to widen the bandwidth of the resonator. Furthermore, if $\Delta\lambda_{\mathrm{ET}}$ is small enough, as it is here for the 50 µm etalon, it will give an effective bandwidth of 249 Å with a saddle-shaped spectral curve (see Fig. 2-4). The principal advantage of this shape is that it will compensate for the fall-off in gain of the Chroma laser amplifier away from the emission line center. The depth of the saddle shape decreases as the laser rod is pumped harder because the bandwidth of the laser rod is narrowed slightly by the higher gain. The asymmetrical plot in Fig. 2-4c is typical of a slight misalignment of the etalon off the emission line center. The smooth curves are computer simulations based on Gaussian line shapes for laser gain and etalon transmission.

To do holographic interferometry on experimental targets the old narrowband oscillator and the regenerative amplifier have to be maintained in their present form. Hence, the new ISI oscillator was set up on a separate table and synchronized with the old oscillator through a common RF modelocking source. Figure 2-5

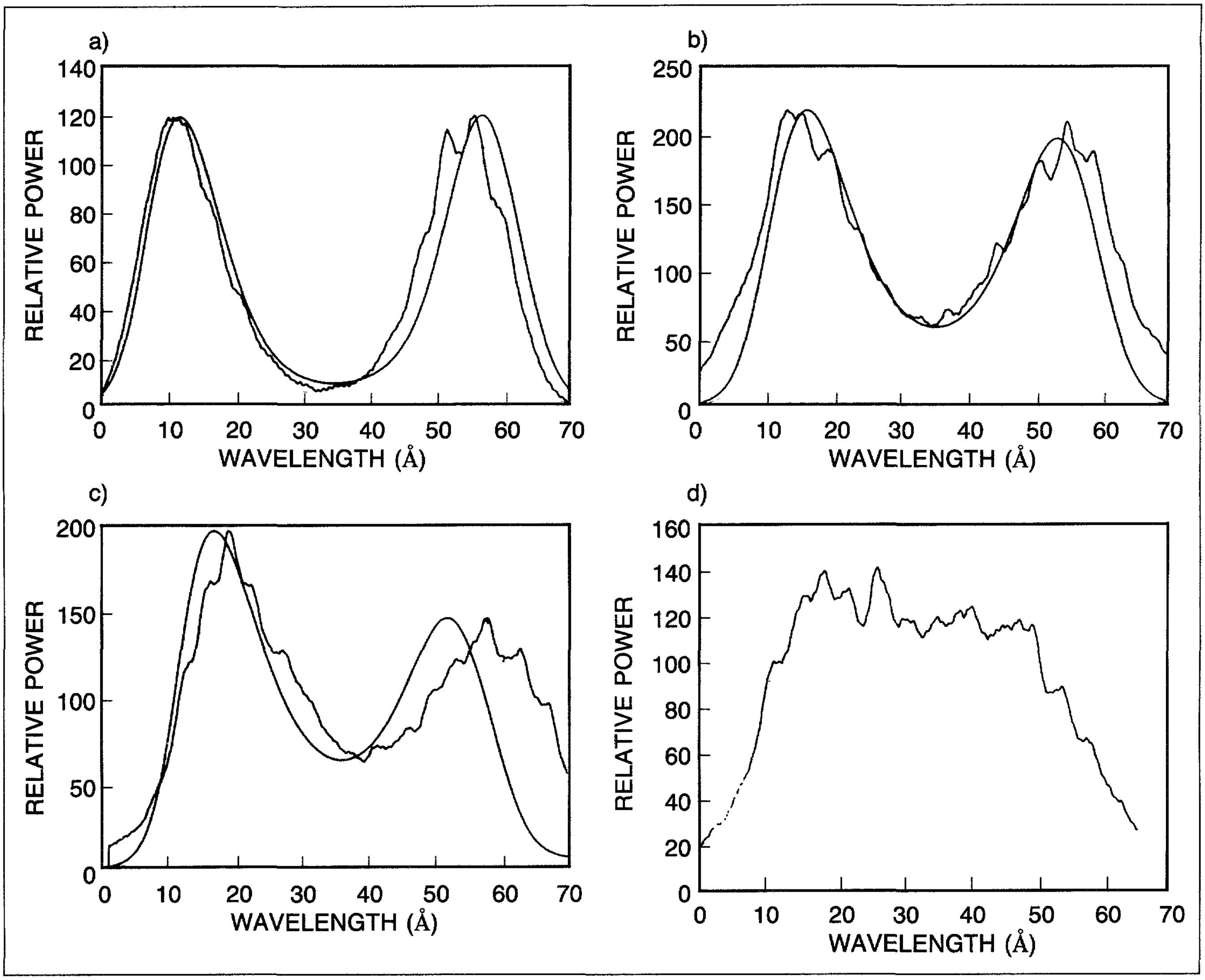

Fig. 2-4. The bandwidth of the wideband oscillator is greatly widened by a 50 μm thick quartz etalon aligned so its transmission trough is at the line center of the Nd:glass laser rod. Plots (a) through (d) show the power spectral density for increasing lamp drive current. The smooth curves are computer simulations based on the foregoing theory.

shows this complete system. The wideband oscillator is injected into the old pulse selector with a polarizer. With this technique, either a narrowband or a wideband pulse can be injected into the Chroma amplifier system simply by rotating waveplates that control the polarization. An optical autocorrelator is used to monitor the coincidence of the two oscillator pulses. Phase shifters in the RF signal to the new ISI oscillator permit fine control of the synchronous timing.

Chroma Amplifier Bandwidth. The same bandwidth narrowing observed in the oscillator is also present in the Nd:glass amplifier. Since the amplifier laser glass (Kiger Q-88 and Hoya LHG-8) is very similar to the oscillator glass, the gain bandwidth Δf_{sp} is about 140 Å like the oscillator. The effective bandwidth is given by

$$\Delta\lambda_{\text{eff}} = \Delta\lambda_{\text{sp}} \frac{1}{\sqrt{\ln G}} ,$$

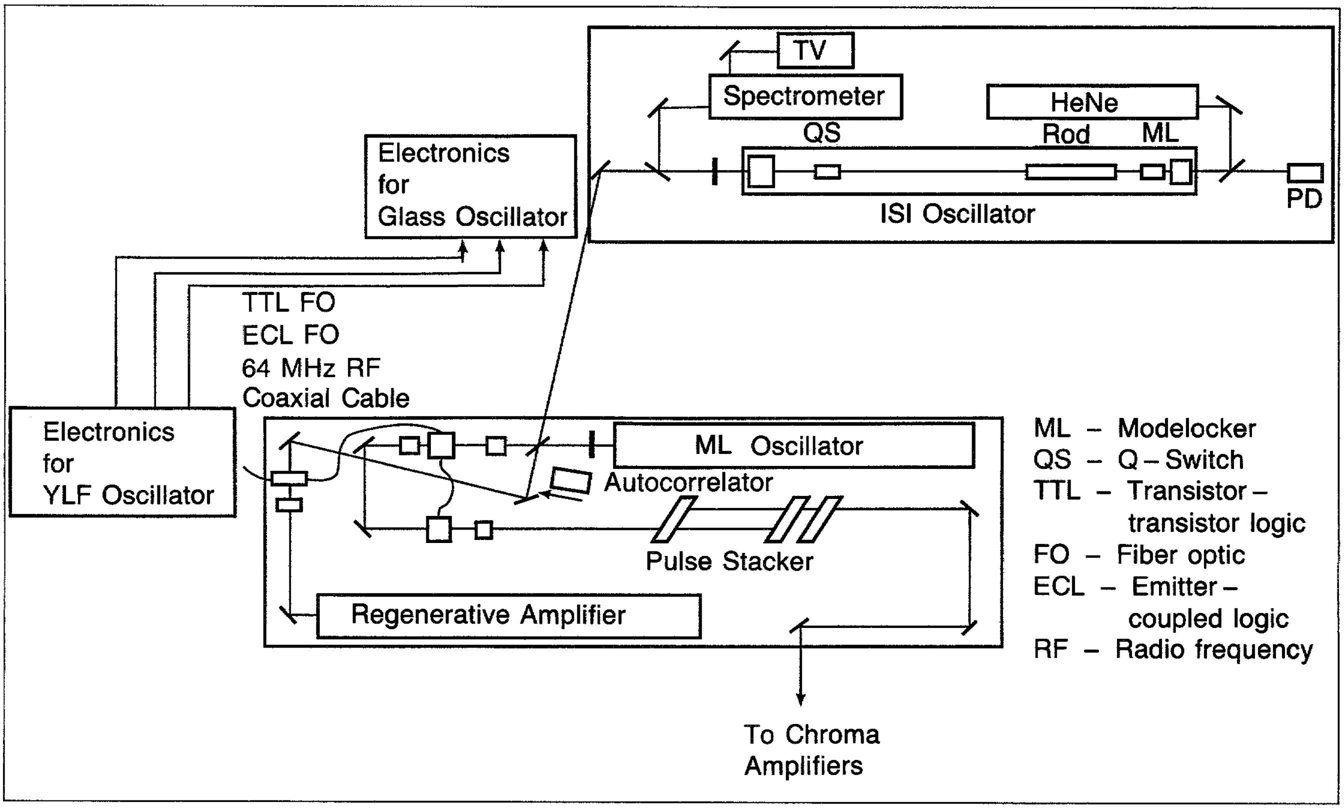

ML	–	Modelocker
QS	–	Q-Switch
TTL	–	Transistor-transistor logic
FO	–	Fiber optic
ECL	–	Emitter-coupled logic
RF	–	Radio frequency

Fig. 2-5. The new wideband oscillator output is injected into the main optical train before the pulse selector, and the old narrowband oscillator output is diverted to the regenerative amplifier for short-pulse diagnostic holography. The two oscillators are modelocked with the same RF source and synchronized by monitoring the cross-correlation between the two oscillator pulse trains.

where G is the total gain of the Chroma amplifier, which is about 10^9. The effective bandwidth is then 31 Å. The cusp-shaped spectral output from the oscillator will tend to broaden this, but not by much.

Frequency Conversion for Induced Spatial Incoherence. The bandwidth tolerance for Type II KDP is 77 Å-cm. This means that a 1 cm thick crystal could tolerate a ±77 Å deviation from line center before the low-power conversion efficiency would drop by a factor of 2. We have both 0.9 cm and 1.5 cm thick crystals for frequency conversion of the wideband ISI laser output. Figure 2-6 shows the doubling efficiency curves for these Type II crystals as a function of spectral deviation from line center. The frequency shift from line center for a 30 Å FWHM bandwidth is 15 Å. Hence, the doubling efficiency is not significantly limited by a simple shift in wavelength for a narrow line. However, a broadband laser beam has phase modulation that travels at the group velocity, and the differences in the group velocities for the fundamental and second harmonic cause phase mismatch, which, in turn, reduces the doubling efficiency significantly. Use of two crystals in quadrature[8] helps a great deal, since the second crystal independently converts the remaining fundamental power without affecting the second harmonic from

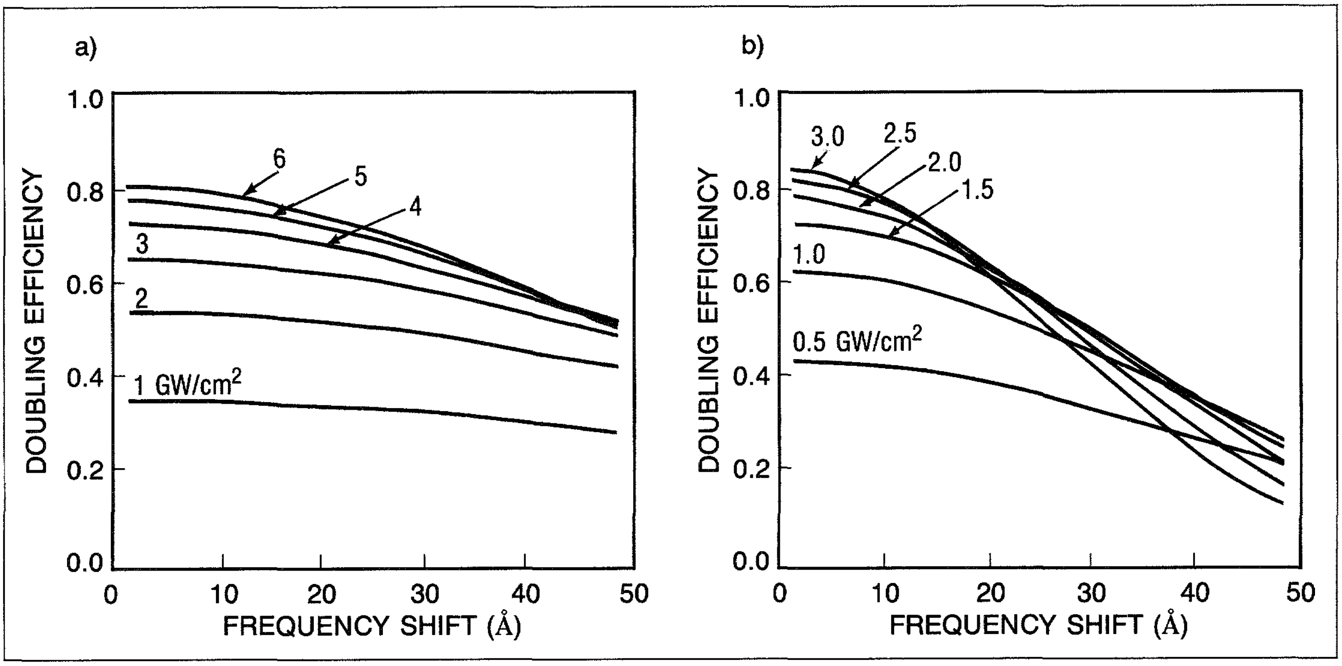

Fig. 2-6. Doubling efficiency is shown as a function of the frequency shift from the line center for various input power densities. Code predictions, accounting for change of phase velocity with frequency, for the 0.9 cm thick Type II KDP crystals (a) and the 1.5 cm thick Type II KDP crystals (b) show little decrease in efficiency for a 30 Å frequency shift.

the first crystal. With the quadrature crystals we expect to get at least 50% conversion efficiency.

For incoherent smoothing of the far field, the bandwidth should be wide enough to make the coherence length less than the optical path length difference between the echelon beamlets. With a 30 Å IR bandwidth, the frequency-doubled bandwidth is 15 Å and the coherence length is 0.19 mm. Since our echelons have an optical path length difference of 0.25 mm, the beamlets will add incoherently.

For additional information, please contact Mr. L. D. Siebert

SECTION 2.2

Optical Phase Aberration Correction by Phase Conjugation and Type II Frequency Doubling

Optical phase conjugation has been a popular technique in recent years for compensation of distortions in laser amplifying media. Many different techniques[9] have been studied for obtaining conjugate laser beams and many different applications have been defined; however, in most cases, the conjugate laser beam must retrace its path through the distorting medium to remove phase aberrations. At KMSF, however, we are exploring a technique in which aberrations in a laser beam can be removed after the beam exits the laser system.

A diagram of this second harmonic aberration correction (SHAC) system is shown in Fig. 2-7. The incoming laser beam

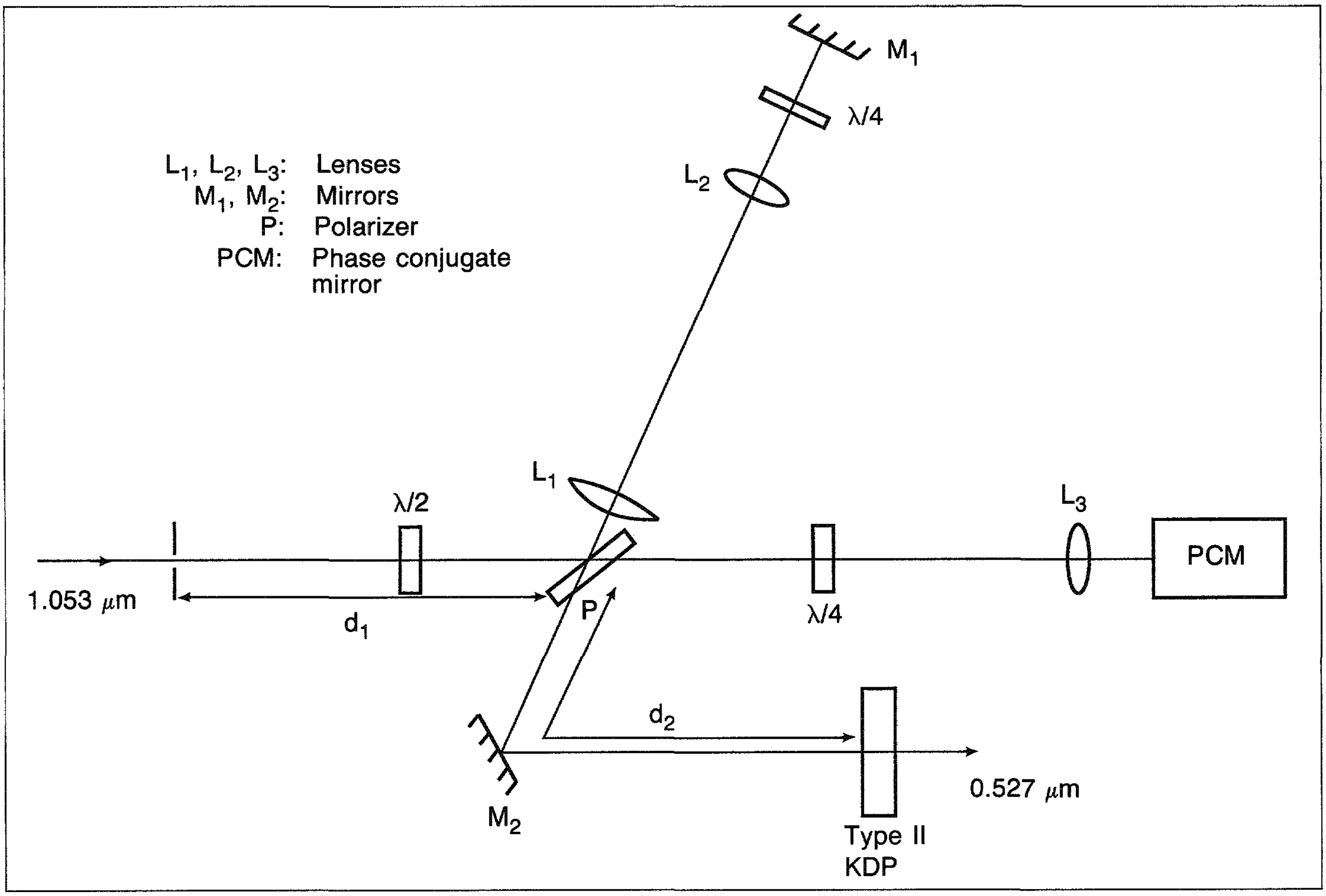

Fig. 2-7. The SHAC uses optical phase conjugation and Type II frequency doubling to produce a high-quality second-harmonic beam from an aberrated fundamental input beam. The input beam is split into two beams of orthogonal polarization. One beam is directed toward a Type II doubling crystal via conventional mirrors and lenses. The second beam is directed to the crystal by a phase conjugate mirror. The frequency-doubled output is then proportional to the product of the two beams, resulting in phase cancellation.

is split into two beams of orthogonal polarization using polarizer P. One of these beams is conventionally imaged with a pair of lenses through a quarter-wave plate to mirror M1 and then re-imaged to a Type II doubling crystal. The second beam is reflected from a phase conjugate mirror (PCM) through a quarter-wave plate and is coincident with the unconjugated beam on the doubling crystal. Equal path lengths $d1$ and $d2$ then provide a reproduction of the input beam and its conjugate with orthogonal polarizations overlapped on the doubling crystal. Since the electric field of the resulting second harmonic beam is proportional to the product of the fields of the two fundamental input beams (i.e., the original input beam and its complex conjugate), the phase distortions in the beams cancel each other, producing a high-quality second-harmonic beam.

The process described here is very similar to that used by Yariv et al.[10] to obtain optical phase conjugation by difference frequency mixing of a good quality second-harmonic beam with an aberrated fundamental, resulting in a phase-conjugated fundamental-frequency beam. In this case, however, the output beam is the good quality second harmonic, and the inputs are the fundamental beam and its conjugate.

This method has been tested using a relatively low-power Nd:YLF laser oscillator. The output pulse consisted of about 5 mJ in 50 ns. Liquid CS_2 was used as the phase conjugation medium and a 1.2 cm thick KDP crystal was used for frequency doubling. The input beam diameter was 4 mm.

A mirror was placed at the input to the system and tilted slightly to deflect the input laser beam, thus producing a distortion. The frequency-doubled output amplitude and propagation direction were then monitored. It was found that, within the limits of the angular acceptance of the KDP crystal, the propagation direction of the frequency-doubled beam was nearly independent of the deflection angle of the input beam. Conversion efficiency dropped off as would be expected due to phase mismatch in the crystal at increasing deflection angles. Relative frequency-doubling efficiency as a function of incident beam deflection angle is shown in Fig. 2-8.

Compensation for focus in the incident beam was also demonstrated. The far-field image of the second-harmonic laser beam was monitored with a charge-coupled device (CCD) TV camera at the focus of a 3.5 m focal length lens. Various lenses were placed at the input of the system without producing a change in the far-field spot size of the second harmonic. Lenses as short as +2 m focal length were used without significant loss of conversion efficiency.

Finally, random phase aberrations were produced by inserting a "low optical quality" petri dish in the input beam. Results of this demonstration can be seen in Fig. 2-9. The unaberrated far-field spot of the infrared beam shown in Fig. 2-9a is nearly diffraction-limited. The same far-field spot shown in Fig. 2-9b after the aberrator was inserted is about five times the diffraction-limited size. On the other hand, the second-harmonic far-field spot size (Figs. 2-9c and 2-9d) varied less than 10%

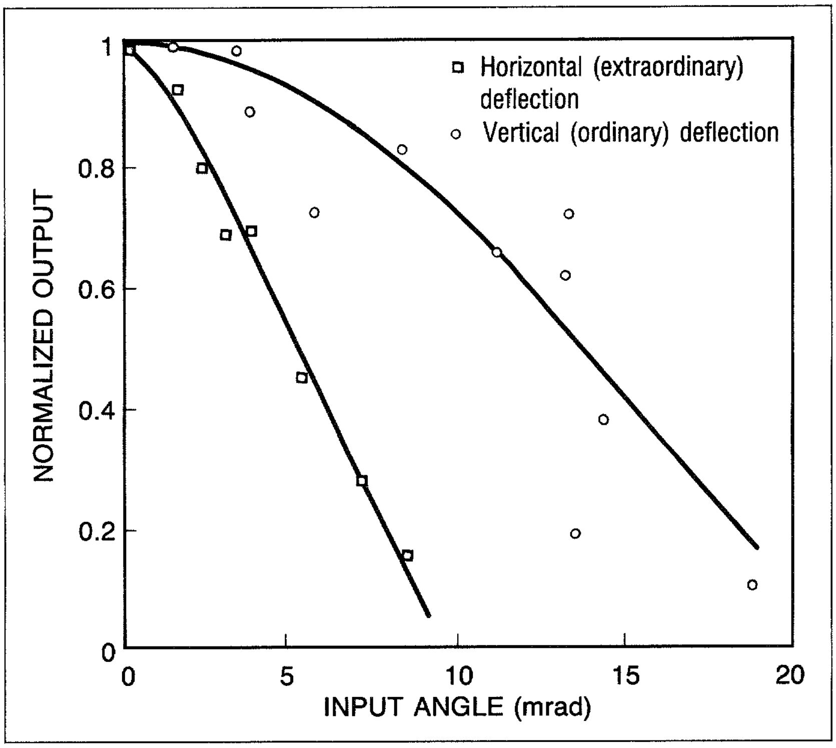

Fig. 2-8. The acceptance angle of the SHAC is determined by phase matching in the doubling crystal. The output efficiency depends on the input deflection angle but the propagation direction of the output does not.

when the aberrator was inserted, indicating almost complete compensation for the aberrations originally induced. Similar results were obtained when aberrations were produced by flowing hot air past the input of the system, creating air turbulence.

In conclusion, SHAC appears to be a useful technique for removing laser beam aberrations. We are continuing to study the effects of high power and conversion efficiency, as well as the subtleties of operation of the system, to determine its applicability to ICF laser systems. A future report will present a theoretical discussion of the process.

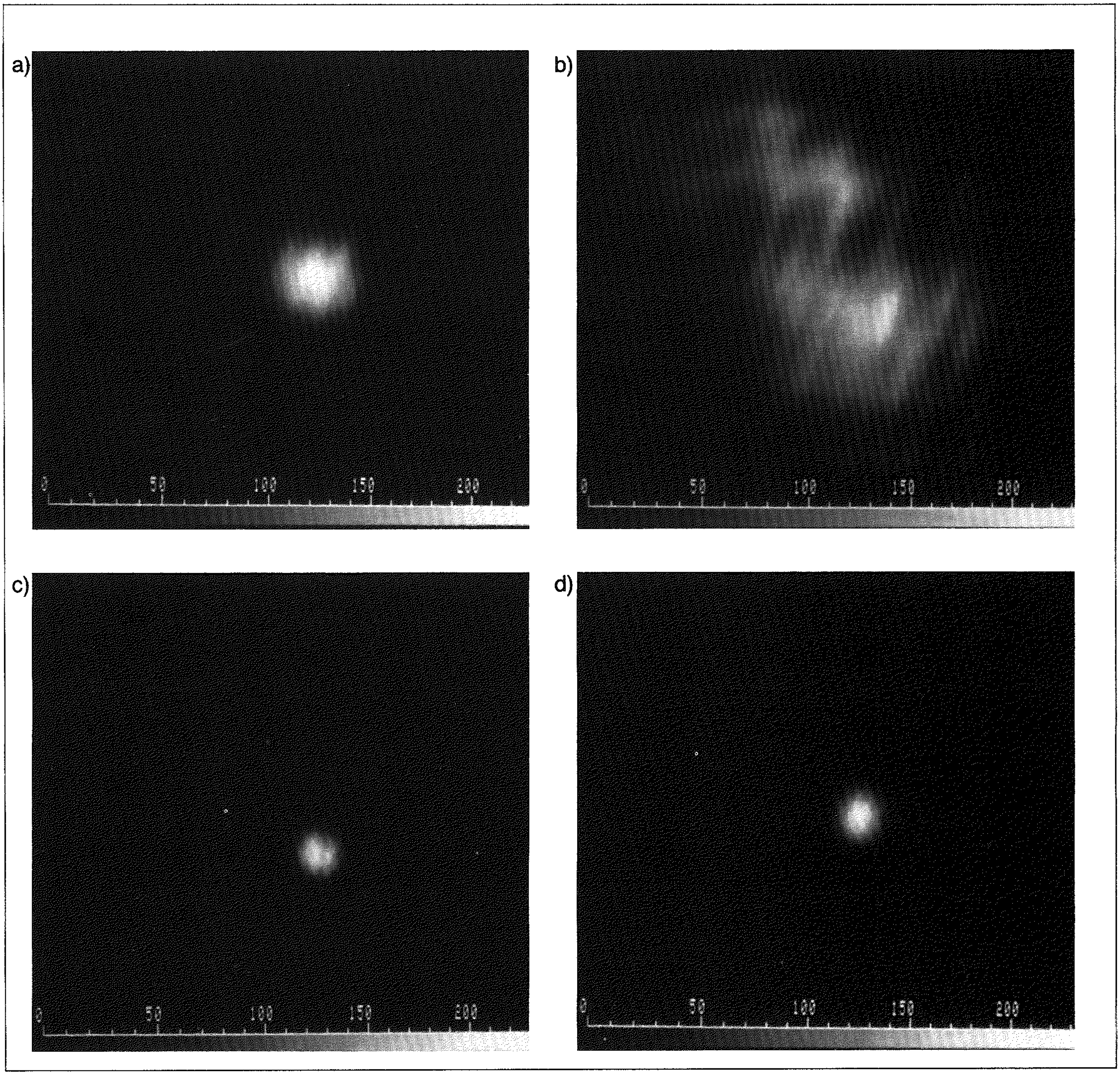

Fig. 2-9. Nearly diffraction-limited second-harmonic beams can be obtained from severely distorted fundamentals by using the SHAC. The diameter of an unaberrated IR beam (a) is nearly diffraction-limited; the diameter of an aberrated IR beam (b) is about five times the diffraction-limited size; the diameter of a frequency-doubled (green) beam derived from an unaberrated IR beam (c) is nearly diffraction-limited; and the diameter of a frequency-doubled (green) beam derived from an aberrated IR beam but corrected by SHAC (d) is less than 1.1 times the diffraction-limited size.

For additional information, please contact Mr. R. P. Johnson

REFERENCES

1. R. H. Lehmberg and S. P. Obenschain, "Use of Induced Spatial Incoherence for Uniform Illumination on Laser Fusion Targets," *NRL Memorandum Report 5029*, Naval Research Laboratory, April 11, 1983.
2. Y. Kato, K. Mima, N. Miyanaga, S. Arinaga, Y. Kitagawa, M. Nakatsuka, and C. Yamanaka, "Random Phasing of High-Power Lasers for Uniform Target Acceleration and Plasma-Instability Suppression," *Phys. Rev. Lett.* **53**(11) (September 10, 1984), p. 1057.
3. S. P. Obenschain, J. Grun, M. J. Herbst, K. J. Kearney, C. K. Manka, E. A. McLean, A. N. Mostovych, J. A. Stamper, R. R. Whitlock, S. E. Bodner, J. H. Gardner, and R. H. Lehmberg, "Laser-Target Interaction with Induced Spatial Incoherence," *Phys. Rev. Lett.* **56**(26) (June 30, 1986), p. 2807.
4. R. H. Lehmberg, A. J. Schmitt, and S. E. Bodner, "Theory of Induced Spatial Incoherence," *J. Appl. Phys.* **62**(7) (October 1, 1987), p. 2680.
5. D. Veron, H. Ayral, C. Gouedard, D. Husson, J. Lauriou, O. Martin, B. Meyer, M. Rostaing, and C. Sauteret, "Optical Spatial Smoothing of Nd-Glass Laser Beam," *Opt. Commun.* **65**(1) (January 1, 1988), p. 42.
6. R. H. Lehmberg, S. P. Obenschain, and M. S. Pronko, "Experimental Studies on the Second Harmonic Generation of Broadband, High-Peak-Power Laser Radiation at 527 nm using a Quadrature Crystal Array," Naval Research Laboratory, Washington, DC; J. Goldhar, U. Maryland, College Park, MD.
7. A. E. Siegman and D. J. Kuizenga, "Active Mode-Coupling Phenomena in Pulsed and Continuous Lasers," *Opto-Electronics* **6** (1974), p. 43.
8. D. Eimerl, "Quadrature Frequency Conversion," *IEEE J. Quantum Electron.* **QE-23**(8) (August 1987), p. 1361.
9. See, for example, R. A. Fisher, *Optical Phase Conjugation* (Academic Press, 1983) and its bibliography.
10. A. Yariv et al., *IEEE J. Quantum Electron.* **QE-14**(9) (September 1978), p. 652.

DO NOT MICROFILM
THIS PAGE

LASER AND PLASMA INTERACTIONS

SECTION THREE

Scientific Editor, Dr. C. J. Armentrout

Introduction

In recent years, laser/plasma investigations at KMS Fusion (KMSF) have been focused on the details of the interaction physics of processes critical to the success of inertial confinement fusion (ICF). Many of our experiments address issues associated with the mainline indirect-drive approach; much of this research is classified.

In this report, we present the unclassified portion of our efforts. Our research program in plasma physics achieved a number of significant results last year. In the following pages, we discuss both work that confirms the theories that motivated it and other research that illuminated unexpected features, which require more experiments and/or a more detailed understanding.

High-Z Plasma Characterization

Our experimental program is the subject of Section 3.1. The thrust of this program has been the study of laser beam interactions with plasmas of high atomic number (high-Z).

Dynamics of Bulk Plasma Behavior for Laser-Irradiated Gold Disk Targets. An experimental campaign was undertaken to examine the evolution of the absorption layer and associated corona produced by short-wavelength irradiation of gold disks; it is reported in Section 3.1.1. The goal of this series was to measure bulk plasma flow and compare the results to theory and to computer simulation. Three different pulse shapes were used; a comparison between the standard "picket-fence" pulse and square pulses was of primary interest.

These experiments revealed that the dynamic behavior of laser-irradiated gold targets shows expected characteristics in gross plasma dynamics and unexpected characteristics in certain details. One of the unexpected results is due to laser nonuniformity; it is the issuance of jets and filamentary structures when picket pulses are used. In an attempt to characterize these jets, the beam was adjusted to produce a high-intensity ring on the target. Controlled, large-scale jetting was observed to arise from the central, low-intensity region. The high-velocity material of the jets is cold relative to the coronal plasma and has a mass density much higher than that of the background corona.

Refractive Induced Distortion of Harmonic Light Images. The effects of refraction on a light ray passing through plasma have been investigated both experimentally and computationally. The experimental study, which is discussed in Section 3.1.2, was prompted by a proposed imaging diagnostic for the two-beam Nova facility chamber at Lawrence Livermore National Laboratory (LLNL). The KMSF Chroma laser was used to identify the conditions that cause severe refractive modifications to the path of a probe beam as it passes through the target. Ten beamlets of 0.26 μm light probed a blow-off plasma. Severe refractive effects were observed for the case of a large, cold, expanding plasma but not for the other conditions tested.

This finding is in qualitative agreement with computer simulations that predicted problems when the refraction is so strong that the beam misses the collection optics of the detector. A simulation code has been applied here at KMSF to the problem of a beam of soft x-rays passing through a plasma. The code is directly applicable to the x-ray backlighter problem (see also Section 3.1.3) where the backlit image may require correction due to refraction. The research reported here is also applicable to the case of a soft x-ray beam passing through a plasma many times and reflecting from a mirror after each passage.

Backlighter Analysis. The efficiency with which various backlighter sources emit x-rays has been studied for very high-intensity laser irradiation. The work discussed in Section 3.1.3 is an extended analysis of the previous backlighter campaign, in which the development of a point backlighter source was started. Recent experimental work will be included in the 1989 KMSF Annual Technical Report.

Time-and Space-Resolved Dot Spectroscopic Characterization of Laser-Produced Plasmas. For several years, we have been performing spectroscopic studies of high-Z dot targets and using the resulting line ratios to measure plasma density and temperature. In Section 3.1.4 we present an analysis of these measurements. The discrepancy between these results and non-ratio measurement techniques revealed the need for a more fundamental understanding of the time-dependent recombination and ionization processes that take place in the corona. We are assembling a data base that we hope will lead to a more accurate predictive capability.

Development of Diagnostic Instruments

Accurate interpretation of our experiments requires versatile and sophisticated diagnostic instruments. In Section 3.2 we report several advances in diagnostic techniques and instrumentation that were developed during the year.

Development of X-ray Diagnostic Instruments and Calibration Facility. Framing cameras, curved crystal spectrographs, multichannel biplanar soft x-ray diodes, and ungated VUV intensifiers have been added to the Chroma laser's array of plasma diagnostic instruments. The effort in instrumentation is discussed in Section 3.2.1. Significant success has been achieved in the effort to use electronic imaging and computer control to acquire digital information that is important to experiments.

Digital Imaging for ICF Diagnostics. The video data-acquisition system is described in Section 3.2.2. Such a system is vital to successful work in advanced ICF facilities because the intense radiation will cause problems with diagnostic instrument access, and film-based instruments will not be feasible. Video techniques are now routinely applied to visible and x-ray streak cameras and are planned for implementation on the framing cameras.

Theoretical Plasma Physics

Theoretical work performed during the year to prepare for future campaigns and to interpret past campaigns is the subject of Section 3.3.

Modeling of Induced Spatial Incoherence. We are preparing a major experimental campaign to study the effects on the plasma of beam smoothing from induced spatial incoherence (ISI). Although the experimental results will be reported in the 1989 Annual Technical Report, theoretical studies have already been performed to analyze the effects of an ISI-smoothed beam on plasma instabilities. The results, discussed in Section 3.3.1, are extensions to two dimensions of calculations started last year. We conclude that (1) the laser frequency bandwidth must be greater than the growth rate of any plasma instability if an ISI beam is to be effective, and (2) that a finite spatial coherence length perpendicular to the beam is useful for diffractive smoothing of the beam.

Ultra-Strong Langmuir Turbulence in Open Systems. Realistic fusion targets will have coronas extending up to ten thousand laser wavelengths. Instabilities previously considered unimportant are receiving new attention because even small loss mechanisms could become significant in these targets. Strong, nonlinear Langmuir turbulence, discussed in Section 3.3.2, has been successfully simulated. The results show a modulational instability in the corona and demonstrate for the first time formation, collapse, burn-out, and renucleation of ion density cavitons. The collapse of these structures could enhance Raman scattering losses.

SRS Inhibition Due to SBS-Enhanced Density Fluctuations in Inhomogeneous Plasma. In Section 3.3.3, highly significant results are reported of stimulated Raman scattering (SRS) suppression below the quarter-critical surface due to the presence of an enhanced level of ion acoustic turbulence from stimulated Brillouin scattering (SBS). This effect, which requires a realistic density gradient, explains recent experimental observations on the interaction between SRS and SBS signals.

Computational Physics

In Section 3.4 is presented the current work in computational physics.

X-ray Refraction in Laser-Produced Plasmas. The RAYPATH code, written to study the effects of refraction, has been modified to account for the effects of the mirrors that might be used in certain x-ray laser schemes. This is important because some of the x-ray diagnostic instruments used to characterize laser-produced plasmas are sensitive to refractive effects of the plasma, especially for the softer x-rays. Preliminary results of the calculations are summarized in Section 3.4.2.

Advances in Computational Mathematics. In Section 3.4.3, techniques are reported that have been implemented for the efficient solution of computationally demanding problems. The topics discussed are implicit spectral method solutions for nonlinear wave equations, dispersion analysis of discretization problems of the von Neuman–Richtmyer equations, and the application of an efficient Abel-transform algorithm for inverting spectral data and obtaining a best-fit emission profile from it.

SECTION 3.1

High-Z Plasma Characterization

3.1.1 Dynamics of Bulk Plasma Behavior for Laser-Irradiated Gold Disk Targets

The evolution of bulk plasma from a laser-irradiated, high-atomic-number (high-Z) target can affect the generation of soft x-rays. Several disk experiments have been carried out in the past that were aimed primarily at measuring the hot electron fraction[1,2] and the efficiency with which laser light is converted to soft x-rays.[2] The experiments described here were done to measure bulk plasma flow and to compare these results to theory and simulation. Two separate experimental campaigns were completed. In laser irradiations using green light ($\lambda = 0.53$ μm), 135 target shots were taken. In blue light ($\lambda = 0.35$ μm), 74 target shots were taken. Data from the green-light experiment have been provided to Lawrence Livermore National Laboratory (LLNL) scientists, who are performing numerical simulations of the experiment, as are KMS Fusion (KMSF) researchers. Data from the blue-light experiment are in the initial stages of reduction. In this report, general features of the green-light data will be discussed.

Experimental Arrangements. Gold disk targets (22 μm thick and 600 μm in diameter) were irradiated using the Chroma laser at $\lambda = 0.53$ μm (the experimental setup is shown in Fig. 3-1). The laser pulse shape was varied by stacking as many as 13 individual variable-amplitude pulses, each 125 ps full width at half-maximum (FWHM) spaced by 170 ps. The pulse shapes used, shown in Fig. 3-2, were the three-picket shaped pulse, 1 ns and 2 ns square pulses, and a pulse that increased parabolically in time (t^2). (The three-picket pulse is one proposed by LLNL scientists to achieve high fuel compression.)

Of primary interest is a comparison between the picket pulse and the square pulses. The picket pulse had power ratios nominally 1:2:3 for the pickets, with separation of 850 ps and 125 ps between the pickets. The first two pickets were 125 ps FWHM, and the third was 850 ps FWHM. Several shots were also made using only the first two pickets. The maximum energy on target was 200 J. An $f/6$ lens was used, with the target placed either 1200 or 3000 μm from best focus. Thus, the peak intensity on target varied from 0.8 to 6×10^{14} W/cm^2.

Most of the targets were shot on the divergent side of best focus. Figure 3-3 shows an equivalent-plane image of the incident beam on the divergent side of best focus (a) and the convergent side of best focus (b). In the nominal 200 μm spot diameter on target for the divergent beam is a random pattern of 20 to 30 μm regions of high and low beam intensities. The peak-to-valley intensity ratio is from 2 to 4. On the convergent

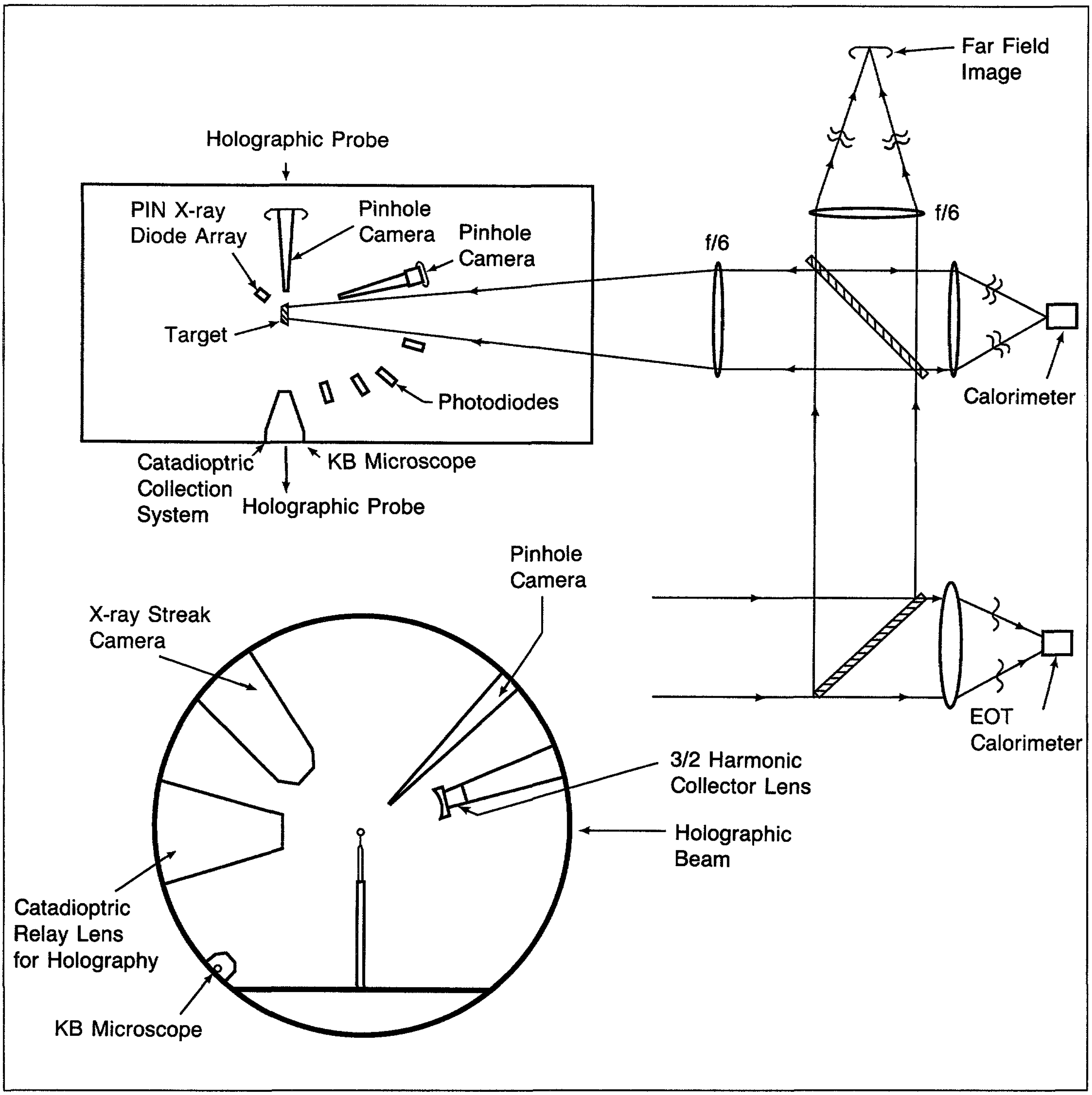

Fig. 3-1. The targets (gold disks, 22 μm thick and 600 μm in diameter), were irradiated by an *f*/6 lens using 0.53 μm light. The experimental setup consisted of optical and x-ray diagnostic instruments arrayed about the target. The major instruments viewed orthogonal to the incident laser beam.

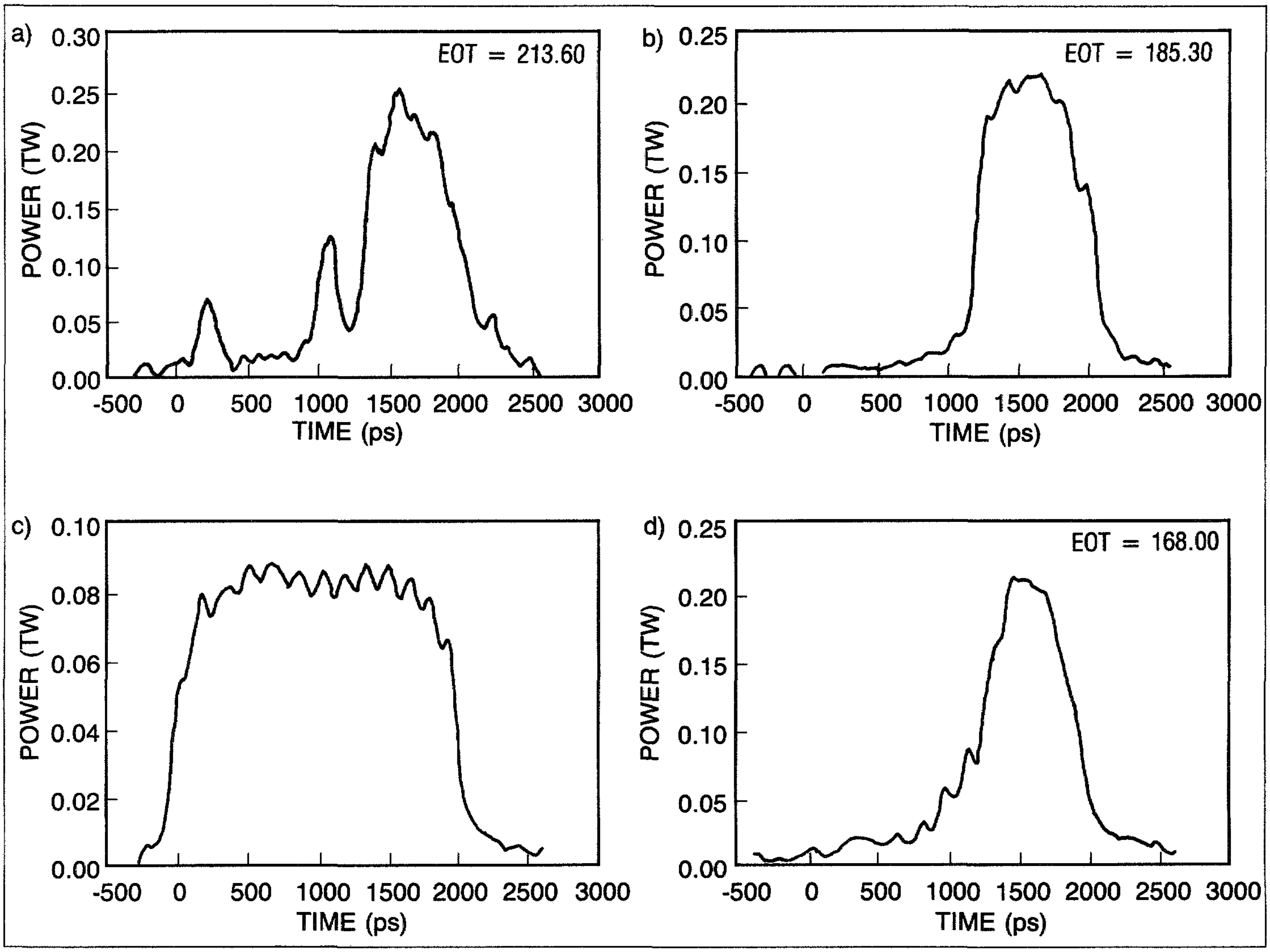

Fig. 3-2. Pulse shapes used in the experiment were a three-picket pulse (a), a 1 ns square pulse (b), a 2 ns square pulse (c), and a t^2 increasing pulse (d).

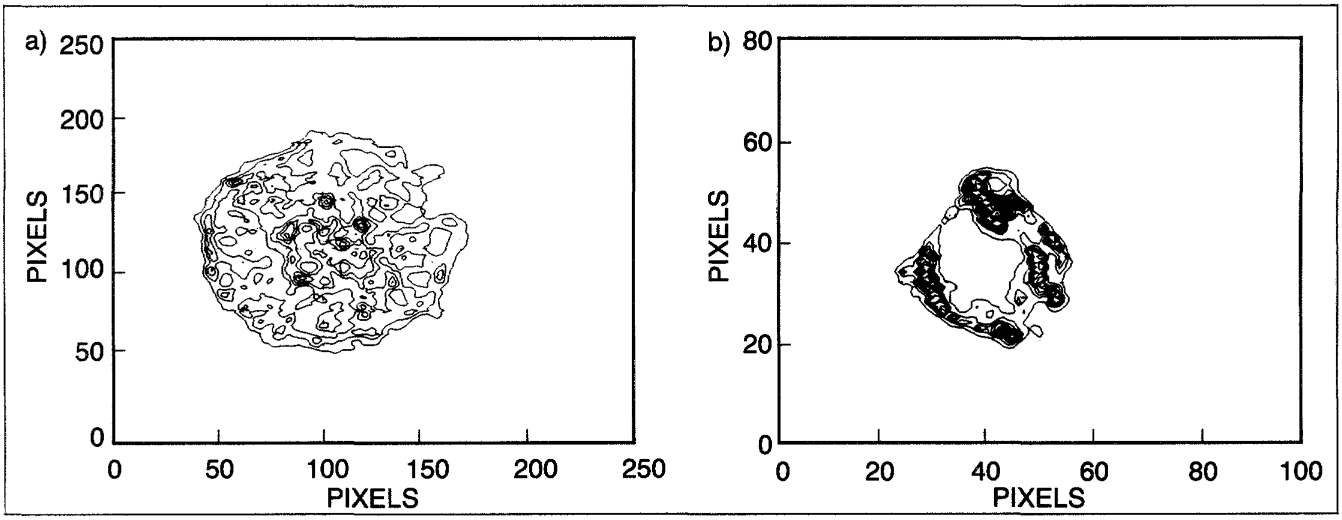

Fig. 3-3. The densitometer scan of the equivalent target plane image on the divergent side of best focus (a) showed a random hot spot pattern. On the convergent side of best focus (b) there was a high-intensity ring. The beam diameter was about 200 μm in both cases.

side of best focus is a high-intensity ring, 50 μm thick, that surrounds a 100 μm diameter low-intensity spot. The intensity of the central spot is 5 to 10 times lower than that of the ring. These features are independent of pulse shape, although the exact details may vary from shot to shot.

Plasma properties were monitored by several instruments; they are listed in Table 3-1.

Holographic interferograms[3] were taken with up to four frames per shot. The frames were spaced by 400 ps and the first frame had a variable time delay relative to the main laser pulse. The wavelength of the probe beam was $\lambda = 0.26$ μm and its duration was 20 ps, which effectively eliminated any blurring due to plasma motion. Electron densities were obtained from the reconstructed interferograms by the Abel inversion technique. Electron densities from $1 \times 10^{19}/\text{cm}^3$ to $1 \times 10^{21}/\text{cm}^3$ could be measured.

The 3/2 harmonic emission, which occurs at quarter-critical density for the incident laser wavelength, was imaged orthogonal to the laser beam onto the slit of a streak camera. This gives a one-dimensional (1-d) temporal history of the quarter-critical trajectory along the laser axis.

The x-ray emission was imaged with a pinhole and slit onto an x-ray streak camera. The sensitivity of the streak camera with its associated filters and photocathode response is shown in Fig. 3-4. The peak sensitivity is in the gold M (2.0 to 4.0 keV) band range. Since this emission occurs primarily near the critical density, the 1-d streak image provides an estimate of the trajectory of the critical surface along the laser axis. Time-integrating

Table 3-1. Diagnostic Instruments and Techniques Used for Bulk Plasma Property Measurements

Instrument/Technique	Measurement
Holographic interferometry	Coronal density
X-ray streak camera	Peak M-band emission trajectory along laser axis
3/2 ω_0 optical streak camera	Peak 3/2 ω_0 emission trajectory along laser axis
Kirkpatrick-Baez microscope	Time-integrated image parallel to target surface
X-ray pinhole cameras	Time-integrated gold M-band emission parallel and perpendicular to target surface
PIN diodes	Time-integrated gold M-band energy
Photodiodes and calorimeter	Backscattered ω_0 energy

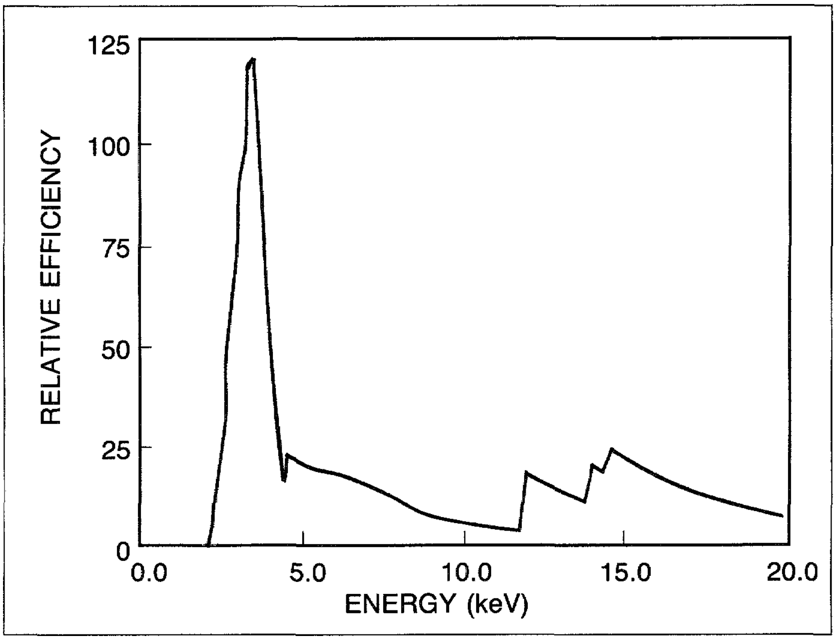

Fig. 3-4. The x-ray streak camera response was greatest in the gold region, 2.0 to 4.0 keV.

pinhole cameras were filtered to image the M band x-ray emission from the target orthogonal and parallel to the laser beam direction.

A Kirkpatrick–Baez (KB) x-ray microscope with 3× magnification was used with appropriate filters to image the target at energies from 600 to 800 eV orthogonal to the laser direction. Absorbed energy was determined by measuring backscattered energy through the focusing lens with a calorimeter and with photodiodes placed outside the cone angle of the lens.

A temporally and spatially averaged coronal electron temperature measurement was made using an array of filtered PIN silicon diodes. The diode array was placed behind the target but viewing the corona to minimize the collected M band emission, which comes primarily from regions near critical density. The data were fit assuming a Maxwell-Boltzmann distribution for electron velocities, with temperature and x-ray flux as parameters to be found.

Results and Discussion. Absorption measurements at $\lambda = 0.53\ \mu m$ are in good agreement with those obtained in previous experiments. For $I = 3$ to $5 \times 10^{14}\ W/cm^2$ (200 μm spot), absorption was 75%. For $I = 0.8$ to $1 \times 10^{14}\ W/cm^2$ (500 μm spot), absorption was 90%. The absorption was independent of pulse shape. Coronal temperatures were $T_e = 2.4 \pm 0.5$ keV for the higher-intensity shots and $T_e = 1.5 \pm 0.3$ keV for the lower-intensity shots, which agree well with preliminary simulation results.

A typical interferogram for a square pulse laser shot is shown in Fig. 3-5. Note that the fringes are relatively smooth. For picket pulses, the fringes are "spikey," particularly between the

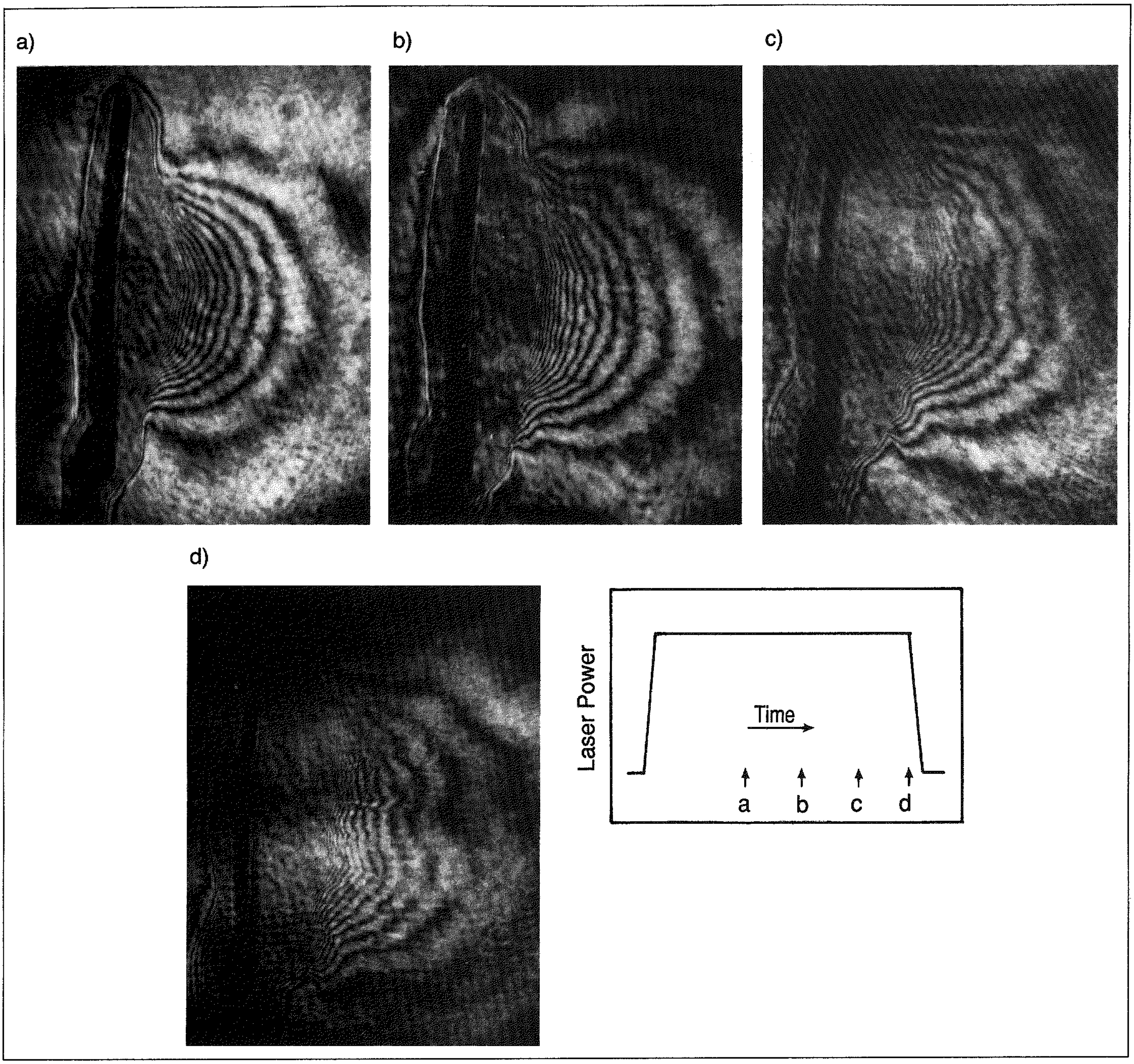

Fig. 3-5. Holographic interferograms for a square laser pulse show smooth fringes. The exposures for shot 8867 were made at 800 ps (a), 1200 ps (b), 1600 ps (c), and 2000 ps (d).

first and second pickets; the fringes were smoothed before digitization. The digitized images are inverted mathematically to give electron density profiles. Typical densities that can be resolved are from $10^{21}/\mathrm{cm}^3$ down to $10^{19}/\mathrm{cm}^3$, with a ± 5 μm uncertainty in the spatial dimension.

Figure 3-6 shows coronal electron densities produced from the Abel inversion for three different laser pulse shapes. Probe pulses were taken about 300 ps into the main pulse. The average intensity of the main pulse is about 5×10^{14} W/cm^2. As expected, the t^2 and picket-shaped pulses yield longer scale lengths and extend farther out than the square pulse. The high-density points at critical density are taken from streak camera data of the gold M band x-ray emissions, which occur from near the critical surface. Note the steepening of the profile in going from underdense to critical density, which is probably due to the transition from subsonic to supersonic flow.

The gold M band x-ray streak records are shown in Fig. 3-7 for a 1 ns square pulse (a) and a picket pulse (b) as viewed by the x-ray streak camera. We tacitly assume that the peak emission corresponds to the position of the critical density surface along the laser axis. For the square pulse, the critical surface

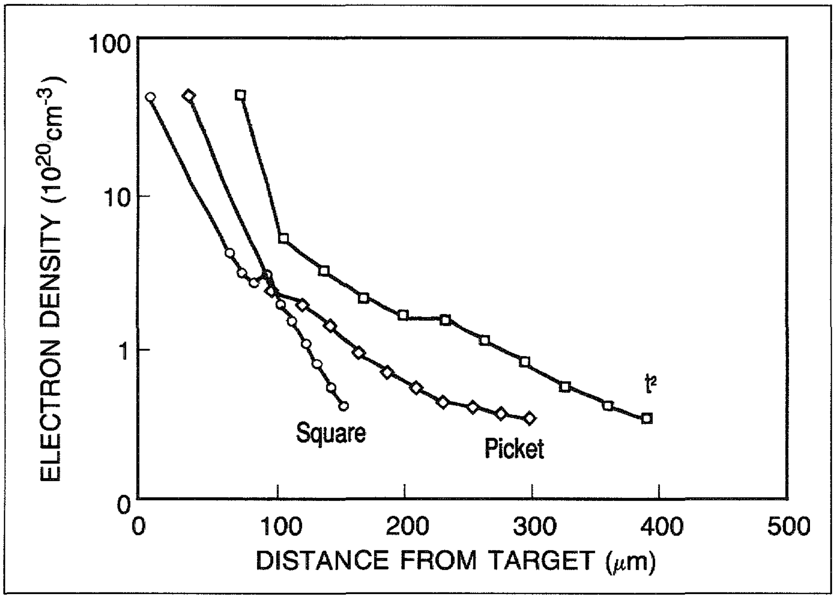

Fig. 3-6. Coronal electron densities were obtained from Abel inversion for t^2, picket, and square laser pulse shapes. (Shots 8896a, 8869c, 8850d.) The profiles were taken about 300 ps from the start of the main laser pulse.

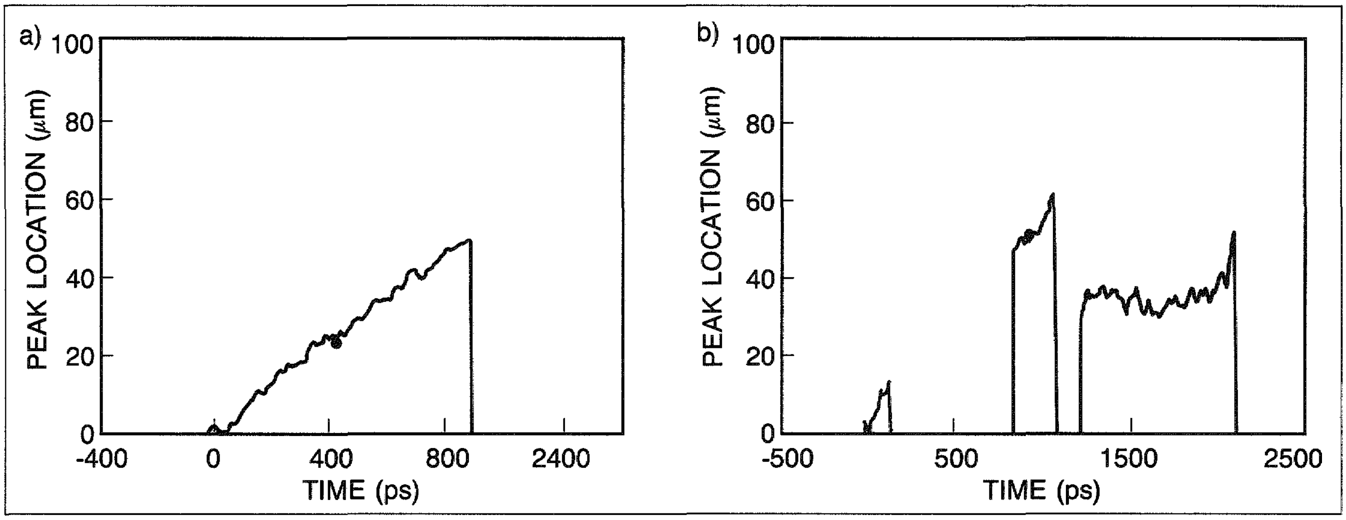

Fig. 3-7. Gold M band x-ray emission moves outward along the laser axis for a square (a) and picket (b) pulse. It is believed that this corresponds to the critical surface trajectory. The critical surface moves linearly for a square pulse but stagnates during the last picket of a picket pulse. The energy on target was 35.5 J (shot 8861, a), and 165.8 J (shot 8857, b).

moves approximately linearly in time, as expected for an isothermal rarefaction expansion. It approaches the peak distance of about 50 μm from the target surface, giving the average velocity of about 5 × 10^6 cm/s. For the picket fence pulse (Fig. 3-7b) the emission is seen for each of the pickets. The first picket shows emission from about 5 to 10 μm from the target surface. When the second picket arrives, the critical density surface has moved out to about 50 μm, giving an average velocity of about 4 × 10^6 cm/s. During the third picket, the emission peak is closer to the target surface than the peak was during the second picket. The emission peak does not appear to move for the duration of the third picket.

The qualitative behavior of the critical density n_c surface trajectory is consistent with the $n_c/4$ surface trajectory (from 3/2 ω_0 emission) as viewed with an optical streak camera. The 3/2 ω_0 harmonic emission location along the laser axis is shown in Fig. 3-8 for a 1 ns square (a) and a picket (b) pulse. The $n_c/4$ surface moves out linearly for a square pulse. For the picket pulse, the retrograde motion of the peak emission during the third picket is apparent.

The expansion along the laser axis due to laser spot size is illustrated in Fig. 3-9. The intensities in both shots are about 1 × 10^{14} W/cm^2. For the smaller spot size (a), the extent of the underdense plasma is not nearly as great as for the larger spot size (c) at all four frame times. The criterion for 1-d (planar) expansion requires the spot size $2R \gg C_s\tau$. With $T_e \sim 1.5$ keV and assuming $Z \sim 50$, $\tau = 2$ ns, then $C_s\tau \sim 400$ μm. Thus we expect that the expansion for the smaller spot size is not one-dimensional and divergence effects are important.

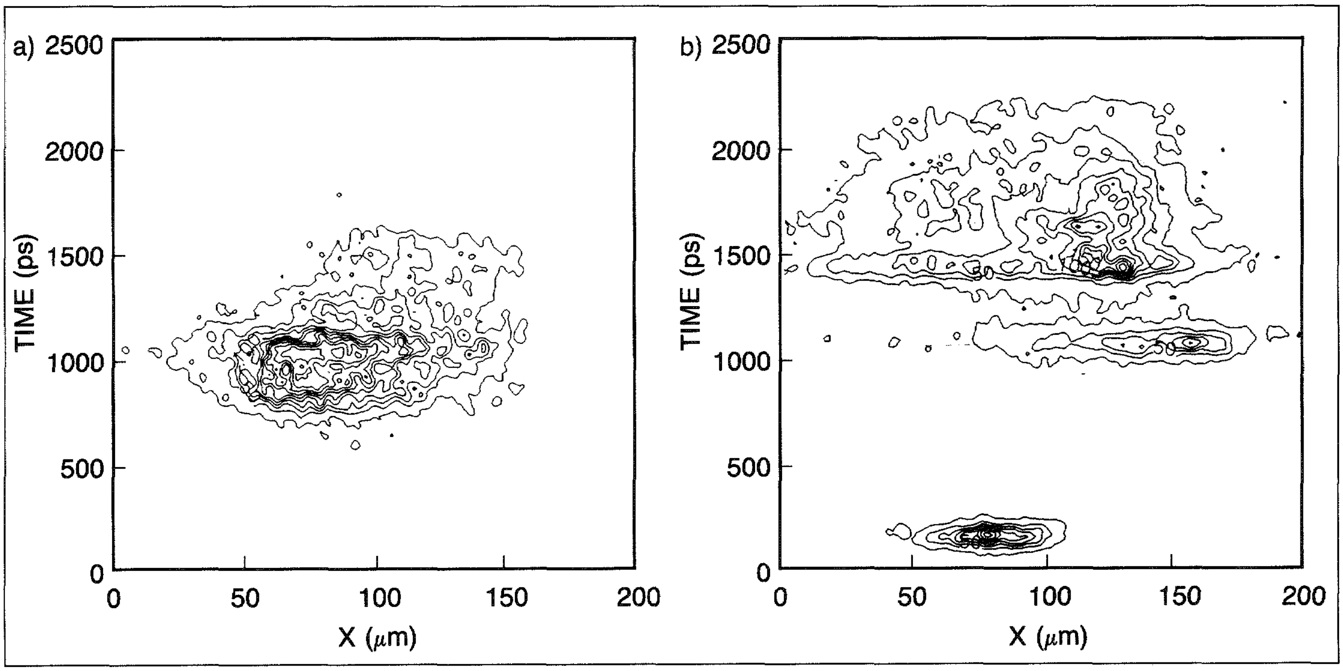

Fig. 3-8. The 3/2 ω_0 harmonic emission along the laser axis shows linear motion of the $n_c/4$ surface for a square pulse (a) and stagnation of the $n_c/4$ surface for a picket pulse (b).

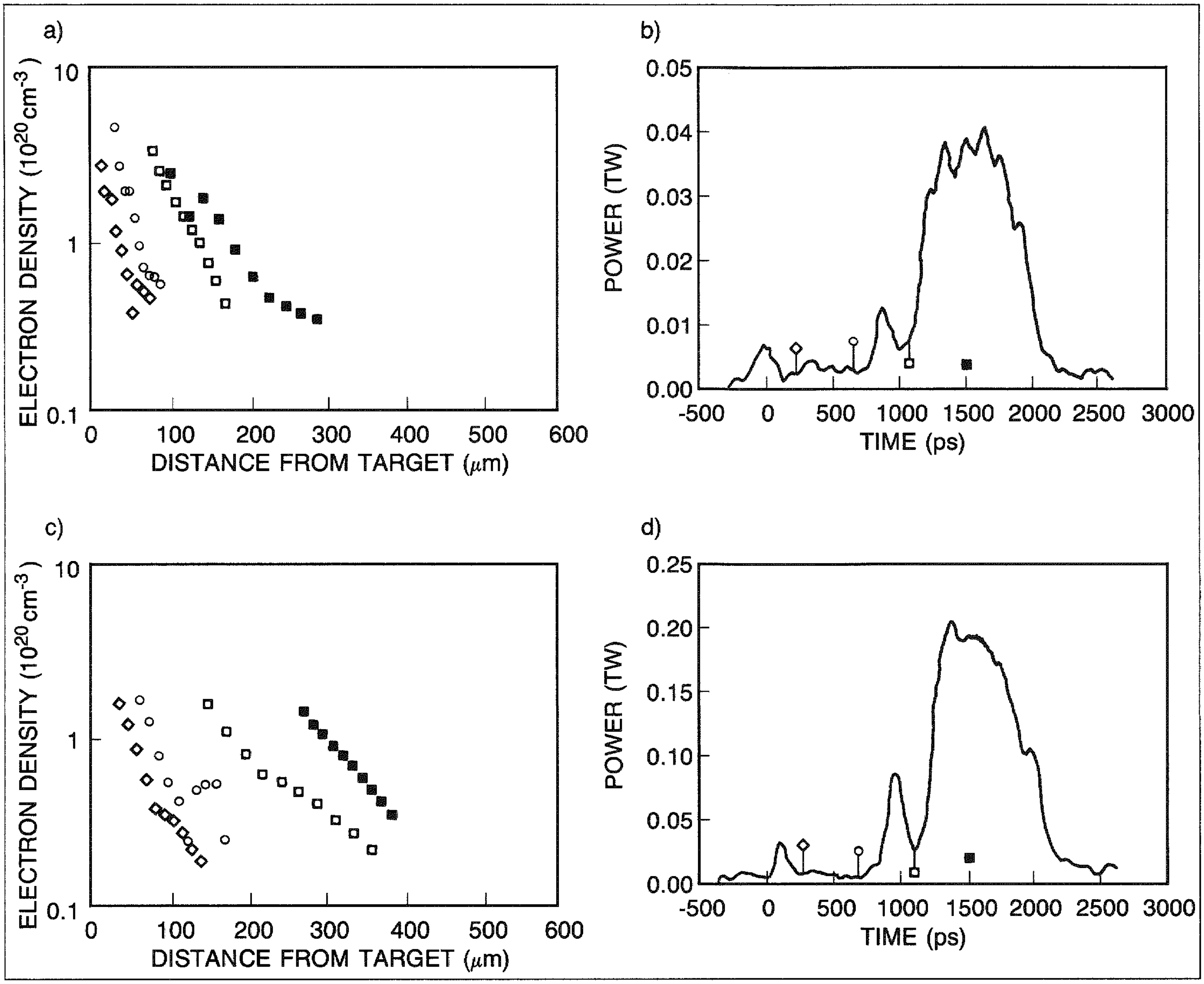

Fig. 3-9. Holographic interferometry shows the effects of spot size on expansion. The small spot (a) has a lower density at any given time than the large spot (c). The probe times and power levels represented by the geometric symbols in (a) and (c) are identified in (b) and (d), respectively.

Time-integrated x-ray pinhole pictures also show the motion of the critical density surface for picket pulses. In Fig. 3-10, we show pinhole pictures for a square (a) and picket (b) laser pulse. For the square pulse, the emission originates from the diameter of the laser spot and extends continuously outward to about 200 μm. For the picket pulse, we see a space between emission near the target surface and emission on the corona. The first burst of emission (near the target surface) comes from the first picket. The second burst comes from the second and third pickets. The space between the two bursts can be used to calculate the average speed of the critical density surface, yielding $v = 3.6 \times 10^6$ cm/s. This agrees with the speed obtained from the streak camera data. We note that the motion of the critical density surface is nearly one-dimensional.

An interesting aspect of some of the KB pictures (soft x-rays) is shown in Fig. 3-11. For intensities $I = 3 \times 10^{14}$ W/cm^2, the

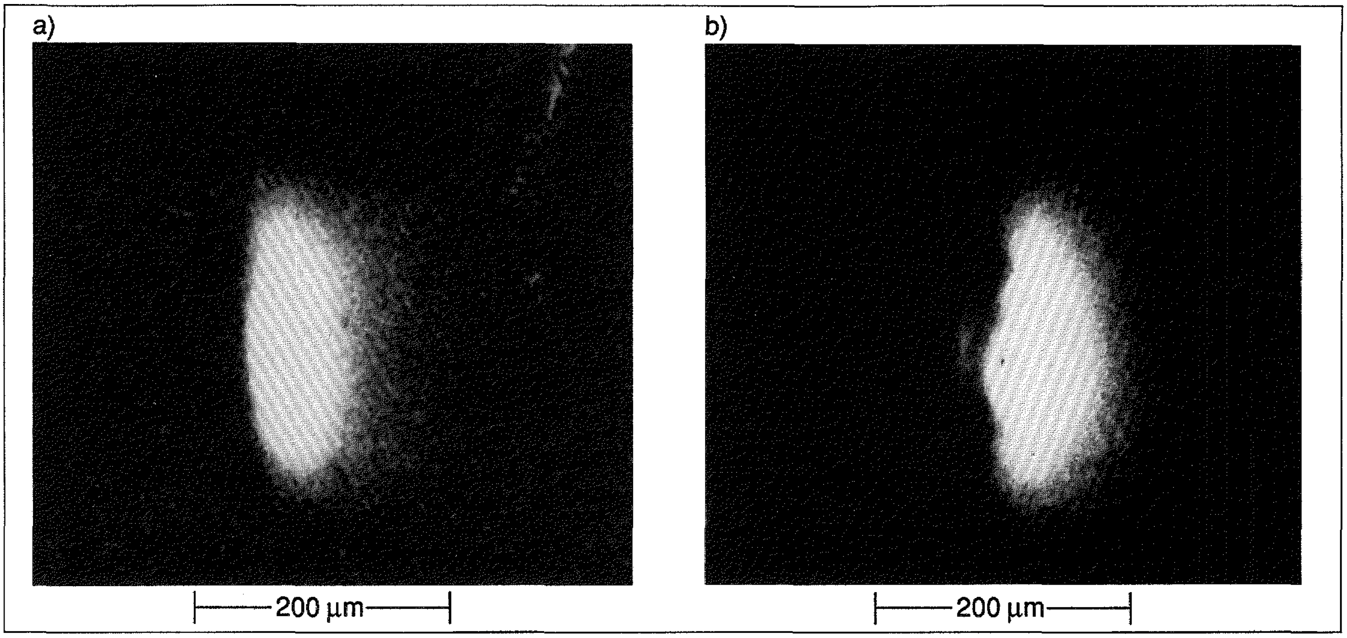

Fig. 3-10. Pinhole images of the gold M band emission are shown for a square (shot 8868, a) and picket (shot 8869, b) laser pulse. The picket pulse image shows the motion of the emission surface between the first and second pickets.

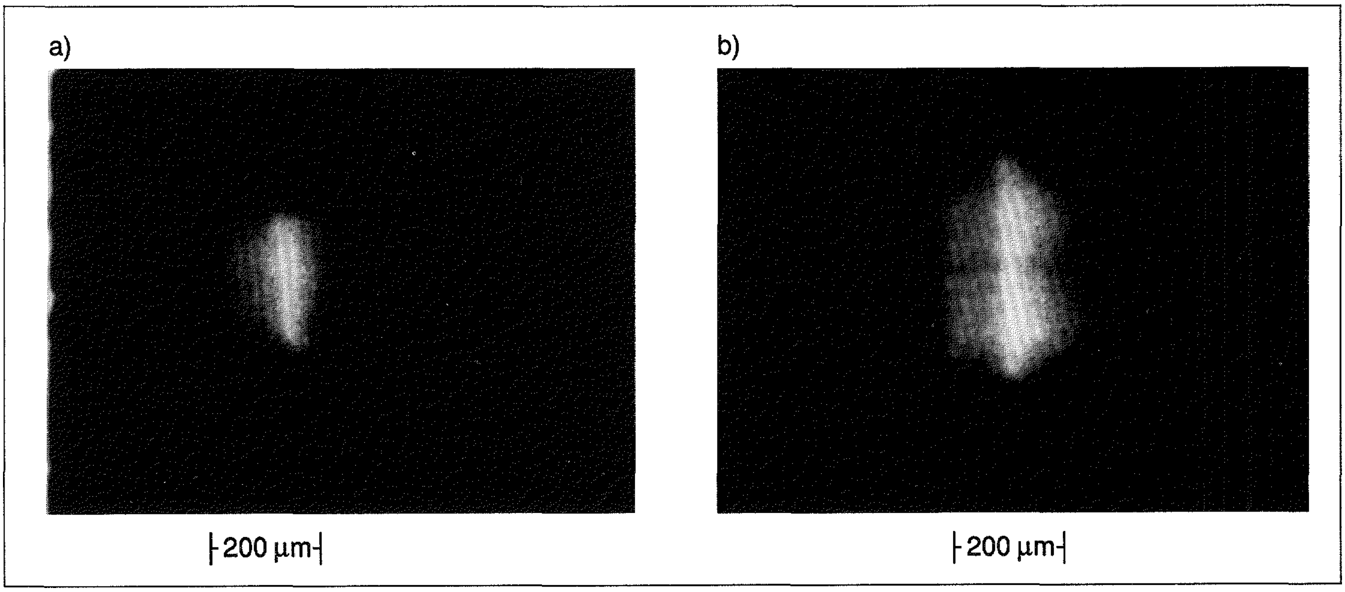

Fig. 3-11. Soft x-ray pictures for high-intensity laser irradiation (shot 8868, a) show the same qualitative shape as the M band emission. For low intensity (shot 8898, b) the hot spot in the beam "burns out" the emission in the center of the plasma.

soft x-ray emission comes from a region of qualitatively the same shape as that of the M band emission (a). At these higher intensities, the soft x-ray emission region extends only about 50 μm from the target surface. At lower average intensity, $I = 0.6 \times 10^{14}$ W/cm^2 (b), the emission extends farther from the target surface—due in part to the larger spot size but also to lower intensity. In the most intense portion of the Gaussian beam, a void in the emission is seen.

We now turn our attention to a three-dimensional aspect of the plasma blowoff—namely, jetting of plasma.

Jets and irregular structures in laser-produced plasma have been observed in a number of experiments under a variety of experimental conditions with various diagnostics. Stamper[4] and Ripin, Stamper, et al.[5] used a 0.53 μm probe to make Faraday rotation measurements on low-Z targets illuminated by a 1.06 μm laser with intensity from 10^{15} to 10^{16} W/cm^2 for 100 ps. Although the primary aim of their experiment was to measure magnetic fields, much structure in the field could be seen in the data presented. Fine-scale jets were seen in Faraday rotation measurements made by Grek et al.,[6] where low-Z targets were irradiated by a CO_2 laser with intensity of 10^{14} W/cm^2 in a 1.4 to 1.7 ns pulse. The jets originated from electron densities up to 16× the critical density and were observed during the laser pulse. Thiell and Meyer[7] took shadowgrams of jet-like structures emerging from either side of aluminum or gold thin-foil targets. The laser was either 1.06 μm or 0.35 μm in an 850 ps pulse with irradiance from 10^{13} to 10^{14} W/cm^2. The small-scale jets were present from 2 to 7 ns after the peak of the laser pulse.

The characteristics of these previously reported structures can be summarized as follows: (1) They are filamentary as opposed to billowing; (2) they are less pronounced for lower Z, lower intensity, and shorter laser wavelength; (3) they are associated with strong azimuthal magnetic fields; and (4) they appear after the laser has shut off (except for the CO_2 illumination). Thermoelectric, radiative cooling, filamentation, and Rayleigh–Taylor instabilities have been invoked to explain these phenomena. The reported jets have been associated with high-intensity "hot" spots in the incident laser beam. Here we present data that show jets and filamentary structures issuing from low-intensity "cold" spots in the incident beam. The material jetting off is cold relative to the coronal plasma, and has a mass density much higher than that of the background corona.

Gold M band x-ray emission from the front view of the target (Fig. 3-12) shows qualitatively the inhomgeneous intensity structure, as do the equivalent target plane pictures. On the divergent side of focus (a), we find 20 to 50 μm regions of high and low intensity x-ray emission corresponding to the high and low intensity variations of the laser beam. The x-ray intensity ratio between these regions is roughly 3:1. On the convergent side of focus (b), the gold M band emission shows the ring structure of the laser beam. The intensity ratio in this case is 10:1.

The most dramatic evidence of plasma jets can be seen with the target placed on the convergent side of best focus. In Fig. 3-13, we show data for a target illuminated with a picket-fence pulse. Figure 3-13 shows four interferograms taken at 320 (a), 720 (b), 1120 (c), and 1520 (d) ps relative to the beginning of the laser pulse, for a picket-fence target shot. Visible in the second frame, 720 ps after the first picket pulse, is a large jet 20 to 30 μm wide at the outermost fringe, issuing from the corona. This jet lengthens out, and by the third frame extends

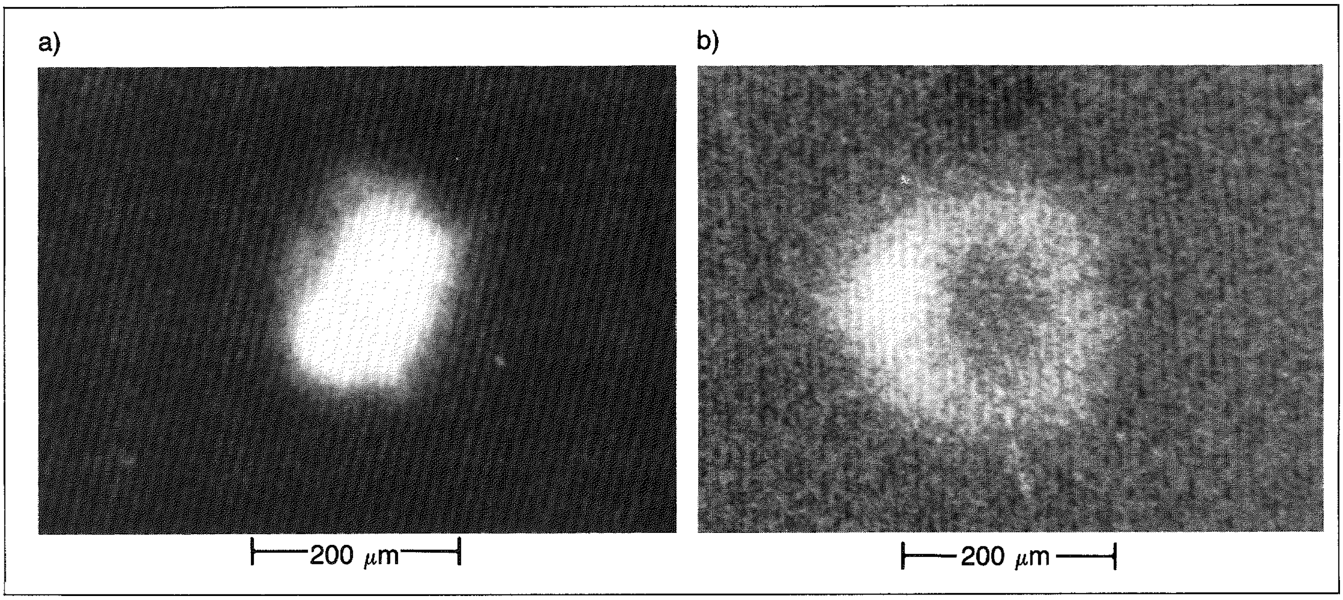

Fig. 3-12. Gold M band emission for a divergent (shot 8896, a) and convergent (shot 8831, b) laser beam focus show qualitatively the same patterns as the equivalent plane images (Fig. 3-3).

320 μm from the target. Using the location of the first fringe, we estimate the velocity to be 5 × 10^7 cm/s. Assuming cylindrical symmetry of the jet and a parabolic profile, the electron density is about 6 × $10^{20}/\text{cm}^3$ at this location. The background coronal density outside of the jet is less than 2 × $10^{19}/\text{cm}^3$. The jet density is of the same magnitude as would be obtained for a smooth fringe system 100 μm from the target surface 300 ps into a square laser pulse. By the fourth frame, the second and third pickets have arrived and the jet is smoothed out. Time-integrated x-ray pictures show analogous features. The pinhole picture (e) taken perpendicular to the laser beam shows a thick region of low emission extending from the target surface out to 125 μm, surrounded by a region of higher emission. Film scans show that the jet is 125 μm FWHM at its base and narrows to 15 μm near its apex. The region of low emission correlates well with the region of high emission measured by the KB microscope (f). This region extends also from 60 to 130 μm from the target surface and is from 90 to 20 μm thick.

The interferometric and x-ray pictures can be explained if the jets are cold relative to the coronal temperature. If the jets are hot initially, or heated by thermal conduction from the corona, we would expect the jet to thermalize and its material to expand uniformly into the background plasma. This appears to occur during the second and third laser pulses, when laser energy is nearly continuously being absorbed by the target. Cold material radiates more in the low x-ray energies, as observed with the KB microscope, and less in the high energies, as observed with the pinhole camera. We can use the relative intensities of the x-ray pictures to estimate the density of the jet. The M band emission of the corona is essentially backlighting the jet. We assume that the jet is cylindrical, its emission in the M band is negligible due

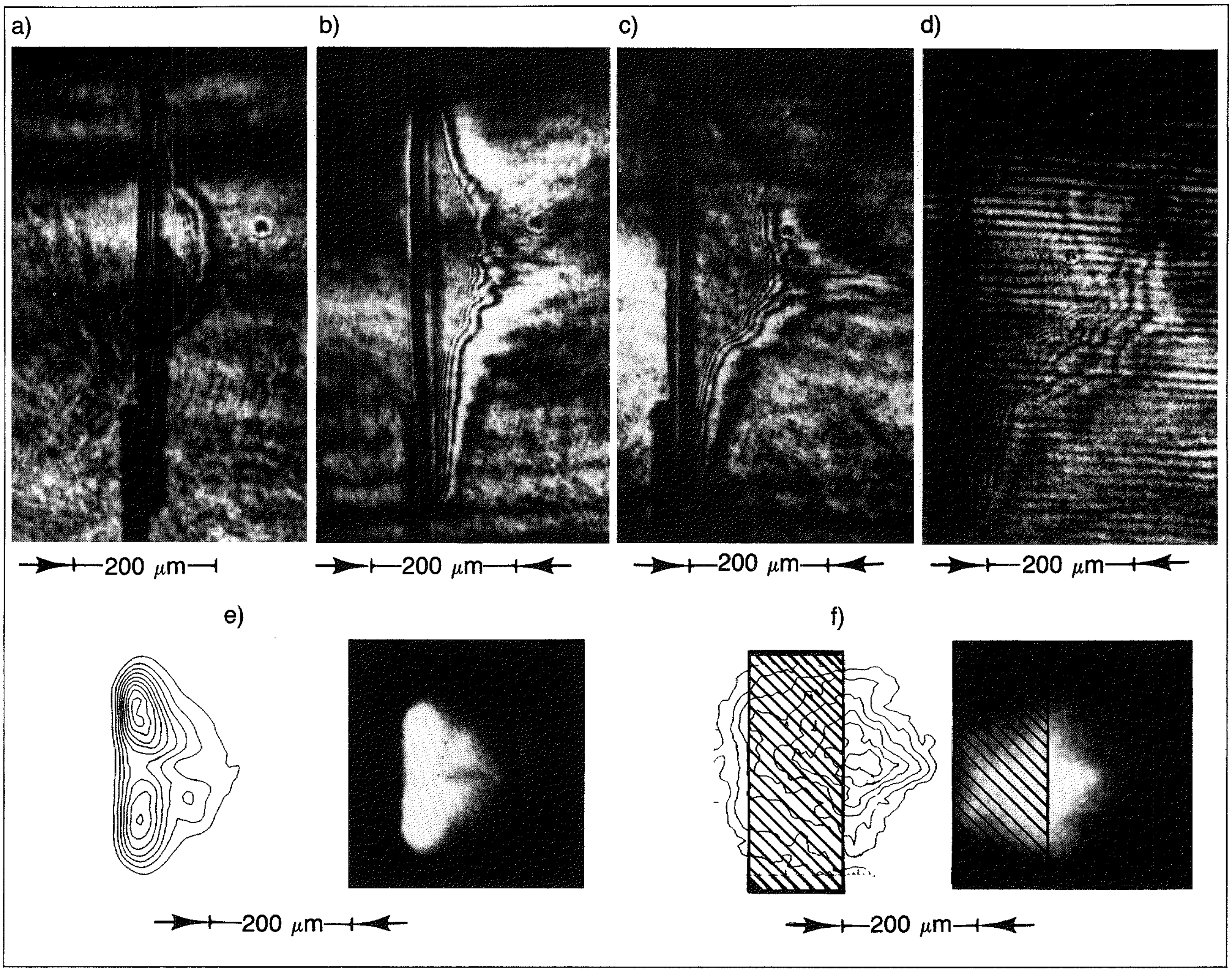

Fig. 3-13. The plasma jet features for a convergent focus appear in the interferograms (a-d), pinhole image (e) and KB image (f). The data are from shot 8833.

to the low temperature, and the surrounding hot corona is cylindrical and optically thin to its own radiation. Using an average opacity of cold gold of 2000 cm^2/g, we obtain a lower bound of the average mass density of about 0.02 g/cm^3 50 μm from the target surface and 0.09 g/cm^3 100 μm from the target surface. This is 1/1000 to 5/1000 of the solid mass density and corresponds to a number density of gold atoms of 3×10^{20} cm^{-3}.

Finer-scale jets are observed with the target placed on the divergent side of best focus. Interferograms for a three-picket pulse are shown in Fig. 3-14. In Figs. 3-14a and b, 20 to 30 μm jets issue from the target with a velocity of 5×10^7 cm/s and density $5 \times 10^{20}/cm^3$. These jets move at an oblique angle away from the laser spot. When the second and third pickets arrive, the jets smooth out. X-ray pictures for two-picket laser pulses show jets corresponding to the features observed in the interferograms. As for the convergent focus, the jets emit more in the softer x-ray region and thus are cooler. Jets were observed

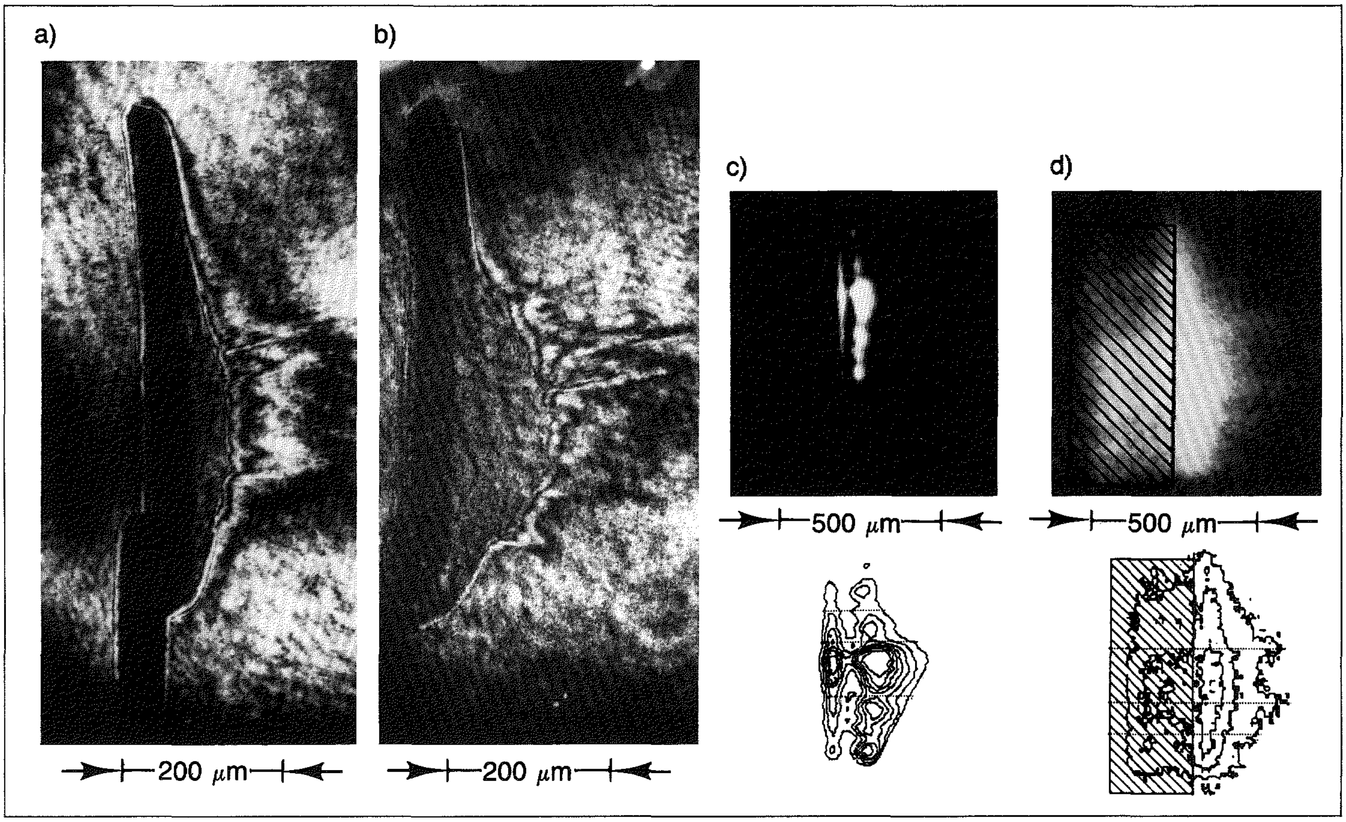

Fig. 3-14. The plasma jet features for a divergent focus appear in the interferograms (a,b) pinhole image (c) and KB image (d). Images (a) and (b) are from shot 8869, (c) and (d) are from shot 8886.

by the x-ray cameras only when two-picket pulses were used. When the third picket was present, the x-ray signal from the jets, measured by the KB microscope and pinhole cameras, was dominated by the signal from the corona. Since these jets were thinner and perhaps more tenuous, they could thermalize faster when the main picket arrived and would tend to absorb less in the M band and emit less in the sub-kilovolt x-ray band.

The plasma jets were observed only for shots with the picket-fence pulses. For square-pulse shots with convergent focus, the fringes from the interferograms showed a smooth distribution—not the spikiness observed for the picket pulses. X-ray pictures showed features corresponding to the hot ring, but these did not extend out from the target as for the picket pulse. This can be interpreted in the same way as the smoothing of the jets observed for picket pulses. Near the ablation surface, material may jet out. Since the laser is on continuously, energy is deposited into the jet from the laser and through radiation and thermal conduction, smoothing the jet.

Low-*Z* targets—CH, aluminum, and titanium—also were shot. Jets were observed to varying degrees in each of these elements; they decreased in spikiness and extent as *Z* was decreased. Since thermal transport is more efficient in low-*Z* targets and the radiative emissions are much less, jets that are formed are expected to thermalize earlier than those for high-*Z* targets. Pinhole pictures of the front surface of the target show a more homogeneous emission pattern, also evidence of increased smoothing.

Summary. The dynamic behavior of laser-irradiated gold targets shows expected characteristics in gross plasma dynamics and unexpected characteristics in certain details. Absorption of the laser energy and the related coronal electron temperature are in good agreement with previous experimental results and preliminary code calculations. Density profiles and $n_c/4$ and n_c trajectories show expected qualitative behavior for square and t^2 pulse shots. One unexpected aspect of the n_c trajectories occurs for picket fence pulses—namely, the n_c surface appears close to the target and remains stationary during the third picket. Another unexpected aspect of target behavior, due to the laser nonuniformity, is the issuance of cold dense material from cold spots for picket fence pulses. If the effect of this plasma is deleterious to target performance, then one may conclude that continuous (in time) pulses should be used or very smooth laser illumination must be attained.

For additional information, please contact Dr. E. F. Gabl

3.1.2 Refractive Induced Distortion of Harmonic Light Images

The characterization of the electron density profile of an evolving plasma produced when an intense laser beam impinges on the surface of a solid material is of fundamental interest in inertial confinement fusion (ICF). The complexity of the physical phenomena taking place in laser-produced plasmas obviates any straightforward means of making direct measurements of such plasma parameters as density, temperature, or expansion velocity. For this reason, spatial and spectral analysis of laser light scattered by the plasma remains a useful technique for investigating high-intensity laser/plasma interactions.

Due to the high electron densities encountered in studying high-density plasmas, the optical emissions technique suffers from refraction (ray bending) of the light to be collected. This fact has several consequences. In experiments where the light is simply collected by a spatially integrating detector, some of the emitted light may never reach the detector. In experiments where the goal is to form an image of the light-emitting region in the plasma, refraction can distort the image to the point where little or no useful information can be inferred.

In the past, much has been learned about the critical and quarter-critical density surfaces by studying the second (2ω) and three-halves ($3/2\ \omega$) harmonics of the laser light emerging from the plasma. Much of the past success was made possible by the fact that smaller lasers produced plasmas of small spatial extent. Because refractive bending of light rays is a path-integrated effect, the shorter the path (the smaller the dimensions of the plasma), the smaller the effect. However, given the capabilities of present-day laser technology and the relevance of large irradiation spots to ICF, the dimensions of plasmas of interest can exceed several thousand laser wavelengths. Under such conditions, it is necessary to reevaluate the effects of refraction when making optical measurements.

Description of Experiment. Our experiment took advantage of the existing 0.26 μm holographic probe beam. This beam, orthogonally incident with respect to the 0.53 μm main beam, was used to backlight an array of pinholes in a gold substrate (two rows, separated by 200 μm; five pinholes per row, separated by 100 μm) mounted outside the vacuum chamber. An *f*/10 optic relayed the image of the backlit pinhole array to the target volume with a 1:1 magnification. The target consisted of a 600 μm diameter, 22 μm thick gold disk oriented face-on to the main 0.53 μm beam and edge-on to the 0.26 μm probe beam. The image of the array was positioned such that the two rows of pinholes were aligned along the target normal, with the first pinhole in each row behind the target and the remaining eight pinholes on the front (interaction) side. The image formed in the plasma volume was then relayed with an *f*/2 catadioptric reflector system to a film-back positioned behind filters, which gave a satisfactory signal-to-noise ratio. It is worth noting that this low *f*/number system allowed even those rays that underwent significant ray bending to be collected, and therefore to some extent facilitated our investigation of refraction without allowing its effects to limit our success.

For each of four laser shots, the 0.53 μm main (150 J, 2 ns) beam was allowed to fall on the target at $t = 0$ ns. The 30 ps probe pulse reached the target volume at a time determined by a variable optical delay path ($t = 0$ to 1200 ps). Prior to each shot, an image of the target was superimposed on the target plane image of the pinhole array at the film-back. This provided a "no plasma" record of the relative positioning of the target and the array for later comparison with the image obtained when the plasma was present. The film-back was then translated several centimeters to the side in preparation for imaging during the shot when the plasma was present.

For the four shots taken, we investigated both low-and high-refraction cases by varying the 0.53 μm laser focal spot size and the time of arrival of the probe pulse. Small spot sizes and early probe pulses can be expected to induce little refractive image distortion. For large spot sizes and late probe pulse times, the probe witnesses a more highly developed, planar plasma and can be expected to undergo significant refraction. The four shots taken had the following parameters:

Shot No.	Spot Size	Probe Delay
8918	200 μm	600 ps
8919	200 μm	200 ps
8920	200 μm	600 ps
8921	400 μm	1200 ps

Results. As stated above, the data for a given shot consist of a "preshot" vacuum image of the pinhole array superimposed on the backlit image of the target and a "shot" image of the pinhole array recorded during a 30 ps time window of the 0.53 μm pulse at a time determined by the time of arrival of the probe. The preshot image is primarily intended as a final check on the positioning of the target with respect to the array.

To aid in the discussion of our observations, we present in Fig. 3-15 a labeling of the pinholes in the array, p1 through p10, where p1 and p2 lie behind the target, p3 through p10 lie in front of the target, and the even p's correspond to pinholes along the laser-axial row.

In Fig. 3-16 we present data from two shots as logarithmic contours of film density. One immediately notices the fact that, on the preshots, different pinholes have different intensities. This is due to imperfect centering of the backlighting beam on the back side of the array and is a normalizable effect. Also, even though an image of the target was taken for each of the preshots, its presence is obvious only in shot 8919 due to insufficient contrast. Shown particularly well in preshot 8919 is the positioning of the target with respect to the array where p1 and p2 lie about 10 to 30 μm behind the target, p3 and p4 are within 10 to 30 μm of the front side, and p5 through p10 are situated at different points in the blowoff region out to about 300 μm (the

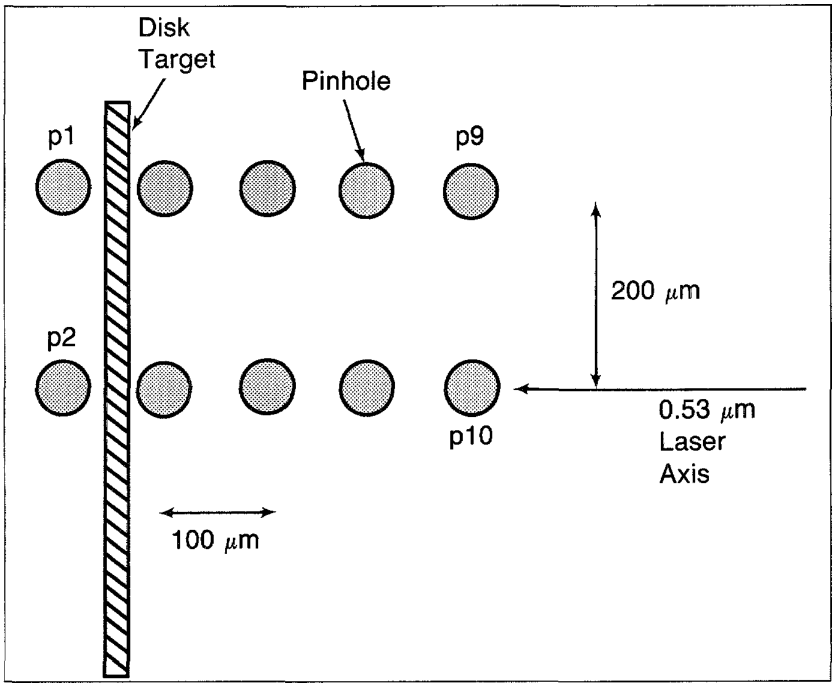

Fig. 3-15. Arrays of two rows (separated by 200 μm), each containing five pinholes (separated by 100 μm), on gold substrates were used for harmonic distortion measurements. The even-numbered pinholes, at the bottom in the figure, correspond to pinholes along the laser-axial row. Pinholes 1 and 2 lie behind the target, pinholes 3 through 10 lie in front of the target. The arrays were imaged onto a plane perpendicular to the target planes.

apparent thickness of the target, about 50 μm, is larger than the actual thickness, 22 μm, because of imperfect target rotation and target curvature). The exact details of the positioning vary from shot to shot, as seen in Fig. 3-16.

As expected, for small irradiation spots and early probe pulse times (for example, shot 8919, 200 μm, 200 ps, Fig. 3-16), distortion of the resulting image of the pinhole array is undetectable. The most noticeable difference between the shot and preshot images is the apparent reduction in intensity and size in the point (pinhole) sources. This effect is greater for the axial pinhole row (the lower of the two rows in Fig. 3-16a). However, the fact that this attenuation is seen both in front and in back of the target and does not significantly change for the pinholes farthest from the target surface leads us to believe that this is nei-

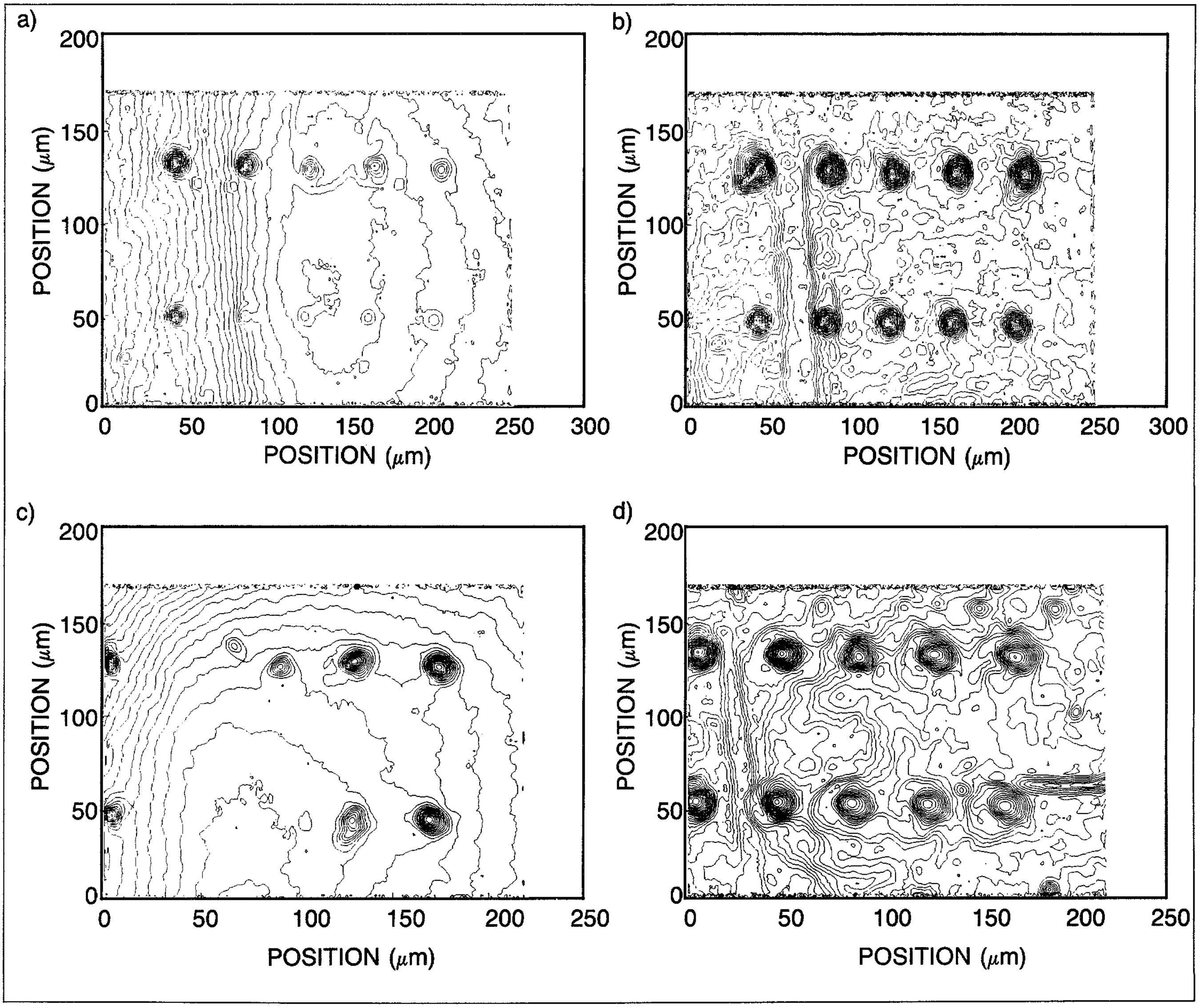

Fig. 3-16. Logarithmic contours of film density are shown for two shots: (a) and (b) for shot 8919, (c) and (d) for shot 8921. Contours (b) and (d) are exposures taken before laser irradiation of the disk target, while (a) and (c) are taken as the plasma expands. Distortion of the pinhole images in (d) is indicative of refractive effects.

ther a refractive nor absorptive effect. Similar results were seen for shot 8920 (no shot data were obtained for shot 8918).

For a large spot size and late probe pulse time (shot 8921, 400 μm, 1200 ps, Fig. 3-16), refractive distortion of the image is readily apparent. For shot 8921, one sees that p4 is absent, and that p3 and p6 have apparent positions about 45 and 15 μm down the density gradient from their preshot positions. Also, p7 and p8 show significant distortions relative to their preshot fiducials. This shows that, as expected, refractive induced image distortion is worse along the laser focal axis (even p's, where the density is higher and the ray optical path is longest) than on the wings of the irradiation spot (odd p's). In particular, for perfect alignment of the array (even p's exactly on axis and odd p's on the wing), the apparent displacements of the pinhole images should be along $+\hat{z}$ for axial positions and along both $\hat{r}$ and $\hat{z}$ for wing positions. This signature is indeed seen in shot 8921 for pinholes p3 and p6.

Raytrace calculations in two dimensions were performed in an attempt to corroborate these experimental observations. The density profile was assumed to be cylindrically symmetric with a solid density in the $z = 0$ plane which decayed along z (exponentially) and r (Gaussian with the $1/e$ points falling at the nominal diameter of the laser focal spot) and all rays were confined to the plane passing through the z-axis. The axial scale length was chosen to give a 0.53 μm critical surface position in space and time that agreed with LASNEX modeling. Because this calculation does not take into account profile steepening above quarter-critical, it to some extent provides a lower bound on the ray refraction angles (which would presumably be larger in a real disk plasma due to the sustained density for positions farther from the target than the quarter-critical surface). This combined modeling predicts critical surfaces for 0.26 μm light at about 10 μm at 200 ps and at about 25 μm at 1200 ps, with axial scale lengths of 6 μm and 14 μm, respectively.

A crude estimate of the effects of refraction can be made by assuming that image degradation occurs when a ray, normally incident on the plasma with respect to the laser axis, is refracted out of the acceptance cone of the $f/2$ collection optic (for $\theta > 14°$). Rays refracted out of this acceptance cone are unable to contribute to the recorded image. Parameters for three shots and their resulting calculated scatter angles (for a ray initially incident along $-\hat{r}$ at $z = 50$ μm) were as follows:

Shot No.	Spot Size	Probe Delay	Scatter Angle
8919	200 μm	200 ps	1°
8920	200 μm	600 ps	10°
8921	400 μm	1200 ps	16°

These scatter angles, which obviously become more severe for rays initially closer to the plane of the target surface, are in qualitative agreement with the data based on the simple image distortion criteria above: The image from shot 8919 is free of displacements or distortions, while the image for shot 8921 quite clearly shows both. Although the image for shot 8920 is an intermediate case, no detectable refractive distortions were evident.

Of more specific interest is how refraction will affect 2ω and $3/2\ \omega$ emissions. The densities at which these emissions are born, expressed as fractions of their respective critical densities, are quarter-critical for 2ω and ninth-critical for $3/2\ \omega$. Some idea of the severity of refractive distortion of the source images for these emissions can be gained by comparing the quality of the pinhole images at points along the profile that correspond to the same fractions of critical density for the 0.26 μm probe light. Based on the simple exponential fit, quarter- and ninth-critical occur at $z = 45\ \mu$m and $z = 55\ \mu$m, well within the region where refractive effects are observed. Clearly, within the accuracy of this comparison, image distortion of 2ω and $3/2\ \omega$ emission sources may be severe.

We again note that, owing to profile steepening between the critical and quarter-critical density surfaces, the results above probably underestimate refractive effects because the assumed exponential profile falls more rapidly with z than we can reasonably expect. While we can expect the situation to be worse for even larger spot sizes than in shot 8921, in practice we image sources that do not depend on light having to propagate into as well as out of the plasma (since the source is embedded in the plasma). Thus, in this respect, these results tend to overestimate distortions.

Summary. A simple experiment was performed in an attempt to assess the extent to which refractive image distortion can be predicted and understood in situations where harmonic emissions can provide information useful in the characterization of laser-produced plasma density profiles. The data, in the form of 0.26 μm light images of a well defined spatial structure (pinhole array), exhibit the expected qualitative features in the limits of large and small plasma dimensions. Future work will aim to check parameters with 0.35 μm irradiation and to investigate the possibility of making use of refractive distortions as a density profile diagnostic.

For additional information, please contact Dr. C. Darrow (LLNL) or Dr. E. F. Gabl (KMSF)

3.1.3 Backlighter Analysis

X radiography provides information about high-density, high-opacity plasmas that can be obtained no other way. For this reason, experimental work has been performed to develop and implement x radiographic measurement techniques. In an earlier article, an experimental series devoted to point-source flash backlighter development was described;[8] in this article further analysis of data from that series is presented in addition to recent advances.

The previous series investigated the feasibility of a point x-ray backlighter source. Prior to the series, backlighter measurements at KMSF had been done with extended sources. A comparison of the two techniques is shown in Fig. 3-17. Advantages of the point source include simplicity of alignment and accessibility to higher x-ray probe energies (since the laser can be focused to higher intensities); disadvantages include degraded signal-to-noise ratio and poorer spatial resolution at high magnification. A point source can be made two ways—the x-ray emitting region can be limited either by the size of the target or by the size of the laser focal spot. This series used target-limited sources, while a future one will investigate laser-spot-limited ones.

Experiment. The experiment was performed using the Chroma laser, operated with green light (0.53 μm wavelength). During the series, data were obtained for two different pulse lengths—35 and 110 ps. At the 35 ps pulse length, an $f/1.4$ optic was used to form a spot size at best focus of 30 μm, which produced a peak intensity of 3×10^{16} W/cm^2. At the 110 ps pulse length, using an $f/3.5$ optic, a spot size of 40 μm gave a peak intensity of about 10^{16} W/cm^2. Equivalent-plane images of the spot at best focus indicated that the spot size was dominated by the laser divergence. For all shots the laser was operated at best focus.

A number of different target types and materials were evaluated. Because the laser spot size was not sufficiently small, the x-ray source had to be delimited by the size of the target. To obtain a small source, wires, coated fibers, and particles (mounted on carbon fibers) were used. Two examples of particle targets are shown in Fig. 3-18. For targets made of wires and fibers, although a section whose length was determined by the laser spot size was illuminated, the effective x-ray source size

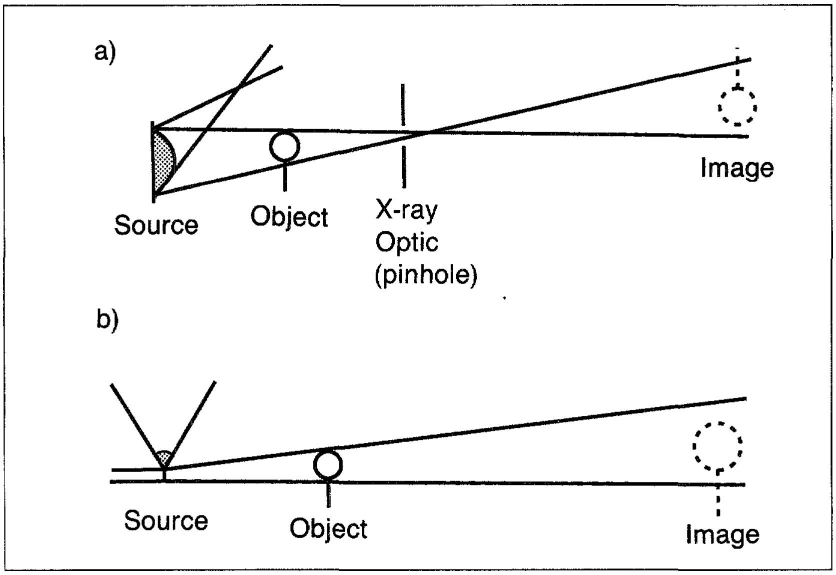

Fig. 3-17. Two techniques are used for producing x-ray backlighter sources. One technique yields a point source (a), while the other yields an extended or broad source (b). Broad-source backlighting requires an x-ray imaging optic.

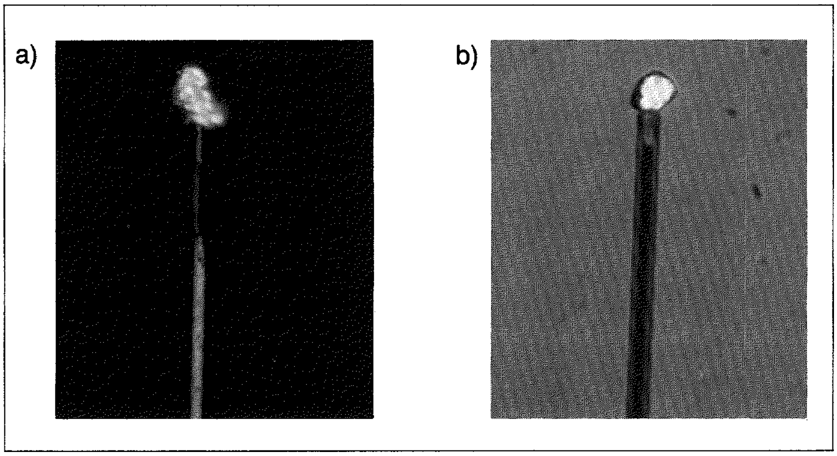

Fig. 3-18. Backlighter targets are formed from specific materials mounted on carbon fibers. A bismuth nugget (a) and a titanuim nugget (b) are shown here.

was reduced since it was viewed end-on; that is, looking down the axis of the fiber. Gold wires were irradiated, as were CsI-, gold-, and silver-coated carbon and glass fibers. In general, the carbon fibers were straighter than the glass ones. Appropriately sized particles were found in commercially available titanium and bismuth powders and mounted on carbon fibers with low-*Z* epoxy. Flakes of silver paint were also selected and mounted in the same way. Disks of titanuim, yttrium, and silver were shot for comparison to previous experimental work.

A variety of diagnostic instruments were used to determine the emission characteristics of the x-ray source. A Fresnel zone plate was used as a resolution grid to determine the effective size of the source, with images recorded on x-ray film. An x-ray streak camera measured the duration of the x-ray flash, while PIN diodes measured the x-ray yield. X-ray spectra were obtained with a time-integrating PET Bragg crystal spectrograph. The incident laser pulse length was measured with an optical streak camera and the energy on target with an optical calorimeter.

Results. X-ray source parameters were found to depend on laser pulse duration and target type. In the discussion that follows, the laser intensity on target was nominally $1.5 \pm 0.5 \times 10^{16}$ W/cm^2. We focused on determining the x-ray flash duration, apparent source size, conversion efficiency, and source reproducibility. In all cases the x-ray emission of interest lies in the band between 2 to 4 keV. For gold and bismuth targets, this corresponds to the M-band, while for silver and CsI it corresponds to L-band emission.

The duration of the x-ray flash was found to vary linearly with the laser pulse length. This dependence for a number of shots is shown in Fig. 3-19. The data indicate that the x-ray flash duration should continue to decrease as the laser pulse length is decreased below 35 ps.

The x-ray source size does not decrease linearly with target size, however. Shown in Fig. 3-20 are the data points and both a

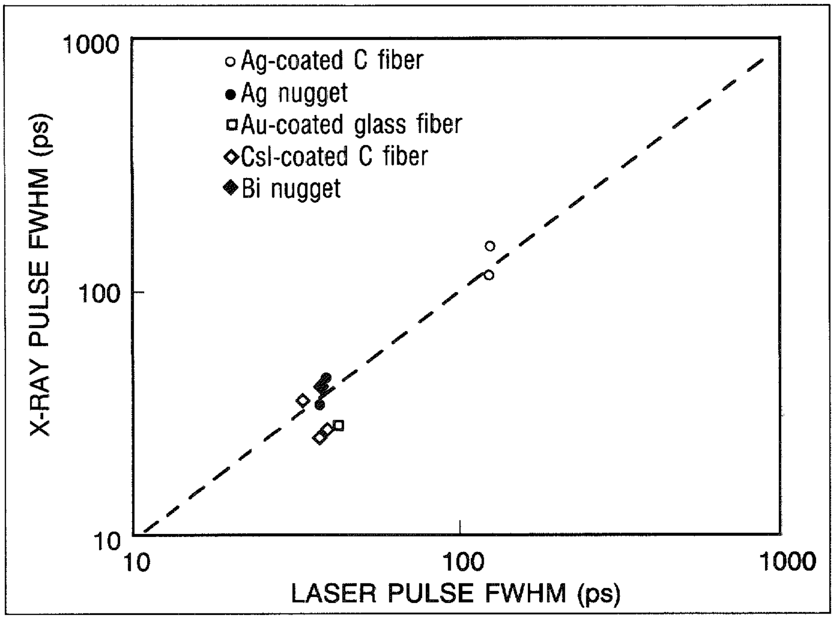

Fig. 3-19. The duration of the x-ray pulse varies linearly with the duration of the laser pulse.

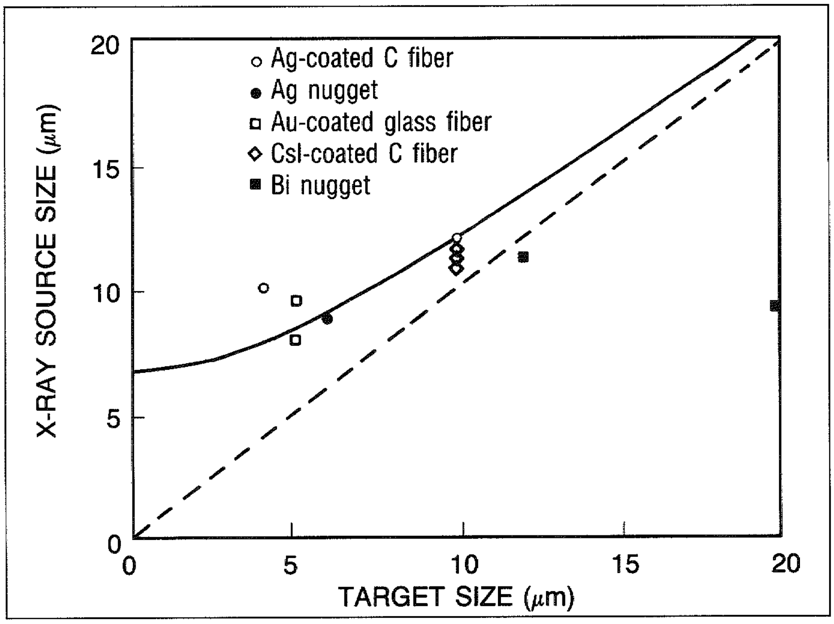

Fig. 3-20. The x-ray source size decreases linearly with target size down to about 10 μm. The smallest source size obtained was 7 μm for a 5 μm target. A quadrature fit to the data is also shown.

linear (dashed) and a quadrature (solid) relationship. Quadrature relationship was found by solving for the parameter Δ in

$$\text{x-ray source size} = \sqrt{\Delta^2 + (\text{target size})^2} \ .$$

The fit indicated a Δ of 6.7 μm, which would correspond physically to the finite plasma size necessary for good laser light absorption to occur. The bismuth nugget points were not included in the fit because they had irregular surface features. These data indicate that the x-ray source size cannot be decreased indefinitely, and that there is a minimum size.

We found x-ray conversion efficiency to depend on target type and laser pulse duration. The data for silver/palladium disks and fibers are shown in Fig. 3-21. For both types of targets, efficiency drops with laser pulse length, indicating that some minimum amount of laser energy is required to produce the optimum plasma conditions for x-ray production. Also, the larger targets exhibit a much higher conversion efficiency, which may be due to the fact that the plasma expansion is different in the two cases.

With respect to source reproducibility, we found that reproducibility dropped with increasing target area. This is shown in Fig. 3-22. This effect could be the result of two causes. First, the plasma coming from the target could be passing through high- and low-intensity regions of the laser beam. Second, alignment is more difficult for the smaller targets, and uncertainties in this area could play a role as well.

Conclusion. Results of this experimental series indicate that point x-ray backlighter sources can be produced. In the next series we will investigate laser-spot-limited backlighter sources. To do this we will implement an *f*/1 optic that should produce focal spots of about 10 μm diameter. Thus we will be operating at a higher laser intensity (approaching 10^{17} W/cm^2). Using a laser-spot-limited source, as opposed to a target-limited one, we hope to increase the x-ray conversion efficiency and improve the reproducibility.

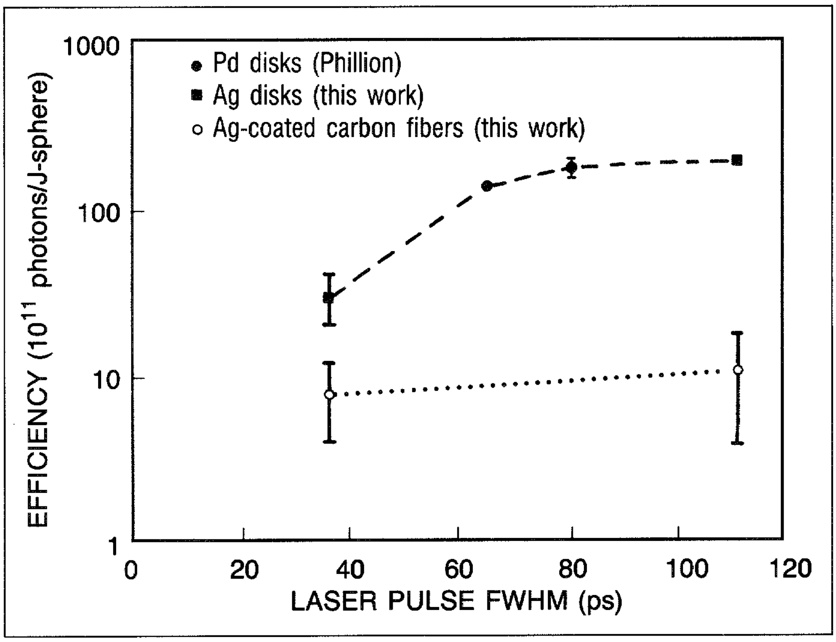

Fig. 3-21. X-ray efficiency decreases with laser pulse duration. Disk targets with larger masses probably create a plasma with density and temperature distributions more favorable for efficient x-ray production. (● from D. W. Phillion and C. J. Hailey, *Phys. Rev. A* 34 (1986), p. 4886.)

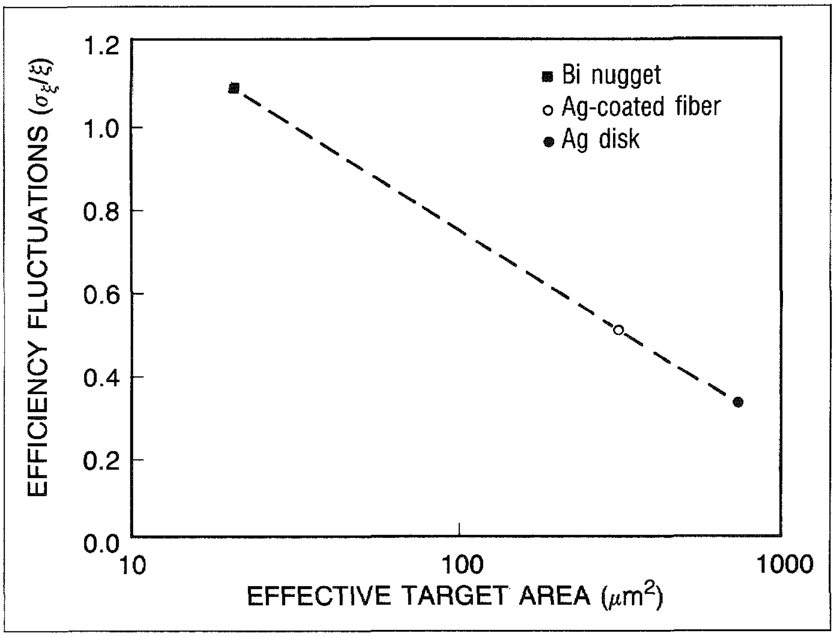

Fig. 3-22. The fluctuations of target efficiency decrease with target area.

For additional information, please contact Dr. B. H. Failor

3.1.4 Time- and Space-Resolved Dot Spectroscopic Characterization of Laser-Produced Plasmas

The determination of electron densities and temperatures of hot, dense plasmas using spectral line ratios can differ by large factors depending upon the assumptions used in the atomic physics model employed in interpreting the line ratio measurements.[9] Moreover, transient and nonuniform plasma distributions may contribute to ambiguous interpretations of available data. Using dot target irradiation techniques[10] in conjunction with new time- and space-resolved diagnostics, we have reported[11] previously on temperatures and densities determined by standard line intensity ratio techniques and compared them to independent temperature and density measuring methods, thus allowing us to make clear tests of theoretical atomic models upon which the line ratio methods are based.[12]

In this report we present an update of our analysis and interpretation of the K-shell line ratio data and apply it to developing diagnostic techniques of L-shell spectra.

The Laser/Target Experiments. The Chroma laser facility at KMSF was used to irradiate dot targets of aluminum and magnesium and high-*Z* (bromine, molybdenum, and silver) dots doped with K-shell emitters. They were irradiated with 10 to 100 J of 0.53 μm light in a 1 ns pulse. An *f*/2.5 lens was used to focus the laser beam on the target to a diameter of 250 μm, resulting in irradiances of 10^{13} to 10^{14} W/cm^2.

Simultaneously time- and space-resolved K-shell and L-shell spectra were measured and compared to dynamic model predictions. The electron temperatures were determined from the slope of the hydrogen-like free/bound continuum and the electron densities were measured using holographic interferometry. Temporal and spatial gradients were resolved simultaneously using three diagnostics: a framing crystal x-ray spectrometer (FCXS)[13,14], an x-ray streaked crystal spectrometer (XSCS) with a spatial imaging slit, and the four-frame holographic interferometer.

Using both the FCXS and XSCS instruments, the plasma electron temperatures were mapped out in space and time from the slope of the hydrogen-like ion continuum[15] and from spectral line ratios. An example of the hydrogen-like free/bound-continuum temperature measurements of a 100 μm diameter aluminum dot target at 1×10^{14} W/cm^2, with a 1 ns stacked laser pulse, using FCXS data, is shown in Fig. 3-23. The line ratios (of aluminum and magnesium) included the helium-like $1s^2(^1S)$-$1s3p(^1P)$ to hydrogen-like 1s-3p line ratio and also the hydrogen-like 1s-2p to helium-like $1s2p(^1P)$-$2p^2(1D)$ dielectronic satellite line ratio. Using a steady state (CRE) atomic modeling code RATION/RATSHOW/SPECTRE[16] (RRS), assuming an optically thin plasma, yielded dramatic differences in the temperature profiles, both in amplitude and shape, between the continuum slope and line ratio measurements. These comparisons have been presented in previous papers in a preliminary analysis of the data.[14,17] The influence of opacity data as they affect the line ratio code results, and their comparison to the free/bound-continuum measurements, will be presented in a later paper.

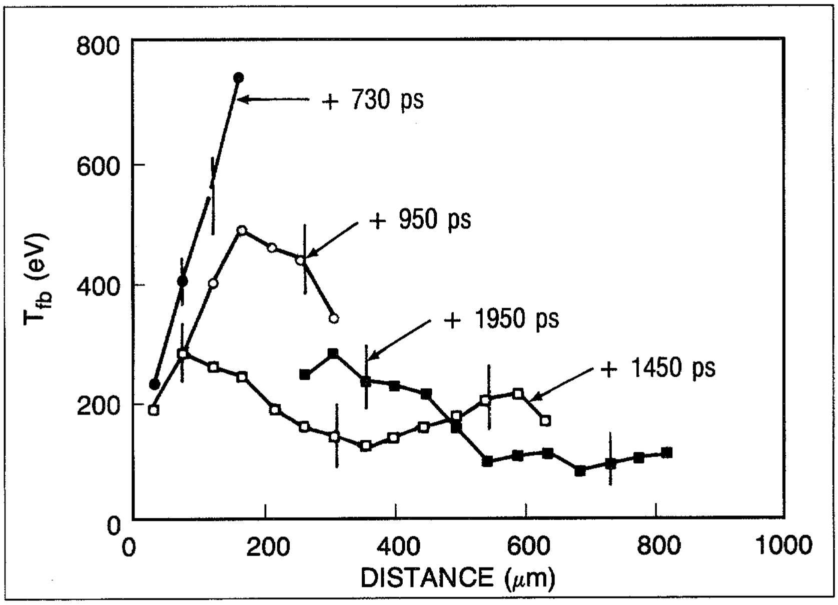

Lawrence Livermore National Laboratory

Fig. 3-23. **Hydrogen-like free/bound continuum temperature measurements from FCXS data show the temperature evolution of the plasma in space and time. The aluminum dot target with a diameter of 100 μm was irradiated with 1×10^{14} W/cm^2 of 0.53 μm laser light in a 1 ns stacked pulse. Each framing interval was 250 ps and the effective plasma column width was assumed to be 50 μm.**

Electron density profiles measured using holographic interferometry were compared to densities determined spectroscopically. The spectroscopic density measurements were obtained via the helium-like $1s^2(^1S)$-$1s3p(^1P)$ to the $1s^2(^1S)$-$1s2p(^3P)$ intercombination (IC) line ratio,[18] again using the (RRS) model. In Fig. 3-24, for a 100 μm aluminum dot target at 1×10^{14} W/cm^2, with a laser pulse of 1 ns, we compare density profiles obtained four ways: (1) via holographic interferometry; (2) via the LASNEX hydrodynamics code; and by applying the RRS code in (3) optically thin and (4) optically thick mode to the aluminum He$_\alpha$/IC line ratio.

The profile obtained using the LASNEX code agrees exceptionally well with the interferometrically determined profile at 1457 ps, and reasonably well with the profile at 1657 ps. However, for the He$_\alpha$/IC ratio measurement using the RRS code, the optically thin case disagrees dramatically with the interferometric measurement. Only when the RRS code is used in the optically thick mode and the effective diameter of the plasma plume is assumed to be 50 μm does the He$_\alpha$/IC line ratio agree with the interferometric profile.

L-Shell Spectroscopy. In the interest of developing diagnostic techniques of L-shell spectra, we have investigated the use of K-shell diagnostics for determining plasma conditions in which L-shell lines occur simultaneously with K-shell lines. We have therefore developed targets containing elements which, under appropriate irradiation conditions, simultaneously produce K-shell spectra of one of the elements and L-shell spectra of the

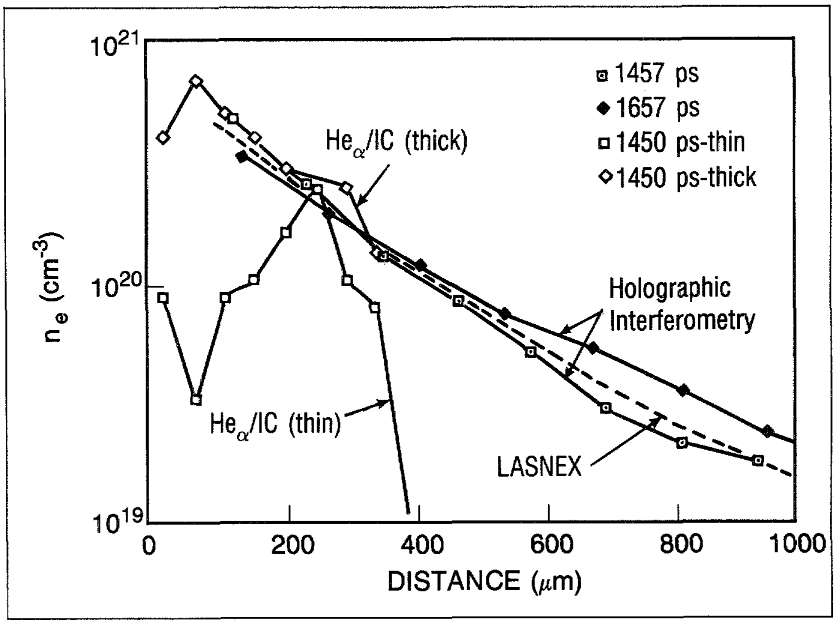

Lawrence Livermore National Laboratory

Fig. 3-24. Good agreement was found between the electron density profiles obtained via holographic interferometry, the LASNEX hydrodynamic code, and by applying the RATION/RATSHOW/SPECTRE code to optically thick aluminum He$_\alpha$/IC line ratios. Modeling of an optically thin plasma shows exceptional disagreement with the experiment, however.

other element. The element pairs we have used include magnesium with bromine, magnesium with molybdenum, and sodium with silver. Comparisons are made of electron densities derived from holographic interferometry with density-sensitive line ratio measurements of K-shell and L-shell lines as predicted by one or more atomic model codes.

A variety of L-shell diagnostic models and techniques for the element pairs tested are being examined and compared to K-shell measurements and will be reported in later publications. We report here on the comparison of experimentally measured density-sensitive L-shell transitions of bromine, as represented by an atomic model, with measurements obtained interferometrically. The density-sensitive intensity pattern of the neon-like bromine lines that dominate these spectra is due to the existence of higher-lying metastable levels. These metastable levels are also responsible for the population inversion that leads to lasing in neon-like ions. At low densities these states decay by radiative cascades contributing largely to the intensities of the two lowest-energy (3s-2p) bromine transitions. But as the electron density is increased, transitions due to electron collisions dominate the decay of these excited levels and a smaller fraction end up contributing to the intensity of the 3s-2p transitions. A simplified atomic model of the neon-like bromine ion, which includes the lowest 37 states but ignores other charge states, reproduces this behavior qualitatively. The atomic model predictions can be checked experimentally via line ratio measurements. Previous time-integrated measurements were in good agreement with the model.[19] However, as illustrated in Fig. 3-25, the quantitative comparison of the electron density profile predicted by the model using the density-sensitive (3s-2p)/(3d-2p) and (3s-2p)/

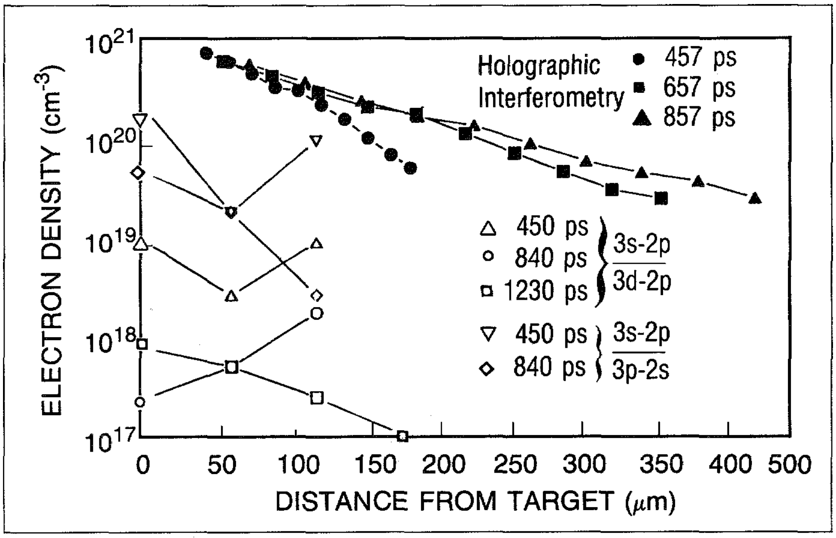

Fig. 3-25. Model electron densities obtained from experimental line ratios of neon-like bromine resonance lines are compared with the time- and space-resolved densities determined from holographic interferometry. The model considers radiative and electron collision processes among the lowest 37 states of neon-like bromine.

Lawrence Livermore National Laboratory

(3p-2s) line ratios, with the time- and space-resolved holographic interferometric measurements, reveals the shortcomings of the atomic model.

It has been noted[20] that the simple model discussed above not only ignores other than the 37 charge states but also leaves out contributions to the excited state populations from dielectronic recombination and inner-shell ionization. These processes can lead to significantly different line intensities for the neon-like resonance lines being modeled. A calculation incorporating these processes has been used to fit the resonance lines in our data.[21] The resultant model electron density is compared with the interferometrically measured profile in Fig. 3-26. The results for the earliest time frame are somewhat in agreement with the interferometric data; however, the trend with time does not match the experiment and further work is needed on the model.

The bromine dot/CH plasma has also been simulated using the LASNEX code. A comparison of the electron density calculated on the basis of initial laser irradiance with the electron density measured via holographic interferometry is shown in Fig. 3-27 as a function of space and time. As in the K-shell (only) experimental measurements, the measured profiles are mimicked by the LASNEX simulations reasonably well, even though, in general, the simulations are slightly steeper than the measured profiles. The LASNEX simulation was also used as input to XRASER to give a detailed picture of the x-ray emission spectra. A comparison of the calculated and measured spectra is shown in Fig. 3-28. Contributions to the spectrum from magnesium ions are not included in the calculation. The calculation does confirm the dominance of the emission of neon- and sodium-like bromine ions. Again some important details are not

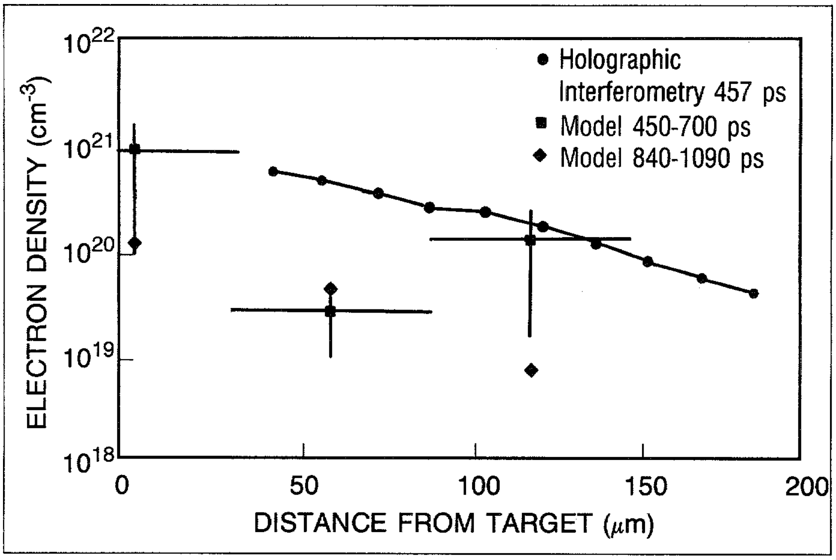

Lawrence Livermore National Laboratory

Fig. 3-26. Model electron densities from line ratios, considering ionization and recombination on neighboring charge states in addition to the radiative and collisional rates of the simple model, are compared with the electron densities determined from interferometric measurements.

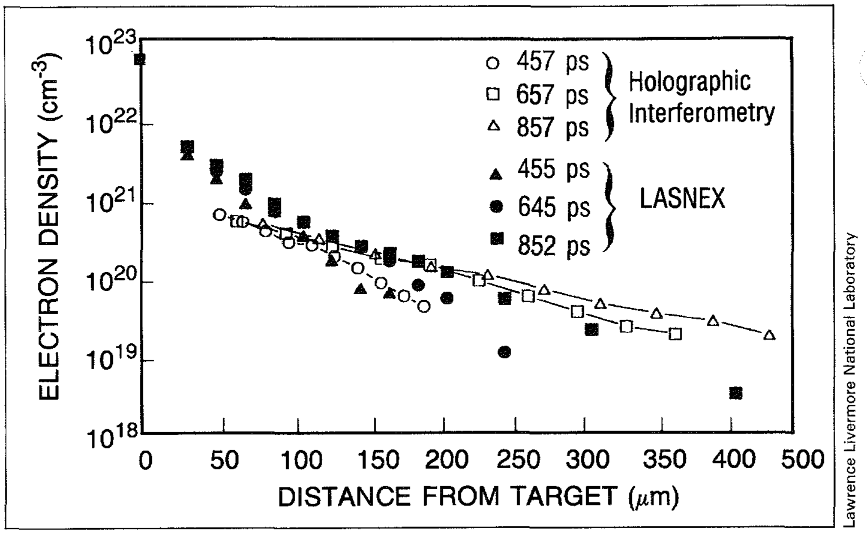

Fig. 3-27. Electron densities derived from LASNEX simulations of a laser shot on a bromine-containing target compare well with those from interferometric measurements. The agreement between simulation and measurement at the high densities is poorer for a variety of reasons.

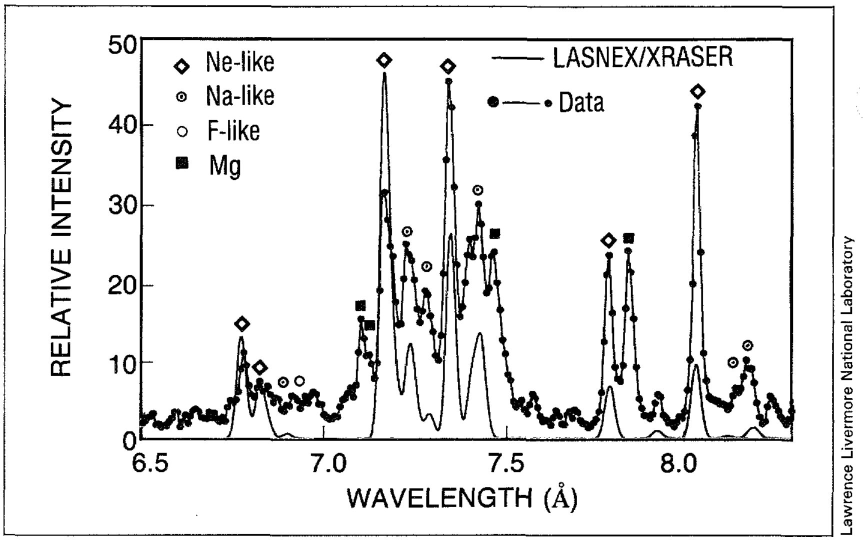

Fig. 3-28. Time- and space-resolved x-ray line intensities observed experimentally are compared with a LASNEX/XRASER simulated spectrum for a time window from 850 to 1090 ps into the pulse and a spatial extent of 59 to 118 μm off the target surface.

evident in the calculation, which is in a preliminary stage. The experimental spectrum shows evidence of a small fluorine-like component. In addition the relative intensities of the neon-like resonance lines are not reproduced. Such discrepancies are probably due to errors in the ionization balance predicted by LASNEX.

Summary. Space- and time-resolved K-shell spectra have been recorded simultaneously for the first time from laser-irradiated dot targets. Spectral line ratio techniques for determining electron temperature and density compared to non-line ratio techniques have been found to exhibit large differences. These differences are mitigated, in part, by including opacity in the simulation codes, which assume steady-state conditions. Newer nonstationary atomic model simulation codes that include recombination and ionization are currently being developed and will be applied to our measurements.

L-shell comparisons of the time- and space-resolved data with atomic and hydrodynamic simulation, though preliminary, is promising. Systematic discrepancies between the data and the simulations suggest improvements in the atomic data or calculational procedures used to model the plasma and further our understanding of the important atomic processes in these plasmas.

For additional information, please contact Dr. G. Charatis

SECTION 3.2

Development of Diagnostic Instruments

3.2.1 Development of X-ray Diagnostic Instruments and Calibration Facility

KMS Fusion has built an array of x-ray diagnostic instruments including a microchannel-plate (MCP) based framing camera, a soft x-ray diode array, and a crystal spectrograph. These instruments have been used in a number of laser/target interaction studies, expanding our diagnostic capabilities. In addition, we have completed various crystal calibrations for both our own use and for other ICF program participants such as Los Alamos National Laboratory (LANL). These calibration were done on our x-ray calibration facility (XCALIBR I).

X-ray Framing Camera and Spectrograph. The x-ray framing camera is a strip-line gated intensifier incorporating a custom-designed MCP built into a microwave circuit for fast pulsing. It is mounted above a phosphor-coated fiberoptic faceplate. A high-voltage source provides a pulse of 1 kV with a 150 ps effective full width at half maximum (FWHM) into each strip line. Each strip is gated successively with the proper delay lines, providing a series of frames on the film that reveal the time history of the x-ray signal or sequential two-dimensional images. Both one-dimensional time-resolved spectral images on multiple strips and a sequence of two-dimensional image snapshots on separate strip lines have been obtained. The gold coating on the MCP acts both as a photocathode and as the electrical conductor. CsI is sometimes used as an overcoat to the gold to enhance the photoconversion efficiency. Both four- and seven-frame cameras have been developed. The phosphor converts the electrons to visible light and the fiberoptic faceplate channels the light to a removable film cartridge or charge-coupled device (CCD) camera.

The spatial resolution of the intensifier was measured with a U.S. Air Force resolution test target placed in front of the MCP. The film density was converted to exposure and the spatial resolution was defined using the Rayleigh criterion for minimum resolution from $(I_{\max} - I_{\min})/I_{\max}$, where $I_{\max}$ is the intensity maximum and $I_{\min}$ is the intensity minimum (over background) between the resolving lines. A plot of the $(I_{\max} - I_{\min})/I_{\max}$ values versus resolution from the test patterns is shown in Fig. 3-29. Using a cut-off at 20% for the Rayleigh criterion, one obtains a resolution of better than 50 μm.

The spatial resolution of these proximity-focused instruments is usually determined by the electron energy spread out of the MCP. Figure 3-30 is a plot of resolution as a function of phosphor gap voltage, showing an inverse square root dependence.

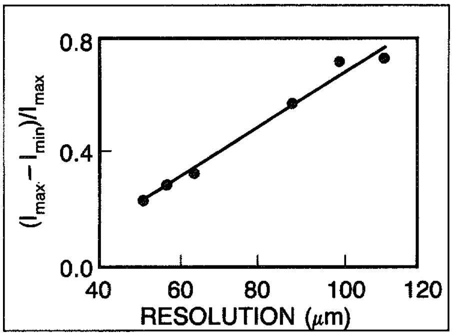

Fig. 3-29. The x-ray framing camera has a spatial resolution of about 20 μm. The measured $(I_{\max} - I_{\min})/I_{\max}$ values are shown for a variety of resolution test patterns.

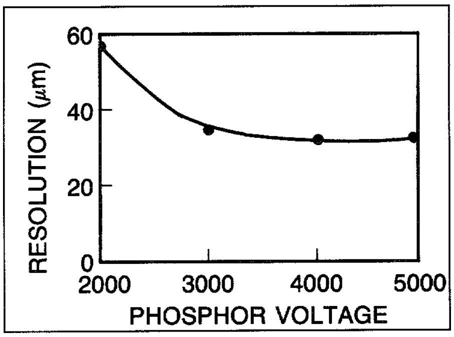

Fig. 3-30. The camera's resolution is also a function of the applied phosphor gap voltage.

A spectrograph developed at KMSF is a wavelength-dispersive instrument that uses a Bragg reflecting crystal coupled to the x-ray framing camera. Low-energy x-ray spectroscopy with crystals and multilayers has been applied to relatively fast, high-efficiency spectral analysis of constant and pulsed sources. The dispersive element and the intensified camera are combined together into a single light- and vacuum-tight unit. Various reflecting crystals have been used, including KAP, PET, and layered synthetic microstructures.

The instruments constructed were demonstrated in experiments performed on the Chroma laser at KMSF in which ~130 J of 0.53 μm laser light 1 ns long was incident on a gold disk target. The spectrograph was set up to look at the sub-keV (12 to 38 Å) region with 150 ps windows and 350 ps spacing between frames (strip lines). Only three strips were required to span the duration of the laser pulse. The x-ray spectrum in this region is a continuum, and is seen only when the laser pulse is on. Figure 3-31 is a digitized example of such a result.

X-ray Calibrations. XCALIBR I provides us with the capability to measure crystal integrated reflectivities. This is an important tool for proper characterization and calibration of x-ray instruments used in ICF experiments. Crystal reflectivity calibrations were performed for LANL and KMSF, and included two large-format (1 in. × 2 in.) PET crystals, one small-format PET (0.5 in. × 2 in.) crystal, and one RAP crystal, also in the smaller format. The large-format PET will be referred to as the "large PET," the small-format PET as "small PET," and the small-format RAP as "RAP."

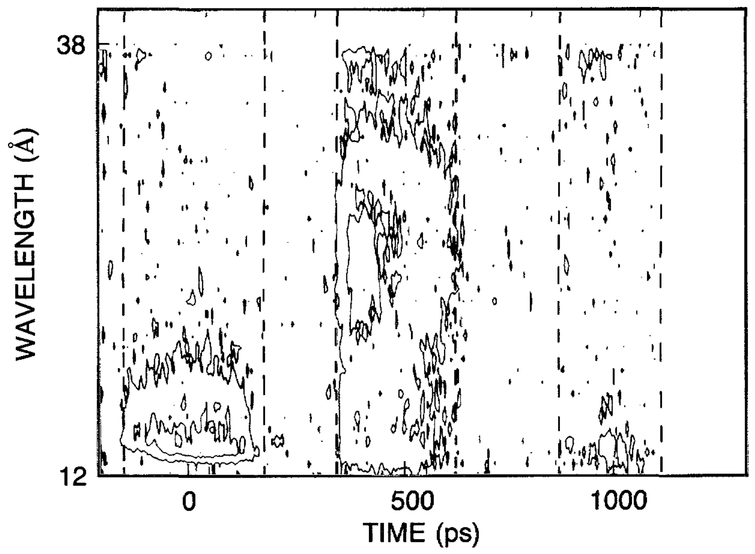

Fig. 3-31. This digitized sample of soft x-ray pulsed data was derived from an experiment in which ~130 J of 0.53 μm laser light 1 ns long was incident on a gold disk target. Only three strips were required to span the duration of the laser pulse.

Each of these crystals was calibrated at three energy points: Si-K_α at 1740 eV, Ag-L_α at 2984 eV, and Ca-K_α at 3690 eV. The results of the calibration are found in Table 3-2. These values are typical for Bragg crystals of this type; theoretical values and measurements of rocking curves of other crystals fall in this same region of $R_c \simeq 10^{-4}$ to 10^{-5}.

The integrated reflectivity was measured using a θ to 2θ table, a Manson x-ray source in XCALIBR I, and a single-wire proportional counter. Both the incident and diffracted energies were then measured; as discussed in Ref. 22, this arrangement allowed us to calculate the reflectivity without factoring in the efficiency of the proportional counter.

Table 3-2. Rocking Curve Calibrations for Selected Crystals

Elemental Line	Energy (keV)	R_c (radians) Large PET	Small PET	RAP	Error (%)
Si-K_α	1.740	1.15×10^{-4}	6.54×10^{-5}	6.62×10^{-5}	± 15
Ag-L_α	2.984	2.95×10^{-4}	1.32×10^{-4}	8.96×10^{-5}	± 20
Ca-K_α	3.690	5.30×10^{-4}	2.72×10^{-4}	1.70×10^{-4}	± 15

For additional information, please contact Dr. Z. M. Koenig

3.2.2 Digital Imaging for ICF Diagnostics

KMS Fusion has been pursuing methods to replace photographic film in many of its ICF diagnostic instruments. This effort has been very successful to date in streamlining our image data collection and improving data reliability, while reducing manpower costs.

KMS Fusion has developed a video data acquisition system (VDAS). It is a multi-channel, real-time digitizing system based on the IBM® PC/AT microcomputer platform (see Figs. 3-32 and 3-33). The low cost and expansion capability of VDAS have encouraged us to produce several identical systems, each of which currently accepts three video inputs. The computer synchronizes video frame acquisition with the firing of the Chroma laser and transfers the digitized video frames to the VAX computer over Ethernet® links.

The VDAS hardware design is based on commercially available video digitizers and CCD cameras with an extended integration feature. Software control of the video digitizers and CCD cameras allows a very simple method of synchronizing to pulsed events, yet retains maximum flexibility for accommodating new camera or digitizer technology.

A video source is, in general, asynchronous with respect to the firing of a laser pulse, so some method has to be used to synchronize the two. We have developed a simple software method

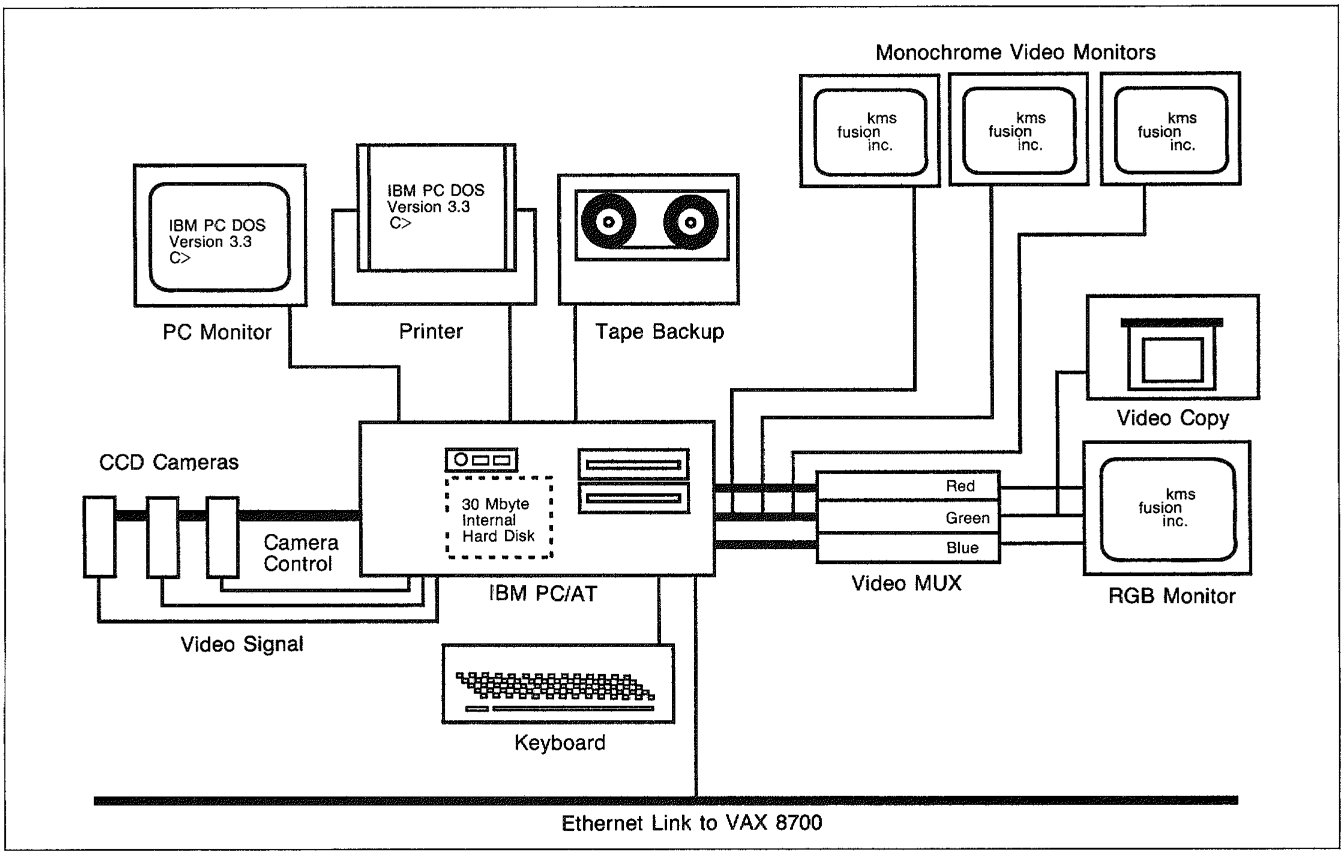

Fig. 3-32. The KMS video data acquisition system (VDAS) is configured for three video sources, RGB color display, and Ethernet connection. Other systems based on this technology are equally flexible.

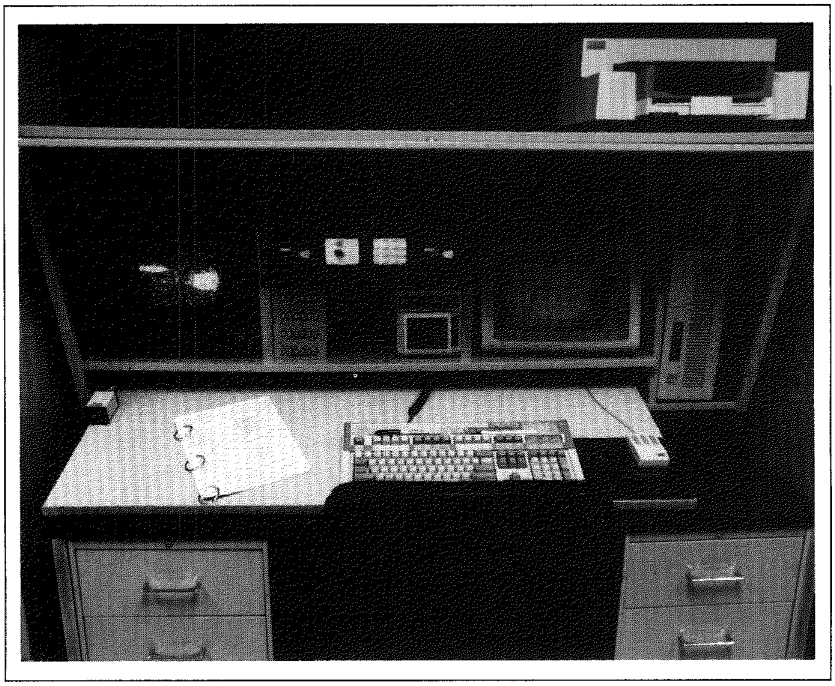

Fig. 3-33. The VDAS workstation provides multiple video displays, local hard-copy, and PC-based image analysis.

that maximizes flexibility compared with hardware-only synchronization methods. Since the frame grabber begins acquisition at the top of a frame, the VDAS control program must anticipate the laser pulse. Therefore, a pre-trigger signal is supplied to the computer in the form of an optical or electrical pulse from the master control console. The VDAS software measures the passage of time after receiving the pre-trigger by polling a status register on the video digitizer. Using the video frame rate (as opposed to software timing loops) as the time base, the program times the integration period on the CCD and digitizes a single video frame at exactly the correct moment. Program timing is independent of processor speed; that is, the software need not be rewritten to run on a computer that uses a different CPU clock speed. We run identical VDAS software on an 8 MHz IBM® PC/AT and on 12 and 20 MHz PC/AT-compatibles without timing problems.

The VDAS software was written in C language under the Microsoft C compiler. We chose C because it generates fast executable code and allows close control of the PC hardware. The first consideration is important for attaining several system-design goals for VDAS. A primary goal of the design was overall simplicity. The critical timing tasks involved in implementing VDAS might have required assembly language subroutines had some other language been used. Not only would a two-language program have enlarged the burden of software support, but also would have had important implications for software portability, since assembly language is processor-specific.

Under software control, each video digitizer can acquire and store two complete video frames in on-board memory. Video data are initially stored on the PC's local hard disk. Then, newly acquired data are backed up to a local streaming tape unit, and transferred to a VAX 8700 via Ethernet immediately following the experiment. DECnet DOS network software transparently converts the PC-DOS file format to VAX/VMS format, giving the scientific staff access to the digital image data within seconds of an experiment. Specialized analysis routines may then be applied to the digital image data by various investigators working in parallel.

The VDAS system is easily expanded, since each video source is connected to its own video digitizer within the IBM® PC/AT. Additional digitizers can be added until backplane space or power supply considerations become limiting. Currently, three video data channels can be accommodated in the IBM® version of the PC/AT. However, a large number of manufacturers produce PC/AT-compatible systems with greater add-in board capacities for even larger VDAS designs. The ready availability of inexpensive industry-standard microcomputer hardware provides dramatic cost savings over CAMAC- or minicomputer-based systems, with no compromise in performance levels. Indeed, PC/AT-compatibles based on the Intel 80386 microprocessor approach or surpass the performance levels of a micro-VAX minicomputer at less than 20% of the cost.

The VDAS system has been successfully applied to optical streak recording, equivalent plane imaging, and near-infrared spectroscopy in the 1 to 2 μm spectral region. Future applications include x-ray streak and x-ray framing camera imaging and optical interferometry.

We currently operate several types of solid-state and tube-type video cameras in the ICF experiments area. Two MCP intensified CCD cameras are being used to image optical streak cameras. Unintensified CCDs are in use on the Chroma equivalent-plane beam profile diagnostic. These cameras offer roughly 400 horizontal × 500 vertical pixel resolution with 12 μm × 18 μm pixel dimensions. The resolution and dynamic range of these devices is well suited to our current applications, but we plan to incorporate megapixel-class (1000 × 1000, 7 μm square pixel) cameras and digitizers, and optical disk storage for the more demanding requirements inherent in reconstructing holographic interferograms.

For additional information, please contact Dr. K. L. Marsh

SECTION 3.3

Theoretical Plasma Physics

In inertial confinement fusion (ICF), lasers are used because they are high-powered, monochromatic, coherent sources of radiation that can deliver energy in a short time to a small volume of plasma. In part because of their coherence, they have drive instabilities that can reflect a large fraction of their energy. However, lasers are naturally more coherent than is necessary for the diffraction spot size to be less than the target diameter. Thus, deliberate introduction of incoherence is one design option we are studying to reduce the deleterious effects of laser plasma instabilities.

3.3.1 Modeling of Induced Spatial Incoherence

Induced spatial incoherence[23] (ISI) is a promising technique under consideration to smooth the spatially nonuniform intensity distribution of high-power laser beams. Some such technique or improvement in laser technology is needed to achieve the uniformity that direct-drive ICF targets require to avoid Rayleigh–Taylor instabilities. A potential benefit may also result if the incoherence increases the intensity threshold for which laser plasma instabilities, such as stimulated Raman scattering (SRS), become a threat to ICF. Experiments at the Naval Research Laboratory (NRL) have shown a reduction in the scattered light amplitude when ISI is used with their laser.[23,24] We have also developed theoretical models that show how sufficient temporal or spatial incoherence can affect parametric instabilities, of which SRS is an example.

Our previous theoretical work in homogeneous or inhomogeneous plasma was essentially one-dimensional.[25] For a homogeneous plasma including damping, we find the dispersion relation for a parametric instability is given by

$$(\gamma + \nu_1)(\gamma + \nu_2 + \Delta\omega + |\vec{\Delta}\kappa \cdot \vec{v}_2|) = \bar{\gamma}_0^2 \ , \tag{1}$$

where γ is the growth rate, ν_1 and ν_2 are the natural damping rates, $\Delta\omega$ is the laser bandwidth, and $|\Delta\vec{\kappa} \cdot \vec{v}_2|$, the effective spatial bandwidth, is the magnitude of the inner product of the group velocity and the inverse of the spatial coherence length. Applying this result to ISI laser beams, we conclude that threshold for instability ($\gamma = 0$) will be lowest when $|\vec{\Delta}\kappa \cdot \vec{v}_2|$ is a minimum. In an isotropic medium, where the group velocity $\vec{v}$ points in the direction of the wavevector $\vec{\kappa}$, the minimum occurs for backscatter because the coherence length along the direction of propagation of the laser beam is much larger than perpendicular to that direction, i.e. $\Delta\kappa_x \ll \Delta\kappa_y$. However the coupled mode equations are not strictly valid if $v_y = 0$ and $\Delta\kappa \neq 0$ because the spatial nonuniformity of the laser will induce spatial variation in the unstable modes perpendicular to the laser propagation direction.

We can account for this transverse variation by including diffractive effects in the equations, i.e.,

$$\left(\frac{\partial}{\partial t} + v_{1x}\frac{\partial}{\partial x} + \nu_1 - \frac{ic^2}{2\omega_1}\frac{\partial^2}{\partial y^2}\right)A_1 = \gamma_0 A_2 \tag{2}$$

and

$$\left(\frac{\partial}{\partial t} + v_{2x}\frac{\partial}{\partial x} + \nu_2 - i\alpha^{-1}\frac{\partial^2}{\partial y^2}\right)A_2 = \gamma_0 A_1 \ . \tag{3}$$

Here c is the speed of light and γ_0 is the coupling strength that depends on x, y, and t. Equation (2) describes the backscattered light wave of frequency ω and group velocity v_{1x} along the laser propagation direction (taken to be the x-axis). Equation (3) describes the propagation of the associated longitudinal plasma wave. The constant α depends on the dispersion characteristics: For a Langmuir wave, $\alpha = 2\omega_2/3v_e^2$; for an ion acoustic wave, $\alpha = 2\omega_2/C_s^2$, where v_e is the electron thermal velocity and C_s is the ion sound speed.

A formal solution for Eq. (3) is given by

$$\begin{aligned} A_2 = e^{\pi i/4}\sqrt{\frac{\alpha}{\pi}}\int_0^t \frac{dt}{\sqrt{t-t'}}\int_{-\infty}^{+\infty} dy' \\ \times \exp[-\nu_2(t-t') - i\alpha(y-y')^2/(t-t')] \\ \times F[x - v_2(t-t'), y', t'] \ , \end{aligned} \tag{4}$$

where

$$F(x,y,t) = \gamma_0^*(x,y,t)A_1(x,y,t) \ . \tag{5}$$

We substitute Eq. (4) in Eq. (2) and use the Bourret approximation that

$$\begin{aligned} &\langle \gamma_0(\vec{x},t)\gamma_0^*(\vec{x}',t')A_1(\vec{x}',t')\rangle \\ &\quad = \gamma_0(\vec{x},t)\gamma_0^*(\vec{x}',t')\rangle\langle A_1(\vec{x}',t)\rangle \\ &\quad \equiv \bar{\gamma}_0^2\Gamma(\vec{x}-\vec{x}', t-t')\langle A_1(\vec{x}',t)\rangle \ , \end{aligned} \tag{6}$$

where the brackets denote a statistical or ensemble average. If the effective correlation time (which we subsequently define explicitly) is short compared to the growth rate, the form of the correlation function Γ is unimportant. We assume for convenience

$$\Gamma(\vec{x},t) = \exp(-\Delta\kappa_i|x_i| - \Delta\omega\ t) \ . \tag{7}$$

Once these substitutions and assumptions are used in Eq. (2), a Fourier–Laplace transform in space and time of the result yields the dispersion relation,

$$\left(-i\omega + ik_x v_{1x} + \nu_1 + \frac{ic^2k_y^2}{2\omega_1}\right) = \bar{\gamma}_0^2 e^{\pi i/4}\sqrt{\frac{\alpha}{\pi}}\int_{-\infty}^{+\infty} dy \int_0^{\infty} \frac{dt}{\sqrt{t}} \exp[i(\omega_\mathrm{r} - k_x v_{2x})t - ik_y y - \Delta k_y|y| - \Delta\tilde{\omega}t - i\alpha y^2/t] \ , \qquad (8)$$

where the inverse of the effective correlation time is

$$\Delta\tilde{\omega} = \gamma + \Delta\omega + \nu_2 + \Delta\kappa_x|v_{2x}| \ , \qquad (9)$$

$$\omega_\mathrm{r} = \mathrm{Real}\ \omega \ , \qquad (10)$$

and

$$\gamma = \mathrm{Im}(\omega) \ .$$

The integrals in Eq. (8) are readily performed, with the result that

$$\left(-i\omega + ik_x v_{1x} + \nu_1 + \frac{ic^2}{2\omega_1}k_y^2\right) = \frac{\bar{\gamma}_0^2}{(\Omega^2 + \Delta\tilde{\omega}^2)^{1/4}}\,\frac{2Qe^{\pi i/4}}{Q^2 + k_y^2/\alpha^2} \ , \qquad (11)$$

where

$$Q \equiv \frac{\Delta\kappa}{\sqrt{\alpha}} + 2(\Omega^2 + \Delta\tilde{\omega}^2)^{1/4}\exp(i\Psi + i\pi/4) \ , \qquad (12)$$

$$\Psi = \frac{1}{2}\tan^{-1}(\Omega/\Delta\tilde{\omega}) \ , \qquad (13)$$

and

$$\Omega = k_x v_2 - \omega_\mathrm{r} \ . \qquad (14)$$

It is easy to show that Eq. (11) reduces to the one-dimensional result (as it must) if $k_y = \Delta k_y = \Psi = 0$ [compare to Eq. (1)].

Examination of Eq. (11) shows that the finite k_y and Ω are stabilizing. Thus we choose $\Omega = k_y = 0$ and choose k_x to satisfy the imaginary part of the dispersion relation. The threshold ($\gamma = 0$) is then determined by the relation,

$$\bar{\gamma}_0^2 = \nu_1 \Delta\tilde{\omega} R(\Delta\omega_t/\Delta\tilde{\omega}) \ , \qquad (15)$$

$$\mathrm{R}(x) = \frac{1 + x + \sqrt{2x}}{1 + \sqrt{x/2}} \ , \qquad (16)$$

and

$$\Delta\omega_\mathrm{T} = \Delta k_y^2/\alpha \ . \qquad (17)$$

For these diffractive effects to be important, it is necessary that R ≫ 1 since, for R = 1, the threshold given in Eq. (16) is the same as the one-dimensional result in Eq. (1). A twofold increase in threshold occurs for $\Delta\omega_T = \Delta\tilde{\omega}$. We look at the case of an ISI beam with narrow bandwidth where $\Delta\kappa_x|v_2| > \Delta\omega$ and $\Delta\kappa_x = \Delta\kappa_y^2/2k_0$, with $k_0 = \omega_0/c$. We conclude that diffractive effects yield a twofold or more increase in threshold if $2k_0 > \alpha|v_{2x}|$. We choose SRS as an example where $v_{2x} \simeq (k_0 + |k_1|)\,(3\,v_e^2/\omega_2)$ and $\alpha = 2\omega_2/3v_e^2$ and find that this inequality cannot be satisfied.

These calculations show that our previous results[25] that neglected diffractive effects were valid and included the most important statistical fluctuations, i.e., those along the direction of propagation. However those and the present theoretical results involved the response to random variations in the overall phase of the pump in space and time. We have seen in our numerical simulations that intensity variations are also present in ISI laser beams and these variations dominate the response if the effective bandwidth $\Delta\tilde{\omega}$ is smaller than $\bar{\gamma}_0$, the spatially and temporally averaged growth rate. The inherent difficulty, of course, with studying interactions with $\Delta\tilde{\omega} < \bar{\gamma}_0$ is that there are large fluctuations in the growth rate about the mean calculated from a statistical average. Thus the average is misleading and difficult to compute numerically (since a large number of cases must be studied). As we stated in our previous reports,[25] the experiments did not in fact have sufficient effective bandwidth according to the theoretical result [Eq. (1)] to suppress SRS. Thus, we speculate that the beneficial effects of ISI that were observed in experiments result from a reduction in the mean size and intensity of the hottest hot spots in the laser beam rather than any direct effect due to a stochastically varying phase. We anticipate presenting results on this latter problem in the near future.

For additional information, please contact Dr. R. L. Berger

3.3.2 Ultra-Strong Langmuir Turbulence in Open Systems

Intense Langmuir waves, produced in the corona of ICF targets by a number of instabilities, have long been recognized as a critical factor in determining target behavior and performance. Recent laser/plasma experiments[26] confirm the importance of interactions between Langmuir waves from SRS and the ion acoustic waves from stimulated Brillouin scatter (SBS) in controlling the evolution of these instabilities in the corona. Virtually all of the theoretical descriptions[27–31] of the evolution of intense Langmuir waves interacting with ion density perturbations, (i.e., strong Langmuir turbulence), can be cast in the form put forth by Zakharov[27] more than fifteen years ago:

$$i\frac{\partial \vec{E}}{\partial t} + \frac{\partial^2 \vec{E}}{\partial x^2} = n\vec{E}\ , \tag{18}$$

$$\frac{\partial^2 n}{\partial t^2} - \frac{\partial^2 n}{\partial x^2} = \frac{\partial^2 |\vec{E}|^2}{\partial x^2}\ , \tag{19}$$

where $\vec{E}$ is the envelope of the electric field of the Langmuir wave and n is the ion density perturbation (in Zakharov units). These equations (the "Zakharov equations") describe the coupling of Langmuir waves to ion density perturbations and the evolution of ion density perturbations acted upon by the ponderomotive force associated with the Langmuir waves. The behavior of the turbulence predicted by these equations is characterized by the formation of Langmuir solitons (nonlinear self-localized regions of enhanced electric field in associated density depressions). The solitons are unstable to catastrophic collapse in multidimensional systems. As the solitons collapse their spatial extent tends toward zero and the associated electric field in the soliton becomes extremely intense. This collapse proceeds until the spatial extent of the soliton is only a few Debye lengths when strong wave-particle interactions dominate. At this point the energy in the trapped electric field is deposited in a population of now-suprathermal electrons. Hence, this phenomenon of Langmuir collapse is a source of copious production of hot electrons deleterious to target performance. This process is called "burn-out."[31] What remains of the remnant soliton is an ion density hole that can trap a pump field if present, thus acting as site for a new soliton to form, a process called nucleation.

The Zakharov model [Eqs. (18) and (19)] and those models derived from it[28,29] incorporate several assumptions that limit their application to high intensities: low-frequency charge quasineutrality, low wave intensity relative to thermal pressure, small density perturbations, and separation of time-scales (i.e., the electric field envelope evolves much more slowly than the high-frequency electron plasma oscillations). Yet the occurrence of the phenomena predicted by these models at small but finite amplitudes, localization and subsequent collapse, point to the breakdown of these same assumptions in the regime of interest. We have therefore proposed[32-36] the use of full two-fluid plasma theory as a model for "ultra-strong Langmuir turbulence":

$$\frac{\partial n_e}{\partial y} + \nabla \cdot (n_e \vec{v}_e) = 0 \ , \tag{20}$$

$$\frac{\partial}{\partial t} \vec{v}_e + \vec{v}_e \cdot \nabla \vec{v}_e = -\frac{1}{n_e m_e} \nabla p_e - \frac{e}{m_e} \vec{E} - \frac{e}{m_e} \vec{E}_0 - \nu_e \vec{v}_e \ , \tag{21}$$

$$\frac{\partial n_i}{\partial t} + \nabla \cdot (n_i \vec{v}_i) = 0 \ , \tag{22}$$

$$\frac{\partial}{\partial t} \vec{v}_i + \vec{v}_i \cdot \nabla \vec{v}_i = -\frac{1}{n_i m_i} \nabla p_i + \frac{e}{m_i} \vec{E} + \frac{e}{m_i} \vec{E}_0 - \nu_i \vec{v}_i \ , \tag{23}$$

$$\nabla \cdot \vec{E} = 4\pi e (n_i - n_e) \ , \tag{24}$$

$$\nabla p_e = \gamma_e T_e \nabla n_e \ , \tag{25}$$

$$\nabla p_i = \gamma_i T_i \nabla n_i \ , \tag{26}$$

where subscripts (e,i) denote variables of the electron and ion fluids, respectively. Here, for the first time, we include new terms in Eqs. (21) and (23) to model the inclusion of a prescribed pump and damping mechanisms. This polytropic (separate electron and ion fluids) model contains none of the assumptions required to obtain the reduced Zakharov model and therefore is free from its inherent limitations. In its latest form, our model easily describes ultra-strong Langmuir turbulence in open systems as is more appropriate to real experimental conditions.

We have previously designed and implemented a new computer code (ESHYDRO) to solve Eqs. (20) through (26) for the evolution of electric fields and densities describing ultra-strong Langmuir turbulence.[32-36] ESHYDRO has recently been modified to accommodate prescribed drivers and damping mechanisms appropriate to real experimental conditions. Most importantly, our simulations confirm the modulational instability of two-fluid theory as predicted in our previous work[32-36] and demonstrated in Fig. 3-34.

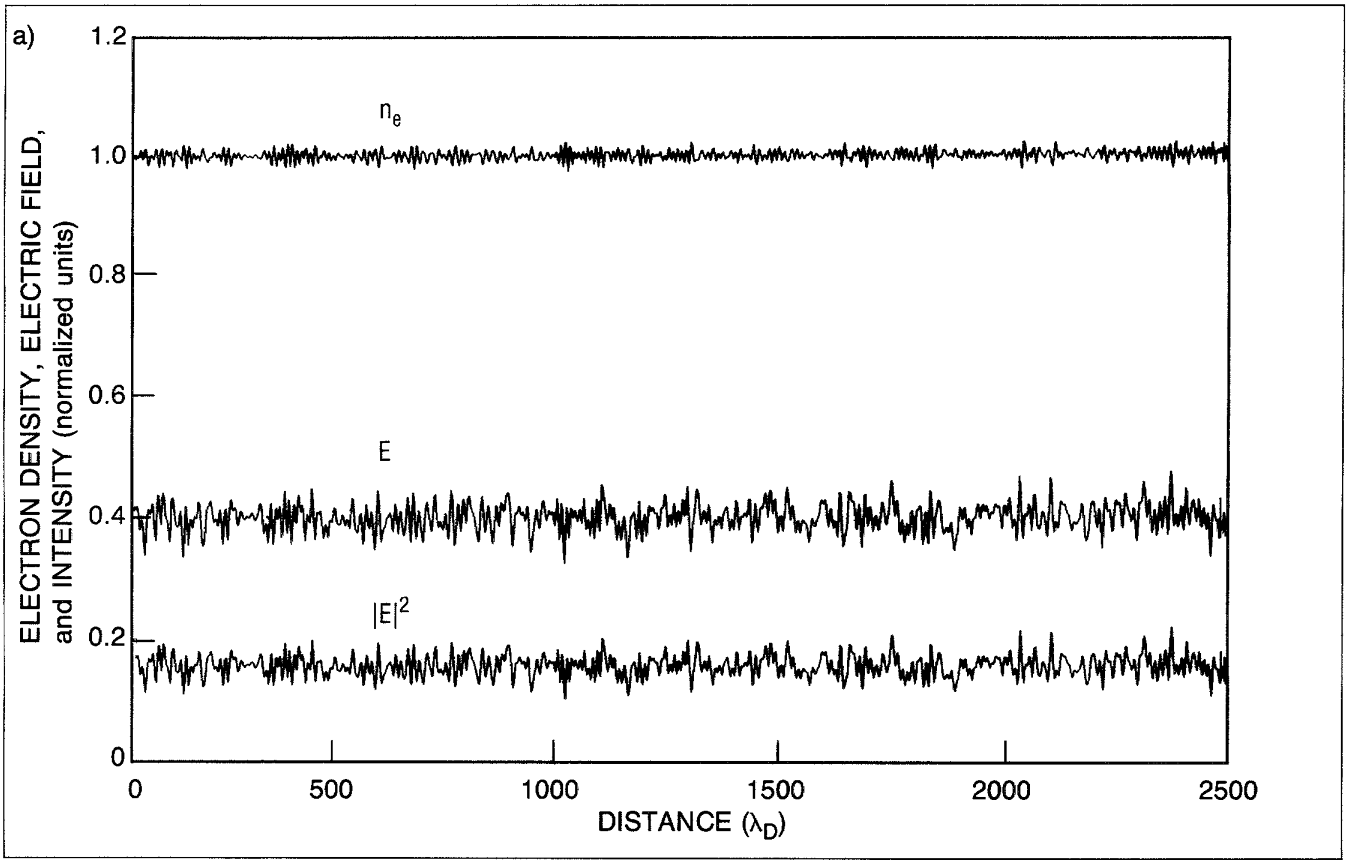

Fig. 3-34. Simulations performed with ESHYDRO confirm the modulational instability of two-fluid theory. Typical initial conditions are shown in (a), where an electric field of value 0.4 (natural electrostatic plasma units) is applied in a uniform plasma. Small random fluctuations imposed about this value give rise to the intensity pattern shown (where n_e is the electron density, E is the electric field, and $|E|^2$ is intensity). The early ($t = 160$ plasma periods) onset of the modulation instability is shown in (b) by the small ion density depressions appearing in the trace of ion density variation (Δn_i). The formation of solitons, characterized by the localization of electric field spikes in ion density holes, is evident in (c), where $t = 600$ plasma periods.

Figure 3-34a shows typical initial conditions. An electric field of value 0.4 (in natural electrostatic plasma units, $T_e/e\lambda_D$) is applied in a uniform plasma. Small random fluctuations imposed about this value give rise to the intensity pattern shown. In addition, small random fluctuations are added to the electron density n_e about its normalized ambient value of unity. The ion density (not shown), however, is initialized at its normalized value of unity without noise fluctuations. Figure 3-34b demonstrates the early onset of the modulational instability, as evidenced by small ion density depressions appearing in the trace of ion density variation Δn_i. In Fig. 3-34c, the formation of solitons, characterized by the localization of electric field spikes in ion density holes, is quite evident by $t = 600\ \omega_{pe}^{-1}$ (electron plasma periods). The similarities of results from ESHYDRO to results previously obtained for the driven-damped Zakharov system[37,38] are striking. At low intensities the predictions of the Zakharov model are confirmed.

Figures 3-35a and b show continued evolution and saturation of the modulational instability. Note that the individual solitons continue to increase in intensity until most remaining solitons have intensity values well in excess of unity. At this point, the damping mechanism saturates further growth and many examples of burn-out are evident. Note also the ever-decreasing number of spikes. There are, however, many examples of solitons

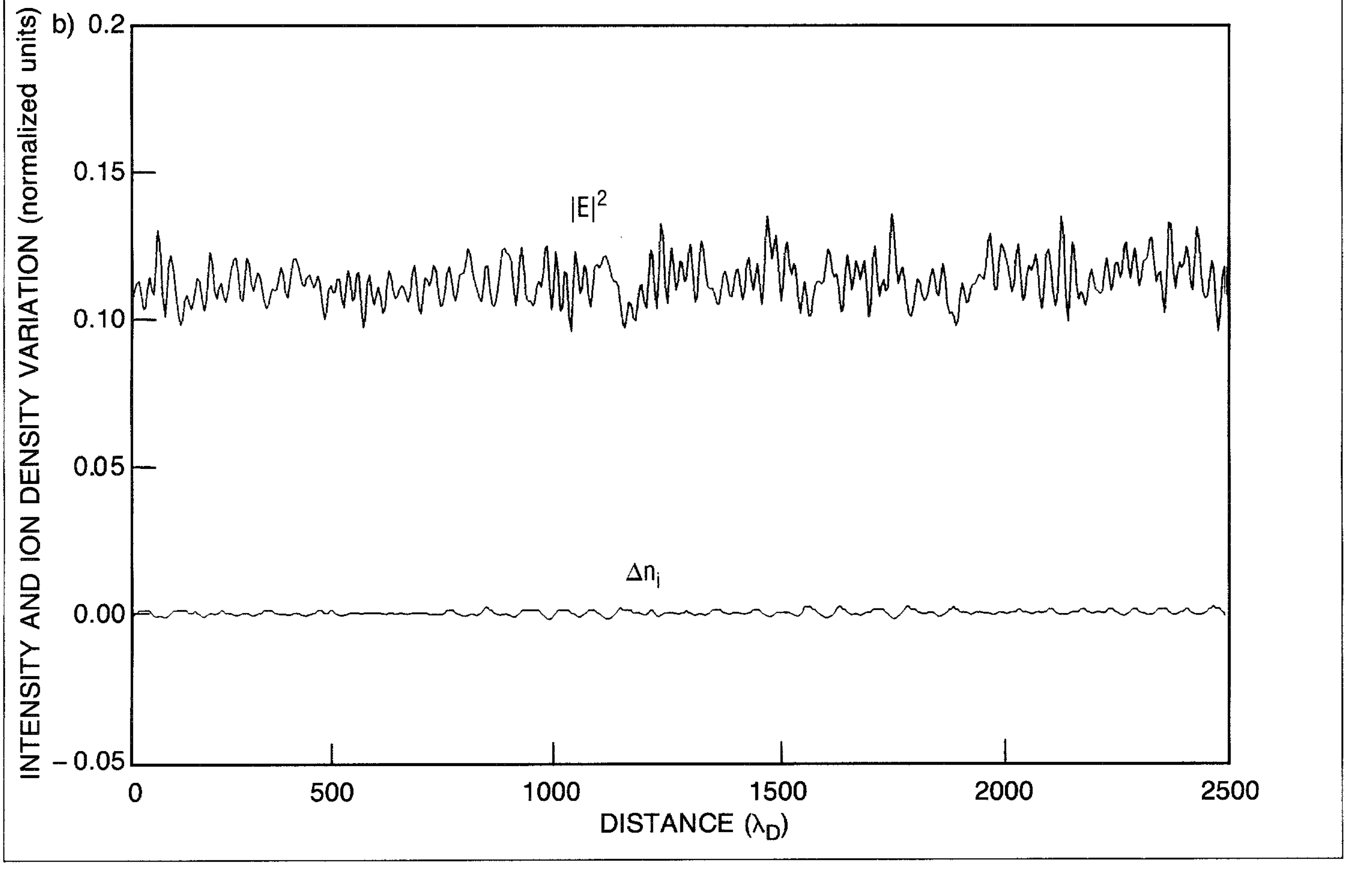

Fig. 3-34. "Simulations performed with ESHYRO confirm . . . ," continued.

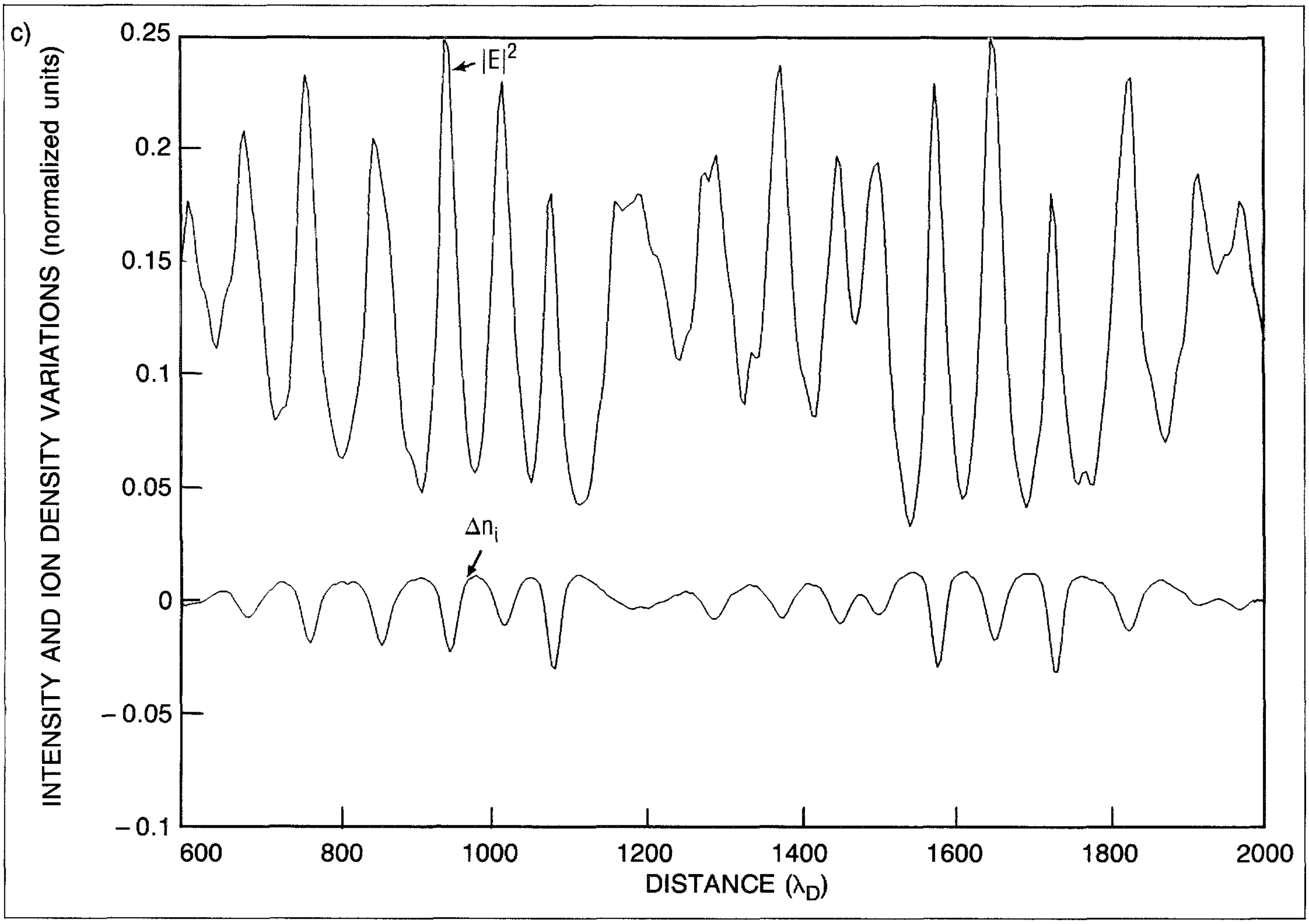

Fig. 3-34. "Simulations performed with ESHYDRO confirm . . . ," concluded.

being "reborn," i.e. nucleation. These processes of cyclical burn-out, nucleation, and collapse characterize the steady-state long-time evolution of the driven-damped two-fluid theory, as demonstrated in Fig. 3-36 for t = 14,400 plasma periods. There are still fewer spikes at the saturated intensity. Note, however, the number of density holes that approach 50% local evacuation of the plasma's density! These solutions are far beyond the reach of Zakharov-type models. They are, however, easily handled by our ultra-strong model, which includes charge separation effects.

When driven at higher intensities, simulations of the full two-fluid theory indicate the onset of wavebreaking and harmonic generation, effects that are lost in Zakharov descriptions, but are important processes in competition with collapse. Because ESHYDRO solves specifically for the electron and ion velocities, the onset of these effects is easily detected. Description of the evolution past the onset of wavebreaking awaits the results of work in progress.

Our investigations give the first confirmation of the modulational instability, soliton formation, collapse, burn-out and nucleation from exact two-fluid theory. Currently, we are

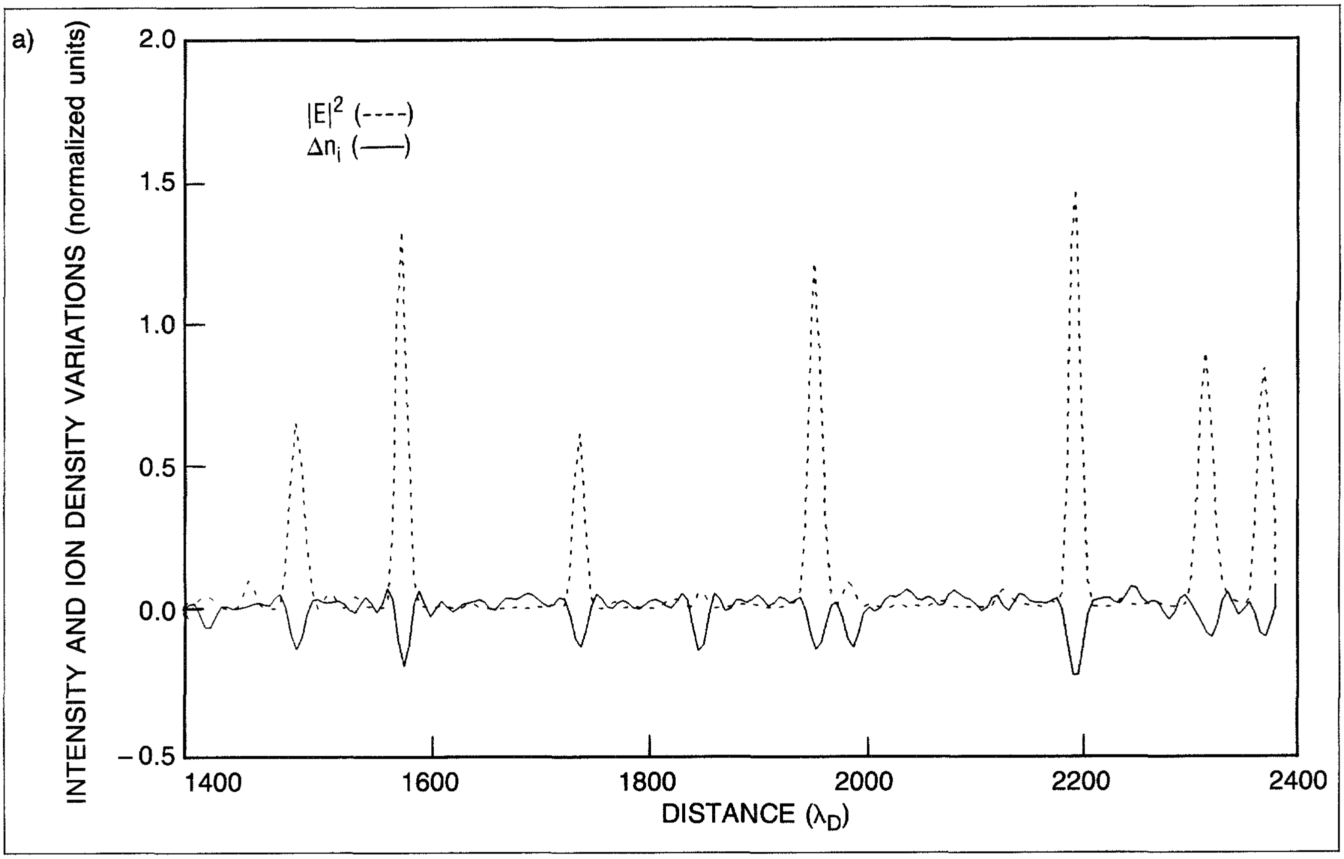

Fig. 3-35. Expanded views of the range between 1400 and 2400 Debye lengths (a) and 1000 and 2000 Debye lengths (b) show that, as burn-out occurs, there are also many examples of solitons being reborn. Comparison of the range between 1400 and 2000 λ_D at 4800 (a) and 6400 (b) plasma periods clearly shows the occurrence of burn-out and nucleation events.

extending this work in several important directions. Among these are the exploration of phenomenological damping and realistic driving terms to model real experimental conditions, solutions in two dimensions, solutions in inhomogeneous plasmas, and the inclusion of electromagnetic terms. A new code that follows the evolution beyond the onset of wavebreaking is under construction. Successful implementation of these more general models will permit the exploration of the nonlinear evolution and saturation of SRS, SBS, two-plasmon decay (TPD), and filamentation instabilities at laser intensities of interest in ICF.

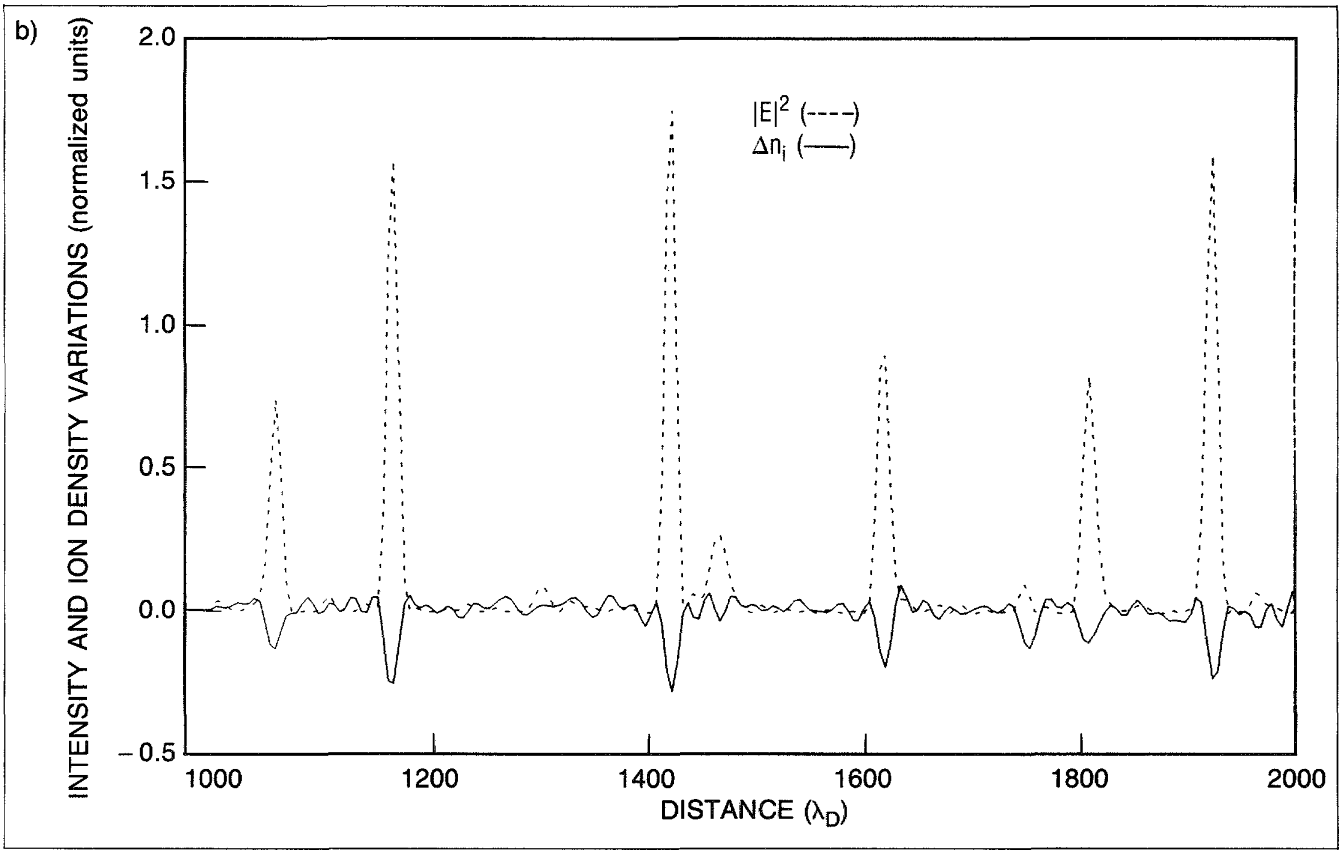

Fig. 3-35. "Expanded views of the range . . . ," concluded.

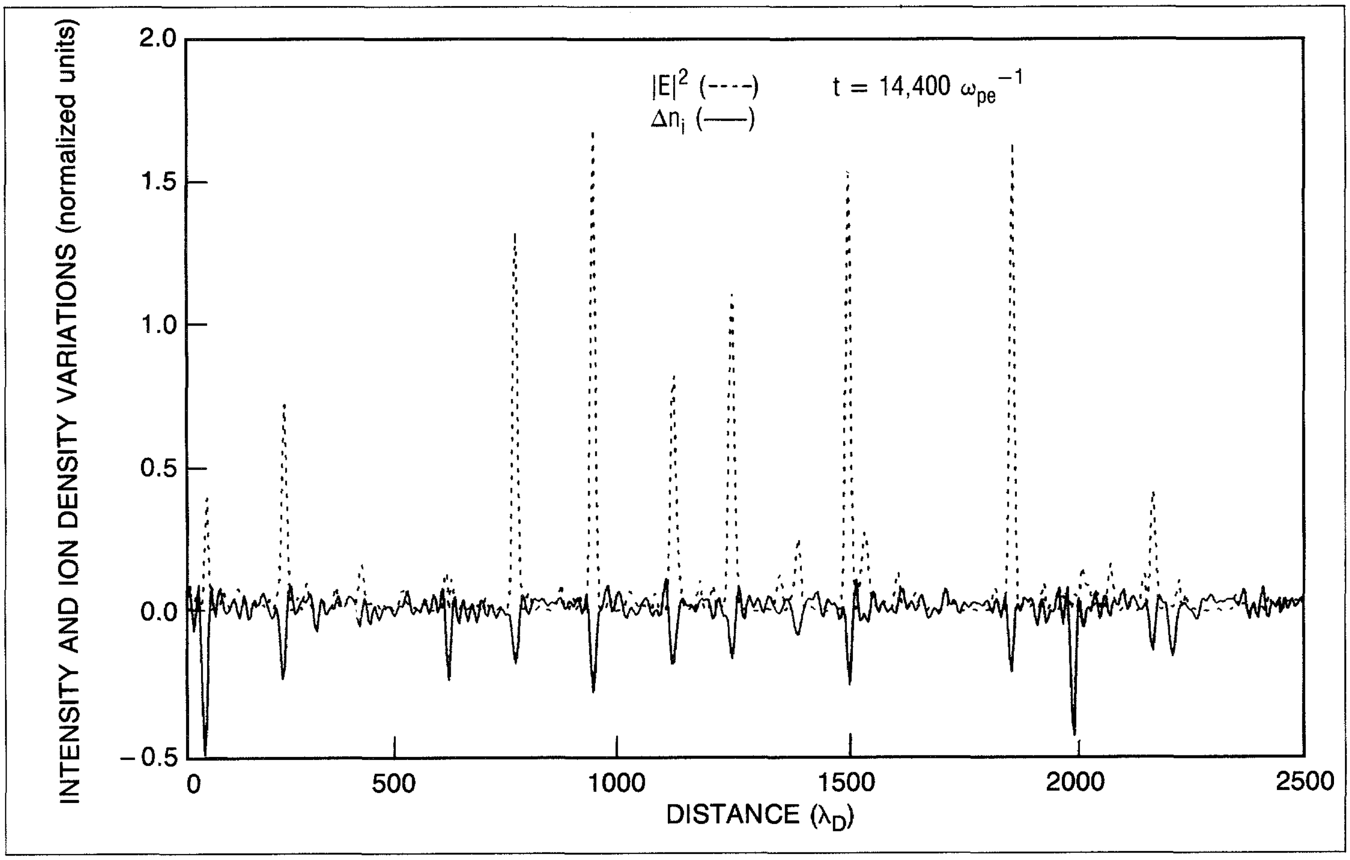

Fig. 3-36. The processes of cyclical burn-out, nucleation, and collapse characterize the steady-state, long-time evolution of the driven-damped two-fluid theory. At t = 14,000 plasma periods, there are fewer solitons and the intensities have saturated. Still, ion density depletions routinely reach over 50%. Several of the depletions appear burned out.

For additional information, please contact Dr. J. P. Sheerin

3.3.3 SRS Inhibition Due to SBS-Enhanced Density Fluctuations in Inhomogeneous Plasma

The role of parametric instabilities in laser/plasma coupling has long been an area of concern in ICF research. Both simulations and experiments indicate that interplay among the various parametric processes can play a major role in determining energy coupling and plasma characteristics. We report here numerical simulations of the competition between the SRS and SBS instabilities in a linear density gradient using the SATIN[39,40] code. In these simulations, SRS is inhibited by enhanced SBS seeded by ~1% backscattered laser light, but is unaffected by SBS growing from thermal fluctuations. In the case of enhanced SBS, the SRS is strongly reduced near quarter-critical density compared to simulations with fixed ions, but SRS growth is uninhibited at densities less than about 0.15 n_c. A major difference between this study and previous work[41] is the presence of a density gradient.

The system of equations solved by the SATIN code is

$$\left(\frac{\partial^2}{\partial x^2} + \Omega_j^2 - N - K_j^2 + 2i\Omega_j \frac{\partial}{\partial \tau}\right)\mathbf{E}_j - (1 - 3V_e^2)\nabla(\nabla\cdot\mathbf{E}_j)$$

$$= \sum_{k,l}\left(\frac{-N}{2\Omega_k\Omega_l}\nabla(\mathbf{E}_k\cdot\mathbf{E}_l) - \frac{\Omega_j}{\Omega_l}(\nabla\cdot\mathbf{E}_k)\mathbf{E}_l\right) + N_\mathrm{i}\mathbf{E}_j \qquad (27)$$

for the amplitudes of the high-frequency electric field components $\mathbf{E}_j$, which include both the transverse (light) waves and longitudinal (Langmuir) waves oscillating at frequency Ω_j. The units in Eq. (27) are related to the pump frequency ω_0, wavenumber k_0, and critical density n_c by the following normalization factors: $mc\omega_0/e$ for the electric field components $\mathbf{E}_j$; ω_0 for the mode frequencies Ω_j; n_c for the background electron density N; c for the velocities; k_0^{-1} for the spatial coordinate x; and ω_0^{-1} for the time variable τ. The high-frequency equations are solved by an implicit finite difference scheme described in Ref. 40. The high-frequency fields are coupled to the ion density perturbation described by the second-order equation,

$$\left(\frac{\partial^2}{\partial \tau^2} + 2\nu_\mathrm{i}\frac{\partial}{\partial \tau} - C_\mathrm{s}^2\frac{\partial^2}{\partial x^2}\right)N_\mathrm{i} = \frac{Zm_\mathrm{e}}{m_\mathrm{i}}\sum_k \frac{\nabla^2|\mathbf{E}_k|^2}{\Omega_k^2}\ , \qquad (28)$$

where the ion density perturbation N_i is normalized to the local plasma density n, the ion damping rate ν_i is normalized to ω_0, and all other quantities have the same units as in the high-frequency equations. The ion equation is solved with a second-order explicit upwind differencing scheme.

The coupling between SRS and SBS in a one-dimensional, linearly inhomogeneous plasma is considered here. Parameter values used in the simulations are $E_0 = v_0/c = 0.02$, 0.03 or 0.045; $v_\mathrm{e}/c = 0.044$; $c_\mathrm{s}/c = 0.003$; $k_0L = 500$ or 1000; and $m_\mathrm{i}/m_\mathrm{e} = 200$. The reduced mass ratio allowed for obtaining qualitative information on the SRS/SBS interaction in a density gradient in relatively economical simulations. The Langmuir wave source for the SRS instability is initialized at the thermal level ($|E| \sim 10^{-5}$). Simulations were performed with fixed ions, with SBS from thermal fluctuations ($|N_\mathrm{i}| \sim 10^{-3}$), and with an enhanced SBS source of 1% reflected laser light (corresponding to about 10 times the thermal level).

For SRS the scattering density is determined by the choice of the center frequency Ω_j. The numerical damping inherent in the difference scheme for the high-frequency equations limits the SRS bandwidth $\Delta\omega$ to approximately the SRS growth rate γ_SRS. In SRS simulations with fixed ions, both absolutely unstable scattering from quarter-critical density ($N = 0.25$) and convective saturation of scattering at low densities ($N < 0.15$) are observed. Scattering from intermediate density ($N = 0.2$) saturates convectively at low intensity ($v_0/c = 0.02$) but becomes absolutely unstable at higher intensity ($v_0/c = 0.045$).

The favored scattering density for SBS in the simulations is determined by the spatial dependence of the source. In runs with both SRS and SBS, the SBS source was chosen so that the scattering densities for SRS and SBS were the same. The ion modes ultimately saturate by pump depletion since no nonlinear saturation mechanism for the ions is currently included in the model.

Figure 3-37 summarizes the results of simulations of SBS and SRS for $\Omega_{SRS} = 0.55$ (corresponding to scattering from density

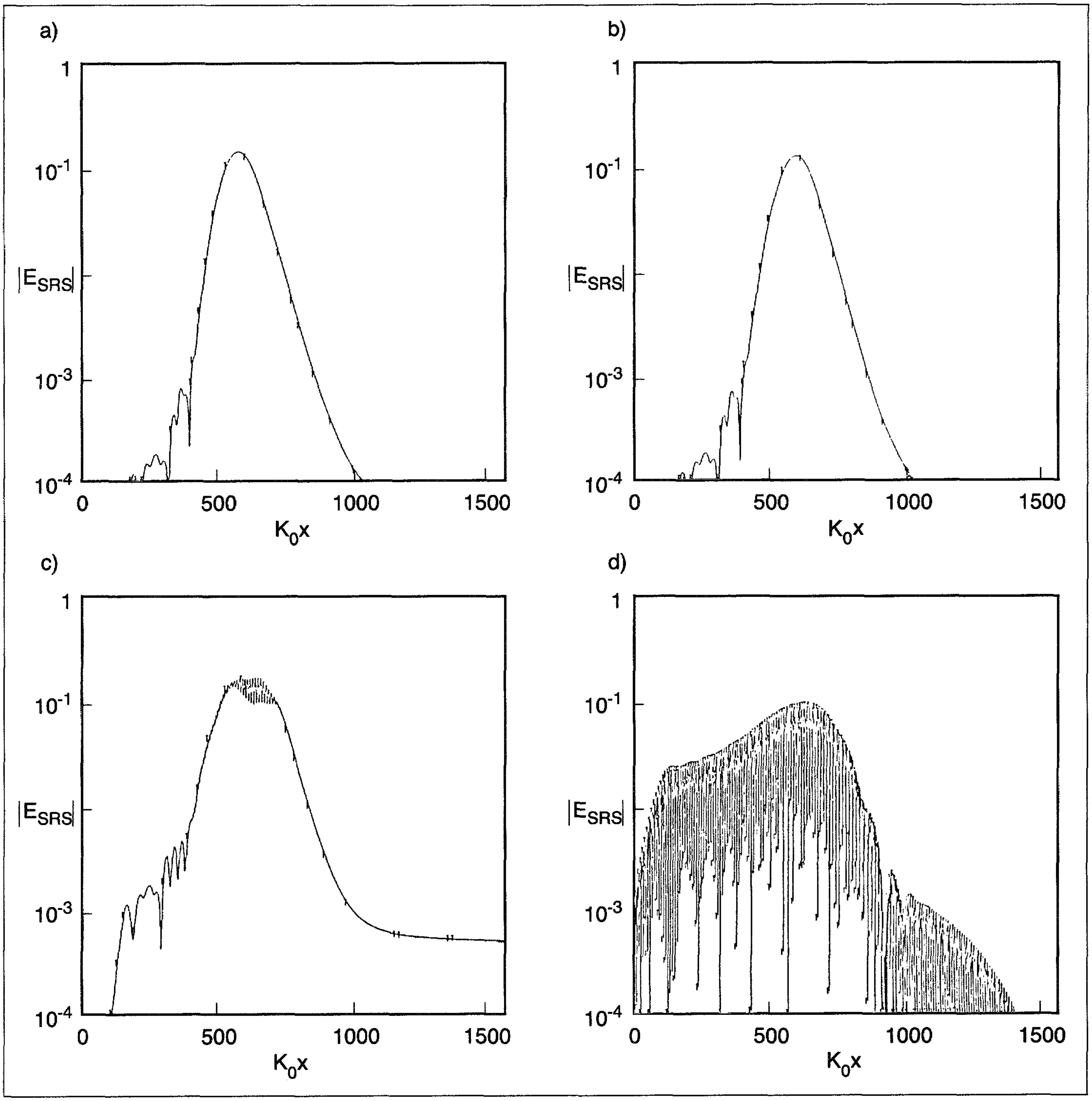

Fig. 3-37. SRS amplitude is shown at t = 400 ω_0^{-1} for parameters $\Omega_{SRS} = 0.55$, $v_0/c = 0.45$, and $k_0L = 1000$. Plotted are the electric field amplitude E_{SRS} of the SRS-scattered light for simulations with fixed ions (a), thermal SBS (b), enhanced SBS (c), and the SBS density fluctuation N_i for the case of enhanced SBS (d).

$N \sim 0.2$), $v_0/c = 0.045$, and $k_0L = 1000$. The amplitude of the SRS-scattered light at $t = 400\ \omega_0^{-1}$ (approximately eight instability growth times) is shown for fixed ions (a), for thermal SBS (b), and for enhanced SBS (c). Simulations with fixed ions and with thermal SBS are virtually identical at this time, indicating that thermal SBS has not inhibited the SRS. In these cases, SRS is just beginning to deplete the pump at $t = 400\ \omega_0^{-1}$. The ion density fluctuations from the enhanced source (d) have grown to large amplitude by $t = 400\ \omega_0^{-1}$, and significant pump depletion due to SBS has occurred. For the enhanced SBS case, the magnitude of $|E_{SRS}|$ is reduced by a factor of ~ 10 below the other cases (corresponding to a factor of ~ 100 reduction in the scattered intensity).

Both absolute and convective SRS are reduced by enhanced SBS in these simulations. Stimulated Raman scattering near quarter-critical is more strongly affected by SBS-generated density perturbations, however, than SRS at lower densities. One contributing factor is that the SRS growth is weaker at lower density even in the absence of SBS due to gradient effects and stronger Landau damping; consequently the SRS growth in the low-density region saturates convectively early in time before the ion waves reach high amplitudes. Another factor is that the SBS instability growth rate, and hence the level of density perturbations, is lower at low density. Figure 3-38 shows the fractional reduction in the saturated value of $|E_{SRS}|$ due to enhanced SBS as a function of scattering density for $v_0/c = 0.45$ and $k_0L = 500$. At low densities the saturation of SRS is convective. For $N = 0.2$ the SRS growth is absolute for this intensity and saturates by pump depletion in the absence of SBS.

Simulations with fixed, large-amplitude ($N_i > v_0/c$) sinusoidal density perturbations showed results similar to those with ion dynamics, while enhancing the SBS growth rate by decreasing the mass ratio did not further reduce SRS. It appears that these parameters, the size of the local density perturbations, play a more important role than ion dynamics in reducing SRS. The ion dynamics are still important in determining the spatial dependence of the ion wave amplitudes in the inhomogeneous case.

Work is currently underway to include nonlinear ion saturation in the model. The SATIN code can also simulate two-dimensional processes such as SRS sidescatter and TPD. The effect of ion density fluctuations on these instabilities will be addressed in future simulations.

For additional information, please contact Dr. L. V. Powers

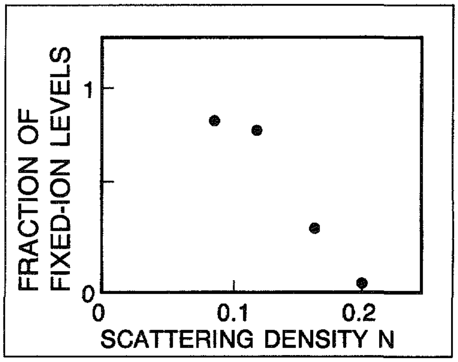

Fig. 3-38. The ratio of SRS growth rate and scattered light amplitude in simulations including SBS to the values obtained in simulations with fixed ions, is shown as a function of the scattering density $N = \sqrt{1 - \Omega_{SRS}}$ for $v_0/c = 0.45$ and $k_0L = 500$.

SECTION 3.4

Computational Physics

Analytical tools were developed to gain insight into the behavior of laser-produced plasmas. This section includes a discussion of the ray-tracing code that we used to simulate x-ray propagation in an ionized medium. The utility of this program is illustrated by the investigation of refractive effects within the gain region of a lasing medium. Our analysis of spectral methods for the solution of nonlinear wave equations answers questions concerning the accuracy and stability of the numerical solutions for plasma instabilities. We developed dispersion relations to produce new information about the relationship between the grid size and the accuracy of the hydrodynamic simulations. Finally, we applied principles of mathematical analysis to the evaluation of plasma emissions from x-ray images. In each case, the work led to consequential results that will provide the foundations for further development.

3.4.1 X-ray Refraction in Laser-Produced Plasmas

Certain x-ray diagnostic instruments used to characterize laser-produced plasmas are sensitive to refractive effects of the plasma, especially for the softer x-rays. In addition, the amplification one can achieve in single-pass x-ray laser schemes is limited by refraction. The laser-produced plasmas generally have steep density gradients, which refract radiation out of the geometrical line of sight. The RAYPTH ray tracing code was written to study the effects of refraction. Recently it has been modified to account for the effects of hemispherical x-ray mirrors with arbitrary foci. Such mirrors might be used in multi-pass x-ray laser schemes, in which the gain region is continuously replenished. The code was used to track representative beams of radiation for various mirror configurations. Preliminary results of these calculations are summarized below.

In all cases described below, a two-dimensional (axi-symetric) lasing medium 1 cm long was assumed. Different problem geometries were set up on a coordinate system with its origin at the center of the medium and its x-axis along the initial axis of the selenium/Formvar® foil used to generate the medium. The width and density distribution of the lasing medium were taken from results generated by the HYRAD two-dimensional hydrocode at 180 ps after the onset of illumination of the foil by 0.53 μm light at 3 to 5×10^{13} W/cm^2. Lasing was assumed at a wavelength of 200 Å. A maximum gain of 6 was legislated in the selenium at a density of $n = 2.0 \times 10^{20}$ cm^{-3}, and was decreed to drop off linearly with increasing and decreasing density, reaching zero at $n = 3.3 \times 10^{20}$ and 5.0×10^{19} cm^{-3}. These assumptions are consistent with experimental observations, although the details of the gain region are still not well understood.

Hemispherical mirrors with a radius of curvature of 58.4 cm and albedo of 0.5 were assumed. The radius of curvature was chosen to agree with the pulse interval achievable with the Chroma laser oscillator. The foci of the mirrors were positioned at various locations above, below, and within the gain region. Various cases involving coincident, overlapping, and nonoverlapping foci were modeled, as shown in Fig. 3-39. For each configuration, a total of 10 beams were started at random positions within the gain region. Initial beam directions were chosen at random within 2 mrad of the axis of the medium. Ten beams hardly make an adequate statistical sample where thousands of beams must be followed to get quantitative estimates of integrated beam intensities and radial distributions. Work with a

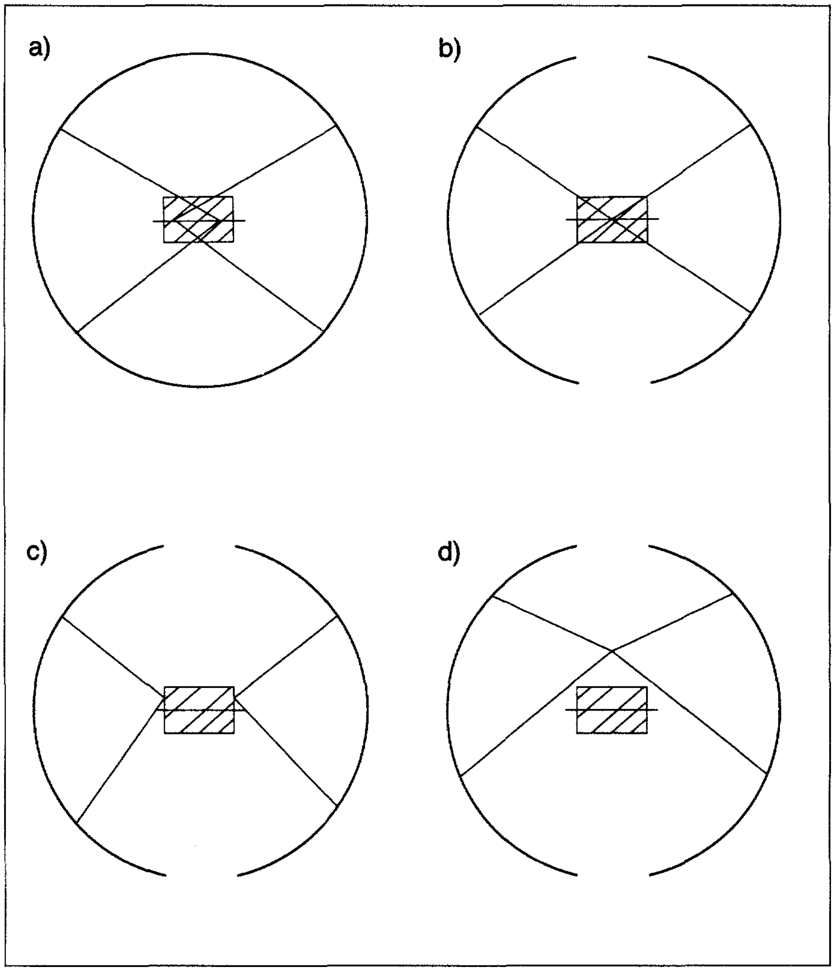

Fig. 3-39. Hemispherical mirrors were placed to the left and right of a gain region for computational studies of the effect of x-ray refraction. Adjustment of the positions of the two foci are shown for four representative configurations: overlapping along original foil axis (a), coincident on original foil axis (b), nonoverlapping in gain region (c), and coincident above gain region (d). The figure is not drawn to scale.

greater number of beams is currently being carried out; however, the limited samples described here give a qualitative idea of the effectiveness of the various configurations and provide us with guidance as to where to concentrate the future work.

In the data shown in Table 3-3, all beam intensities are normalized to 1 after the first pass through the medium. Thus, the "beam intensities" are intended only to give qualitative estimates of the effectiveness of various configurations. Their actual magnitudes are arbitrary, and do not take into account effects such as gain saturation. Mirror I is assumed to be on the right of the lasing medium as seen by the observer, and Mirror II is on the left.

The results indicate that hemispherical mirrors would be most effective when oriented with coincident foci at the center of the region of maximum gain. Moving the foci away from each other along an axis parallel to that of the medium does not improve the performance of the system. Moving the foci so that they overlap seems to impair system performance much more rapidly than moving the foci away from each other in the opposite direction. At the 200 Å wavelength for which the Table 3-3 results were obtained, beams started below the gain region were quickly refracted down and away from the gain region. At first glance, the results obtained for an axis above the gain region seem better than those for the axis below, even though the upper axis used was an order of magnitude farther away from the axis of maximum gain. However, these results are deceptive. It was found that the beam is directed down and out of the gain region on alternate bounces for the case of foci above the gain region. In a real multipass system, this implies that the beam would probably strike the solid surface from which the lasing medium was being regenerated for each pass.

Table 3-3. Effect on Beam Intensity of Moving Spherical Mirror Foci

Mirror I Coordinates	Mirror II Coordinates	Maximum Multiplication	Minimum Multiplication	Mean Multiplication
(0.0, −0.5)	(0.0, 0.5)	4.031 +4	1.953 −3	1.223 −2
(0.0, −0.25)	(0.0, 0.25)	2.984 +3	4.327 −2	4.616
(0.0, 0.0)	(0.0, 0.0)	4.388	0.771	2.399
(0.0, 0.25)	(0.0, 0.25)	4.610 −3	1.953 −3	2.288 −3
(0.0, 0.5)	(0.0, −0.5)	1.953 −3	1.953 −3	1.953 −3
(0.006, −0.5)	(0.006, 0.5)	2.237 +4	3.853 −3	2.553
(0.006, −0.25)	(0.006, 0.25)	9.837 +6	6.053	1.561 +3
(0.006, 0.0)	(0.006, 0.0)	2.572 +14	7.531 +6	5.981 +13
(0.006, 0.25)	(0.006, −0.25)	2.595 +14	3.879 +4	1.547 +11
(0.006, 0.5)	(0.006, −0.5)	8.364 +6	2.518 −3	3.970 +5
(0.06, −0.5)	(0.06, 0.5)	1.058 +1	1.105 −2	1.304 −1
(0.06, 0.0)	(0.06, 0.0)	5.816 +3	1.297	1.301 +3
(0.06, 0.5)	(0.06, −0.5)	1.628 +1	3.218 −2	6.058 −1

Results similar to those given above were obtained for a hypothetical 40 Å laser. As expected, at this wavelength, refraction effects were much less severe, and the performance of the system was less sensitive to small changes in foci location. However, once again, the most effective configuration seemed to be with coincident foci in the center of the region of maximum gain.

In conclusion, it is felt that, despite the limited size of the samples used to arrive at the above results, they give a good qualitative indication of the effectiveness of various multipass mirror configurations. Further work involving samples with thousands of beams is in progress, and is expected to yield more detailed information on beam intensities and radial distributions.

For additional information, please contact Dr. D. J. Drake

3.4.2 Advances in Computational Mathematics

Implicit Spectral Methods for the Nonlinear Wave Equation

General Form of the Equations. A central issue in inertial confinement fusion (ICF) is the interaction of laser light with normal modes (ion-acoustic or Langmuir) of the plasma.[42] The time-dependent, nonlinear wave equations that describe these interactions do not, in general, have known analytic solutions that can be expressed in terms of arbitrary initial conditions.[43] This difficulty leads us to use numerical techniques for approximating solutions to the wave equations. The general form of the equations is an initial value problem,

$$L(\vec{u}) + N(\vec{u}) = 0 \ , \tag{29}$$

$$\vec{u}(\vec{x},0) = u_0(\vec{x}) \ , \tag{30}$$

where $\vec{u} = \vec{u}(\vec{x},t)$ is a vector of unknown functions of time t and of the vector of space variables $\vec{x}$, L is a linear differential operator involving time and space derivatives, and N is a nonlinear differential operator involving only space derivatives.

Our general strategy for numerically approximating the solution $\vec{u}$ is to use spectral methods[43,44] to discretize Eq. (29) in space and to employ standard methods, such as the Crank–Nicolson numerical integration, to advance the solution in time.

Wave Propagation Equations. There are several wave propagation equations that can be effectively discretized via spectral methods. These include the equations of the Korteweg-de Vries (K–dV) type (in moving coordinates),

$$u_t + \Phi(u)_x + u_{xxx} = 0 \ , \tag{31}$$

and equations of the Kadomtsev–Petviashvili (K–P) type,

$$(u_t + \Phi(u)_x + u_{xxx})_x \pm u_{yy} = 0 \ . \tag{32}$$

Two families of equations, one for each sign, are defined by various constant coefficients for the four terms in Eq. (32).[45] For example, the classical case considered in the *KMS Fusion 1985 Annual Technical Report* has $\Phi(u) = 3u^2$.

The Fourier transform F of Eqs. (31) and (32) can be written in the form,

$$v_t + f(v) + w(K)\, v = 0 \ , \tag{33}$$

where $v := F(u)$ and the spectral variable is denoted by $K = (K_1, \ldots, K_d)$ with $d = 1$ for Eq. (31) and $d = 2$ for Eq. (32). (Note that the symbol := indicates a definition.) The function f for both Eqs. (31) and (32) is of the form,

$$f(v)(K) := iK_1 F\{\Phi[F^{-1}(v)]\} \ , \tag{34}$$

where F^{-1} denotes the inverse Fourier transform and i is the imaginary unit.

The dispersion relations are

$$w(K) := -iK^3 \tag{35}$$

and

$$w(K_1, K_2) := -iK_1^3 \pm i(K_2^2/K_1) \tag{36}$$

for the K–dV and the K–P equations, respectively.

Discretization Techniques. The use of an implicit method for the solution of Eq. (33) avoids severe time step restrictions.[46] The Crank–Nicolson scheme for the $m + 1$ time step,

$$v_K^{m+1} - v_K^m + \frac{\Delta t}{2} \left[f_n(v^{m+1})_K + w(K) v_K^{m+1} \right.$$
$$\left. + f_n(v^m)_K + w(K) v_K^m \right] = 0 \ , \tag{37}$$

is an implicit method that involves solving a nonlinear equation for v^{m+1} at each time step. Although the simplest approach to solving the system [Eq. (37)] is fixed-point iteration, convergence would require Δt to be of $0(\Delta x^3)$; this is a severe restriction, similar to the time-step limitations associated with explicit methods.

Equation (37) can be solved explicitly for the linear terms. Since $w(K)$ is purely imaginary, the $r + 1$ iteration,

$$v_K^{m+1,r+1} = \left[1 + \frac{\Delta t}{2}\, w(K) \right]^{-1}$$
$$\times \left\{ v_K^m - \frac{\Delta t}{2} \left[f_n(v^{m+1,r})_K + f_n(v^m)_K + w(K) v_K^m \right] \right\} , \tag{38}$$

has a much smaller spectral radius than fixed point iteration. In fact, we may write Eq. (38) in the form,

$$v_K^{m+1,r+1} = iK_1 \frac{\Delta t}{2} \left[1 + \frac{\Delta t}{2} w(K)\right]^{-1} F_n\left\{\Phi\left[F_n^{-1}(v^{m+1,r})\right]\right\}_K + g$$

$$= z(K)\, F_n\left\{\Phi\left[F_n^{-1}(v^{m+1,r})\right]\right\}_K + g \ , \tag{39}$$

where $|z|$ is bounded independently of n and Δt, and g is the collection of constant terms from Eq. (38).

Predictor-Corrector Schemes. From an analysis of the spectral radius of $z(K)$ (Ref. 46), one can propose efficient predictor-corrector schemes, based on the Crank-Nicolson discretization, that retain second-order accuracy for both K-dV and K-P equations. Perhaps the simplest approach involves the result from the previous time step as the initial guess for the nonlinear iteration. That is, set

$$v_K^{m+1,0} = v_K^m \tag{40}$$

and re-evaluate Eq. (38) twice, once with $r = 0$ and the second time with $r = 1$. Then set

$$v_K^{m+1} = v_K^{m+1,2} \tag{41}$$

and increment m.

For the K-P $(-u_{yy})$ equation, the final iterate $v^{m+1,2}$ is an approximate solution to Eq. (37) that is accurate to $0(\Delta t^{7/3})$, slightly better than second-order accuracy. The second-order accuracy for the K-P $(+u_{yy})$ equation follows from the restriction,

$$\Delta t \leq c \max\, [n_1^{-2}, n_2^{-1}] \ , \tag{42}$$

for some constant c. Other methods applied to Eq. (37) have produced better than $0(\Delta t^2)$ accuracy for all three of the K-dV, K-P $(-u_{yy})$, and K-P $(+u_{yy})$ equations.[46]

Dispersion Analysis of the von Neumann-Richtmyer Hydrocode Equations

Conservation Equations. In a hydrodynamics simulation code, a discrete version of the conservation laws of material dynamics is solved numerically on a specified mesh in the material. The mesh size has associated with it certain dispersion characteristics. That is, disturbances with different wavelengths have their wave speeds distorted to differing extents, depending on the mesh size and the stability conditions.

A dispersion analysis provides a mechanism for estimating the errors associated with the discretization of the continuum model. This is a fairly well known but underutilized approach to the error analysis of computational continuum dynamics.[47,48]

Dispersion relations for the conservation equations used in our simulation codes have been derived. The results provide the means for estimating the mesh size that will yield the desired resolution for the simulation of the material behavior.[49] The analysis was developed in a manner appropriate and useful for other ICF simulation hydrocodes. That is, while the details were derived for the von Neumann–Richtmyer (vNR) differencing scheme for a linearized system, the results have more general applications.

The dispersion analysis of the differencing scheme amounts to a finite Fourier analysis of the wave speeds and the wavelengths (or frequencies) of the modes that can be represented by the numerical solution. The work done at KMS Fusion (KMSF) was for the dispersion analysis of the vNR scheme for which the material law is the linear p-V equation of state.

The hydrodynamic equations for the continuum model are the conservation of volume, momentum, and energy,

$$\frac{\partial V}{\partial t} = \frac{\partial u}{\partial \mu} , \quad \frac{\partial u}{\partial t} = -\frac{\partial p}{\partial \mu} , \quad \frac{\partial E}{\partial t} = -\frac{\partial (up)}{\partial \mu} , \tag{43}$$

where V, u, and E are the specific volume, specific momentum (or velocity), and specific total energy, respectively.[50,51] The independent variable μ is the mass per cross-sectional area and p is the internal material pressure. An equation of state (EOS) for p is needed to complete the system. In order to perform the dispersion analysis, the system was linearized with the linear p-V equation of state,

$$p - p_0 = -a^2 (V - V_0) \ . \tag{44}$$

In this case, only the conservation laws for volume and momentum are needed to form a complete system in conjunction with the equation of state [Eq. (44)].

The motion function x is related to the specific volume and the specific momentum by the equations,

$$\frac{\partial x}{\partial \mu} = V \text{ and } \frac{\partial x}{\partial t} = u \ . \tag{45}$$

In the case of the linear p-V law [Eq. (44)], the foregoing equations reduce to the linear wave equation,

$$\frac{\partial^2 x}{\partial t^2} = a^2 \frac{\partial^2 x}{\partial \mu^2} \ . \tag{46}$$

The vNR discretizations[50,51] of the continuum Eqs. (43) for the conservation of volume and momentum are

$$\frac{V_{j+1/2}^{n+1} - V_{j+1/2}^{n}}{t^{n+1} - t^{n}} = \frac{u_{j+1}^{n+1/2} - u_{j}^{n+1/2}}{\mu_{j+1} - \mu_{j}} \tag{47}$$

and

$$\frac{u_{j}^{n+1/2} - u_{j}^{n-1/2}}{t^{n+1/2} - t^{n-1/2}} = -\frac{p_{j+1/2}^{n} - p_{j-1/2}^{n}}{\mu_{j+1/2} - \mu_{j-1/2}} \ . \tag{48}$$

Note that the notational convention adopted for this report uses integer and half-integer superscripts to indicate the location of the variable in time while the subscripts indicate the location in the material. Thus,

$$t^{n+1/2} = \frac{1}{2}\left(t^{n} + t^{n+1}\right) \quad \text{and} \quad \mu_{j+1/2} = \frac{1}{2}\left(\mu_{j} + \mu_{j+1}\right) \ . \tag{49}$$

The discrete forms of Eqs. (44) and (45) are

$$p_{j+1/2}^{n} = p_{0} - a^{2}\left(V_{j+1/2}^{n} - V_{0}\right) \ , \tag{50}$$

$$\frac{x_{j+1}^{n} - x_{j}^{n}}{\mu_{j+1} - \mu_{j}} = V_{j+1/2}^{n} \ , \quad \text{and} \quad \frac{x_{j}^{n+1} - x_{j}^{n}}{t^{n+1} - t^{n}} = u_{j}^{n+1/2} \ , \tag{51}$$

respectively.

By substituting the expressions (50) and (51) into the vNR difference Eqs. (47) and (48), we get

$$\frac{x_{j}^{n+1} - 2x_{j}^{n} + x_{j}^{n-1}}{\Delta t^{2}} = a^{2}\left(\frac{x_{j+1}^{n} - 2x_{j}^{n} + x_{j-1}^{n}}{\Delta\mu^{2}}\right) \tag{52}$$

as the discretization for the linear wave equation for a mesh that is uniform in Δt and $\Delta\mu$. The dispersion analysis for Eq. (52), as summarized below, was performed this year at KMSF.

The von Neumann-Richtmyer differencing scheme for all three conservation laws has been discussed by the authors in previous work.[52] However, the details of the corresponding dispersion analysis have not yet been worked out for the various equations of state and material laws that are very important to material dynamics research.

The Dispersion Analysis. Assume that the initial conditions $x(\mu,0)$ and $u(\mu,0)$ are given on the interval $[\mu_0,\mu_r]$. The boundary conditions for u or p are specified at the endpoints. For simplicity in the Fourier analysis, we assume that $[\mu_0,\mu_r] = [0,2\pi]$, which can be achieved by a simple linear scaling. A uniform mesh M_e was imposed on the material. The discretization contains $2M$ subintervals of the size

$$\Delta\mu = \pi/M \text{ with } \mu_j = j\Delta\mu \tag{53}$$

for $0 \leq j \leq 2M - 1$. There is an even number of points in M_e because the periodicity requirement makes it unnecessary to include the node μ_{2M}.

Since the wavenumber is

$$k = \frac{2\pi}{\lambda} , \tag{54}$$

the wavelength associated with $k = M$ is

$$\lambda = 2\Delta\mu \tag{55}$$

from Eq. (53). Equation (55) represents the shortest possible wavelength that can be resolved by the mesh. The characteristic that identifies a numerical instability is a growing oscillation at the noise wavelength defined by Eq. (55). It turns out that the wave speed distortion is most severe at this wavelength in the vNR scheme.

It is well known that the waves modeled by Eq. (46) all travel with speeds $\pm a$. In other words, for all wavenumbers k, the function,

$$x(\mu,t) = e^{ik(\mu \pm at)} , \tag{56}$$

is a solution to the linear wave Eq. (46). Thus, the Fourier expansion,

$$x(\mu,t) = y(\mu) + \sum_{-\infty}^{\infty} b_k e^{ik(\mu+at)} + c_k e^{ik(\mu-at)} , \tag{57}$$

yields the general solution, where $y(\mu)$ is a linear function satisfying the boundary conditions.

In a similar fashion, the solution to the discrete linear wave equation satisfying the initial and boundary values is derived using a finite Fourier analysis. That is, we now seek a_k, the numerical wave speed for wavenumber k, such that

$$x_j^n = e^{ik(\mu_j \pm a_k t^n)} \tag{58}$$

is a solution to the vNR scheme [Eq. (52)]. Thus, the discrete linear wave equation satisfying the initial and boundary conditions may be expressed in the form,

$$x_j^n = y_j + \sum_{k=-M}^{M} b_k e^{ik(\mu_j + a_k t^n)} + c_k e^{ik(\mu_j - a_k t^n)} , \tag{59}$$

where $y_j = y(\mu_j)$.

The deviation of the a_k's from the wave speed a is an indication of the dispersion tendency. The formula for a_k in terms of k is called the dispersion relation. If the discrete equation were a perfect analog of the continuum equation, then a_k would be equal to a for all k. However, we have found that, in general, $a_k < a$ for the linearized vNR equations. The wave speed a_k is equal to a only in isolated circumstances.

From Eq. (52), the vNR discretization may be rewritten as

$$x_j^{n+1} - 2x_j^n + x_j^{n-1} = C_{FL}^2 (x_{j+1}^n - 2x_j^n + x_{j-1}^n) \ , \tag{60}$$

where the C_{FL} (Courant–Friedrich–Lewy) number is defined by

$$C_{FL} = \frac{a\Delta t}{\Delta\mu} \ . \tag{61}$$

The solution x_j^n can be written in the form,

$$x_j^n = A^n B^j \ , \tag{62}$$

where

$$A = e^{i\alpha} \quad \text{and} \quad B = e^{i\theta} \ , \tag{63}$$

with the definitions,

$$\alpha = \frac{a_k}{a} C_{FL}\theta \quad \text{and} \quad \theta = k\Delta\mu \ . \tag{64}$$

The domain of θ *is*

$$0 \leq \theta \leq \pi \ . \tag{65}$$

Substituting the expression (62) for x_j^n into the vNR discretization (60) yields

$$A - 2 + A^{-1} = C_{FL}^2 (B - 2 + B^{-1}) \tag{66}$$

or, with Euler's identity,

$$\cos\alpha - 1 = C_{FL}^2 (\cos\theta - 1) \ , \tag{67}$$

for $0 \leq \theta \leq \pi$. This is the dispersion relation for the vNR discretization.

Analysis of Eq. (67) has shown that, when $C_{FL} = 1$,

$$a_k = a \tag{68}$$

for all k. Thus, for this case, the vNR discretization provides a perfect analog to the linear wave equation. This phenomenon for the linear p-V law (50) is called the CFL1 property.[53]

Values for the ratio of the wave speeds,

$$r(\theta) = \frac{a_k}{a} \ , \tag{69}$$

were calculated from the dispersion relation [Eq. (67)] for $0 \leq \theta \leq \pi$ where θ is defined by Eq. (64). The function $r(\theta)$ is plotted on Fig. 3-40. Nine different curves, $c_0, c_1, \ldots, c_8$, are shown, where curve c_j has a C_{FL} number of $j/8$ for $j = 0, 1, \ldots, 8$. For all j, the c_j curve lies below the c_{j+1} curve. In other words, the a_k/a ratio decreases monotonically with the C_{FL} number for each value of θ.

It is interesting to note that on the c_0 curve at $\theta = \pi/2$ the value of $r(\theta)$ is approximately 0.9. For the wavelength $\lambda = 4\Delta\mu$ (or $k = M/2$), the least possible ($C_{FL} = 0$) value of a_k/a is about 0.9. In other words, the numerical wave speed for wavelength $\lambda = 4\Delta\mu$ is about 90% of the wave speed for the continuum model.

For a more complete analysis of the dispersion relation, we can also include various forms of the viscous stress. By following the steps in the dispersion analysis demonstrated above, it is possible to redo the work for variations to the basic vNR differencing scheme. We have illustrated the utility of the dispersion analysis with a numerical example.[49]

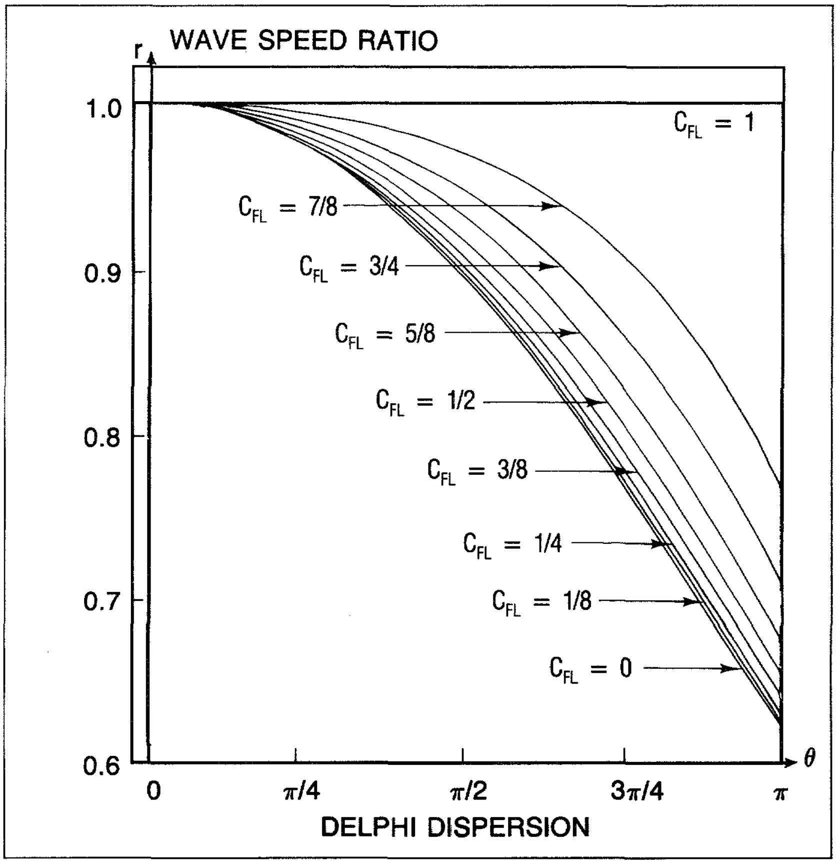

Fig. 3-40. The plots of the function (69) show increasing dispersion (or decreasing numerical wave speed) for decreasing values of C_{FL} and increasing values of θ. The dispersion relation is given by Eq. (67).

Inversion of a First-Kind Integral Equation as a Plasma Diagnostic

The Plasma Diagnostic. The radiation energy emitted from a plasma contains information about its electron density and temperature. These are important properties in many laser/material interaction experiments. Some of the diagnostic equipment at KMSF focuses the radiation from a plasma through an image-forming x-ray slit onto a potassium acid phthalate (KAP) crystal. A second x-ray slit selects a cross-section of the spectrally separated reflections. An x-ray camera streaks the images across the film. Thus, the film records time-resolved images of the x-ray intensities from a cross-section of the plasma.

The Mathematical Problem. From an x-ray image recorded on film, it is our task to calculate the radiation profile of the plasma. In laser-driven experiments, the radiation from a three-dimensional plasma is projected onto the two-dimensional (2-d) surface of a film. Inverting this projection for the radiation density is a classic poorly posed problem. A one-dimensional (1-d) slice of the data is the projection of a 2-d cross-section of the plasma. If the plasma is cylindrically symmetric, a slice of the data corresponding to a cross-section that is orthogonal to the axis of symmetry is a collection of discrete values of the Abel transform of the radiation profile.

In recent work at KMSF, an improvement has been developed for the computational deconvolution of the data. Using the techniques expounded in reports by Wing[54] and by Faber and Wing[55], a 1-d slice of real data is inverted for the radiation profile in a cross-section of the plasma, based on the assumption of cylindrical symmetry. The solution is computed in terms of the singular value decomposition of the Abel transform.[56] An explanation of the theory of the singular value decomposition method is contained in the reference by Forsythe, Malcolm, and Moler.[57]

Numerical Solution – Cylindrical Symmetry. A column of data corresponding to a slice through an x-ray image orthogonal to the laser beam axis has been selected for demonstrating the analysis discussed in this report. It is reproduced in Fig. 3-41. Each point on this plot of radiation intensity represents the value of the integral of the power density in normalized units along a line of sight through the plasma. Figure 3-42 illustrates the mathematical model for the plasma diagnostic. Note that the model is based on the assumption of a refractionless plasma. That is, the electron density is sufficiently low for the x-ray energy to travel along the line of sight.

The value of $\phi(y)$ in Fig. 3-42 is the measured intensity due to the power density $f(x,y)$ along the horizontal line with coordinate y. Thus, $\phi(y)$ is the line integral of $f(x,y)$,

$$\phi(y) = \int_{-\sqrt{R^2-y^2}}^{\sqrt{R^2-y^2}} f(x,y)\,dx \ . \tag{70}$$

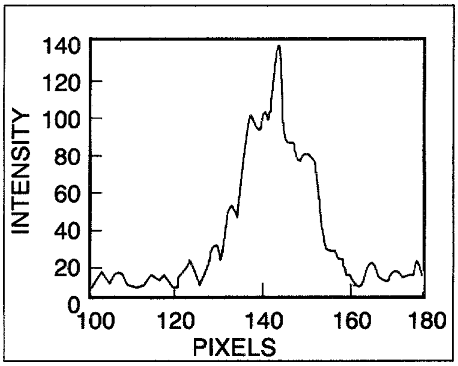

Fig. 3-41. A densitometer trace along a line orthogonal to the axis of a cylindrically symmetric plasma was converted to values of the radiation intensity in the plane of the film of an x-ray streak camera. The curve shows the measurement values of the Abel transform of the emission of x- rays from the plasma.

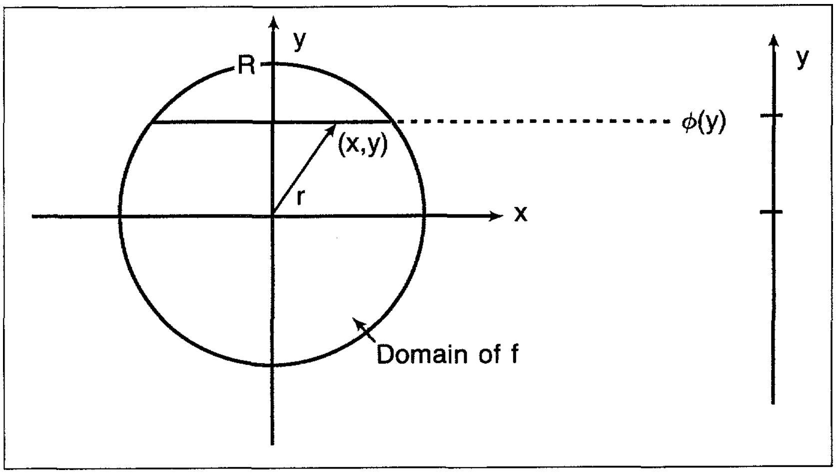

Fig. 3-42. The intensity at the "film plane" $\phi(y)$ is the line integral of the radiation density f along the path through the plasma at coordinate y.

The assumption of cylindrical symmetry implies symmetry with respect to the origin in Fig. 3-42. Thus, the function f can be redefined by

$$f(r) = f(x,y). \tag{71}$$

A change of variables converts the line integral for $\phi(y)$ in Eq. (70) into

$$2\int_y^R \frac{rf(r)\,dr}{\sqrt{r^2-y^2}} = \phi(y) \ , \tag{72}$$

which is referred to as the Abel transform of the function f (or of $rf(r)$). Equation (72) is a first-kind Volterra integral equation, a mathematically poorly posed and numerically ill conditioned problem. The solution can be evaluated numerically by representing f in terms of the singular vectors of the discrete analog to Eq. (72).

For simplicity, y is assumed to be positive in Eq. (72) and in the following discussion. It is easy to generalize the mathematics to allow y to be negative. Indeed, our implementation for computing solutions takes measurements at negative values of y into account.

Let

$$K(y,r) = \begin{cases} \dfrac{2r}{\sqrt{r^2-y^2}} & \text{for } r > y \\ 0 & \text{for } r \le y \end{cases} . \tag{73}$$

Select an arbitrary partition of the interval $[0,R]$ defined by

$$0 = r_0 < r_1 < \ldots < r_N = R. \tag{74}$$

Also define

$$r_{j-1/2} = \frac{1}{2}\,(r_{j-1} + r_j) \qquad (75)$$

for $j = 1, 2, \ldots, N$. For each measurement at the points

$$0 \le y_1 < y_2 < \ldots < y_M \le R \qquad (76)$$

the generalized midpoint quadrature rule for the Abel transform yields

$$\phi(y_i) \simeq 2\sqrt{r_k^2 - y_i^2}\, f_{k-1/2} + 2 \sum_{j=k+1}^{N} \left(\sqrt{r_j^2 - y_i^2} - \sqrt{r_{j-1}^2 - y_i^2}\right) f_{j-1/2} \qquad (77)$$

for

$$r_{k-1} \le y_i < r_k \ , \qquad (78)$$

where $f_{j-1/2}$ is the approximate value of $f(r_{j-1/2})$.

The linear system defined by Eq. (77) can be written in the form,

$$Kf = \phi \ , \qquad (79)$$

where

$$f = (f_{1/2}, f_{3/2}, \ldots, f_{N-1/2})^T \text{ and } \phi = (\phi_1\ , \phi_2, \ldots, \phi_M)^T \ . \qquad (80)$$

For example, if the r's and y's are distributed between 0 and R such that

$$0 = r_0 < y_1 < y_2 < r_1 < y_3 < r_2 < y_4 < y_5 < r_3 = R \ , \qquad (81)$$

then K is the following 5×3 matrix:

$$\begin{bmatrix} 2\sqrt{r_1^2 - y_1^2} & 2\left(\sqrt{r_2^2 - y_1^2} - \sqrt{r_1^2 - y_1^2}\right) & 2\left(\sqrt{r_3^2 - y_1^2} - \sqrt{r_2^2 - y_1^2}\right) \\ 2\sqrt{r_1^2 - y_2^2} & 2\left(\sqrt{r_2^2 - y_2^2} - \sqrt{r_1^2 - y_2^2}\right) & 2\left(\sqrt{r_3^2 - y_2^2} - \sqrt{r_2^2 - y_2^2}\right) \\ 0 & 2\sqrt{r_2^2 - y_3^2} & 2\left(\sqrt{r_3^2 - y_3^2} - \sqrt{r_2^2 - y_3^2}\right) \\ 0 & 0 & 2\sqrt{r_3^2 - y_4^2} \\ 0 & 0 & 2\sqrt{r_3^2 - y_5^2} \end{bmatrix} \qquad (82)$$

We have solved Eq. (79) twice, once with the data to the right of the peak in Fig. 3-41 and again with the data to the left. The results are displayed in Fig. 3-43. While the two solutions show similar qualitative behavior, they are not the same.

In the preceding analysis, only positive values of y were taken into account. However, the discussion requires only slight modifications to take into account measurements $\phi(y_i)$ for any

$$|y_i| < R \ . \qquad (83)$$

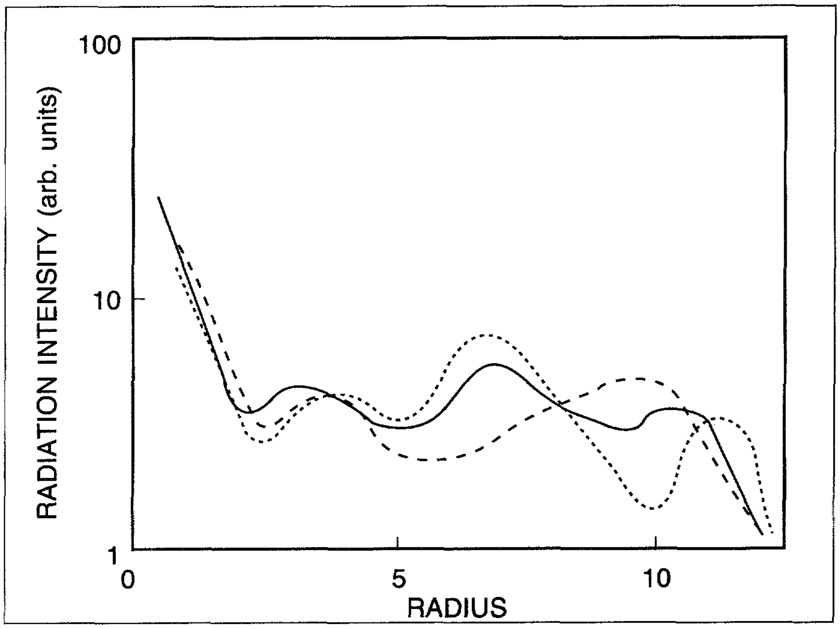

Fig. 3-43. The solution to Eq. (79) in normalized units was calculated for three sets of data: The dashed line represents the solution for the data to the right of the peak intensity shown in Fig. 3-41, the dotted line for the data to the left, and the solid for the two sets combined.

Our computer code incorporates this generalization. Consequently, we solved Eq. (79) a third time using the data from both sides of the peak in Fig. 3-41. This result is also shown in Fig. 3-43.

The computer program generates the solution in terms of the singular vectors corresponding to the largest singular values. Also, the least-squares solution is computed when $M > N$; that is, when f is calculated at a smaller number of points than there are measurements. Thus, there are two mechanisms for smoothing the solution: calculating the best value of $P \leq N$ and choosing $N < M$ where P, N, and M are the number of singular vectors used to resolve the solution f, the number of degrees of freedom in the solution (the number of unknowns), and the number of measurements, respectively.

For the solutions shown in Fig. 3-43, there were $M = 22$ measurements from the right side of the peak in Fig. 3-41 and $M =$ 19 measurements from the left. The dashed curve shows the solution from the data to the right of the peak with $P = N = 14$. The dotted curve came from the data to the left of the peak with $P = N = 12$. Finally, the solid curve on Fig. 3-43 is the solution from the $M = 40$ measurements from both sides of the peak with $N = 26$ and $P = 22$. For the smooth curves shown in Fig. 3-43, a cubic spline that respects monotonicity was used to interpolate the discrete data.

For additional information, please contact Dr. J. F. McGrath

REFERENCES

1. C. L. Shepard, J. A. Tarvin, R. L. Berger, Gar. E. Busch, R. R. Johnson, and R. J. Schroeder, *Phys. Fluids* **29**(2) (1986), p. 583.
2. W. C. Mead, E. M. Campbell, K. G. Estabrook, R. E. Turner, W. L. Kruer, P. H. Y. Lee, B. Pruett, V. C. Rupert, K. G. Tirsell, G. L. Stradling, F. Ze, C. E. Max, M. D. Rosen, and B. F. Lasinski, *Phys. Fluids* **26**(8) (1983), p. 2316.
3. Gar. E. Busch, C. L. Shepard, L. D. Siebert, and J. A. Tarvin, *Rev. Sci. Instrum.* **56**(5) (1985), p. 879.
4. J. A. Stamper and B. H. Ripin, *Phys. Rev. Lett.* **34** (1975), p. 138.
5. J. A. Stamper, E. A. McLean, and B. H. Ripin, *Phys. Rev. Lett.* **40** (1978), p. 1177.
6. B. Grek, F. Martin, T. W. Johnston, H. Pepin, G. Mitchel, and F. Rheault, *Phys. Rev. Lett.* **41** (1978), p. 1811.
7. G. Thiell and B. Meyer, *Laser and Particle Beams* **3** (1985), p. 51.
8. *KMS Fusion 1987 Annual Technical Report on Inertial Fusion Research* (KMS Fusion, Inc., Ann Arbor, MI), pp. 35–42. KMSF-U1962.
9. S. R. Stone and J. C. Weisheit, Lawrence Livermore National Laboratory Report UCID-20262 (Lawrence Livermore National Laboratory, Livermore, CA, 1984); V. A. Boiko et al., *Sov. J. Plasma Phys.* **10** (1984), pp. 82–86; R. L. Kauffman et al., *Phys. Rev. A* **35**(10) (1987), pp. 4286–4294.
10. M. J. Herbst et al., *Rev. Sci. Instrum.* **53**(9) (1982), pp. 1418–1422.
11. *KMS Fusion January–March 1988 Quarterly Progress Report* (KMS Fusion, Inc., Ann Arbor, MI), pp. 10–27. KMSF-U2055.
12. Gar. E. Busch et al., *Rev. Sci. Instrum.* **56**(5) (1985), pp. 879–884.
13. B. K. F. Young et al., *Rev. Sci. Instrum.* **57**(11) (1986), pp. 2729–2732.
14. B. K. F. Young et al., *SPIE Atomic Proc. in Plasmas*, Santa Fe (1987).
15. C. DeMichelis and M. Mattioli, *Nucl. Fusion* **21**(6) (1984), pp. 677–754.
16. R. W. Lee, *J. Quant. Spectrosc. Radiat. Transf.* **31** (1984), pp. 91–101.
17. G. Charatis et al., *J. de Physique* (December 1987).
18. V. A. Boiko et al., *Sov. J. Quant. Electron.* **4** (1975), p. 1212.
19. J. F. Seely et al., *Phys. Rev. A* **34** (1986), p. 2942.
20. J. Bailey et al., *J. Phys. B* **19** (1986), p. 2639.
21. W. H. Goldstein et al., *Phys. Rev. Lett.* **58** (1987), p. 2300.
22. P. D. Rockett et al., *Proc. SPIE* Vol. 689 (1986), p. 114.
23. S. P. Obenschain, et al., "Laser-Target Interaction with Induced Spatial Incoherence," *Phys. Rev. Lett.* **56** (1988), p. 2802.
24. A. N. Mostovych, et al., "Brillouin Scattering Measurements from Plasmas Irradiated with Spatially and Temporally Incoherent Light," Naval Research Laboratory Report #6105 (1987).
25. R. L. Berger, "Parametric Instabilities in a Spatially Incoherent Laser Beam," *KMS Fusion 1987 Annual Technical Report on Inertial Fusion Research* (KMS Fusion, Inc., Ann Arbor, MI), pp. 56–60. KMSF-U1962.
26. C. J. Walsh, D. M. Villeneuve, and H. A. Baldis, *Phys. Rev. Lett.* **53** (1985), p. 1445.
27. V. E. Zakharov, *Zh. Eksp. Teor. Fiz.* **62** (1972), p. 1745 [*Sov. Phys. JETP* **35** (1972), p. 908].
28. H. A. Rose, D. F. DuBois, and B. Bezzerides, *Phys. Rev. Lett.* **58** (1987), p. 2547.
29. *KMS Fusion 1986 Annual Technical Report on Inertial Fusion Research* (KMS Fusion, Inc., Ann Arbor, MI), pp. 46–50. KMSF-U1871.
30. G. D. Doolen, D. F. DuBois, and H. A. Rose, *Phys. Rev. Lett.* **54** (1985), p. 804.
31. D. Russell, D. F. DuBois, and H. A. Rose, *Phys. Rev. Lett.* **56** (1986), p. 838.

32. J. P. Sheerin, D. R. Nicholson, and G. L. Payne, *Bull. Am. Phys. Soc.* **31** (1986), p. 1446.

33. J. P. Sheerin, "Numerical Studies of Ultra-Strong Langmuir Turbulence," *Seventeenth Annual Anomalous Absorption Conference*, Tahoe City, CA (1987).

34. *KMS Fusion April–June 1987 Quarterly Progress Report* (KMS Fusion, Inc., Ann Arbor, MI). KMSF-U1938.

35. *KMS Fusion 1987 Annual Technical Report on Inertial Fusion Research* (KMS Fusion, Inc., Ann Arbor, MI), pp. 52–55. KMSF-U1962.

36. J. P. Sheerin, *Bull. Am. Phys. Soc.* **32** (1987), p. 1716.

37. D. R. Nicholson, G. L. Payne, R. M. Downie, and J. P. Sheerin, *Phys. Rev. Lett.* **52** (1984), p. 2152.

38. G. L. Payne, D. R. Nicholson, R. M. Downie, and J. P. Sheerin, *J. Geophys. Res.* **89** (1984), p. 10921.

39. L. V. Powers and R. L. Berger, "Nonlinear behavior of coupled two-plasmon decay and stimulated Raman scattering," *Bull. Am. Phys. Soc.* **30** (1988), p. 1527.

40. L. V. Powers and R. L. Berger, "SATIN: a fluid code to study the nonlinear evolution of two-plasmon decay and stimulated Raman scattering," *Proceedings of the 1985 CECAM Workshop*, Orsay, France, September 16–27, 1985.

41. H. A. Rose, D. F. DuBois and B. Bezzerides, "Nonlinear coupling of stimulated Raman and Brillouin scattering in laser-plasma interactions," *Phys. Rev. Lett.* **58** (1987), p. 2547; G. Bonnaud and D. Pesme, "Stimulated Raman scattering and ion dynamics: the role of Langmuir wave nonlinearities," to be published in *Laser Interaction and Related Plasma Phenomena*, Vol. 8 (1988).

42. J. F. Drake, P. K. Kaw, Y. C. Lee, G. Schmidt, C. S. Liu, and M. N. Rosenbluth, *Phys. Fluids* **17** (1974), p. 778.

43. D. Gottlieb and S. A. Orszag, *Numerical Analysis of Spectral Methods: Theory and Applications* (SIAM, Philadelphia, 1981).

44. *KMS Fusion 1985 Annual Technical Report on Inertial Fusion Research* (KMS Fusion, Inc., Ann Arbor, MI), pp. 52–54. KMSF-U1728.

45. M. J. Ablawit and H. Segur, *Solitons and the Inverse Scattering Transform* (SIAM, Philadelphia, 1981).

46. L. R. Scott, E. F. Gabl, J. F. McGrath, S. B. Wineberg, and C. E. Southwell, "Implicit Spectral Methods for Wave Propagation Problems," KMS Fusion Technical Report KMSF-U2115 (KMS Fusion, Inc., Ann Arbor, MI, 1988).

47. R. Vichnevetsky, "Energy and Group Velocity in Semidiscretizations of Hyperbolic Equations," *Math. & Comp. in Sim.* **23** (1981), pp. 333–343.

48. R. Vichnevetsky, "Propagation through Numerical Mesh Refinement for Hyperbolic Equations," *Math. & Comp. in Sim.* **23** (1981), pp. 344–353.

49. D. L. Hicks, J. F. McGrath, and L. M. Liebrock, "Dispersion Analysis of the von Neumann–Richtmyer Hydrocode Equations," KMS Fusion Technical Report KMSF-U2070 (KMS Fusion, Inc., Ann Arbor, MI, 1988).

50. J. von Neumann and R. D. Richtmyer, "A Method for the Numerical Calculation of Hydrodynamic Shocks," *J. Appl. Phys.* **21** (1950), pp. 232–237.

51. R. D. Richtmyer and K. W. Morton, *Difference Methods for Initial Value Problems* (Interscience, New York, 1967).

52. D. L. Hicks, L. M. Liebrock, and J. F. McGrath, "A Lagrangian Hydrocode in One Spatial Dimension," KMS Fusion Technical Report KMSF-U1957 (KMS Fusion, Inc., Ann Arbor, MI, 1988).

53. D. L. Hicks and M. M. Madsen, "An Accuracy Property of Certain Hyperbolic Difference Schemes," Sandia National Laboratories Report SAND-76-0389 (Sandia National Laboratories, Albuquerque, NM, 1976).

54. G. Milton Wing, "A Primer on Integral Equations of the First Kind," Los Alamos National Laboratory Report LA-UR–84-1234, to be published by SIAM.

55. V. Faber and G. Milton Wing, "The Abel Integral Equation," Los Alamos National Laboratory Report LA-11016-MS (1987).

56. J. F. McGrath, G. Charatis, R. J. Schroeder, and S. B. Wineberg, "Inversion of a First Kind Integral Equation as a Plasma Diagnostic," *Proc. Conf. on Transport Theory, Invariant Imbedding, and Integral Equations*, edited by P. Nelson et al. (Marcel Dekker, Inc., New York and Basel, 1989), pp. 325–341.

57. G. E. Forsythe, M. A. Malcolm, and C. B. Moler, *Computer Methods for Mathematical Computations* (Prentice Hall, Englewood Cliffs, NJ, 1977).

PRESENTATIONS AND PUBLICATIONS

SECTION FOUR

Introduction

The inertial confinement fusion (ICF) research performed at KMS Fusion (KMSF) is of value not only to KMSF and the other participants in the national ICF program, but also to the broader scientific community. The results of our unclassified research are shared via technical reports such as this, presentations at scientific conferences, and articles published in technical journals. This final section of our 1988 Annual Technical Report provides a record of the ICF-related articles presented and published by KMSF personnel for the reporting period, October 1, 1987, through September 30, 1988.

Some of these presentations and publications describe research projects conducted jointly with other laboratories. In these cases, the affiliations of non-KMSF authors are indicated in parentheses after their names. For reasons of space, abbreviations are used for Lawrence Livermore National Laboratory (LLNL), Los Alamos National Laboratory (LANL), and the National Bureau of Standards (NBS).

SECTION 4.1

Presentations

C. J. Armentrout, J. B. Geddes, P. Lee (GA Tech.), R. T. Snider (GA Tech.), L. R. Canfield (GA Tech.), "UV to SXR Surveys Using a Compact, Biplanar Diode Array," *7th Topical Conference on High Temperature Plasma Diagnostics*, Napa, CA, March 13–17, 1988. KMSF-U2018ab.

C. J. Armentrout, E. F. Gabl, G. E. Busch, B. H. Failor, R. J. Schroeder, and Z. M. Koenig, "Survey of Recent KMS Gold Disk Experiments," *18th Annual Anomalous Absorption Conference*, L'Estérel, PQ, June 27–July 1, 1988. KMSF-U2040ab.

R. L. Berger, J. R. Albritton (LLNL), and C. J. Randall (LLNL), "Stopping and Thermalization of Interpenetrating Plasma Streams," *18th Annual Anomalous Absorption Conference*, L'Estérel, PQ, June 27–July 1, 1988. KMSF-U2041ab.

R. L. Crawley, H. K. Lintz, J. C. Daukas, and S. R. Murrell, "The Incorporation of OH Groups in Plasma Polymers for Use as Permeation-Resistant Coatings," *34th National Symposium of the American Vacuum Society/Topical Conference on Superconductivity*, Anaheim, CA, November 2–5, 1987. KMSF-U1876ab.

R. L. Downs, "ICF Target Technology at KMS Fusion, Inc.," *International Symposium on Fusion Nuclear Technology*, Tokyo, Japan, April 10–15, 1988. KMSF-U2022ab.

M. A. Ebner, L. T. Thompson, and W. J. Miller, "The Reactivity of Residual Blowing Gases in Glass Shells," *6th Target Fabrication Specialists Meeting*, Los Alamos, NM, June 20–24, 1988. KMSF-U1976ab.

B. H. Failor, E. F. Gabl, G. E. Busch, R. J. Schroeder, C. J. Armentrout, and Z. M. Koenig, "Dynamics of Au Plasmas Produced by Temporally Shaped Laser Pulses," *18th Annual Anomalous Absorption Conference*, L'Estérel, PQ, June 27–July 1, 1988. KMSF-U2036ab.

W. B. Fechner, "Theoretical Analysis of Recent KMS Gold Disk Experiments," *18th Annual Anomalous Absorption Conference*, L'Estérel, PQ, June 27–July 1, 1988. KMSF-U2037ab.

E. F. Gabl, B. H. Failor, R. R. Johnson, C. L. Shepard, and G. Charatis, "Recent Point/Flash X-ray Backlighting Experiments at KMSF: Source, Spectra, and X-ray Conversion Measurements," *29th Annual Meeting of the Division of Plasma Physics of the American Physical Society*, San Diego, CA, November 2–6, 1987. KMSF-U1930ab.

R. L. Hays, "Introduction to SMG, the VMS Screen Management Utility," *1987 Fall Digital Equipment Computer Users' Society Symposium*, Anaheim, CA, December 7–11, 1987. KMSF-U1896ab.

R. L. Hays, "Vectoring Privileged Tasks and RSX-11/M+V3.0," *1987 Fall Digital Equipment Computer Users' Society Symposium*, Anaheim, CA, December 7–11, 1987. KMSF-U1897ab.

R. L. Hays, “Archiving Under VAX/VMS—Problems, Pitfalls, and Solutions,” *1988 Spring Digital Equipment Computer Users’ Society Symposium*, Cincinnati, OH, May 16–20, 1988. KMSF-U1973ab.

R. P. Johnson and L. D. Siebert, “Output Pulse Shape Control on a High Power Solid State Laser Using Electronic Feedback,” *International Conference on Lasers*, Lake Tahoe, NV, December 7–11, 1987. KMSF-U1911ab.

R. R. Johnson, “Development of a High Resolution X-ray Backlighter for Measurements in High Density Implosions,” *8th International Workshop on Laser Interaction and Related Plasma Phenomena*, Monterey, CA, October 26–30, 1987. KMSF-U1940ab.

T. M. Henderson, “Status of ICF Coating Technology,” *34th National Symposium of the American Vacuum Society/Topical Conference on Superconductivity*, Anaheim, CA, November 2–5, 1987. KMSF-U1934ab.

T. M. Henderson, “Target Fabrication Requirements for the LMC,” *6th Target Fabrication Specialists Meeting*, Los Alamos, NM, June 20–24, 1988. KMSF-U2029ab.

Z. M. Koenig, “A Soft X-ray Bragg Spectrograph with an Intensified Framing Camera,” *7th Topical Conference on High Temperature Plasma Diagnostics*, Napa, CA, March 13–17, 1988. KMSF-U2017ab.

K. L. Marsh and A. J. Twarowski, “RED-DEVL: Red Dioxetane Energized Vapor Laser,” *1st Winter Conference of the International American Photochemical Society*, Clearwater, FL, January 3–7, 1988. KMSF-U1956ab.

J. F. McGrath, G. Charatis, and S. B. Wineberg, “Inversion of a First-kind Integral Equation as a Plasma Diagnostic,” *Conference on Transport Theory, Invariant Imbedding, and Integral Equations*, Santa Fe, NM, January 20–22, 1988. KMSF-U1954ab.

W. J. Miller and R. P. Belanger, “Recent Results in Glass Shell Fabrication,” *6th Target Fabrication Specialists Meeting*, Los Alamos, NM, June 20–24, 1988. KMSF-U1972ab.

M. T. Mruzek and D. L. Musinski, “Design Strategy for the Cryogenic DT Pressure Intensifier System at LANL,” *6th Target Fabrication Specialists Meeting*, Los Alamos, NM, June 20–24, 1988. KMSF-U1987ab.

S. R. Murrell, G. B. DeMaggio, H. K. Lintz, J. A. Ruppe, and J. C. Daukas, “The Fabrication of ‘Gaussian Bumps’ on Small Spherical Substrates,” *6th Target Fabrication Specialists Meeting*, Los Alamos, NM, June 20–24, 1988. KMSF-U1985ab.

D. L. Musinski, M. T. Mruzek, and W. J. Felmlee, “The Beta Heating Redistribution of DT Solid Fuel in Glass Shells,” *6th Target Fabrication Specialists Meeting*, Los Alamos, NM, June 20–24, 1988. KMSF-U1994ab.

L. V. Powers, R. L. Berger, and J. P. Sheerin, “Density Gradient Effects in the Competition Between Stimulated Raman Scattering and Brillouin Scattering,” *18th Annual Anomalous Absorption Conference*, L’Estérel, PQ, June 27–July 1, 1988. KMSF-U2031ab.

L. V. Powers, J. P. Sheerin, and R. L. Berger, “Effect of Ion Motion on Two-Plasmon Decay in Stimulated Raman Scattering,” *29th Annual Meeting of the Division of Plasma Physics of the American Physical Society*, San Diego, CA, November 2–6, 1987. KMSF-U1926ab.

R. G. Schneggenburger, "DT Out Permeation Rates in PVA Shells at Subambient Temperatures," *6th Target Fabrication Specialists Meeting*, Los Alamos, NM, June 20–24, 1988. KMSF-U1984ab.

R. G. Schneggenburger, L. A. Laughrey, D. A. Butkiewicz, and K. A. Bandy, "Measurement of Glass Shell Buckling Strength Using Piezoelectric Film Sensor," *6th Target Fabrication Specialists Meeting*, Los Alamos, NM, June 20–23, 1988. KMSF-U1993ab.

R. J. Schroeder, E. F. Gabl, B. H. Failor, W. B. Fechner, and K. L. Marsh, "Critical and 1/4 Critical Density Trajectories in High-Z Planar Targets," *18th Annual Anomalous Absorption Conference*, L'Estérel, PQ, June 27–July 1, 1988. KMSF-U2039ab.

R. J. Schroeder, B. H. Failor, and R. L. Hays, "A Lens-Coupled Intensified CCD Streak Camera Readout System," *29th Annual Meeting of the Division of Plasma Physics of the American Physical Society*, San Diego, CA, November 2–6, 1987. KMSF-U1932ab.

L. A. Scott and A. J. Martin, "Fabrication of Macroshell® Targets for β-Heating Experiments," *6th Target Fabrication Specialists Meeting*, Los Alamos, NM, June 20–24, 1988. KMSF-U1981ab.

J. P. Sheerin, "Ultra-strong Langmuir Collapse in Open Systems," *29th Annual Meeting of the Division of Plasma Physics of the American Physical Society*, San Diego, CA, November 2–6, 1987. KMSF-U1931ab.

J. P. Sheerin, "Simulations of Ultra-strong Langmuir Turbulence in Open Systems," *18th Annual Anomalous Absorption Conference*, L'Estérel, PQ, June 27–July 1, 1988. KMSF-U2033ab.

C. L. Shepard, R. R. Johnson, B. H. Failor, E. F. Gabl, Gar. E. Busch, G. Charatis, and R. J. Schroeder, "Development of a Bright X-ray Source of $\simeq$ 10 μm Size in 3–5 keV Photon Energy," *29th Annual Meeting of the Division of Plasma Physics of the American Physical Society*, San Diego, CA, November 2–6, 1987. KMSF-U1928ab.

D. A. Steinman, "An Automatic Technique for Spheroidizing Glass Shells," *6th Target Fabrication Specialists Meeting*, Los Alamos, NM, June 20–24, 1988. KMSF-U1995ab.

L. T. Thompson, "Aerodynamic Drag on Hollow Liquid Droplets," *6th Target Fabrication Specialists Meeting*, Los Alamos, NM, June 20–24, 1988. KMSF-U1991ab.

SECTION 4.2

Publications

J. S. Ankney, M. T. Mruzek, and D. N. Decker, "Imaging System for Solid Deuterium-Tritium Layers Held in an Isothermal Environment," *J. Vac. Sci. Technol. A* **6**(3) (May–June 1988), p. 1898. KMSF-U1888.

G. Charatis, G. E. Busch, B. K. F. Young (LLNL), and R. E. Stewart (LLNL), "Diagnostic Characterization of Laser-Irradiated Dot Targets," Proceedings of the IAU Colloquium No. 102 on UV and X-ray Spectroscopy of Astrophysical and Laboratory Plasmas, edited by F. Bely-Dubau and P. Faucher, *J. Phys.* supplément au no. 3, **49** (March 1988), C1-375–C1-378.

R. L. Downs, M. A. Ebner, and W. J. Miller, "Hollow Glass Microspheres by Sol-gel Technology," *Sol-gel Technology for Thin Films, Fibers, Preforms, Electronics, and Specialty Shapes*, edited by L. C. Klein (Noyes Publishers, Park Ridge, NJ, 1988), pp. 330–381. KMSF-U1799.

R. L. Hays, "Introduction to SMG, the VMS Screen Management Utility," *Proceedings of the Digital Equipment Computer Users' Society (DECUS) Symposium* (Fall 1987), pp. 131–135. KMSF-U1978.

R. L. Hays and F. S. Schebor, "Mass-11 Document Archiving System," *Proceedings of the Digital Equipment Computer Users' Society (DECUS) Symposium* (Spring 1988), pp. 257–262. KMSF-U2076.

M. B. Knickelbein, K. L. Marsh, J. Sercel, L. D. Siebert, and Geo. E. Busch, "A Proposed Chemically Pumped Laser Based on the b → X Transition in O_2," *IEEE J. Quantum Electron.* **QE-24**(7) (July 1988), pp. 1278–1288. KMSF-U1882.

Z. M. Koenig, "A Soft X-ray Bragg Spectrograph with an Intensified Framing Camera," *Rev. Sci. Instrum.* **59**(8) (August 1988) pp. 1813–1815. KMSF-U2034.

H. K. Lintz, S. R. Murrell, R. L. Crawley, and J. C. Daukas, "The Deposition Rate Dependence of Plasma Polymerization on the Radius of Curvature of the Substrate," *J. Vac. Sci. Technol. A* **6**(3) (May–June 1988) pp. 1869–1871. KMSF-U1877.

A. J. Martin, R. J. Simms, and R. B. Jacobs (R. B. Jacobs Associates), "Beta Energy Driven Uniform Deuterium-Tritium Ice Layers in Reactor-size Cryogenic Inertial Fusion Targets," *J. Vac. Sci. Technol. A* **6**(3) (May–June 1988), pp. 1885–1888. KMSF-U1886.

P. D. Morley and J. Sugar (NBS) "Exploding Foil Photoionization X-ray Laser," *Phys. Rev. A* **38**(6) (September 1988), p. 3139. KMSF-U2016.

P. D. Morley and I. Schmidt (Univ. Santa Maria, Chile), "Quark Distributions in Nuclei," *Phys. Rev. C* **38**(3) (September 1988), pp. 1356–1364. KMSF-U2117.

M. T. Mruzek, J. S. Ankney, and D. N. Decker, "Apparatus for Verification of Beta Heating Driven Layer Uniformity in Solid Deuterium-Tritium," *J. Vac. Sci. Technol. A* **6**(3), (May–June 1988), pp. 1889–1890. KMSF-U1887.

M. T. Mruzek, D. L. Musinski, and J. S. Ankney, "Experimental Verification of Beta-Decay-Driven Sublimation in Deuterium-Tritium Ice Held in Spherical Fusion Targets," *J. Appl. Phys.* **63**(7) (April 1988), pp. 2217–2220. KMSF-U1960.

T. R. Pattinson and W. J. Felmlee, "A Real-Time Holographic Interferometry Technique for Measuring Cryogenic Fuel Layers in Large Inertial Confinement Fusion Targets," *J. Vac. Sci. Technol. A* **6**(3) (May–June 1988), pp. 1882–1884. KMSF-U1885.

D. A. Steinman, V. D. Caldwell, D. O. Husband, J. A. Ruppe, and S. C. Welch, "Spot Spectroscopy Targets Made from Powder," *J. Vac. Sci. Technol. A* **6**(3) (May–June 1988), pp. 1899–1900. KMSF-U1883.

R. G. Watt (LANL), R. S. Dingus (LANL), R. Green (LANL), R. R. Johnson, J. F. Kephart (LANL), R. Kopp (LANL), L. Lee (LANL), N. Moncur, W. Z. Osborne (LANL), T. A. Pucik (LANL), and T. J. Roemer (LANL), "The Long-Pulse Phase I Experiment," Los Alamos National Laboratory Technical Report DNA-TR-87-118 (November 3, 1987).

B. K. F. Young (LLNL), R. E. Stewart (LLNL), M. D. Rosen (LLNL), G. Charatis, and Gar. E. Busch, "Simultaneously Time- and Space-Resolved Characterization of Laser-Produced Plasmas," *X-Rays from Laser Plasmas*, edited by M. C. Richardson, Proc. SPIE 831 (1988), pp. 18–24.

DISTRIBUTION LIST FOR KMSF-U2116

University of California
Lawrence Livermore National Laboratory
P. O. Box 5508
Livermore, California 94550
- L. P. Altbaum, L-481
- T. P. Bernat, L-482
- E. M. Campbell, L-473
- L. W. Coleman, L-481
- J. L. Emmett, L-488
- K. G. Estabrook, L-477
- A. J. Glass, L-1
- C. W. Hatcher, L-482
- J. F. Holzrichter, L-481
- R. L. Kauffman, L-473
- W. L. Kruer, L-477
- W. F. Krupke, L-488
- B. F. Lasinski, L-477
- J. D. Lindl, L-477
- D. L. Matthews, L-473
- G. H. Miller, L-38
- J. H. Nuckolls, L-295
- R. L. Pond, L-302
- V. W. Slivinsky, L-45
- E. K. Storm, L-481

University of California
Lawrence Livermore National Laboratory
Attn: Laser Program Library
P. O. Box 5508
Livermore, California 94550

U.S. Department of Energy
Inertial Fusion Division
Mail Stop A-362, DP-243
Washington, DC 20545
- D. N. Bixler
- G. M. Chenevert
- G. J. D'Alessio
- C. B. Hilland
- S. L. Kahalas
- T. G. Owen
- M. W. Sluyter
- Thomas Wright

U.S. Department of Energy
San Francisco Operations Office
Attn: Henry Bowden, Administration & Information Services Division
1333 Broadway
Oakland, California 94612
- Dennis E. Neely
- M. K. Hooper

U. S. Department of Energy
Office of Scientific and Technical Information
Technical Information Center
P. O. Box 62 UC-400
Oak Ridge, Tennessee 37831

Sandia National Laboratory
Organization 1260
P.O. Box 5880
Attn: J. P. VanDevender
Albuquerque, New Mexico 87185

Los Alamos National Laboratory
Attn: ICF Program Manager
DAD/IF, M/S 527, P.O. Box 1663
Los Alamos, New Mexico 87545
- D. C. Cartwright, E-527
- D. V. Duchane, E-549
- D. W. Forslund, E-532
- W. C. Mead, E-531
- D. C. Wilson, E-531

Naval Research Laboratory
Washington, D.C. 20375
- S. E. Bodner

University of Rochester
250 East River Road
Rochester, New York 14627
- R. L. McCrory

U. S. Department of Energy
Attn: A. Bryan Siebert, Jr.
Office of Classification and Technology Policy
P.O. Box A/DP-32
Washington, DC 20545

DO NOT MICROFILM
THIS PAGE